NASA Technical Memorandum 83199
Part 3

Aircraft Noise Prediction Program Theoretical Manual

Propeller Aerodynamics and Noise

N8710491, 3 vol

Edited by
William E. Zorumski
Langley Research Center
Hampton, Virginia

Donald S. Weir
PRC Kentron, Inc.
Hampton, Virginia

P1444730

National Aeronautics
and Space Administration

**Scientific and Technical
Information Branch**

1986

PREFACE

The NASA Aircraft Noise Prediction Program (ANOPP) was developed originally for the prediction of airport community noise from turbofan-powered aircraft. The theoretical manuals for the original prediction system were published as NASA TM-83199, parts 1 and 2, in February 1982. Part 1 describes program modules which define the atmosphere, the flight of the aircraft, the propagation of the noise, and the subjective effects of the noise on the receiver. Part 2 describes program modules which define the turbofan engine noise sources and the airframe noise sources of CTOL aircraft.

The purpose of part 3 of the theoretical manual is to describe those additional program modules which are used to define propeller noise sources and the propagation of pure tones. Even though this part begins with chapter 10 to follow the numbered chapters of parts 1 and 2, the manual is written such that the chapters have minimal interdependence. The program user may rely on this part of the manual to define the propeller noise sources and then refer to parts 1 and 2 to find the effect of these sources on the airport community.

PRECEDING PAGE BLANK NOT FILMED

CONTENTS

Part 1*

2. AIRCRAFT FLIGHT DYNAMICS

3. PROPAGATION EFFECTS

4. SOURCE NOISE PARAMETERS

5. PROPAGATION

6. RECEIVED NOISE

7. UTILITIES

---

*Chapters 1 to 7 were published under separate cover in February 1982.

PRECEDING PAGE BLANK NOT FILMED

Part 2[†]

8. NOISE SOURCES

9. PREDICTION PROCEDURES

Part 3

10. PROPELLER AERODYNAMICS

[†] Chapters 8 and 9 were published under separate cover in February 1982.

11. PROPELLER NOISE

12. TONE PROPAGATION EFFECTS

10. PROPELLER AERODYNAMICS

10.1 PROPELLER ANALYSIS SYSTEM

William E. Zorumski
Langley Research Center

SUMMARY

The NASA Aircraft Noise Prediction Program (ANOPP) Propeller Analysis System is a set of computational modules for predicting the aerodynamics, performance, and noise of propellers. Propeller blade geometry is given in terms of blade surface coordinates derived from a Joukowski transform of the blade sections. Potential flow around the blade sections is computed by Theodorsen's method by using the Kutta condition to fix the circulation. Blade boundary layers are computed by using the Holstein-Bohlen method in the laminar region and the Truckenbrodt method in the turbulent region. Profile drag is predicted by the method of Young and Squires. Performance and induced flow are computed by Lock's method with the Prandtl circulation function near the blade tip. Discrete tone noise is predicted from blade shape and aerodynamic loads by using Farassat's methods: the blade surface integral method for subsonic propellers and the collapsing sphere method for transonic propellers. Broadband trailing-edge noise is computed by the method of Schlinker and Amiet. The results of this prediction system are compared with measurements on two propellers: one subsonic and one transonic. Near-field levels on the subsonic propeller are accurately predicted if the predicted power coefficient is adjusted to match the measured power coefficient of the propeller. The lower frequency harmonics of the subsonic propeller spectrum match the measured values but the high frequency harmonics are underpredicted. This underprediction is believed to be caused by the omission of unsteady loading effects in the predictions. The far-field or flyover noise of the subsonic propeller is scattered by atmospheric and ground effects but the general trend of the data indicates overprediction of far-field levels. Transonic propeller noise measured on the fuselage of the aircraft is significantly influenced by the refraction effects of the boundary layer on the fuselage. When these effects are included and when the power is matched, the transonic predictions agree with the data except in a small region just behind the propeller plane on the aircraft surface. It is believed that fuselage scattering effects may be the cause of this discrepancy.

INTRODUCTION

Propeller noise prediction is based on two disciplines: aerodynamics and acoustics. NASA has developed the Aircraft Noise Prediction Program (ANOPP) for aircraft noise prediction. This part of the manual develops the methods for propeller noise prediction by using the assumption that these disciplines are separable; that is, the flow field can be separated into an aerodynamic part and acoustic part. This separation allows the computations to be made sequentially. Classical aerodynamic theory is used to find the surface pressures and frictional stresses on the blade surfaces, and then acoustic theories are used to predict the noise.

The ANOPP propeller noise prediction system is diagrammed in figure 1. The different computational tasks are assigned to independent blocks of computer code called functional modules. These modules are managed by an executive system, the ANOPP executive program (ref. 1). One group of modules deals with the aerodynamic computations. Not shown are modules which compute atmospheric properties and flight dynamics. These modules are described in reference 2. The end products of the aerodynamics modules are the propeller blade motions and loads. Motions include only the aircraft motion and rotational effects. Flexing and vibration, while possibly important, are not included at this time. The loads are the pressure and frictional stress on the propeller blade surface. These loads are generally a function of both surface position and time. Given the blade motions and loads, it is theoretically possible to predict the noise. As a practical matter, however, this prediction is impossible. The loads are really nonstationary random processes, and there is presently no feasible computational procedure which will produce a complete description of the noise. The approximation is made that the noise may be divided into two parts: discrete and random. The discrete (tone) noise is computed directly from the blade motions and loads, whereas the random (broadband) noise is estimated by semi-empirical methods. The discrete noise computations are made entirely with time domain techniques, and random noise estimates use a blend of frequency and time domain concepts.

Noise predictions are needed in both the near and far fields. Near-field noise predictions are needed to find the noise transmitted to the interior of an aircraft. There are two important near-field effects on propeller-generated noise. These effects are the refraction caused by nonuniform flow over the aircraft and the scattering by the aircraft body. Far-field effects are needed to accurately predict community noise. These effects are the atmospheric attenuation and refraction, and the ground effects of reflection and absorption. Further information on the far-field propagation modules may be found in reference 2. Modules for the near-field effects are described in detail herein.

Agreement with experiment is the ultimate goal of a prediction system. Any prediction method - a guess, a curve fit, or a solution to a partial differential equation - is acceptable if it agrees with experimental data according to some objective rule. The question is how many experiments and how good must the agreement be to prove that a prediction is correct. This question raises another question: prove it to whom? You cannot prove to a member of the Flat Earth Society that the Earth is round.

Despite these minor difficulties, we gather data from experiments in the hope of proving that the prediction system is correct. These are described as flight data and tunnel data to denote the two types of facilities most frequently used to conduct the experiments. The flight data are usually but not always full-scale. Results will be shown later for two propellers: one subsonic design and one transonic design. The subsonic propeller is made by the TRW Hartzell Propeller Products Division and its noise was measured by a wing-mounted boom microphone in flight. The transonic propeller is the NASA SR-3 Propfan design. This roughly quarter-scale propeller was tested in flight mounted atop a JetStar aircraft.

SYMBOLS

a	radius of perfect circle
b	Joukowski transform parameter
C	blade section chord
C_D	energy dissipation coefficient
C_d	blade section drag coefficient, re section dynamic pressure and chord
C_f	skin friction coefficient, re section dynamic pressure
C_ℓ	blade section lift coefficient, re section dynamic pressure and chord
C_n	Theodorsen transform coefficients
C_P	power coefficient
C_p	coefficient of pressure, re section dynamic pressure
C_T	wall shear stress coefficient, re local dynamic pressure
c_∞	ambient speed of sound
D	drag
F	Prandtl tip vorticity function
H	altitude
H_{ij}	boundary-layer shape factors, $i \neq j = 1, 2, 3$
$H_m^{(1)}$, $H_m^{(2)}$	Hankel functions of the first and second kinds
J	advance ratio, V_∞/nD

k	$= \omega / c_\infty$
k_x, k_y, k_r	wave numbers
L	lift
ℓ	$= \lvert \vec{\ell} \rvert$
$\vec{\ell}$	loading intensity vector
ℓ_r	component of $\vec{\ell}$ in radiation direction
ℓ_y	empirical broadband correlation length
M	blade section Mach number
M_f	forward Mach number
M_h	tip helical Mach number
M_n	normal Mach number
M_r	radiation Mach number
M_t	tip rotational Mach number
M_∞	free-stream or forward Mach number
m	circumferential harmonic number
N	number of blades
n	revolutions per second
$\vec{n}$	normal to blade surface
OASPL	overall sound pressure level
p	acoustic pressure
p_{rms}	root-mean-square pressure
Q	torque
R	propeller disk radius
r, θ, z	cylindrical coordinates
$\vec{r}$	radiation vector, $\vec{x} - \vec{y}$
$\hat{r}$	unit radiation vector

SPL	sound pressure level at a single frequency
S	surface area
$S(\omega)$	empirical broadband spectrum
T	thrust, period of signal, or transfer function
t	time
$\vec{t}_1$, $\vec{t}_2$	tangents to blade surface in spanwise and chordwise directions, respectively
$U(x)$	velocity at edge of boundary layer
$U(y)$	local Mach number in boundary layer
V_∞	free-stream velocity
v	normal acoustic velocity
$\vec{v}$	acoustic velocity vector
v_δ	normal acoustic velocity at edge of boundary layer
$W(\zeta)$	complex velocity field around perfect circle
x	distance along chord or distance along airfoil surface measured from stagnation point; coordinate in flow direction
$\vec{x}$	observer position in media-fixed reference frame
y	coordinate normal to flow direction
$\vec{y}$	source position in media-fixed reference frame
z	complex plane of the airfoil section
α	blade section angle of attack
α'	angle-of-attack perturbation
$\beta_{.75}$	blade pitch at 3/4 span
Γ	circulation around airfoil section or curve of intersection of collapsing sphere and propeller blade surface
δ	boundary-layer thickness
δ_1	boundary-layer displacement thickness
δ_2	boundary-layer momentum thickness
δ_3	boundary-layer energy thickness

ε	polar coordinate angle difference between near circle and perfect circle
ζ	complex plane of airfoil section represented as a perfect circle
ζ'	complex plane of airfoil section represented as a near-circle
η_1, η_2, η_3	pitch axis coordinates fixed to propeller; η_2 is along pitch axis and η_3 is along forward shaft axis
θ	angle between normal vector and radiation vector
λ	advance ratio, M_∞/M_t
ξ_1, ξ_2	blade surface coordinates; ξ_1 varies with span, ξ_2 varies with chord
ρ_∞	ambient density
σ	propeller solidity
τ	retarded time
ϕ	blade section inflow angle
ψ	elliptic blade thickness function
Ω	propeller angular velocity
ω	angular frequency

Subscripts:

i	induced
L	leading edge
r	refraction effect
S	stagnation point
s	scattering effect
T	trailing edge
tr	transition point
∞	free stream

Notation:

~	time dependent
—	mean
→	vector
'	derivative with respect to argument

AERODYNAMIC PREDICTION

Geometry

Although geometry is given rather than predicted, it is worthwhile to carefully consider the way geometric data are utilized. Two coordinates are required to specify a point on a surface. It is important to choose surface coordinates such that the functions of these coordinates will be single valued and free of singularities at least up to their second derivatives; that is, functions of the surface coordinates will be of class C^2. The selected surface coordinates should also provide a convenient computational grid.

Figure 2 shows the basic coordinate system (y_1, y_2, y_3) used to describe the propeller. At time $t = 0$, a rotating coordinate system (η_1, η_2, η_3) coincides with the (y_1, y_2, y_3) system. The shaft axis is η_3, the blade pitch axis is η_2, and the η_1-axis completes an orthogonal triad. Section A-A through the blade at constant span positions gives the first surface coordinate

$$\xi_1 = \eta_2 \tag{1}$$

At each section, a Joukowski transform (see ref. 3, for example)

$$z = \zeta' + \frac{b^2}{\zeta'} \tag{2}$$

where

$$z = \eta_1 + i\eta_3 \tag{3}$$

$$\zeta' = be^{\psi + 2\pi i \xi_2} \tag{4}$$

is used to introduce the second surface coordinate ξ_2. The blade section elliptical coordinate $\psi(\xi_2)$ resulting from this transformation is shown in figure 3. The blade section is described by the function $\psi(\xi_2)$. The blade surface is unwrapped by the Joukowski transform if the first surface coordinate ξ_1 is chosen to equal η_2. The surface function $\psi(\xi_1, \xi_2)$ is single valued, continuous, and slowly varying in the surface coordinates (ξ_1, ξ_2) as shown in figure 3. The computation grid stretches the region near the leading edge, $\xi_2 = 0.5$, so that aerodynamic functions such as the coefficient of pressure C_p will be slowly varying in this region. In this computational space, bicubic splines are suitable interpolating functions and will be used in all subsequent computations.

Potential Field

The potential flow field around each airfoil section ξ_1 = Constant is given by a conformal transformation of the flow around a perfect cylinder (ref. 3). The blade geometry analysis has already produced part of the desired transformation by mapping the airfoil section in the z-plane as shown in figure 4. Recall that the airfoil thickness function $\psi(\xi_1,\xi_2)$ was generated by inverting the Joukowski transformation:

$$z = \zeta' + \frac{b^2}{\zeta'} \tag{5}$$

This transformation may now be used directly to map a given flow around the near-circle into a flow around the airfoil section.

Theodorsen's transformation (ref. 4) maps the ζ-plane of the perfect circle into the ζ'-plane of the near-circle

$$\zeta' = \zeta \exp\left(\sum_{n=1}^{\infty} \frac{C_n}{\zeta^n}\right) \tag{6}$$

The constants C_n in Theodorsen's transformation are found from the shape of the airfoil in the ζ'-plane. After numerically solving for these constants, it is found that the trailing-edge point of the airfoil is displaced by a small angle ε_T from the real axis of the ζ-plane. This point is required to be a stagnation point for the flow around the cylinder in order to satisfy the Kutta condition that trailing-edge velocities are finite.

The complex flow function around the perfect circle is

$$W(\zeta) = M\left(e^{-i\alpha} - \frac{a^2}{\zeta^2}e^{i\alpha}\right) + \frac{i\Gamma}{2\pi\zeta} \tag{7}$$

where M is the local Mach number (for the section), α is the angle of attack, a is the radius of the circle, and Γ is the circulation. The trailing-edge stagnation point is

$$\zeta_{ST} = ae^{i\varepsilon_T}$$

which, with $W(\zeta_{ST}) = 0$, gives the circulation Γ as

$$\Gamma = 4\pi aM \sin(\alpha - \varepsilon_T) \tag{8}$$

The leading-edge stagnation point, a second solution to the equation for $W(\zeta_S)$ is

$$\zeta_{SL} = ae^{i(2\alpha-\varepsilon_T+\pi)} \tag{9}$$

The cross product of the velocity vector and the circulation vector gives the lift

$$C_\ell = 2\pi \frac{4a}{C} \sin(\alpha - \varepsilon_T) \tag{10}$$

The coefficient of pressure is found from the velocity in the z-plane of the airfoil:

$$C_p = 1 - \left| \frac{W(z)}{M} \right|^2 \tag{11}$$

The complex velocity in the z-plane is found by using the derivatives of the transformations

$$W(z) = \frac{d\zeta}{d\zeta'} \frac{W(\zeta)}{\frac{dz}{d\zeta'}} \qquad (\zeta' \neq \zeta'_S) \tag{12}$$

At the stagnation points in the ζ-plane, the limit of equation (12) is used:

$$W(z) = \frac{d\zeta}{d\zeta'} \lim_{\zeta' \to \zeta'_S} \frac{W(\zeta)}{\frac{dz}{d\zeta'}} \tag{13}$$

Since the Joukowski transformation has a singularity at the trailing edge, $W(\zeta)$ will have a finite nonzero limit at this point. This limit causes the coefficient of pressure at the trailing edge to have magnitude less than 1.

Figure 5 shows the blade section data computed by the blade section potential flow analysis. The coefficient of pressure C_p has a maximum of unity at the leading-edge stagnation point ξ_{2S}. The lower surface C_p is generally positive, decreasing to a small value near the trailing edge $\xi_2 = 1.0$, where the airfoil surface velocity is near the free-stream velocity. The upper surface C_p may become negative with high velocities around the highly curved leading edge. The upper surface C_p then approaches a small negative value at the trailing edge $\xi_2 = 0$. The lift coefficient C_L has a slope of approximately 2π when plotted as a function of α.

The function of the Blade Section Aerodynamics Module is summarized as follows. Input is the blade shape function $\psi(\xi_1, \xi_2)$ and the parameters α and M. The module maps the flow around a perfect cylinder into the flow around the blade by using the Theodorsen and Joukowski transforms. Outputs are the section lift coefficient C_ℓ

and leading-edge stagnation point ξ_{2S} as a function of span position ξ_1 and the parameters α and M. The output coefficient of pressure depends on surface position (ξ_1,ξ_2) and the parameters α and M. The stagnation-point location and the coefficient of pressure are used in the boundary-layer analysis which follows.

Boundary Layer

The Blade Section Boundary-Layer Module computes the two-dimensional boundary layer on each airfoil section as shown in figure 6. The blade arc length x is measured from the stagnation point on the leading edge. The initial portion of the boundary layer is laminar. Transition to turbulent flow occurs near the point where the external velocity $U(x)$ is a maximum. This turbulent layer continues to the trailing edge unless separation occurs.

The governing equations for the boundary-layer thicknesses are the integral momentum equation for $\delta_2(x)$ and the integral energy equation for $\delta_3(x)$. The displacement thickness $\delta_1(x)$ is related to the momentum and energy thicknesses through the assumed profile $U(y)$ for the boundary layer.

The governing equations for $\delta_2(x)$ and $\delta_3(x)$ are

$$\frac{d\delta_2(x)}{dx} + \left(\frac{2 + H_{12}}{U} \frac{dU}{dx}\right) \delta_2(x) = C_T \tag{14}$$

$$\frac{d\delta_3(x)}{dx} + \frac{3}{U} \delta_3(x) = C_D \tag{15}$$

The shape factor H_{12} is a given function of the thicknesses δ_2 and δ_3 and the external velocity gradient $\frac{dU}{dx}$. The coefficient C_T is the local wall shear stress coefficient and the coefficient C_D is the energy dissipation coefficient.

In the laminar layer, C_T is known from the assumed boundary-layer velocity profile and equation (14) can be integrated to find $\delta_2(x)$ without solving for the energy thickness. The method of Holstein and Bohlen (ch. X of ref. 5) is used to integrate this equation. Transition is assumed to occur when the external velocity is a maximum; that is, where

$$\frac{dU(x_{tr})}{dx} = 0 \tag{16}$$

Both equations must be integrated in the turbulent region. Truckenbrodt's method (ch. XXII of ref. 5) is used for this purpose. The coefficients C_T and C_D are given by empirical functions in the turbulent region.

The section profile drag coefficient is computed by the method of Young and Squire (ch. XXV of ref. 5). In this method, the wake thickness at infinity is estimated by the empirical formula

$$\delta_{2,\infty} = \delta_2(x_T) \left(\frac{U(x_T)}{U_\infty} \right)^{3.2} \tag{17}$$

and the section drag coefficient, referred to the chord, is

$$C_d = 2\left(\frac{\delta_{2,\infty}}{C}\right) \tag{18}$$

The Blade Section Boundary-Layer Module computes the skin friction coefficient C_f (fig. 7) for use later in the Propeller Loading Module. It provides the drag coefficient C_d for propeller performance analysis and for the computation of lifting line (compact source) loads. The trailing-edge thicknesses $\delta_1(x_T)$ and $\delta_2(x_T)$ are used in the scaling laws for trailing-edge broadband noise.

Propeller Performance

Computation of the propeller performance depends on a solution for the induced velocity field. This induced field at a blade section is shown in figure 8. Propeller performance is predicted by the method of Lock (ref. 6). The Blade Section Aerodynamic Module gives tables of section lift functions $C_\ell(\xi_1,\alpha,M)$. The Blade Section Boundary-Layer Module gives tables of $C_d(\xi_1,\alpha,M)$. These tables are used in the prediction of propeller performance coefficients C_P and C_T for given tip and forward Mach numbers M_t and M_∞ of the propeller. The helical Mach number at a blade section M_h (fig. 9) is known from its components. These components are the axial Mach number of the propeller M_∞ and the rotational Mach number at the section $\xi_1 M_t$, where M_t is the tip rotational Mach number $R\Omega/c_\infty$. The local induced Mach vector M_i must be found to compute the total local Mach vector by

$$\vec{M}_h = \vec{M}_i + \vec{M} \tag{19}$$

This vector is represented by its magnitude M and the inflow direction angle ϕ as shown in figure 9. Differential components of lift dL and drag dD on the section are rotated through the inflow angle ϕ to give the differential thrust force dT and torque force dQ. These differentials are then integrated over the blade length and converted to performance coefficients: the torque or power coefficient C_P and the thrust coefficient C_T. The two components of the induced Mach vector are supplied by solving the two equations for the change of momentum in the far wake of the propeller. The increase in axial momentum, the value downstream minus the value upstream, is equal to the thrust force. The increase in angular momentum is equal to the propeller torque. These balance equations are

$$2M \sin \phi \, (M \sin \phi - M_\infty) \, F(\xi_1,\lambda) = \frac{1}{2} M^2 \sigma(\xi_1)[C_\ell \cos \phi - C_d \sin \phi] \tag{20}$$

$$2M \sin \phi \, (\xi_1 M_t - M \cos \phi) \, F(\xi_1,\lambda) = \frac{1}{2} M^2 \sigma(\xi_1)[C_\ell \sin \phi + C_d \cos \phi] \tag{21}$$

The factor of 2 on the left side of these equations represents the fact that velocities in the far wake are twice those at the propeller disk. The factor $M \sin \phi$ represents the mass flow through the disk. The factor $(M \sin \phi - M_\infty)$ in the thrust equation is the axial-induced Mach number and the factor $(\xi_1 M_t - M \cos \phi)$ is the angular-induced Mach number. The Prandtl circulation function $F(\xi_1,\lambda)$ (ref. 7) is derived from vorticity theory. It is defined by

$$F = \frac{2}{\pi} \text{Arccos} \left\{ \exp \left[- \frac{N}{2} (1 - \xi_1) \frac{(1 + \lambda^2)^{1/2}}{\lambda} \right] \right\} \tag{22}$$

and is an approximate way of representing Goldstein's circulation function (ref. 8). This solution procedure was developed in 1930 by Lock (ref. 6).

Loading

Blade loads are computed by combining results of the aerodynamics, boundary layer, and performance modules as shown in figure 10. The lift and drag coefficients are three-dimensional tables in terms of span position ξ_1, angle of attack α, and Mach number M. The surface stress coefficients C_p and C_f are four-dimensional tables in terms of surface position ξ_1 and ξ_2, angle of attack α, and section Mach number M. The performance analysis produces actual values $\alpha(\xi_1)$ and $M(\xi_1)$ for the propeller operating conditions M_∞ and M_t. There may be an additional angle-of-attack perturbation $\alpha'(\xi_1,t)$ due to small nonuniformities in the propeller inflow.

When the stress and loading coefficient tables are interpolated with these functions, the coefficients become actual time-dependent values

$$C_\ell(\xi_1,t) = C_\ell[\xi_1,\tilde{\alpha}(\xi_1,t),M(\xi_1)] \tag{23}$$

$$C_d(\xi_1,t) = C_d[\xi_1,\tilde{\alpha}(\xi_1,t),M(\xi_1)] \tag{24}$$

$$C_p(\xi_1,\xi_2,t) = C_p[\xi_1,\xi_2,\tilde{\alpha}(\xi_1,t),M(\xi_1)] \tag{25}$$

$$C_f(\xi_1,\xi_2,t) = C_f[\xi_1,\xi_2,\tilde{\alpha}(\xi_1,t),M(\xi_1)] \tag{26}$$

where

$$\tilde{\alpha}(\xi_1,t) = \alpha(\xi_1,t) + \alpha'(\xi_1,t) \tag{27}$$

Replacing the parametric arguments α and M by actual arguments reduces the lift and drag tables to two dimensions and the stress coefficient tables to three dimensions. If steady loadings are assumed, the loading tables are reduced by a further dimension. These loading tables are passed to the discrete noise prediction module for noise prediction. The line loads $C_\ell(\xi_1,t)$ and $C_d(\xi_1,t)$ are used in compact source theories and the distributed loads $C_p(\xi_1,\xi_2,t)$ and $C_f(\xi_1,\xi_2,t)$ are used in the general noncompact source theories. A similar transformation of the boundary-layer thicknesses is used to supply data to the Propeller Trailing-Edge Noise Module.

ACOUSTIC PREDICTION

Discrete Tone Noise

Subsonic Noise.- Discrete tone noise is predicted by the method of Farassat (ref. 9). Farassat's equation for the noise of a subsonic propeller is

$$4\pi p(\vec{x},t) = \frac{\partial}{\partial t}\int_{\text{blade}}\left(\frac{M_n + \ell_r}{r\left|1-M_r\right|}\right)_\tau dS + \int_{\text{blade}}\left(\frac{\ell_r}{r^2\left|1-M_r\right|}\right)_\tau dS \tag{28}$$

The terms in equation (28) are illustrated in figure 11. Pressure is computed at a particular observer position $\vec{x}$ and time t. Two integrals are evaluated to give the total pressure. The integrals are over the surface area of the propeller blade and the integrands are evaluated at the time τ when the sound is emitted at the surface position $\vec{y}(\tau)$. The radiation vector $\vec{r}$ is the difference between the observer and source positions

$$\vec{r} = \vec{x}(t) - \vec{y}(\tau) \tag{29}$$

The normal vector $\vec{n}$ and surface area dS are given by

$$\vec{n}dS = \frac{\partial\vec{n}}{\partial\xi_1} \times \frac{\partial\vec{n}}{\partial\xi_2} \tag{30}$$

and the velocity vector is

$$\vec{v} = \vec{M}_\infty + \vec{\Omega} \times \vec{n} \tag{31}$$

The loading vector is

$$\vec{\ell} = \frac{M^2}{2}\left(\pm C_f\vec{t}_2 + C_p\vec{n}\right) \tag{32}$$

where the positive sign is used on the lower surface between the stagnation point on the lower surface and the trailing edge. The base vector $\vec{t}_2$ is tangent to the surface and in the chordwise direction. A unit vector in the radiation direction $\hat{r}$ is used to define

$$M_r = \hat{r} \cdot \vec{v} \tag{33}$$

and

$$\ell = \hat{r} \cdot \vec{\ell} \tag{34}$$

Integration of equation (28) is straightforward except for the solution for retarded time. The basic retarded-time equation requires the distance from the source to the observer to be compatible with the propagation time:

$$\vec{r} \cdot \vec{r} = \left|\vec{x}(t) - \vec{y}(\tau)\right|^2 = (t - \tau)^2 \tag{35}$$

In the case of a propeller moving along its own axis, the retarded time equation can be reduced to

$$A_0(t - \tau)^2 + 2B_0(t - \tau) + C_0 + C_1 \cos \tau = 0 \tag{36}$$

Equation (36) has the appearance of a quadratic equation in $(t - \tau)$ except for the coefficient $C = C_0 + C_1 \cos \tau$. It can be shown, however, that there is a single real solution $\tau < t$ to this equation as long as the motion of the propeller is subsonic.

Transonic noise.- Supersonic noise is computed by Farassat's collapsing-sphere method. The subsonic equation cannot be used on any portion of the blade when M_r may exceed unity because of the $|1 - M_r|$ singularity. In addition, the retarded time equation has multiple roots. The collapsing-sphere method is illustrated in figure 12. The collapsing sphere intersects the blade surface in a curve called the Γ-curve. Farassat has shown that

$$\frac{dS}{\left|1 - M_r\right|} = \frac{d\Gamma \, d\tau}{\sin \theta} \tag{37}$$

The integrals for noise are thus evaluated by choosing a set of times τ and integrating first along the Γ-curves with fixed source time and then over source time. This method was developed by Nystrom and Farassat in reference 10.

Recent advances.- The time derivative $\frac{\partial}{\partial t}$ in Farassat's acoustic equation increases the computation time because at least two integrals must be evaluated to numerically compute the derivative. Numerical differentiation also introduces some spurious wiggles in the pressure signature which appear as increases in the higher harmonics of the transformed signal. Recently, Farassat (ref. 11) has taken the derivatives inside the integral for both the subsonic and supersonic cases. The differentiation under the integral has shown that the noise depends on blade surface curvatures. The full implications of this exciting new result are not completely known at this time and are a subject of continuing research. The subsonic method used here has the derivatives taken inside the integral. The transonic method has the derivative left outside the integral.

Broadband Noise

Broadband noise is generated by turbulence convected past the trailing edge of the airfoil as shown in figure 13. The mean-square pressure spectrum is given by Schlinker and Amiet (ref. 12) as

$$\langle p^2(\vec{x},\omega)\rangle = \int_{\substack{\text{Trailing}\\ \text{edge}}} \frac{1}{4}\left[\frac{k_x M z C}{2\pi\sigma^2}\left|L^2\right| \ell_y(\omega)\; S(\omega)\right]_\tau ds \qquad (38)$$

where

$$k_x = \frac{\omega}{U} \qquad (39)$$

$$\sigma = \left[x^2 + \beta^2(y^2 + z^2)\right]^{1/2} \qquad (40)$$

and β is the compressibility factor $\left(=(1 - M^2)^{1/2}\right)$. The function L is the "effective lift" function derived by Amiet (ref. 12) for an observer at retarded position (x,y,z). The function $\ell_y(\omega)$ is an empirical correlation length

$$\ell_y(\omega) = \frac{2.1U_c}{\omega} \qquad (41)$$

where U_c is the turbulence convection velocity which is about 0.8U.

The spectrum function $S(\omega)$ is an empirical function for the blade surface pressure spectrum at the trailing edge:

$$S(\omega) = \left(2 \times 10^{-5}\right)\left(\frac{1}{2}\rho_\infty U^2\right)^2 \frac{\delta_1}{U} F(\tilde{\omega}) \qquad (42)$$

where

$$\tilde{\omega} = \frac{\omega\delta_1}{U}$$

and

$$F(\tilde{\omega}) = 33.28\tilde{\omega}\,(1 - 5.49\tilde{\omega} + 36.7\tilde{\omega}^2 + 0.151\tilde{\omega}^4)^{-1} \qquad (43)$$

Near-Field Effects

Two effects are present in the near field of the propeller which may significantly alter the received noise. These effects are the scattering by the aircraft wings and fuselage and the refraction by the boundary layer on the surface of the aircraft.

Scattering.- The scattering effect is illustrated in figure 14 for a cylindrical fuselage. The free-field levels on the surface of a cylindrical fuselage are calculated by one of the previously described methods for discrete noise. This incident field $p_i(\omega,\theta,x)$ is transformed by

$$p_i(\omega,m,k_x) = \frac{1}{2\pi}\int_0^{2\pi}\int_{-\infty}^{\infty} e^{-i(k_x x+m\theta)} \quad p_i(\omega,\theta,x)\ dx\ d\theta \qquad (44)$$

to give the incident field in a wave-number space. The solution for the total pressure on the fuselage surface can then be found by superimposing the general solutions for incident and scattered cylindrical waves such that the boundary condition

$$\left.\frac{\partial p(\omega,m,k_x)}{\partial r}\right|_{r=a} = 0 \qquad (45)$$

is satisfied. The result for the total surface pressure can be given by the transfer function:

$$p_t(\omega,m,k_x) = 2T_s(\omega,m,k_x)\ p_i(\omega,m,k_x) \qquad (46)$$

where

$$T_s(\omega,m,k_x) = -\frac{i\pi k_r a}{2}\ H_m^{(1)'}(k_r a)^{-1} \qquad (47)$$

$$k_r = (\omega^2 - k_x{}^2)^{1/2} \qquad (48)$$

The factor of 2 in equation (46) is shown explicitly to represent the effect of pressure doubling. With this form, the transfer function for scattering approaches unity for high frequencies as may be seen from the asymptotic forms for the Hankel functions. Following the computation of total pressure p_t in wave-number space, an inverse transform is used to find the surface pressure as a function of position (θ,x).

Refraction.- The boundary-layer velocity profile alters the sound pressure level on the surface of the fuselage by turning the waves propagated upstream away from the surface and turning waves propagated downstream into the surface. This effect is depicted in figure 15. This refraction effect is small for aircraft in low speed flight but becomes significant at the higher subsonic Mach numbers.

A simple model of the refraction effect neglects scattering and uses the two-dimensional wave equation in a sheared flow as the basis for finding a transfer function. The sheared-flow wave equation is

$$(\omega - Uk_x)\frac{d^2p}{dy^2} + 2\frac{dU}{dy}\ k_x\frac{dp}{dy} + (\omega - Uk_x)[(\omega - Uk_y)^2 - k_x^2]p = 0 \qquad (49)$$

This equation can be integrated, given the boundary-layer velocity profile $U(y)$, from the surface where $y = 0$ to the edge of the boundary layer where $y = \delta$. Initial conditions at the surface are an assumed unit pressure and zero pressure gradient:

$$p(0) = 1 \tag{50a}$$

$$\frac{dp(0)}{dy} = 0 \tag{50b}$$

Integrating equation (49) with initial conditions (eqs. (50)) gives the pressure p_δ and velocity v_δ at the edge of the boundary layer. These results must be scaled to match the pressure in the known incident wave field. The process of matching the incident field produces a transfer function for refraction:

$$T_r(\omega,k,k_x) = \frac{k_y}{k_y\, p_\delta(\omega,k_x) - (\omega - Uk_x)\, v_\delta(\omega,k_x)} \tag{51}$$

Numerical integration of the sheared flow equation breaks down at the regular singular point $\omega - Uk_x = 0$, which corresponds to the coincidence of wave speed with flow speed in the boundary layer. Special techniques beyond the scope of this paper have been used to integrate the sheared-flow wave equation (49) in these cases.

Combined effects.- The combined effects of scattering and refraction may be found by integrating the sheared-flow equation in cylindrical coordinates to find the cylindrical wave pressure p_δ and velocity v_δ at the edge of the boundary layer. Matching the external field then gives a combined transfer function:

$$T_{sr}(\omega,m,k_x) = \frac{k_r\, H_m^{(2)}(z)}{\{[-i\, \frac{\pi z}{2}\, H_m^{(1)'}(z)\, H_m^{(2)}(z)]k_r p_\delta - [\frac{\pi z}{2}\, H_m^{(1)}(z)\, H_m^{(2)}(z)](\omega - Mk_x)v_\delta\}} \tag{52}$$

where

$$z = k_r(a + \delta) \tag{53}$$

Far-Field Effects

Noise propagated to the far field is modified by the effects of atmospheric attenuation and ground reflections and attenuation. Since phase information tends to be lost after propagation over long distances, far-field noise effects are applied to the mean-squared pressure spectrum of the noise rather than to the pressure itself (ref. 2).

Atmospheric attenuation.- The effect of atmospheric attenuation is computed by the ANSI method described in section 3.1 of reference 2. The mean-squared pressure on a source sphere of fixed radius r_s is reduced by the spherical spreading effect and atmospheric attenuation. The transfer function for attenuation T_a is a decaying exponential function $\exp(-2\alpha r)$. The attenuation rate α is a function of frequency. The lower frequencies are dominated by the effect of nitrogen relaxation. Mid frequencies are usually dominated by oxygen relaxation effects and the higher frequencies are dominated by the classical absorption effects of conductivity, viscosity, and rotational modes of molecular vibration. The ANSI-proposed standard method is used for the calculation of attenuation effects for both standard and nonstandard conditions.

Ground effects.- The far-field noise is reflected and attenuated by the ground. This effect may be represented in the transfer function T_g developed by Pao, Wenzel, and Oncley in reference 13. This transfer function is based on the complex reflection coefficient $Re^{i\phi}$ for a spherical wave over an impedance plane. The factor R is the magnitude of the reflection which is equal to or less than unity. The factor ϕ is the phase shift between the reflected and incident waves. The magnitude of the noise at the observer depends on the difference in the lengths of the direct ray path and the reflected or image ray path. The magnitude of the received noise is diminished slightly by the loss of coherence of the direct and reflected signals. This coherence loss also depends on the path length difference.

COMPARISONS WITH EXPERIMENTS

Subsonic Propeller

Noise predicted by this system has been compared with noise measured during the flight of the twin-engined aircraft shown in figure 16. The aircraft was fitted with a wing-mounted microphone boom which could be moved to measure the noise in front of and behind the propeller plane. Noise was also measured on the ground with level flights over the measurement point.

Propeller performance.- An intermediate check of the prediction system was made by Block and Martin (ref. 14) by using a 1/4-scale model of the twin aircraft propeller on a propeller test stand (fig. 17) at the Langley Research Center.

Computed and measured power coefficients are shown in figure 18 as a function of advance ratio $J = V_\infty/nD$ and 3/4-span pitch setting $\beta_{.75}$. The predicted power coefficient is near the measured values at the lower pitch settings but rises above the measured power at the higher settings where it is believed that the propeller is in a condition of partial stall. Similarly, the predicted thrust coefficient C_T (fig. 19) is above the measured value with fair agreement at the low pitch settings and poor agreement at the high pitch and thrust values.

Effective pitch.- Pitch was not measured during the flight of the aircraft when the noise was measured. In order to find an effective value for the pitch setting $\beta_{.75}$ to use in noise predictions, the measured power in flight was used to compute the power coefficient C_P. An effective pitch setting $(\beta_{.75})_{eff}$ was then found such that the predicted power coefficient matched the measured value. This effective pitch will be less than the pitch setting on the 1/4-scale model for the same C_P.

Propeller noise. Near-field noise measured in flight is shown in figure 20. The measured noise data were sampled with data blocks of 96 time points per shaft revolution which gave 32 points per blade for the three-blade propeller. Fifty blocks of data were ensemble averaged to find the mean signal $p(t)$ shown in figure 20. Signal number 1 is for one-third of a propeller revolution. Signals 2 and 3 which complete the revolution are similar. The standard deviation $\sigma(t)$ was nearly constant, indicating that the measured noise could be decomposed into discrete and random parts as follows:

$$p(t) = \bar{p}(t) + p'(t) \tag{54}$$

where $p'(t)$ is a stationary random signal. Sound pressure spectra were generated for each data block and for the ensemble-averaged data. The discrete spectrum $|\bar{p}(\omega)|^2$ and the random spectrum $|p'(\omega)|^2$ are added to give the total spectrum $|p(\omega)|^2$.

$$|p(\omega)|^2 = |\bar{p}(\omega)|^2 + |p'(\omega)|^2 \tag{55}$$

The spectral data shown in figure 21 are relative to the overall mean-squared pressure

$$\langle \bar{p}^2 \rangle = \lim_{T \to \infty} \frac{1}{2T} \int_{-T}^{T} \bar{p}^2(t)\, dt \tag{56}$$

The overall mean-squared pressure in figure 21 is within 1.8 dB of the measured value. This agreement may be due in part to the matching of power through the effective pitch setting procedure.

The predicted spectrum agrees well with the data for the first few harmonics. Starting at about the 5th harmonic, the measured discrete spectrum shows a cyclic pattern suggestive of cancellation and reinforcement which is not predicted. This pattern gives levels from the 10th and 15th harmonics which are more than 20 dB above the predicted values. A significant part of this underprediction is probably due to the omission of unsteady loads in the analysis. Despite these high-frequency errors, the predicted A-weighted sound pressure level will be in good agreement with the measured values because of the rapid decay of the levels with frequency.

The error in the discrete spectrum may be due to any of several effects, including the obvious possibility of an error in the prediction method. Scattering from the wing and fuselage was not included in these computations. Computations are made for one propeller and there may be a small contribution from the second propeller which contributes to the error.

In making the predictions, it was assumed that all blades are identical, whereas, in practice, there are slight blade-to-blade differences which may result in the reinforcement patterns seen here. There is regrettably no way to examine these possible sources of error without further detailed experimentation.

Far-field noise from the flyover of the twin-propeller aircraft is shown in figures 22 and 23. The limited data shown in figure 22 are for flyovers with the reception angle $\theta = 90°$ being the directivity angle when the sound is received. The prediction is 5 to 6 dBA above the average of the measured levels. The reason for the overprediction is shown in figure 23. The level for the first harmonic, which dominates the predicted source spectrum, is indicated by the data to be less than the second harmonic. The reason for this effect is unknown and a much larger data set should be examined before any conclusions are drawn. Flyover noise data for propellers typically scatter over a range of about 10 dB (see ref. 15) so that statistical methods must be used to assess the accuracy of predictions.

Advanced Turboprop

Predictions have been made for the eight-bladed advanced turboprop propeller designated as SR-3. Since this propeller was operating at transonic conditions, the elementary aerodynamics and loading methods described earlier could not be used. A loading distribution was estimated by the propeller manufacturer and this distribution was adjusted such that the computed power matched the power measured during the flight test of the propeller.

The propeller was tested in flight atop the JetStar aircraft shown in figure 24. Performance data were also obtained in the wind tunnel as shown in figure 25. Microphones were mounted in the surface of the fuselage along a line under the axis of the propeller. Measured noise data were reduced by using ensemble-averaging techniques as described earlier. Only the results of the discrete noise data and predictions are shown herein.

Figure 26 shows a comparison of the measured and predicted noise at the cruise Mach number of 0.80. The helical Mach number of the blade tip is 1.13 for this example. Levels shown are for the blade passing harmonic which, remembering the subsonic results, is expected to give the best agreement with the measured data. Nystrom and Farassat's PROPFAN program (ref. 10) was used to predict the free-field noise at the top of the boundary layer. The boundary-layer profile was measured with rakes mounted on the fuselage of the JetStar. The two-dimensional transfer function for the boundary layer was then used to predict the noise on the surface beneath the boundary layer. It is apparent that the boundary layer has a significant effect on the surface noise at this flight speed. The predictions agree better with the data both in front of and behind the plane of the propeller.

The causes of the discrepancy between predicted and measured levels on the JetStar just behind the propeller plane are being investigated at this time. The scattering effect given by equation (47) will be evaluated first to see how scattering modifies the predicted surface pressures in the absence of a boundary layer. Following this the combined effects of scattering and refraction will be computed by using the transfer function (eq. (52)).

CONCLUDING REMARKS

NASA ANOPP system for predicting propeller noise has been described in this section. The objective of this system is to predict noise directly from the shape and motion of the propeller blades. This objective requires aerodynamic computations to be made as a basis for the acoustic computations. The aerodynamic theories used are simple classical methods.

These methods overpredict the performance of the propellers which results in an error in the acoustic predictions. An empirical correction procedure of matching predicted and measured power was used to compensate for the known error in aerodynamic performance. The acoustic predictions give good agreement with the low-frequency discrete noise when they are adjusted by the power matching procedure. It is believed that improved aerodynamic theories will give good low-frequency predictions for subsonic propellers without an empirical correction for power.

The accuracy of the acoustic predictions decreases with increasing frequency. Errors of 10 dB or more may occur at or above the 10th harmonic of the blade passing frequency in the case of subsonic propellers. When the propeller has nearly steady loading, these errors do not seriously affect integrated measures of noise such as the A-weighted sound pressure level because the A-level is dominated by lower harmonics. The prediction methods used are believed to be adequate for subsonic propellers operating in a tractor configuration where the loads are nearly steady. There is a need for further investigation of noise from subsonic propellers operating as pushers where the unsteady loads increase the levels of the higher harmonics relative to the fundamental.

Near-field effects of scattering and boundary-layer refraction significantly alter the noise levels of the fuselage of the aircraft. The boundary-layer refraction effect reduces the surface noise in front of the propeller and increases the noise behind the propeller. This effect is significant for an aircraft with high subsonic Mach number such as the 0.80 Mach number envisioned for advanced turboprop-powered aircraft. The two-dimensional model of the boundary layer fails to explain a significant discrepancy between predicted and measured data just behind the plane of the SR-3 turboprop on the JetStar aircraft. Three-dimensional refraction and scattering effects are being studied in an attempt to resolve this discrepancy.

Far-field effects of atmospheric attenuation and ground reflections modify the noise measured during the flyover of a propeller aircraft. The largest effect is that of ground reflection which introduces the "ground-dip" in the measured flyover noise. Available theories and methods are adequate for predicting these effects when the ground reflection angle is large. Although measurements from outdoor flyover tests have a typically large scatter of data, the flyover noise from propellers can usually be predicted within a standard deviation of about 4 dB.

REFERENCES

1. Gillian, Ronnie E.; Brown, Christine G.; Bartlett, Robert W.; and Baucom, Patricia H.: ANOPP Programmers' Reference Manual for the Executive System. NASA TM X-74029, 1977.

2. Zorumski, William E.: Aircraft Noise Prediction Program Theoretical Manual. NASA TM-83199, Pts. 1 and 2, 1982.

3. Karamcheti, Krishnamurty: Principles of Ideal-Fluid Aerodynamics. John Wiley & Sons, Inc., c.1966.

4. Theodorsen, T.; and Garrick, I. E.: General Potential Theory of Arbitrary Wing Sections. NACA Rep. 452, 1933.

5. Schlichting, Hermann (J. Kestin, transl.): Boundary-Layer Theory, Seventh ed. McGraw-Hill Book Co., c.1979.

6. Lock, C. N. H.: The Application of Goldstein's Airscrew Theory to Design. R. & M. No. 1977, British A.R.C., 1930.

7. Glauert, H.: Airplane Propellers. Aerodynamic Theory, div. L, Volume IV, W. F. Durand, ed., Dover Publ., Inc., 1963, pp. 169-360.

8. Goldstein, Sydney: On the Vortex Theory of Screw Propellers. Proc. R. Soc. London, ser. A, vol. CXXIII, Apr. 1929, pp. 440-465.

9. Farassat, F.: Theory of Noise Generation From Moving Bodies With an Application to Helicopter Rotors. NASA TR R-451, 1975.

10. Nystrom, Paul A.; and Farassat, F.: A Numerical Technique for Calculation of the Noise of High-Speed Propellers With Advanced Blade Geometry. NASA TP-1662, 1980.

11. Farassat, F.: The Prediction of the Noise of Supersonic Propellers in Time Domain - New Theoretical Results. AIAA-83-0743, Apr. 1983.

12. Schlinker, Robert H.; and Amiet, Roy K.: Helicopter Rotor Trailing Edge Noise. NASA CR-3470, 1981.

13. Pao, S. Paul; Wenzel, Alan R.; and Oncley, Paul B.: Prediction of Ground Effects on Aircraft Noise. NASA TP-1104, 1978.

14. Block, Patricia J. W.; and Martin, Ruth M.: Results From Performance and Noise Tests of Model Scale Propellers. SAE Tech. Paper Ser. 830730, Apr. 1983.

15. Heller, Hanno: Propeller Aircraft Noise - Certification and Flight-Testing. DFVLR-Mitt. 82-16, Nov. 1982.

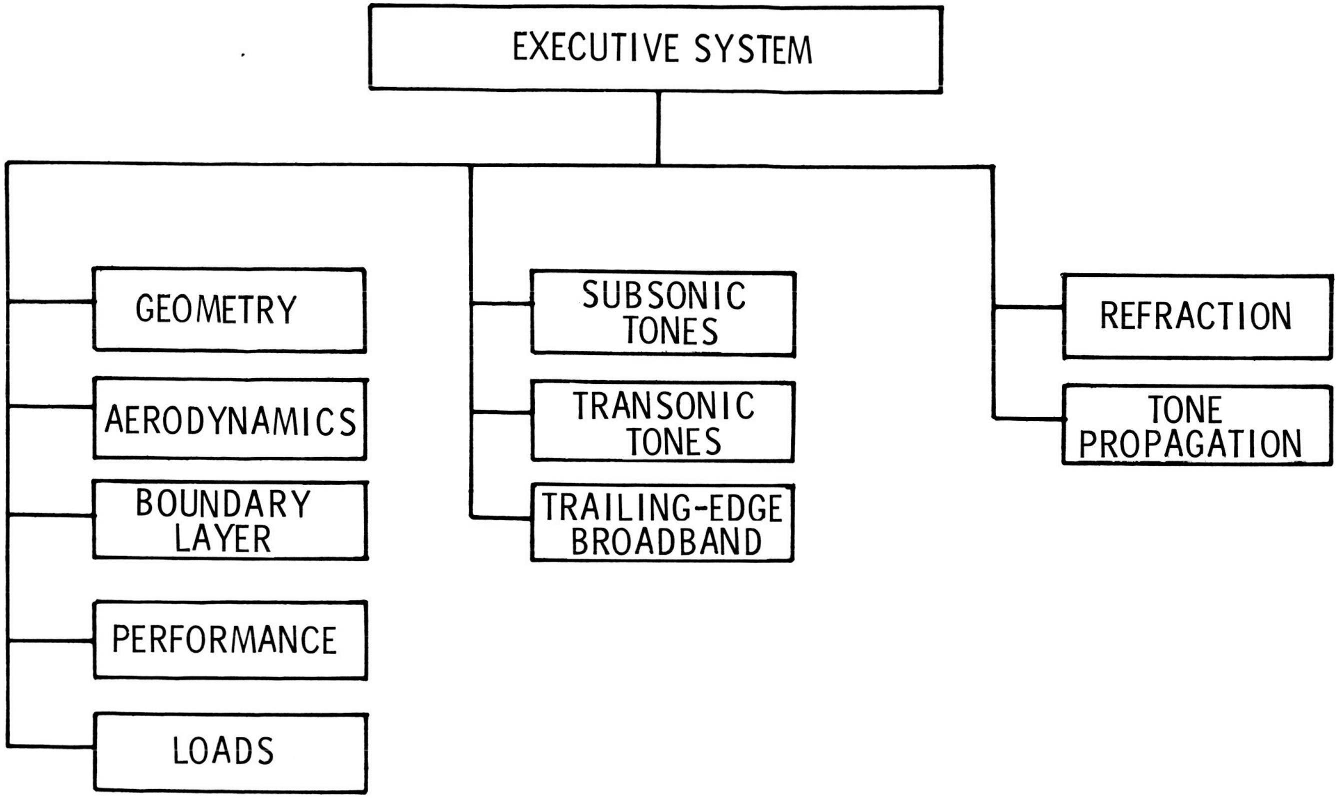

Figure 1.- ANOPP propeller noise prediction system.

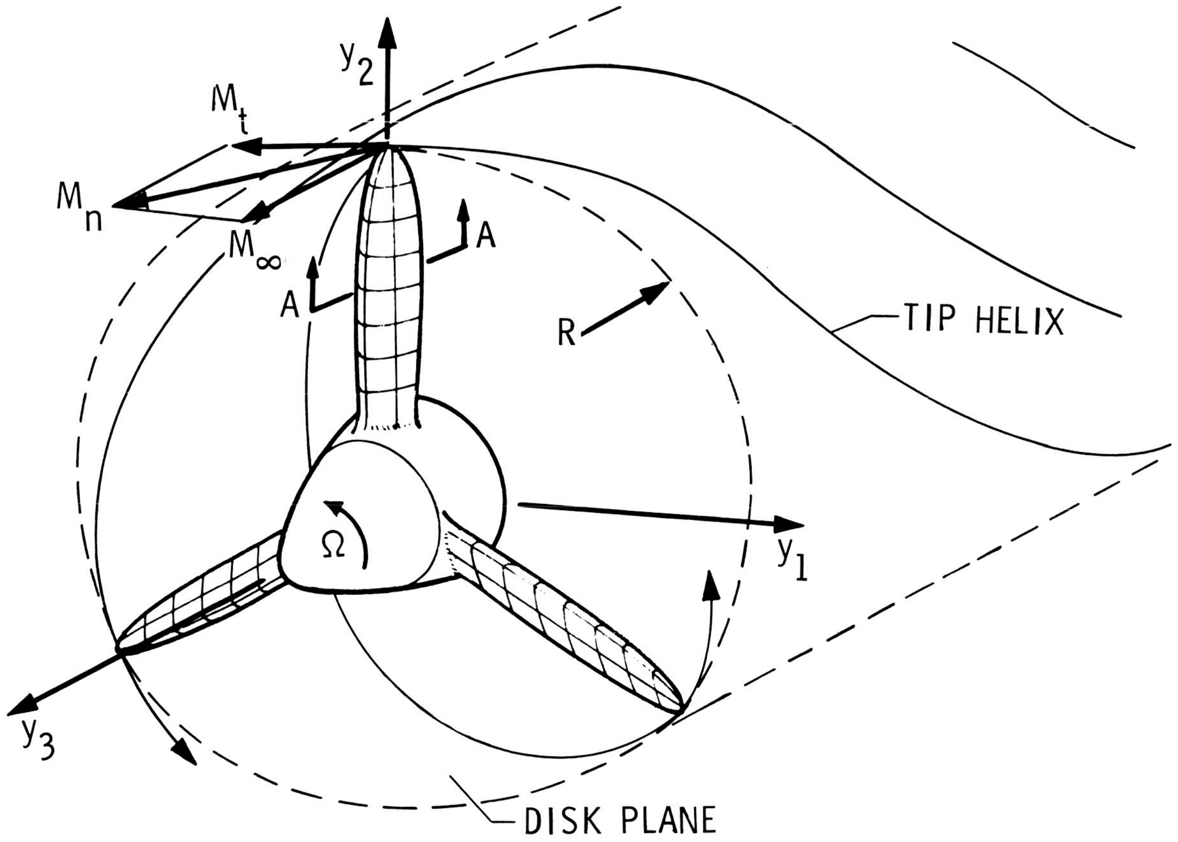

Figure 2.- Aircraft propeller geometry and motion.

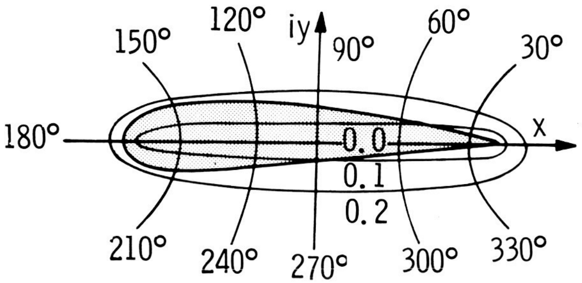

(a) Section A-A elliptical coordinates.

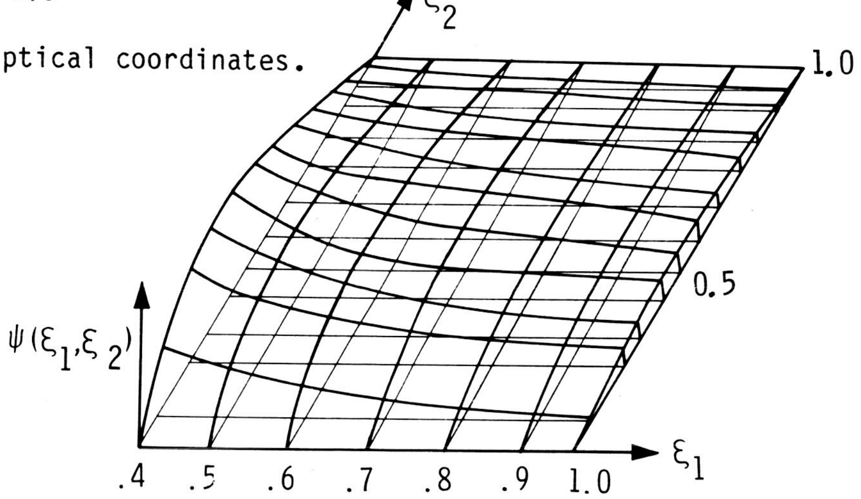

(b) Elliptic thickness function.

Figure 3.- Propeller blade shape in surface coordinate system.

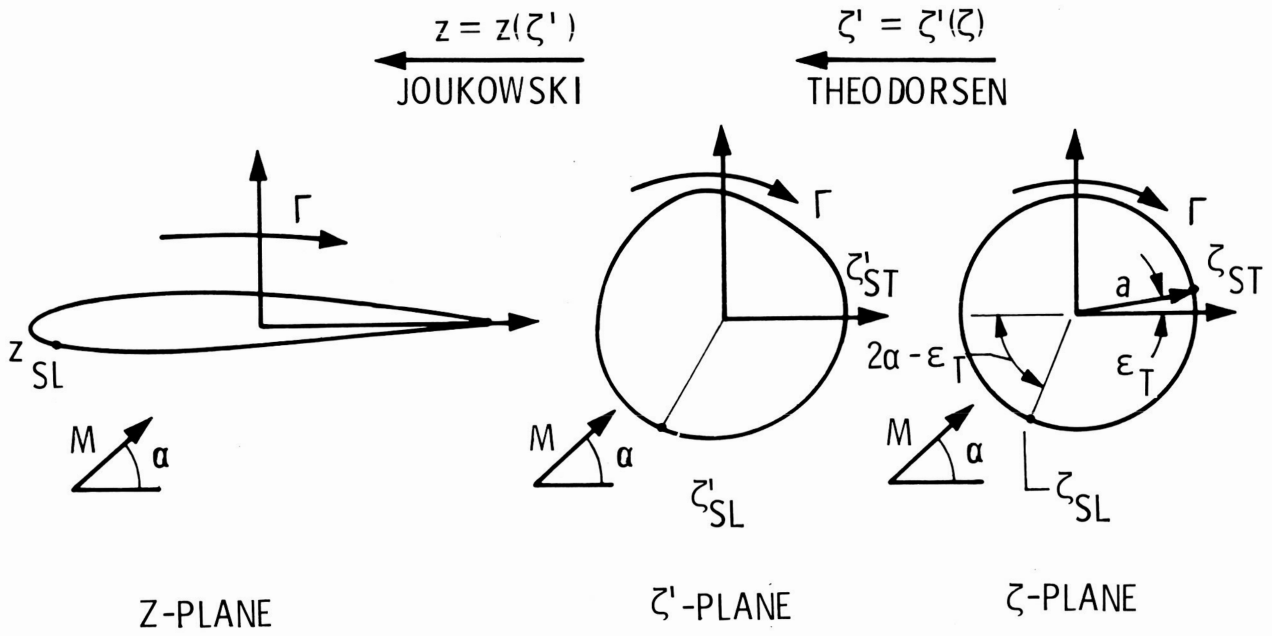

Figure 4.- Potential flow mapping for blade section.

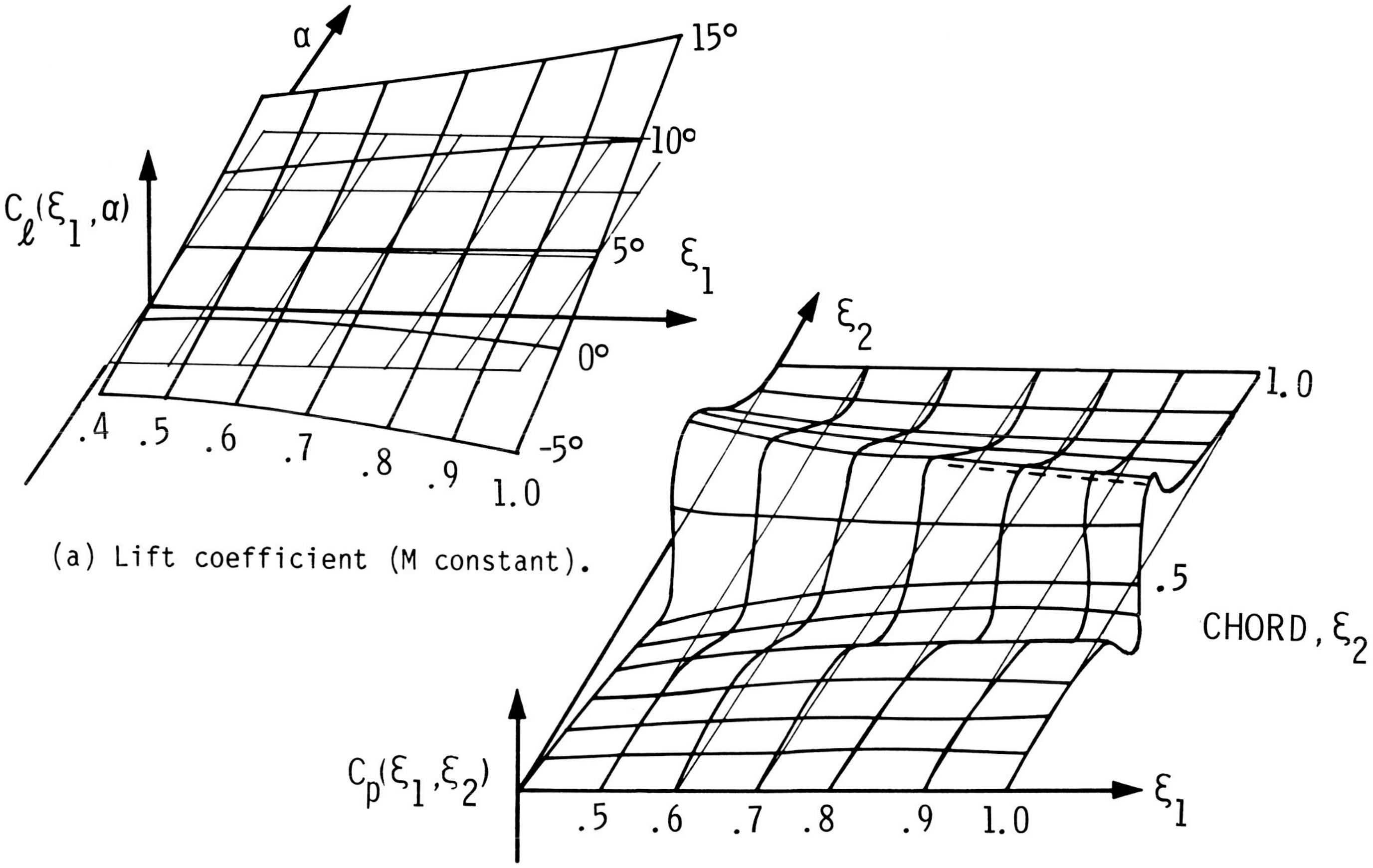

(a) Lift coefficient (M constant).

(b) Coefficient of pressure (α, M constant).

Figure 5.- Propeller blade lift and pressure coefficient functions.

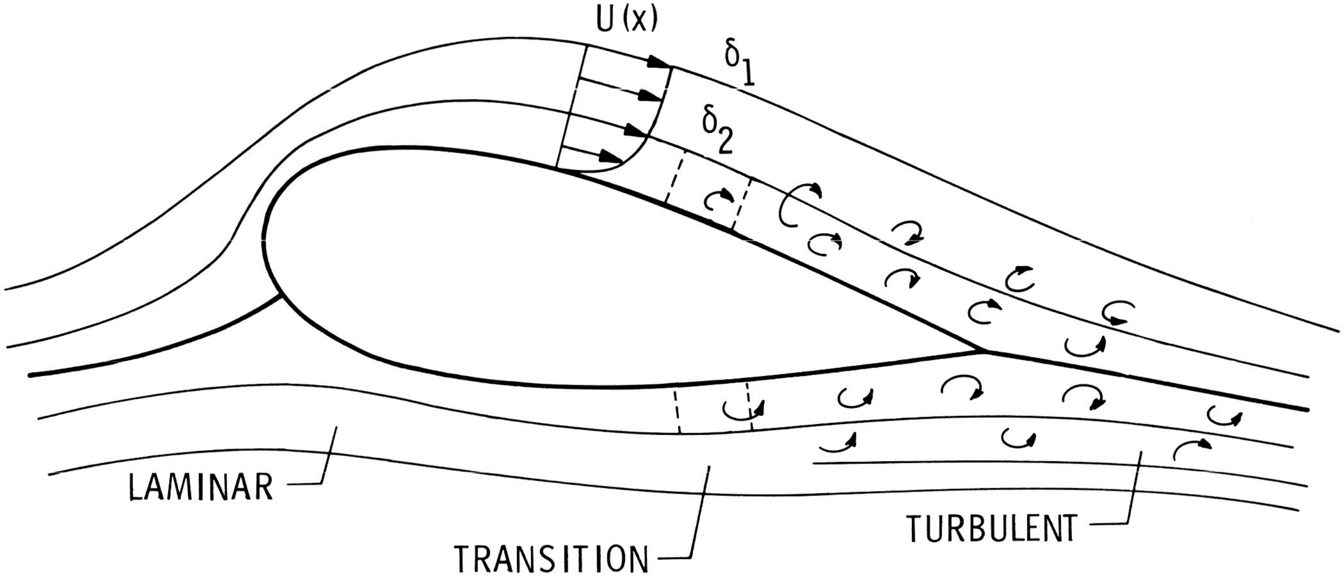

$$\frac{d\delta_2}{dx} + \left(\frac{2 + \delta_1 / \delta_2}{U}\right)\frac{dU}{dx}\,\delta_2 = C_T$$

HOLSTEIN-BOHLEN

$$\frac{d\delta_3}{dx} + \left(\frac{3}{U}\right)\delta_3 = C_D$$

TRUCKENBRODT

Figure 6.- Airfoil boundary-layer analysis.

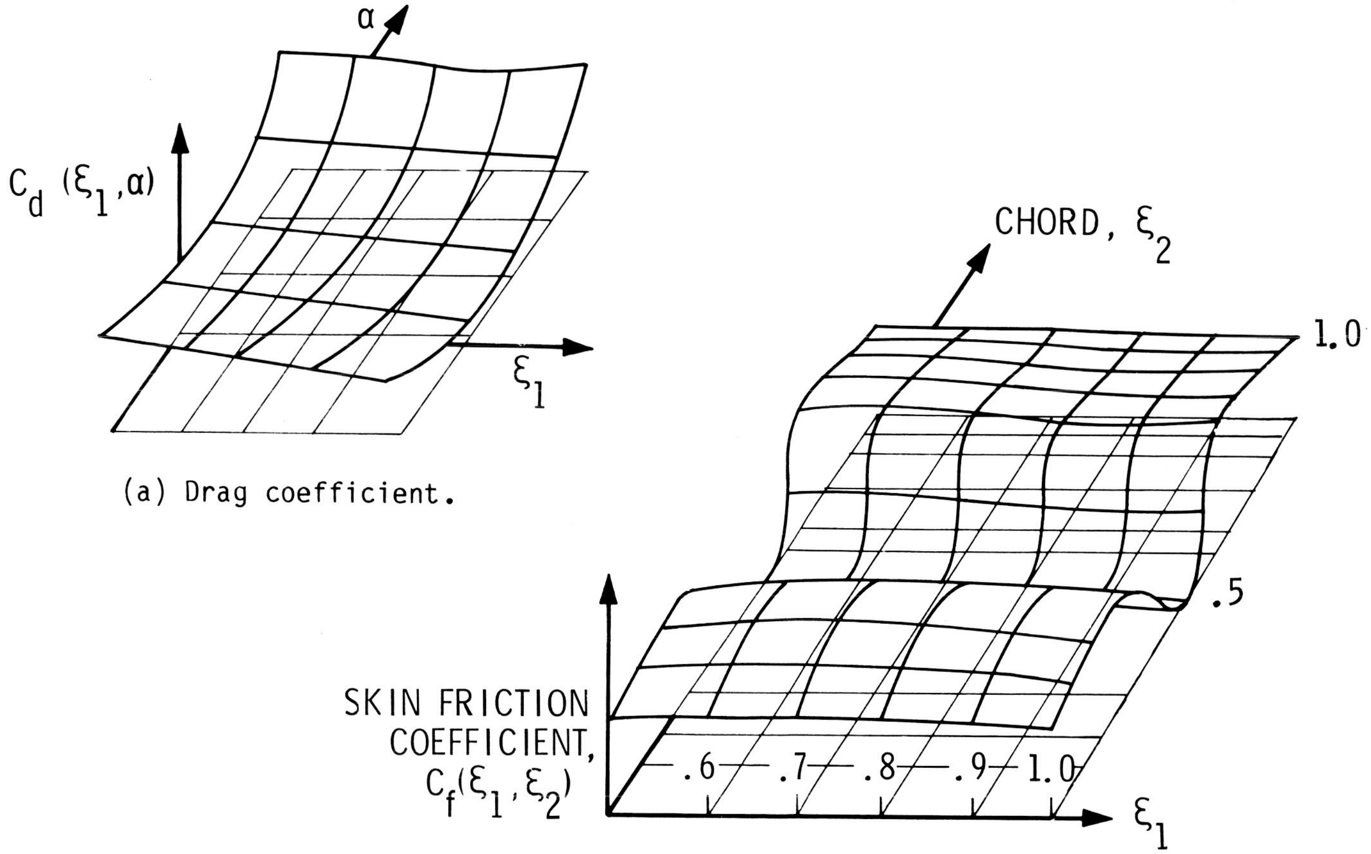

(a) Drag coefficient.

(b) Skin friction coefficient.

Figure 7.- Propeller blade drag and skin friction coefficient functions.

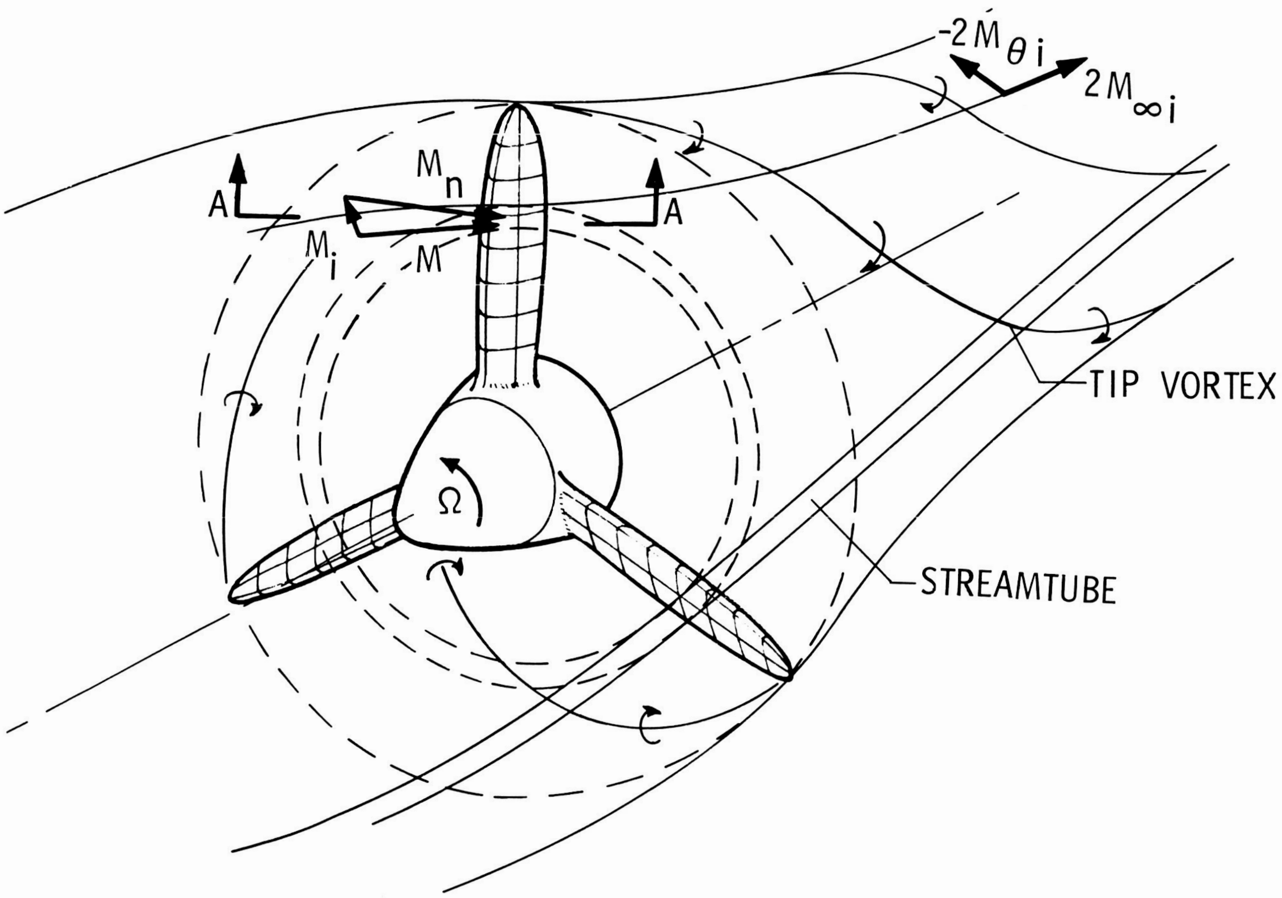

Figure 8.- Propeller induced flow.

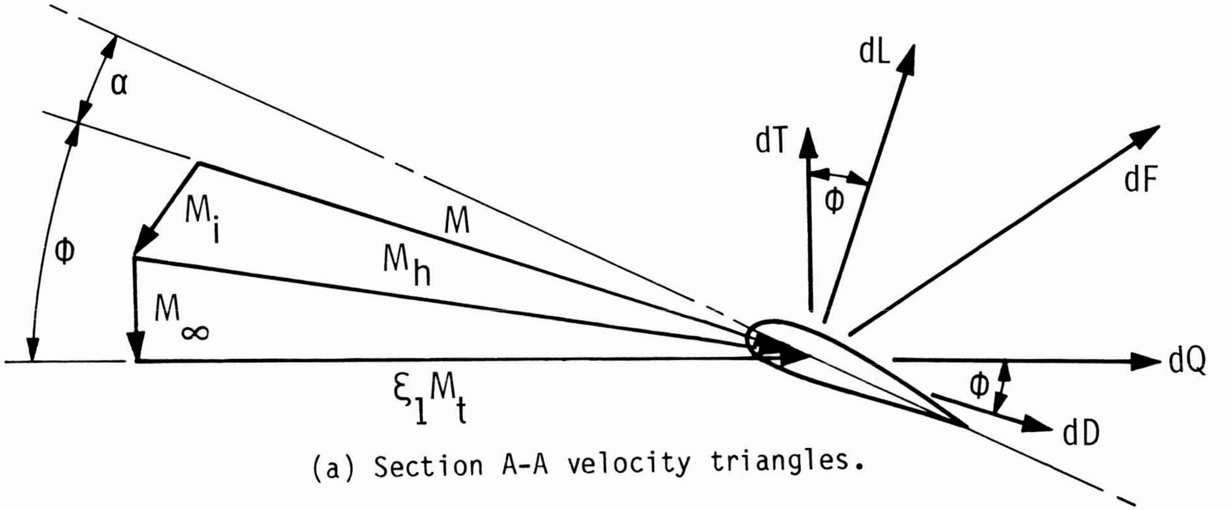

(a) Section A-A velocity triangles.

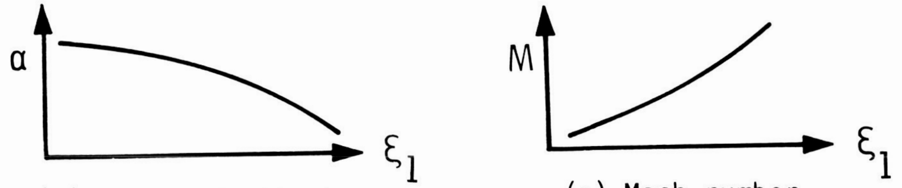

(b) Angle of attack.

(c) Mach number.

Figure 9.- Local Mach vectors and forces for a blade section.

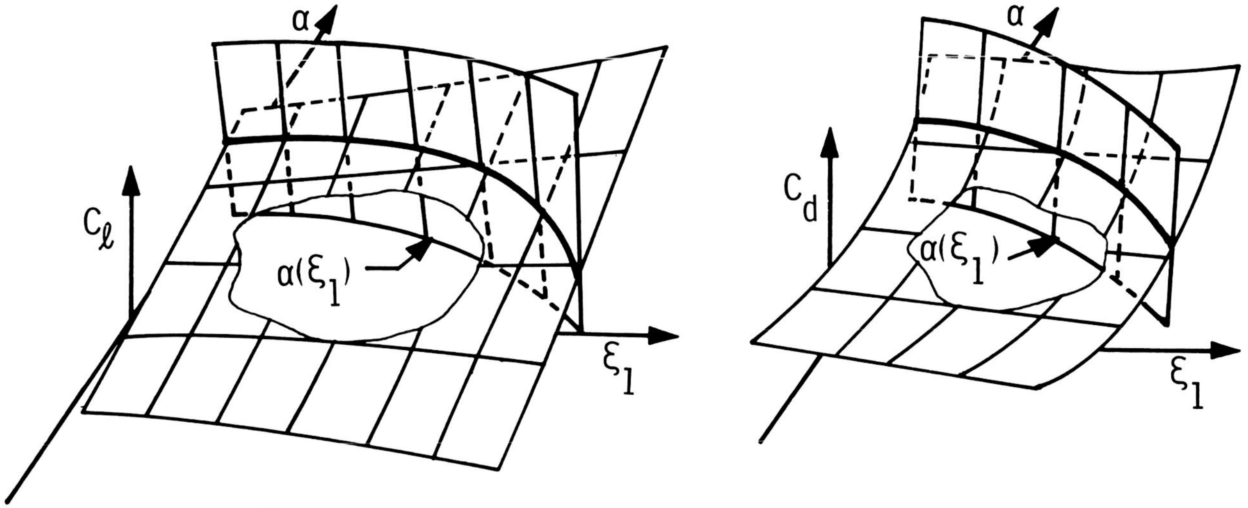

$$\tilde{C}_\ell(\xi_1) = C_\ell\left[\xi_1, \alpha(\xi_1)\right]$$

(a) Lift.

$$\tilde{C}_d(\xi_1) = C_d\left[\xi_1, \alpha(\xi_1)\right]$$

(b) Drag loading.

Figure 10.- Blade lift and drag loading function.

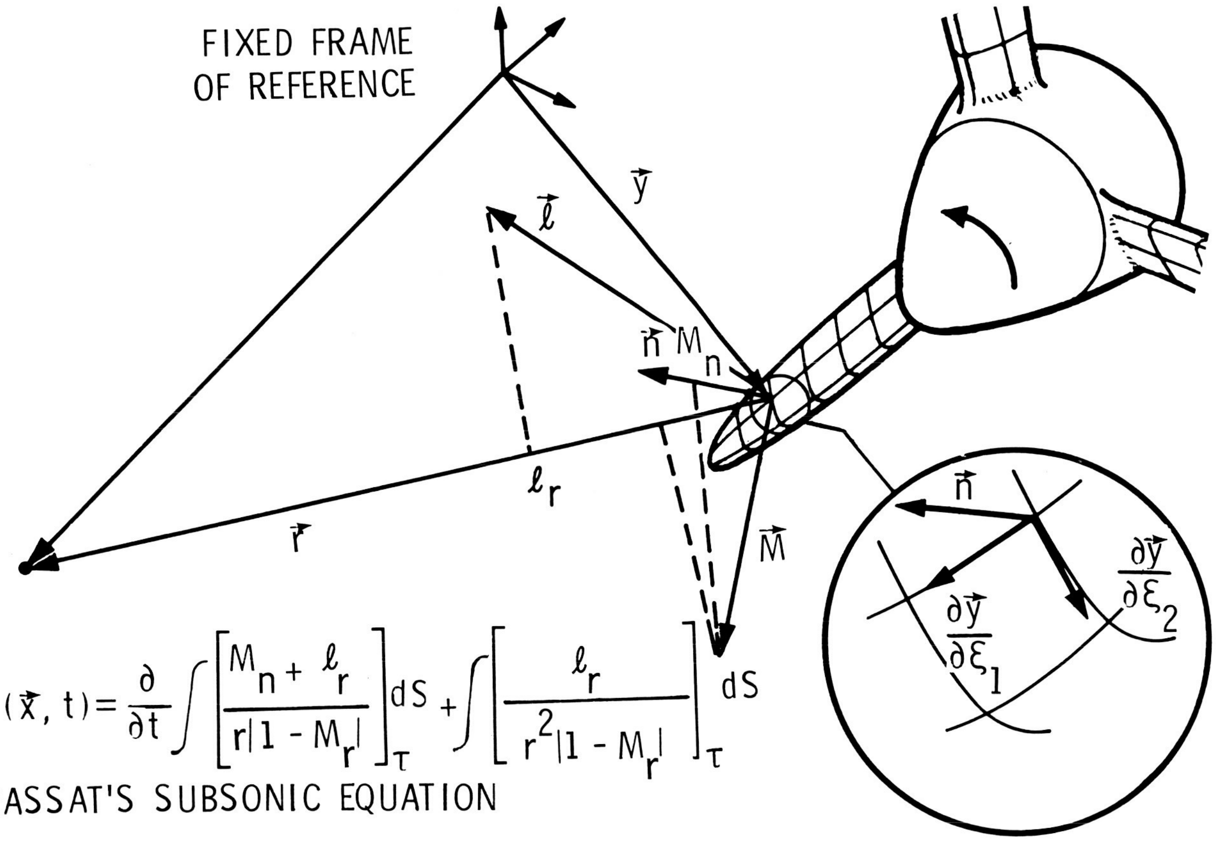

$$4\pi\, p(\vec{x}, t) = \frac{\partial}{\partial t}\int\left[\frac{M_n + \ell_r}{r|1 - M_r|}\right]_\tau dS + \int\left[\frac{\ell_r}{r^2|1 - M_r|}\right]_\tau dS$$

FARASSAT'S SUBSONIC EQUATION

$$\vec{n}\,dS = \frac{\partial\vec{y}}{\partial\xi_1} \times \frac{\partial\vec{y}}{\partial\xi_2}$$

Figure 11.- Farassat's method for predicting discrete subsonic propeller noise.

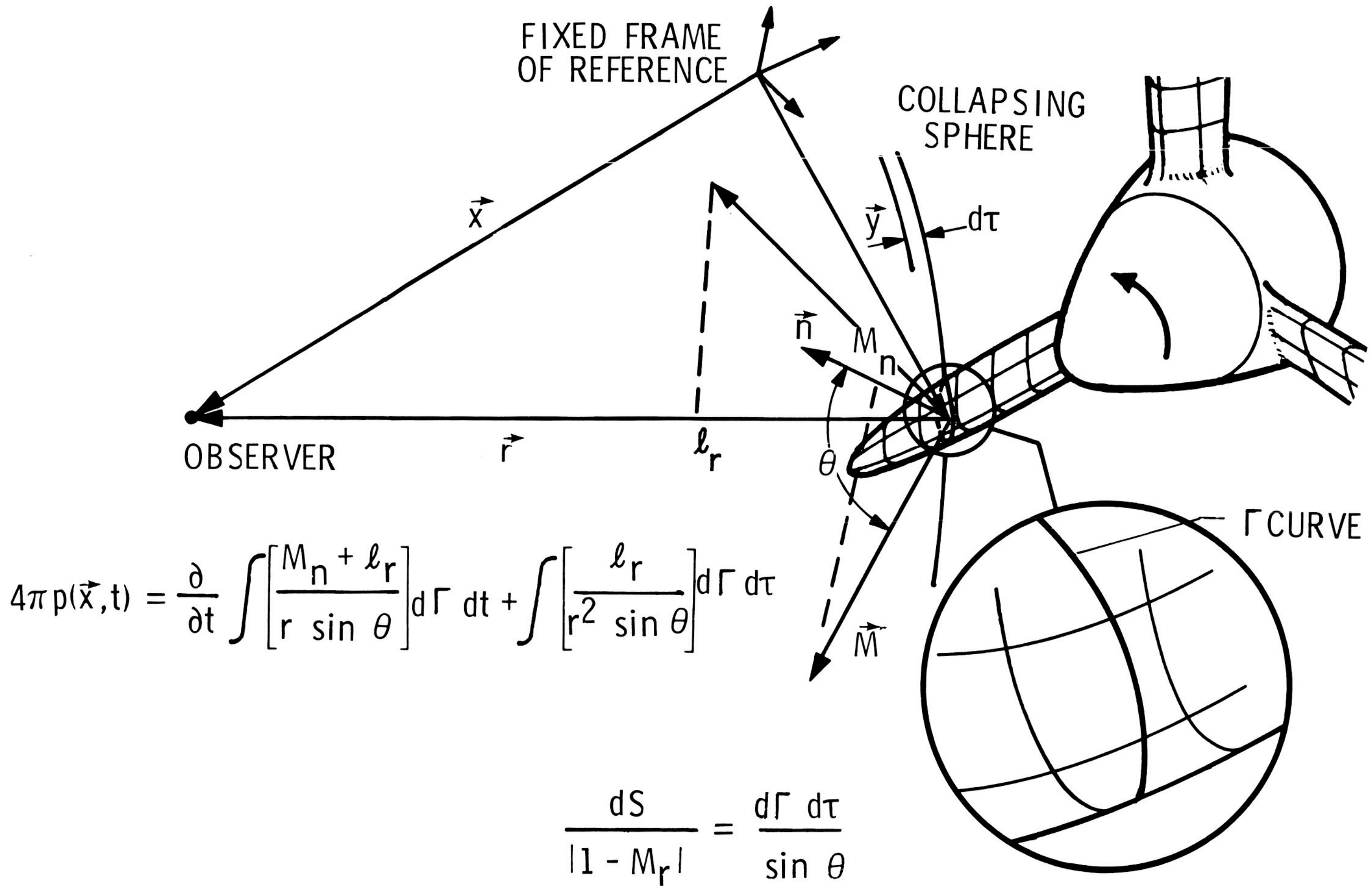

$$4\pi p(\vec{x},t) = \frac{\partial}{\partial t}\int\left[\frac{M_n + \ell_r}{r \sin\theta}\right]d\Gamma\, dt + \int\left[\frac{\ell_r}{r^2 \sin\theta}\right]d\Gamma\, d\tau$$

$$\frac{dS}{|1 - M_r|} = \frac{d\Gamma\, d\tau}{\sin\theta}$$

Figure 12.- Farassat's method for predicting discrete transonic propeller noise.

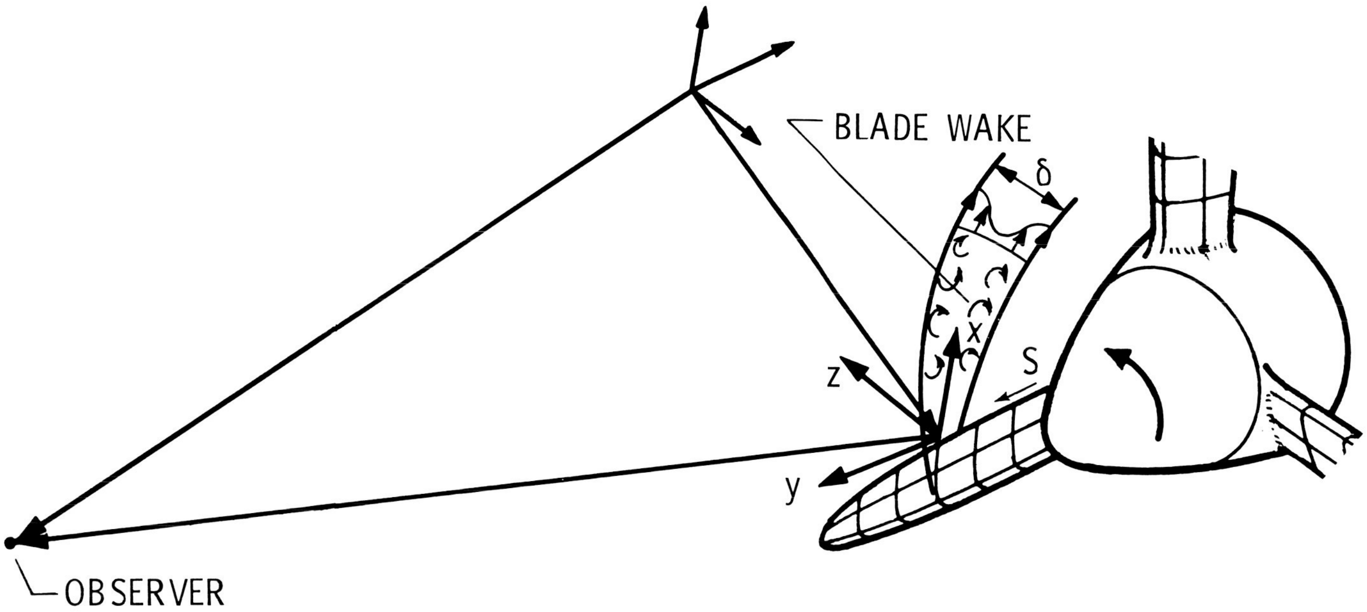

$$\langle p^2(\vec{x}, \omega, t) \rangle = \int_{\text{Hub}}^{\text{Tip}} \left[\frac{1}{4} \left(\frac{k_x M z C}{2\pi\sigma^2} \right) \left| L^2 \right| \ell_y(\omega)\ S(\omega) \right]_\tau dS$$

Figure 13.- Schlinker and Amiet's method for predicting trailing-edge broadband noise.

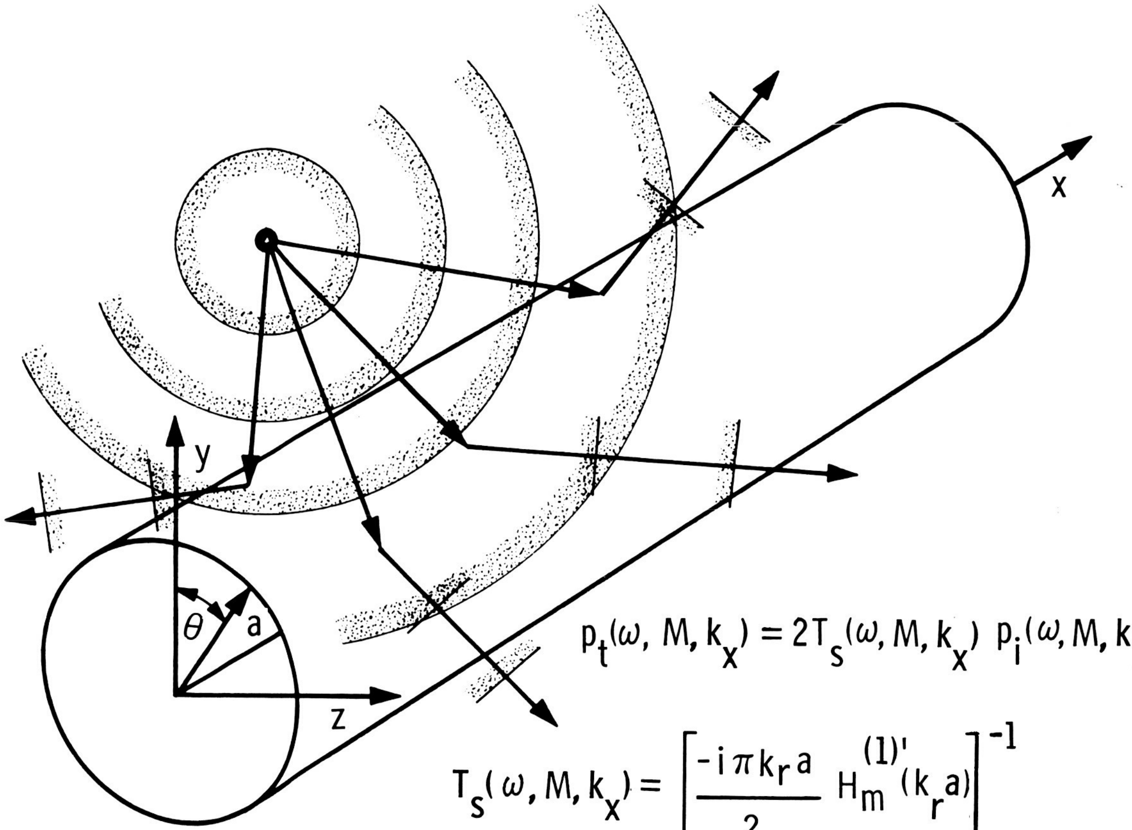

$$p_t(\omega, M, k_x) = 2T_s(\omega, M, k_x)\ p_i(\omega, M, k_x)$$

$$T_s(\omega, M, k_x) = \left[\frac{-i\pi k_r a}{2} H_m^{(1)'}(k_r a)\right]^{-1}$$

Figure 14.- Scattering of near-field source noise by a cylindrical fuselage.

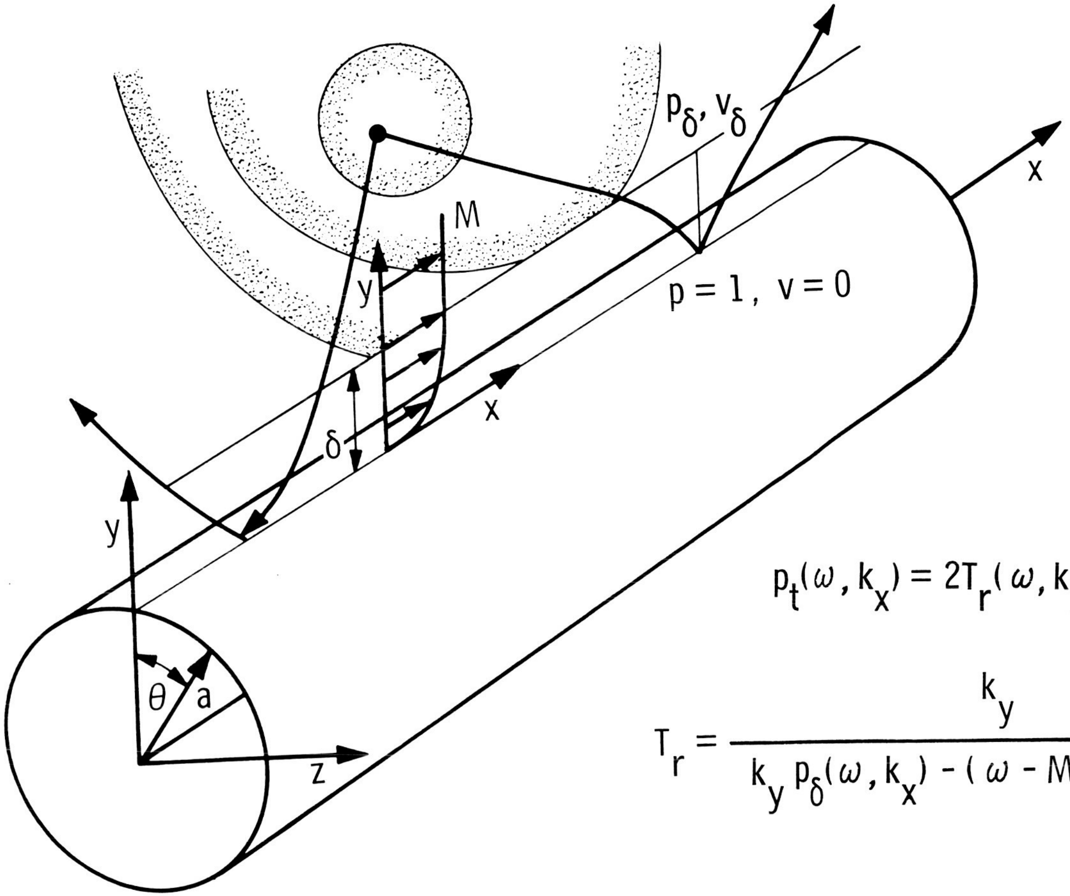

$$p_t(\omega, k_x) = 2T_r(\omega, k_x)\, p_i(\omega, k_x)$$

$$T_r = \frac{k_y}{k_y\, p_\delta(\omega, k_x) - (\omega - Mk_x)\, v_\delta(\omega, k_x)}$$

Figure 15.- Fuselage boundary-layer refraction of near-field source noise.

ORIGINAL PAGE IS
OF POOR QUALITY

Figure 16.- Twin subsonic propeller aircraft in flight.

ORIGINAL PAGE IS
OF POOR QUALITY

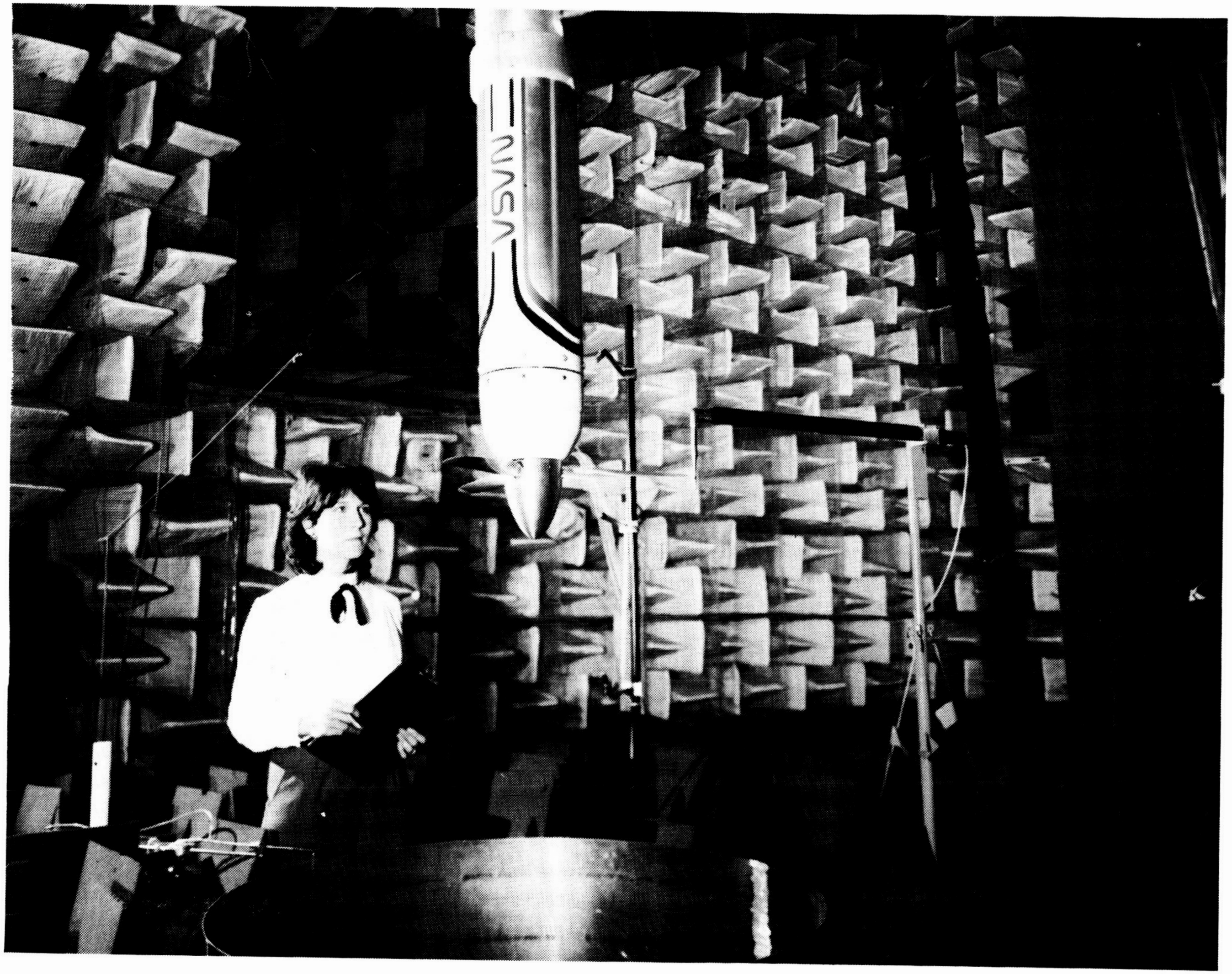

Figure 17.- Quarter-scale subsonic propeller in test chamber.

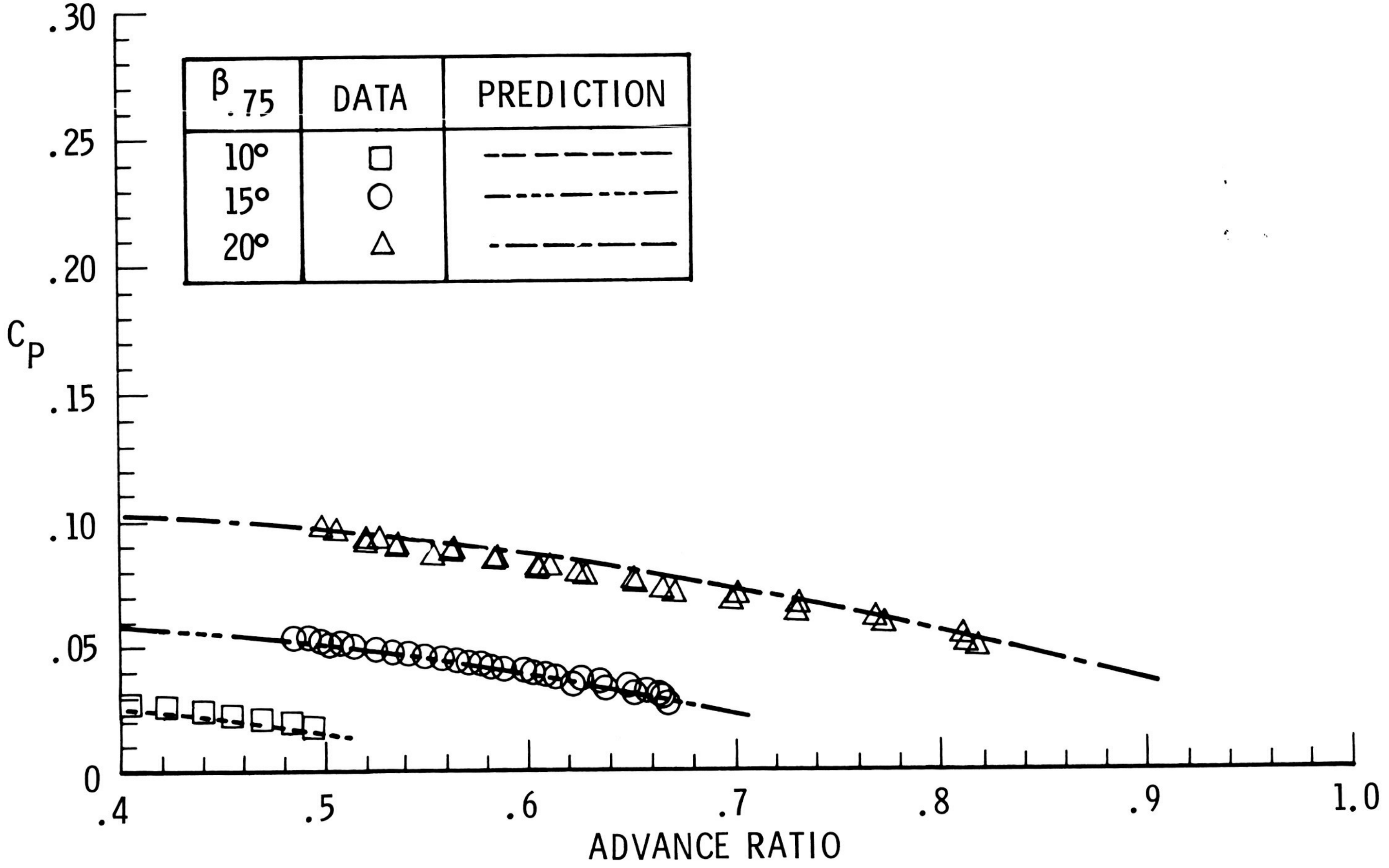

Figure 18.- Power coefficient of 1/4-scale subsonic propeller.

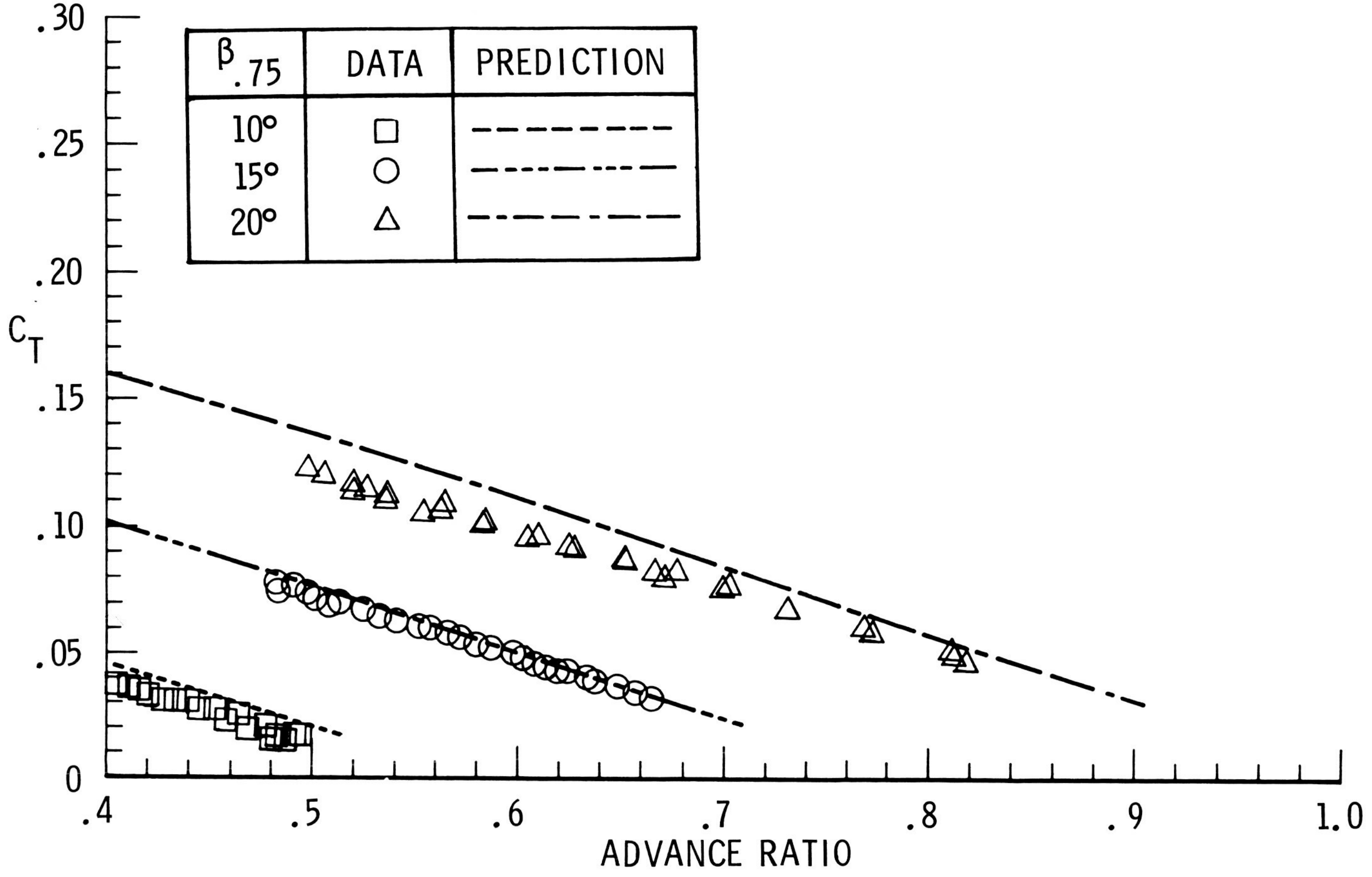

Figure 19.- Thrust coefficient of 1/4-scale subsonic propeller.

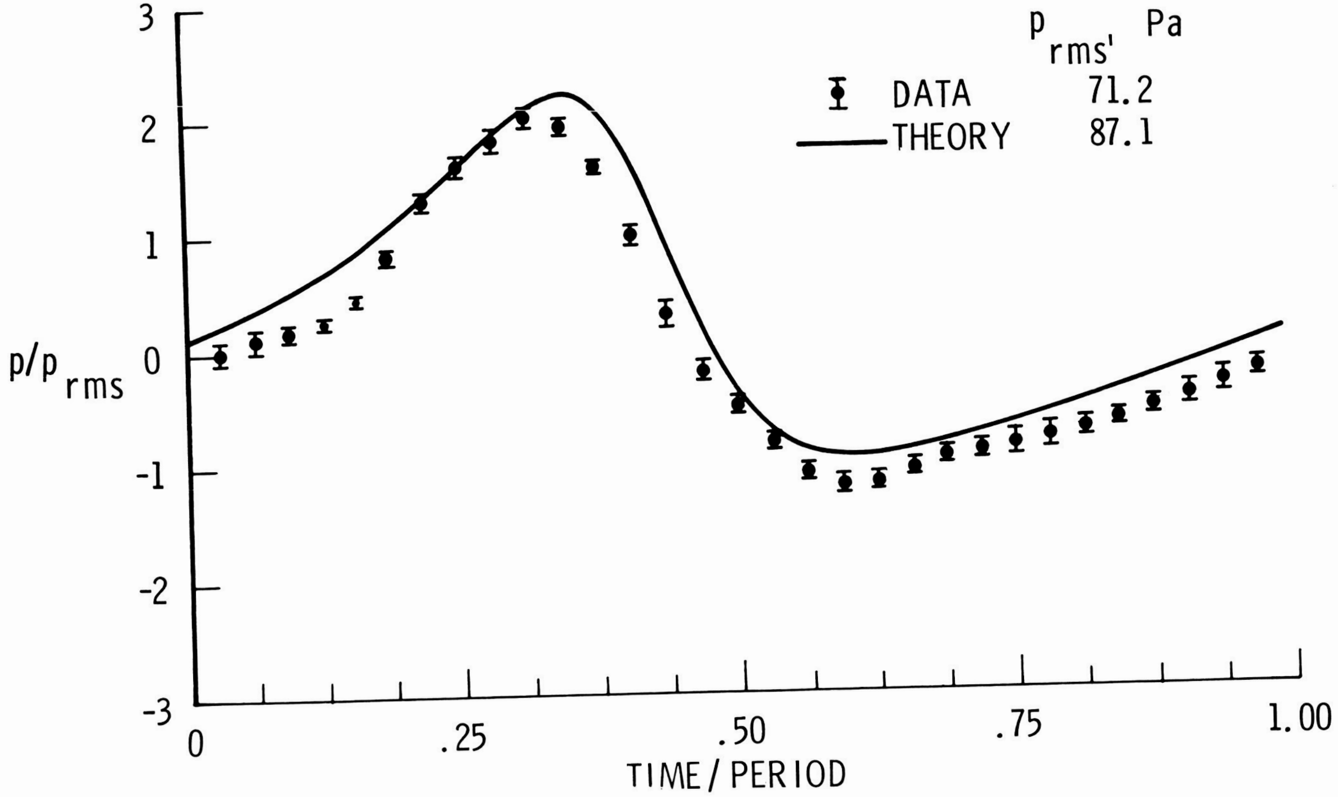

rpm = 1583.7   PITCH = 36.1° $M_f = 0.23$ $M_T = 0.65$

Figure 20.- In-flight near-field subsonic propeller noise signal.

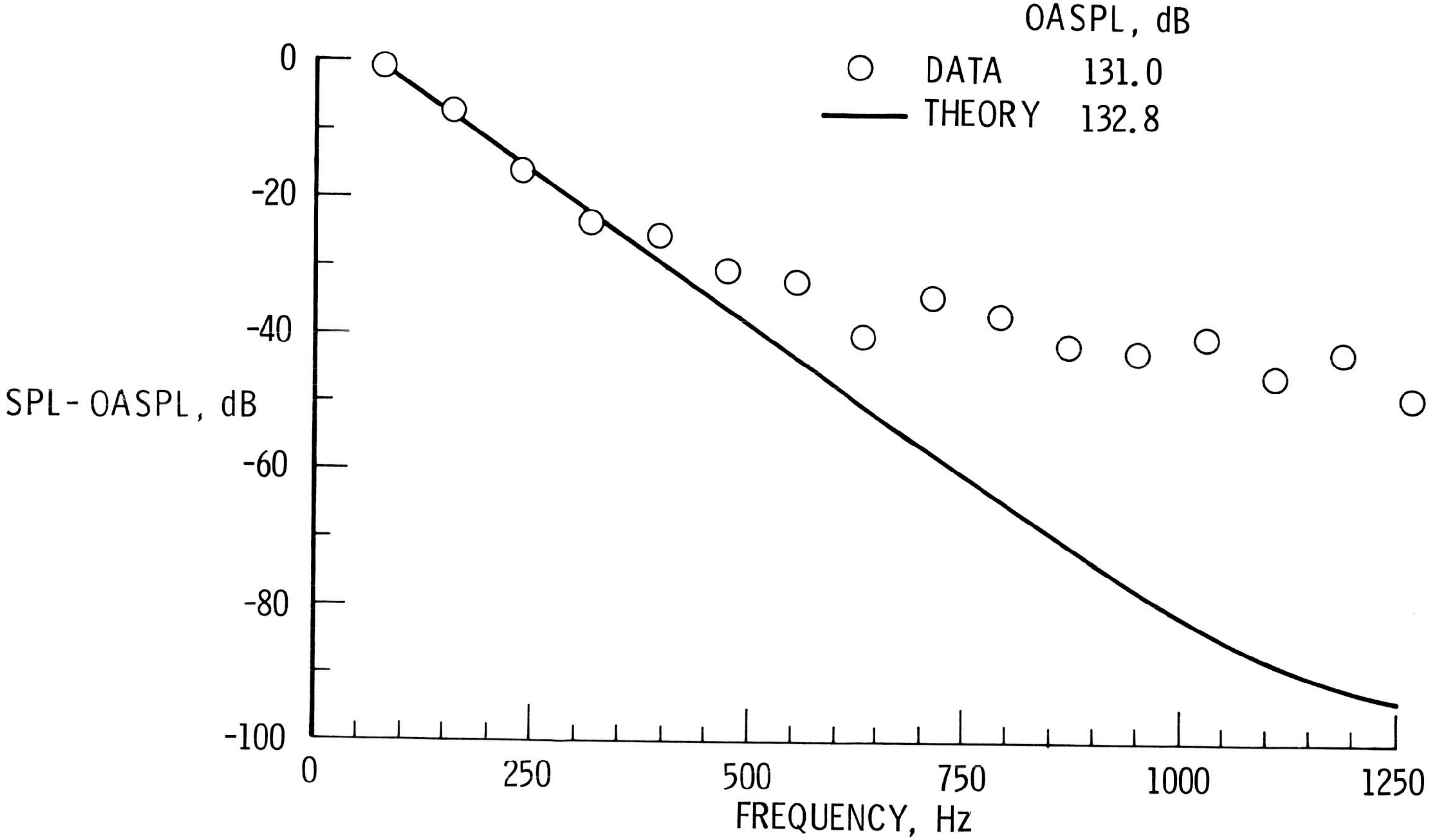

rpm = 1583.7 PITCH = 36.1° $M_f = 0.23$ $M_T = 0.65$

Figure 21.- In-flight near-field subsonic propeller noise spectrum.

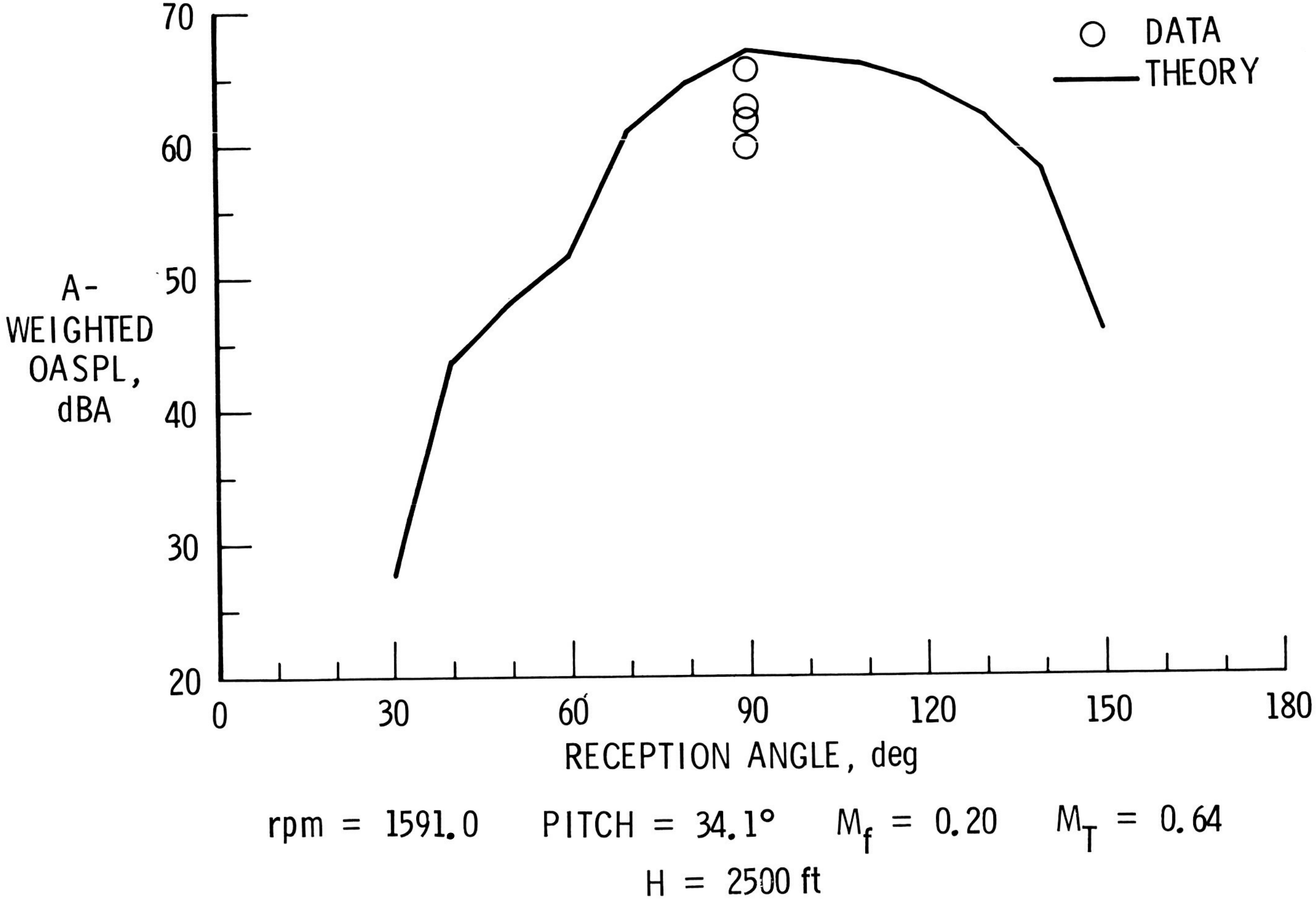

Figure 22.- Noise levels from flyover of twin-propeller aircraft at subsonic speeds.

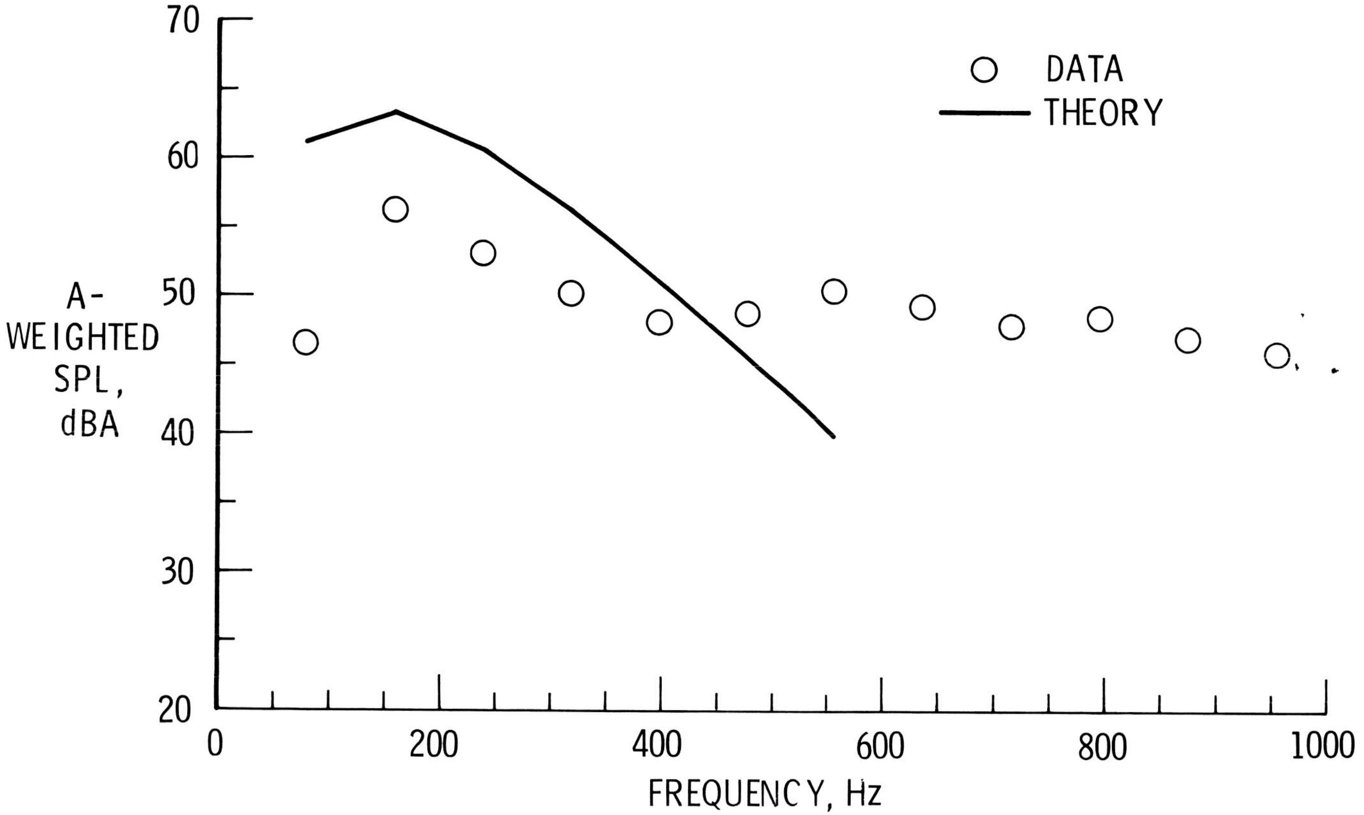

rpm = 1591.0 PITCH = 34.1° M_f = 0.20 M_T = 0.64
θ_r = 90° H = 2500 ft

Figure 23.- Noise spectrum from flyover of twin-propeller aircraft at subsonic speeds.

ORIGINAL PAGE IS
OF POOR QUALITY

Figure 24.- JetStar/propfan flight tests.

Figure 25.- Propfan performance tests.

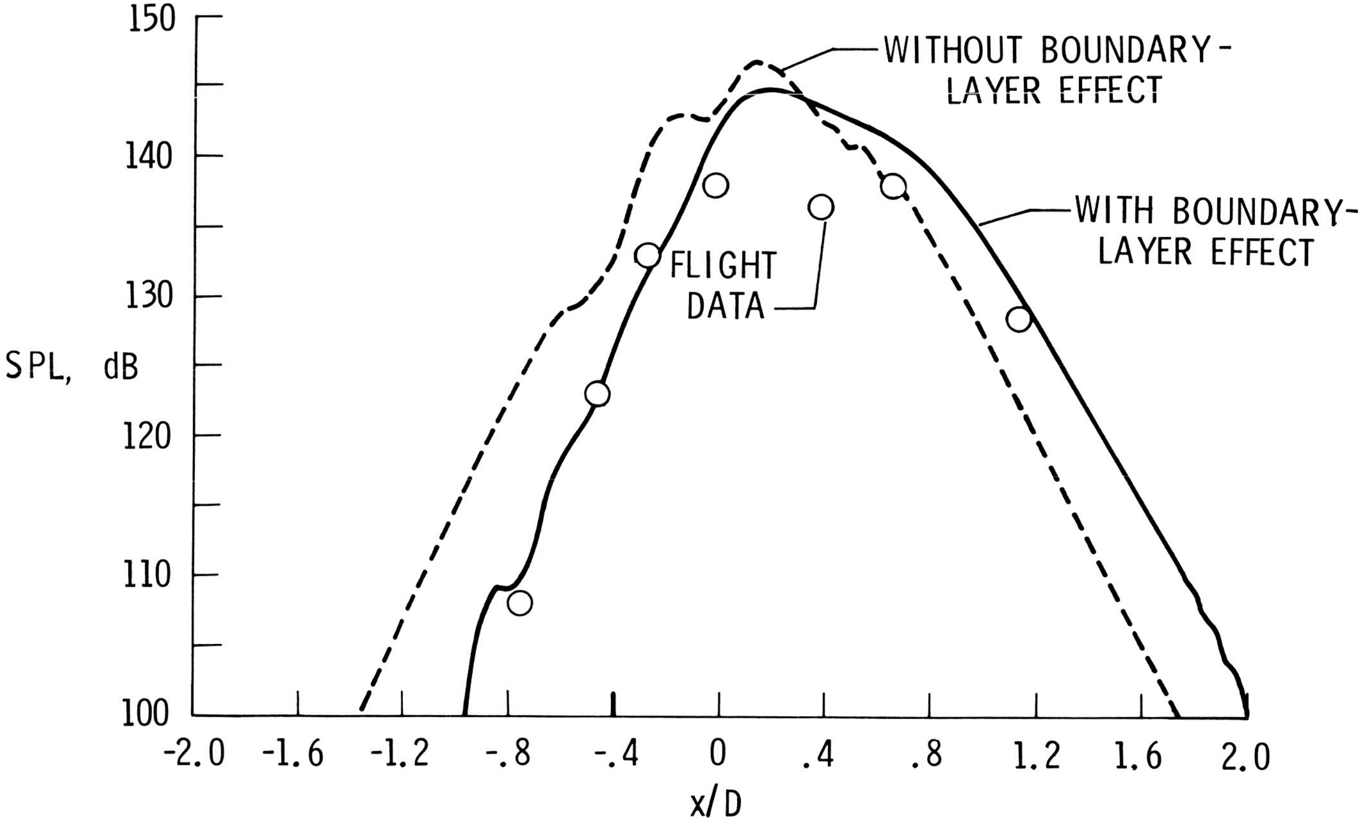

Figure 26.- JetStar fuselage surface noise. M = 0.80.

10.2 BLADE SHAPE MODULE

John W. Rawls, Jr.
PRC Kentron, Inc.

INTRODUCTION

A numerical description of the airfoil surface is the first step in rotor noise prediction. Virtually every calculation in the process of rotor noise prediction depends on the accuracy of the blade surface model. The purpose of the Blade Shape Module is to formulate a functional representation of the blade surface suitable for aeroacoustic and aerodynamic calculations.

Blade sections are generated by cutting planes normal to the pitch axis η_2 as shown in figure 1. A sectional view looking outward is shown in figure 2. The position and orientation of the section are given by the coordinates of the leading edge $\eta_{1,\ell}$ and $\eta_{3,\ell}$ and by the twist angle θ_T which is the angle between the chord line and the η_1-η_2 plane. The shape of the section is assumed to be given (fig. 3) in terms of upper surface y_U and lower surface y_L values as a function of distance along the chord x_c.

The first step in the modeling of the airfoil surface is to transform the airfoil section data supplied as input from a Cartesian coordinate system to an elliptical coordinate system defined by an inverse Joukowski transformation (fig. 4). The Joukowski transformation, used by Theodorsen (ref. 1) in the early 1930's to solve for incompressible flow over airfoils of arbitrary shape, offers two advantages in modeling the blade surface. The most important advantage is in the description of the leading edge. The air flowing over the blade surface is disturbed by the leading edge, resulting in the emission of sound waves. Thus, the description of the leading edge is very important in the noise calculation. In the elliptical coordinates, 20 to 30 percent of the airfoil shape, starting at the leading edge, can be approximated by a single ellipse. As a result, interpolation between data points on such a smooth function gives good agreement with the actual airfoil shape.

A second advantage is that elliptical coordinates allow the blade section to be represented analytically by a single monotonically increasing parameter. In the Cartesian coordinate system (fig. 3), the airfoil section is a multivalued function of the chord. That is, for a given value on the chord line, two values of the surface are given, one for the upper surface and a second for the lower surface. The elliptical coordinates eliminate the problem of having separate analytical representations for the upper and lower surfaces. The blade surface is represented by the function $\psi(\xi_1,\xi_2)$ in the computational space as shown in figure 5.

After the section data have been transformed to the elliptical coordinates, a cubic spline is fit in the chordwise direction. This fit is made in the least-squares sense and a weighting may be applied to the input points. With the cubic spline interpolation, the blade surface is represented by a two-dimensional computational grid so that any point on the surface can be determined by specifying two independent surface parameters, ξ_1 and ξ_2. These parameters give the spanwise position $\eta_2 = \xi_1$ and the elliptical coordinates $\theta = 2\pi\xi_2$ and $\psi(\xi_1,\xi_2)$.

The final step is to transform the surface points to the pitch axis coordinate system. This coordinate system is the reference coordinate system for the aeroacoustic calculations.

SYMBOLS

A	blade section area, re R^2
AF	activity factor
AR	aspect ratio
b	Joukowski transformation parameter
C	chord length, re R
$N_{\xi 1}$	number of output spanwise stations
$N_{\xi 2}$	number of output chordwise stations
R	blade length measured from axis to tip, m (ft)
r	radius of curvature, re C
r_ℓ	leading-edge radius, re C
x,y	surface coordinates in complex z-plane
x_ℓ	abscissa of leading edge in complex z-plane, re C
x_t	abscissa of trailing edge in complex z-plane, re C
V	blade volume, re R^3
β	basis function coefficient
ζ	complex plane of airfoil section represented as a near-circle
η_1,η_2,η_3	pitch axis coordinates, re R

$\eta_{1,e},\eta_{2,e},\eta_{3,e}$	coordinates of origin of elliptical axis system in pitch axis system, re R
$\eta_{1,\ell},\eta_{2,\ell},\eta_{3,\ell}$	coordinates of leading edge in pitch axis system, re R
θ	elliptic angular coordinate, $2\pi\xi_2$, rad
θ_T	blade twist angle measured positive clockwise looking outboard, rad
ξ_1	spanwise surface coordinate, $0 \leq \xi_1 \leq 1$
ξ_2	chordwise surface coordinate, $0 \leq \xi_2 \leq 1$
ϕ	basic function
ψ	elliptic system radial coordinate

Subscripts:

L	lower surface
U	upper surface

INPUT

Description of the airfoil surface begins by defining a sequence of cross sections, each of which is defined in a Cartesian coordinate system. The leading edge is the origin, with the chord line being the x_c-axis. The upper and lower surface coordinates are designated with respect to the chord line along with a leading-edge radius. This section data is given in percent chord length, so that the actual size of the blade section is determined by the chord length C. Figure 3 shows a typical airfoil section in the input Cartesian coordinate system.

Associated with each blade section is a twist angle, defined as the angle between the chord line and the η_1-η_2 reference plane. The reference coordinate system (the pitch axis coordinate system) is a right-handed system with axes η_1, η_2, and η_3. As shown in figure 1, the blade is oriented spanwise along the η_2-axis, with the origin through the center of the hub. The description of the blade surface is completed by designating the coordinates of the leading edge and the blade length R.

The input consists of parameters which are functions of span and the blade section table which is a function of both span and chord. The blade section table is input such that the first point is the trailing edge, corresponding to $x_c = 1$ and entering upper surface points with x_c decreasing to $x_c = 0$ or the leading edge. The process is continued over the lower surface with x_c increasing until again $x_c = 1$. The trailing edge is entered twice due to the discontinuity of the slope at the trailing edge. If the leading-edge ordinate $y_U(x_c = 0)$ is not exactly zero, the chord line will be rotated to make $y_U(0) = 0$, and all other ordinates will be adjusted accordingly.

The interpolation of surface points is accomplished by a one-dimensional cubic spline. The output controls specify the node locations in the chordwise direction through the parameters $N_{\xi 2}$ and ξ_2.

Spanwise Functions

$N_{\eta 2}$	number of input sections
η_2	array of spanwise coordinates, re R
$\eta_{1,\ell}(\eta_2)$	leading-edge abscissa, re R
$\eta_{3,\ell}(\eta_2)$	leading-edge ordinate, re R
$C(\eta_2)$	chord length, re R
$r_\ell(\eta_2)$	leading-edge radius, re $C(\eta_2)$
$\theta_T(\eta_2)$	blade twist angle measured positive clockwise looking outboard, rad

Blade Section Tables

$N_U(\eta_2)$	number of input points on upper surface
$x_U(\eta_2)$	array of upper surface abscissa values, re $C(\eta_2)$
$y_U(\eta_2)$	array of upper surface ordinate values, re $C(\eta_2)$
$w_U(\eta_2)$	array of upper surface weighting constants
$N_L(\eta_2)$	number of input points on lower surface
$x_L(\eta_2)$	array of lower surface abscissa values, re $C(\eta_2)$
$y_L(\eta_2)$	array of lower surface ordinate values, re $C(\eta_2)$
$w_L(\eta_2)$	array of lower surface weighting constants

Output Controls

$N_{\xi 2}$	number of chordwise stations
ξ_2	array of chordwise stations, $0 \leq \xi_2 \leq 1$

OUTPUT

The outputs of this module are twice-differentiable functions of the surface coordinates. These functions are the surface position vector $\eta_i(\xi_1,\xi_2)$, the leading-edge position vector $\eta_{i,\ell}(\xi_1)$, and the elliptic coordinate system data $\eta_{i,e}(\xi_1)$, $b(\xi_1)$, $C(\xi_1)$, and $\theta_T(\xi_1)$. All functions have continuous second derivatives defined by bicubic splines. This module also outputs the first derivatives of the cubic spline basis functions at the node points.

The aspect ratio, activity factor, and blade volume computations are defined in appendix A.

AF	activity factor
AR	aspect ratio
$N_{\xi 1}$	number of spanwise stations
$N_{\xi 2}$	number of chordwise stations
V	blade volume, re R^3
ξ_1	array of spanwise stations, re R, $0 < \xi_1 < 1$
ξ_2	array of chordwise stations, re 2π, $0 < \xi_2 < 1$

Functions of Span

$\eta_{1,\ell}(\xi_1)$	leading-edge abscissa, re R
$\eta_{3,\ell}(\xi_1)$	leading-edge ordinate, re R
$b(\xi_1)$	Joukowski transformation parameter, re R
$C(\xi_1)$	chord length, re R
$\eta_{1,e}(\xi_1)$	elliptic system origin abscissa, re R
$\eta_{3,e}(\xi_1)$	elliptic system origin ordinate, re R
$\theta_T(\xi_1)$	blade elliptic axis twist angle, measured positive clockwise looking outboard, rad
$A(\xi_1)$	blade section area, re R^2

Functions of Span and Chord

$\eta_1(\xi_1,\xi_2)$	blade surface abscissa, re R
$\eta_3(\xi_1,\xi_2)$	blade surface ordinate, re R
$\psi(\xi_1,\xi_2)$	blade surface elliptic radial coordinate, rad

Basis Function Slopes

$\phi'_{1_{ij}} = \phi'_{1_j}(\xi_{1_i}) \qquad (i,j = 1,2,\ldots,N_{\xi 1})$

$\phi'_{2_{ij}} = \phi'_{2_j}(\xi_{2_i}) \qquad (i,j = 1,2,\ldots,N_{\xi 2})$

METHOD

The modeling of the airfoil surface follows three basic steps. The first step transforms the section data into an elliptic coordinate system through the use of the inverse Joukowski transformation. The second step fits the blade surface coordinates with cubic splines in the chordwise direction. Finally, the third step transforms the surface coordinates from the elliptic system to the pitch axis system. Each of these steps are discussed in detail.

Development of Elliptic Coordinate System

The Joukowski transformation, defined by

$$z = \zeta + \frac{b^2}{\zeta} \tag{1}$$

maps the airfoil section from the complex z-plane to the complex ζ-plane, where ζ is given by

$$\zeta = be^{\psi+i\theta} \tag{2}$$

In the ζ-plane the airfoil shape is nearly circular. Recall from complex variables that $z = re^{i\theta}$ is the equation of a circle. If ψ is constant in equation (2), the airfoil shape in the ζ-plane is exactly a circle. In general, however, ψ is not constant but is rather a function of θ. The values of ψ are very small so that ζ does not deviate very far from a circle.

To find the representation of an airfoil section in terms of ψ and θ, z can be rewritten as

$$z = be^{\psi+i\theta} + be^{-\psi-i\theta} \tag{3}$$

or in terms of hyperbolic functions as

$$z = 2b \cosh \psi \cos \theta + i2b \sinh \psi \sin \theta \tag{4}$$

Since $z = x + iy$ in Cartesian coordinates, the coordinates of the airfoil section x,y are given by

$$x = 2b \cosh \psi \cos \theta \tag{5a}$$

$$y = 2b \sinh \psi \sin \theta \tag{5b}$$

Solving for $\cos \theta$ and $\sin \theta$ in terms of x, y, and ψ gives the following two relations:

$$\cos \theta = \frac{x}{2b \cosh \psi} \tag{6a}$$

$$\sin \theta = \frac{y}{2b \sinh \psi} \tag{6b}$$

Using the identity $\cos^2 \theta + \sin^2 \theta = 1$ together with equations (6) yields

$$\left(\frac{x}{2b \cosh \psi}\right)^2 + \left(\frac{y}{2b \sinh \psi}\right)^2 = 1 \tag{7}$$

For constant ψ, equation (7) is the equation on an ellipse with foci located at $\underline{+}2b$. Consequently, lines of constant ψ form ellipses in the z-plane. Similarly, a relation for $\cosh \psi$ and $\sinh \psi$ can be found by solving equations (5) in terms of x, y, and θ to yield

$$\cosh \psi = \frac{x}{2b \cos \theta} \tag{8a}$$

$$\sinh \psi = \frac{y}{2b \sin \theta} \tag{8b}$$

Using the hyperbolic identity $\cosh^2 \psi - \sinh^2 \psi = 1$ results in

$$\left(\frac{x}{2b \cos \theta}\right)^2 - \left(\frac{y}{2b \sin \theta}\right)^2 = 1 \tag{9}$$

Equation (9) is the equation of a hyperbola with foci also located at $\underline{+}2b$. Lines of constant θ form an infinite set of hyperbolas in the z-plane.

Figure 4 shows an airfoil section plotted in the complex z-plane with the elliptic and hyperbolic coordinates superimposed on the airfoil. A description of the airfoil surface is sought in terms of coordinates ψ and θ rather than x and y.

Transformation to Elliptic Coordinates

In mapping the airfoil to the complex z-plane, the leading and trailing edges must be located in the elliptic coordinate system. Note that the derivative of the Joukowski transformation

$$\frac{dz}{d\zeta} = 1 - \frac{b^2}{\zeta^2} \tag{10}$$

becomes infinite for $\zeta=0$ and zero for $\zeta=\pm b$. By choosing $\zeta_t = b$, the trailing edge becomes a stagnation point. This choice satisfies the Kutta-Joukowski condition, which requires the flow field in the neighborhood of the trailing edge to be finite even though there is a discontinuity in the slope of the surface at the trailing edge. In the z-plane, the trailing edge is mapped to the point

$$x_t = 2b \tag{11}$$

Next, the leading edge must be located such that the remaining discontinuity is within the airfoil and, thus, will not cause a singularity in the flow field.

Recall from equation (7) that lines of constant ψ form ellipses in the z-plane. The radius of curvature along ψ = Constant is given by

$$r = \frac{2b\ (\cosh^2 \psi \sin^2 \theta + \sinh^2 \psi \cos^2 \theta)^{3/2}}{\sinh \psi \cosh \psi} \tag{12}$$

With the leading edge located at $\theta = \pi$, the radius of curvature becomes

$$r_\ell = \frac{2b \sinh^2 \psi}{\cosh \psi} \tag{13}$$

Retaining terms of order ψ^2 in the Taylor series expansions for $\sinh \psi$ and $\cosh \psi$, the radius of curvature is approximately given by

$$r_\ell \approx 2b\psi^2 \tag{14}$$

The location of the leading edge in the z-plane can be found by substituting $y = 0$ into equation (7) and solving for x to yield

$$x_\ell = -2b \cosh \psi \tag{15}$$

Again by using the Taylor series expansion for $\cosh \psi$, equation (15) becomes

$$x_\ell = -2b(1 + \frac{\psi^2}{2}) \tag{16}$$

or in terms of the radius of curvature the location of the leading edge is given by

$$x_\ell = -2b - \frac{r_\ell}{2} \tag{17}$$

Now the chord length of the airfoil section can be found from

$$C = x_t - x_\ell = 4b + \frac{r_\ell}{2} \tag{18}$$

Since the chord length is normalized to unity in terms of section input data,

$$x_t - x_\ell = 1 \tag{19}$$

The Joukowski transformation parameter is given by

$$b = \frac{1}{4} - \frac{r_\ell}{8} \tag{20}$$

Before the airfoil coordinates can be computed in the ζ-plane, the airfoil coordinates must be transformed to the z-plane by the following transformations:

$$x = x_c + x_L \tag{21}$$

$$y = \begin{cases} y_U \\ y_L \end{cases} \tag{22}$$

and

$$z = x + iy \tag{23}$$

Solution for Elliptic Coordinates

Now that the airfoil coordinates have been transformed to the z-plane a solution can be found for the coordinates in the ζ-plane. To solve for the elliptic coordinates, variable z is normalized by $2b$ and ζ is normalized by b such that

$$z = \frac{x + iy}{2b} \tag{24}$$

and

$$\zeta = e^{\psi+i\theta} \tag{25}$$

Rewriting equation (1) in terms of z and ζ,

$$\zeta^2 - 2z\zeta + 1 = 0 \tag{26}$$

and solving for ζ yields

$$\zeta = z \pm \sqrt{z^2 - 1} \tag{27}$$

The negative root in equation (27) can be written as

$$\frac{1}{z + \sqrt{z^2 - 1}} = z - \sqrt{z^2 - 1} \tag{28}$$

Consequently, the second solution to equation (26) is the reciprocal of the first solution. The elliptical coordinates for the surface points z may therefore be found by taking

$$\psi + i\theta = \ln \zeta \tag{29}$$

It is assumed that the function $\ln \zeta$ is uniquely defined by a branch cut on the negative real axis, that is, $-\pi < \arg(\ln \zeta) \leq \pi$. If the point is an upper surface point, θ is always positive, so that

$$\theta = \theta \text{ sign } [\arg(\ln \zeta)] \tag{30}$$

$$\psi = \psi \text{ sign } [\arg(\ln \zeta)] \tag{31}$$

where sign is defined as

$$\text{sign}(A) = \left\{ \begin{array}{ll} 1 & (A \geq 0) \\ -1 & (A < 0) \end{array} \right\} \tag{32}$$

Similarly, for the lower surface, θ is always negative so that

$$\theta = -\theta \text{ sign } [\arg(\ln \zeta)] \tag{33}$$

$$\psi = -\psi \text{ sign } [\arg(\ln \zeta)] \tag{34}$$

For θ to be monotonically increasing, 2π must be added to the value of θ on the lower surface. This corresponds to placing the branch cut for $\ln \zeta$ on the positive axis such that $0 \leq \arg(\ln \zeta) < 2\pi$.

Cubic Spline

Now that the sections are described in elliptic coordinates, the airfoil parameters are fit with a cubic spline. (The interpolation procedure is described in detail in appendix B.) Introducing new variables

$$\xi_1 = \eta_2 C \tag{35}$$

to describe the spanwise direction and

$$\xi_2 = \theta/2\pi \tag{36}$$

to describe the chordwise direction, a computational grid is formed. The $N_{\xi 2}$ values of ξ_2 are input so that

$$0 < \xi_2 < 1 \tag{37}$$

As indicated in appendix B, the variables ξ_1 and ξ_2 do not have to be evenly spaced.

The cubic spline interpolation procedure allows for two optional boundary conditions, one with zero slope or one with zero curvature. The zero slope condition gives a rounded edge on the trailing edge, whereas the zero curvature condition gives a sharp trailing edge. A cubic spline is fit in the chordwise direction ξ_2 for $\psi(\xi_1,\xi_2)$ in a least-squares sense for the case where the number of input points are greater than the number of output points. The fit also allows for weighting of specific input surface points. If the number of output points is equal to or greater than the number of input points, then the input grid is used for interpolation.

Solution for Pitch Axis Coordinates

The next step is to find the pitch axis coordinates of the grid points (ξ_1,ξ_2). All lengths in the pitch axis coordinates are referred to the blade length R so that the Joukowski parameter is scaled by

$$b(\xi_1) = C(\xi_1)\ b \tag{38}$$

The pitch axis coordinates are given by

$$x(\xi_1,\xi_2) = 2b(\xi_1) \cosh \psi(\xi_1,\xi_2) \cos 2\pi\xi_2 \tag{39}$$

and

$$y(\xi_1,\xi_2) = 2b(\xi_1) \sinh \psi(\xi_1,\xi_2) \sin 2\pi\xi_2 \tag{40}$$

Let $\eta_{1,e}$, $\eta_{2,e}$, and $\eta_{3,e}$ denote the location of the origin of the elliptic coordinate system in the pitch axis system. Then

$$\eta_{1,e}(\xi_1) = \eta_{1,\ell}(\xi_1) - x_\ell \cos \theta_T(\xi_1) \tag{41}$$

$$\eta_{2,e} = \xi_1 \tag{42}$$

and

$$\eta_{3,e}(\xi_1) = \eta_{3,\ell}(\xi_1) + x_\ell \sin \theta_T(\xi_1) \tag{43}$$

where x_ℓ is the location of the leading edge given by

$$x_\ell(\xi_1) = x(\xi_1, \xi_2{=}0.5) \tag{44}$$

The components of the surface points in the pitch axis system are given by

$$\eta_1(\xi_1,\xi_2) = \eta_{1,e}(\xi_1) + [x_\ell(\xi_1,\xi_2) \cos \theta_T(\xi_1) + y_\ell(\xi_1,\xi_2) \sin \theta_T(\xi_1)] \tag{45}$$

$$\eta_2(\xi_1,\xi_2) = \xi_1 \tag{46}$$

and

$$\eta_3(\xi_1,\xi_2) = \eta_{3,e}(\xi_1) + [-x_\ell(\xi_1,\xi_2) \sin \theta_T(\xi_1) + y_\ell(\xi_1,\xi_2) \cos \theta_T(\xi_1)] \tag{47}$$

Finally, the blade section area is computed by

$$A(\xi_1) = \int_0^1 \eta_1(\xi_1,\xi_2) \frac{\partial \eta_3}{\partial \xi_2}(\xi_1,\xi_2)\, d\xi_2 \tag{48}$$

APPENDIX A

ASPECT RATIO, ACTIVITY FACTOR, AND BLADE VOLUME

The aspect ratio is defined as the blade length squared divided by the blade surface area. The equation used in this module is

$$AR = \frac{(1 - \xi_{1,m})^2}{\int_{\xi_{1,m}}^{1} C(\xi_1)\, d\xi_1}$$

where $\xi_{1,m}$ is the minimum value of ξ_1.

The activity factor is a measure of the capacity of the blade to absorb power. It is defined as

$$AF = \frac{100\ 000}{32} \int_{\xi_{1,m}}^{1} C(\xi_1)\, \xi_1^{3}\, d\xi_1$$

The blade volume is computed by integrating the blade section area as

$$V = \int_{\xi_{1,m}}^{1} A(\xi_1)\, d\xi_1$$

APPENDIX B

SPLINE INTERPOLATION PROCEDURE

This appendix describes the basic cubic spline interpolation procedure and then extends it to a piecewise linear finite-element approximation (ref. 2). The one-dimensional case is described in detail, which allows for the types of boundary conditions. With the finite-element approach, the interpolation procedure is then easily extended to two dimensions.

One-Dimensional Cubic Spline Interpolation

One of the simplest ways to interpolate between two data points is to construct a polynomial. Assuming that the slope and magnitude of a function at two points x_i and x_{i+1} are known, a cubic polynomial can be constructed which is uniquely defined by

$$F(x) = F_i + F_i'(x - x_i) + \left[3\frac{\Delta F_{i+1}}{\Delta x_{i+1}^{2}} - \frac{F_{i+1}' + 2F_i'}{\Delta x_{i+1}}\right](x - x_i)^2 + \left[-2\frac{\Delta F_{i+1}}{\Delta x_{i+1}^{3}} + \frac{F_{i+1}' + F_i'}{\Delta x_{i+1}^{2}}\right](x - x_i)^3 \tag{B1}$$

where

$$F(x_i) = F_i \tag{B2}$$

$$\Delta x_i = x_i - x_{i-1} \tag{B3}$$

and

$$\Delta F_i = F_i - F_{i-1} \tag{B4}$$

Adding an additional point, two separate cubic polynomials, that is, piecewise polynomials, can be constructed which have continuous first and second derivatives at x_i. Assume $f(x)$ is a cubic polynomial on the interval $x_{i-1} \le x \le x_i$ and $g(x)$ is a cubic polynomial the interval $x_i \le x \le x_{i+1}$. Further assume the following information is known concerning $f(x)$ and $g(x)$:

$$f(x_{i-1}) = F_{i-1} \tag{B5a}$$

$$f'(x_{i-1}) = F_{i-1}' \tag{B5b}$$

$$f(x_i) = g(x_i) = F_i \tag{B5c}$$

$$g(x_{i+1}) = F_{i+1} \tag{B5d}$$

$$g'(x_{i+1}) = F'_{i+1} \tag{B5e}$$

Differentiating equation (B1) twice and evaluating both functions $f(x)$ and $g(x)$ at x_i yields

$$f''(x_i) = \frac{2}{\Delta x_i}\left[-3\,\frac{\Delta F_i}{\Delta x_i} + 2F'_i + F'_{i-1}\right] \tag{B6}$$

and

$$g''(x_i) = \frac{2}{\Delta x_{i+1}}\left[3\,\frac{\Delta F_{i+1}}{\Delta x_{i+1}} - 2F'_i - F'_{i+1}\right] \tag{B7}$$

Setting

$$f''(x_i) = g''(x_i) \tag{B8}$$

and collecting terms of F'_i yield

$$\Delta x_{i+1}\, F'_{i-1} + 2(\Delta x_{i+1} + \Delta x_i)\, F'_i + \Delta x_i\, F'_{i+1}$$
$$= 3\left[\frac{\Delta x_i}{\Delta x_{i+1}}\left(F_{i+1} - F_i\right) + \frac{\Delta x_{i+1}}{\Delta x_i}\left(F_i - F_{i-1}\right)\right] \tag{B9}$$

This equation relates the slope at intermediate nodes to the magnitudes at the nodes and the slope boundary condition such that first and second derivatives are continuous. Equation (B9) can be extended to I values of x_i, resulting in I - 2 simultaneous equations. The two additional equations are provided by the boundary conditions. Two options are considered, one with zero slope on the boundary and one with zero curvature on the boundary.

For zero slope, the two additional equations are simply

$$F'_1 = 0 \tag{B10}$$

$$F'_I = 0 \tag{B11}$$

For zero curvature, the two additional equations are found by setting $f''(x_I) = 0$ in equation (B6) and $g''(x_1) = 0$ in equation (B7). From equation (B7) an expression for zero curvature on the x_1 boundary is given by

$$F'_1 + \frac{F'_2}{2} = \frac{3}{2} \frac{\Delta F_2}{\Delta x_2} \tag{B12}$$

and from equation (B6) an equation for zero curvature on the x_I boundary is given by

$$\frac{F'_{I-1}}{2} + F'_I = \frac{3}{2} \frac{\Delta F_I}{\Delta x_I} \tag{B13}$$

Having solved for F'_i, $i = 1,2,\ldots I$, then any value of $F(x)$ can be determined by locating

$$x_i \leq x \leq x_{i+1} \tag{B14}$$

and solving equation (B1). This procedure, which uses a cubic polynomial as the interpolating function and requires continuity of first and second derivatives at the nodes, is commonly referred to as a cubic spline.

The cubic spline interpolation procedure can be extended to a piecewise linear finite-element approach where $F(x)$ is given by

$$F(x) = \sum_{j=1}^{J} \beta_j \phi_j(x) \tag{B15}$$

where J is the number of nodes. The function $F(x)$ is defined in terms of a set of coefficients β_j and a set of basis functions $\phi_j(x)$. The basis functions have the following conditions

$$\phi_j(x_i) = \delta_{ij} = \begin{Bmatrix} 0 & (i \neq j) \\ 1 & (i = j) \end{Bmatrix} \tag{B16}$$

and a linear homogeneous boundary condition such that

$$\phi'_j(x_1) = \phi'_j(x_I) = 0 \qquad (j = 1, 2, \ldots, J) \tag{B17}$$

The index i refers to the node and the index j refers to the basis function. For $J = 3$, note in figure 6 that ϕ_1 is unity at x_1, whereas the remaining basis functions ϕ_2 and ϕ_3 are zero. The coefficient β_1 is therefore the magnitude of $F(x)$ at x_1. Similarly, the coefficients β_j are the magnitude of $F(x)$ at the corresponding node. Note, also that the nodes x_i do not have to be evenly spaced.

The set of basis functions $\phi_j(x)$ are piecewise continuous cubic polynomials over the entire range of x. Consequently an array of magnitudes and slopes must be determined for each basis function $\phi_j(x)$ at each node x_i. This results in two matrices,

$$\phi_{ij} = \phi_j(x_i) \qquad (i,\ j = 1,\ 2,\ \ldots,\ J) \qquad \text{(B18)}$$

and

$$\phi'_{ij} = \frac{d}{dx}\,\phi_j(x_i) \qquad (i,\ j = 1,\ 2,\ \ldots,\ J) \qquad \text{(B19)}$$

The magnitude matrix ϕ_{ij} is simply the identity matrix defined by equation (B16). The slope matrix ϕ'_{ij} is computed by solving the following equations for the slopes of each basis function

$$[A_{ki}]\ [\phi'_{ij}] = [B_{kj}] \qquad (i,\ j,\ k = 1,\ 2,\ \ldots,\ J) \qquad \text{(B20)}$$

The slope vector solutions from equation (B20) are collected to form the slope matrix. Equation (B20) is constructed for the two optional boundary conditions by choosing $M = 0$ and $K = 1$ for zero slope or $M = 1$ and $K = 0$ for zero curvature. The $k = 1$ row of equation (B20) is given by

$$M(2\phi'_{ij} + \phi'_{i+1,j}) + K\phi'_{ij} = 3M(\delta_{i+1,j} - \delta_{ij})/\Delta x_{i+1} \qquad \begin{pmatrix} i = 1; \\ j = 1,\ 2,\ \ldots,\ J \end{pmatrix} \qquad \text{(B21)}$$

The intermediate rows of equation (B20) are given by

$$\Delta x_{i+1}\ \phi'_{i-1,j} + 2(\Delta x_{i+1} + \Delta x_i)\ \phi'_{ij} + \Delta x_i\ \phi'_{i+1,j}$$

$$= 3\left[\frac{\Delta x_i}{\Delta x_{i+1}}(\delta_{i+1,j} - \delta_{ij}) + \frac{\Delta x_{i+1}}{\Delta x_i}\ (\delta_{ij} - \delta_{i-1,j})\right]$$

$$(i = 2,\ 3,\ \ldots,\ I - 1;\ j = 1,\ 2,\ \ldots,\ J) \qquad \text{(B22)}$$

and finally the $k = J$ row of equation (B20) is given by

$$M(\phi'_{i-1,j} + 2\phi'_{ij}) + K\phi'_{ij} = 3M(\delta_{ij} - \delta_{i-1,j})/\Delta x_i \qquad \begin{pmatrix} i = I = J; \\ j = 1,\ 2,\ \ldots,\ J \end{pmatrix} \qquad \text{(B23)}$$

With the slope matrix determined, each basis function can be evaluated by calculating i such that

$$x_i \le x < x_{i+1} \qquad \text{(B24)}$$

and evaluating ϕ_j by

$$\phi_j(x) = \delta_{ij} + \phi'_{ij}(x - x_i)$$

$$+ \left[3 \frac{(\delta_{i+1,j} - \delta_{ij})}{\Delta x_{i+1}^{2}} - \frac{\phi'_{i+1,j} + 2\phi'_{ij}}{\Delta x_{i+1}} \right] (x - x_i$$

$$+ \left[-2 \frac{\delta_{i+1,j} - \delta_{ij}}{\Delta x_{i+1}^{3}} + \frac{\phi'_{i+1,j} + \phi'_{ij}}{\Delta x_{i+1}^{2}} \right] (x - x_i$$

The coefficients β_j are determined by a least-squares solution
the equation

$$[\phi_j(x_i')]\ \{\beta_j\} = \{F(x_i')\} \qquad \left(\begin{array}{r} j = 1, 2, \ldots, J \\ i' = 1, 2, \ldots, I' > J \end{array} \right.$$

where $\phi_j(x_i')$ is the matrix of values of the basis function a
the data points.

Two-Dimensional Cubic Spline Interpolation

The one-dimensional interpolation procedure may be extende
dimensions through the basis functions. The function $F(x_1,x_2$
given by

$$F(x_1,x_2) = \sum_{j1=1}^{J_1} \sum_{j2=1}^{J_2} \beta_{j1j2}\ \phi_{1j}(x_1)\ \phi_{2j}(x_2)$$

The basis functions $\phi_{1j}(x_1)$ and $\phi_{2j}(x_2)$ are piecewise cubic
polynomials, each a function of only one variable. Therefore,
basis functions are evaluated in exactly the same manner as in
one-dimensional case. The coefficients $\beta_{j_1j_2}$ are determined
least-squares solution of a given set of points
$F(x_{1i},x_{2i}) = F_{i1i2}$

REFERENCES

1. Theodorsen, Theodore: Theory of Wing Sections of Arbitrary Shape. NACA Rep. 411, 1931.

2. De Boor, Carl: Bicubic Spline Interpolation. J. Math. & Phys., vol. 41, 1962, pp. 212-218.

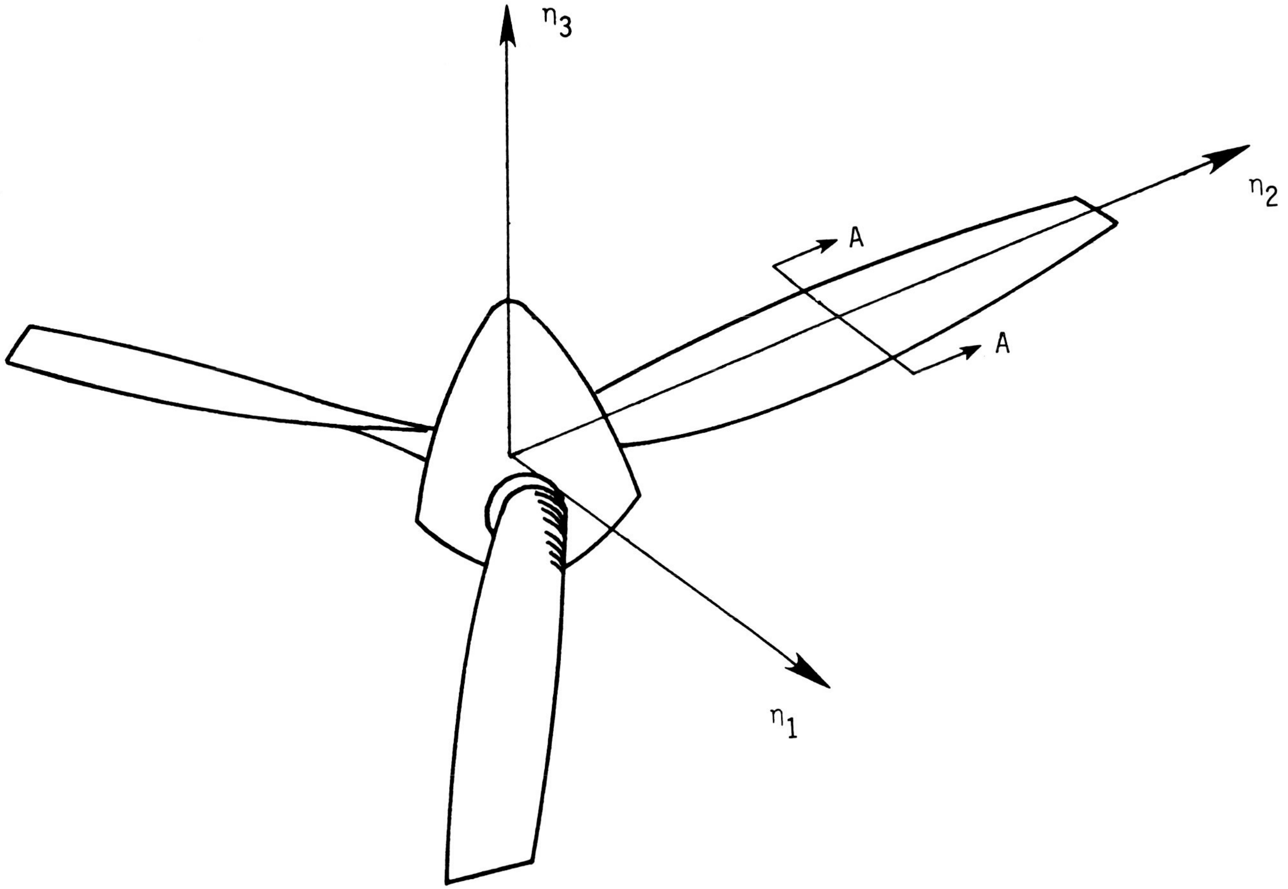

Figure 1.- Airfoil orientation in pitch axis coordinate system.

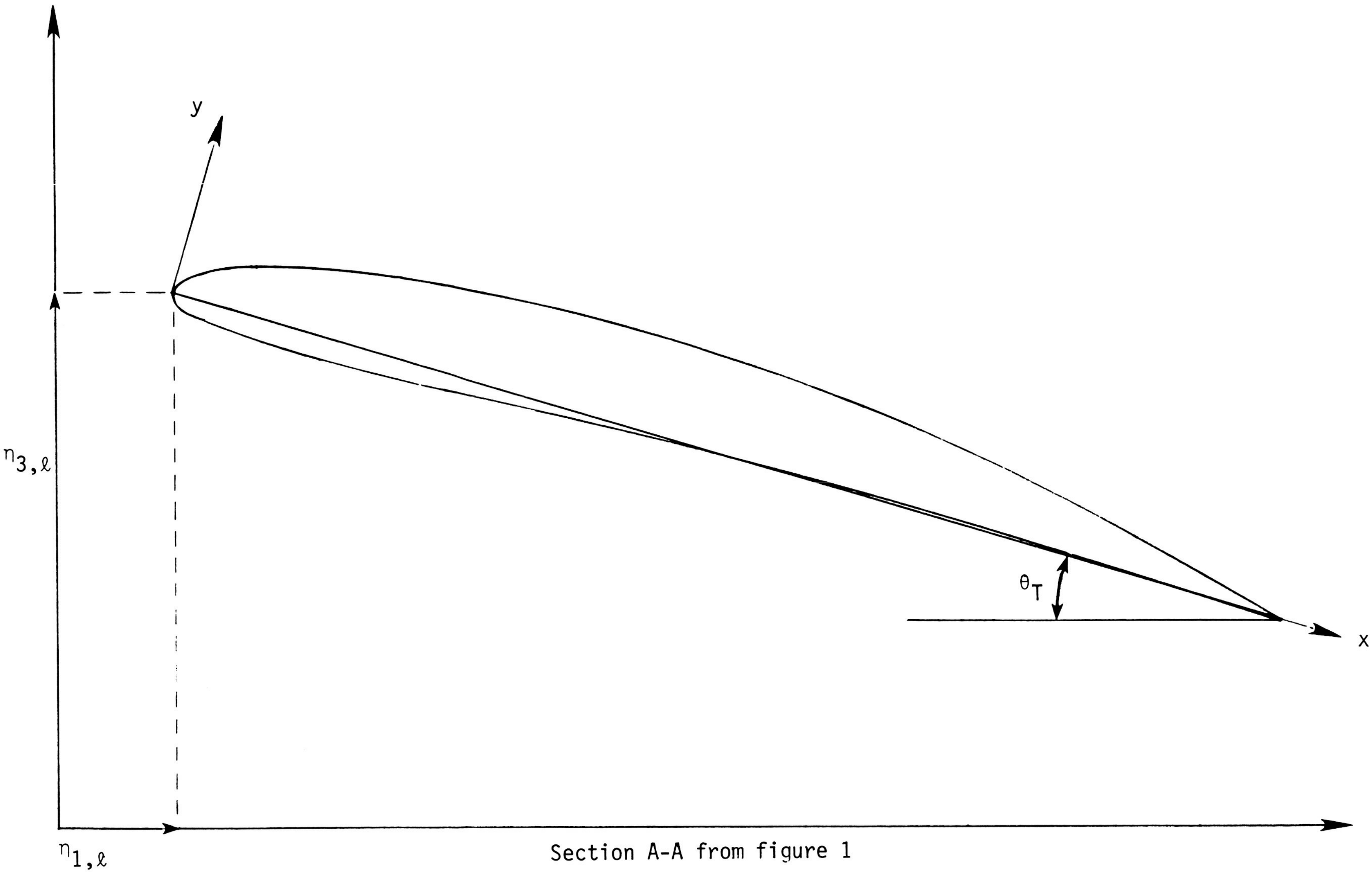

Section A-A from figure 1

Figure 2.- Typical airfoil section in pitch axis coordinate system.

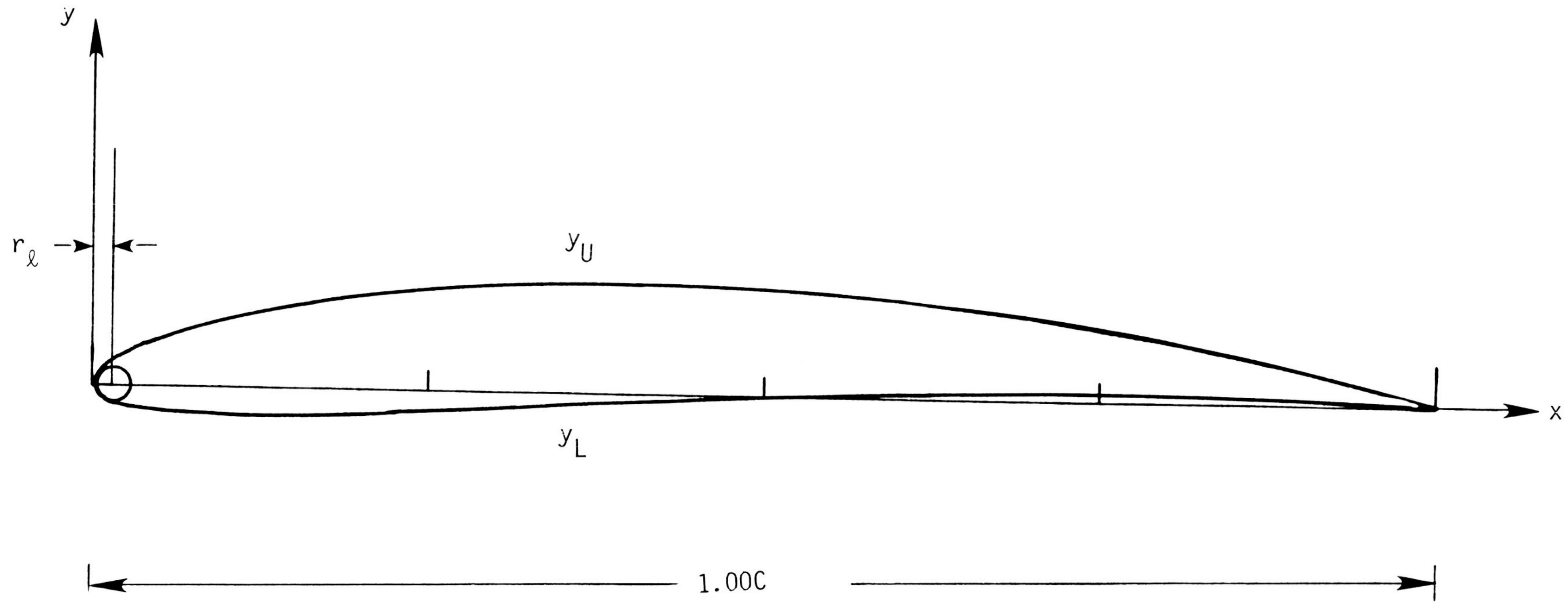

Figure 3.- Typical airfoil section in input Cartesian coordinate system.

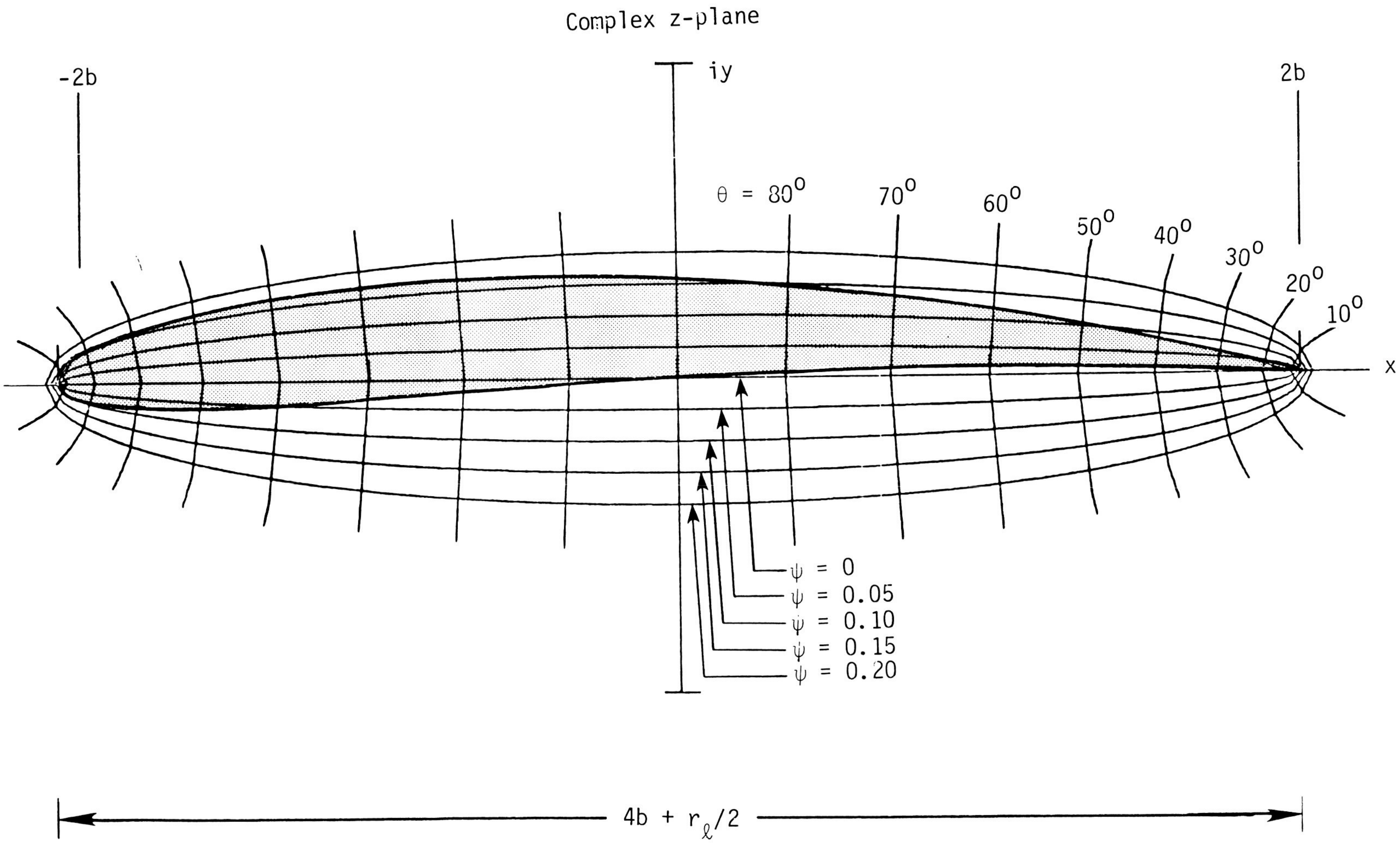

Figure 4.- Typical airfoil section in complex z-plane.

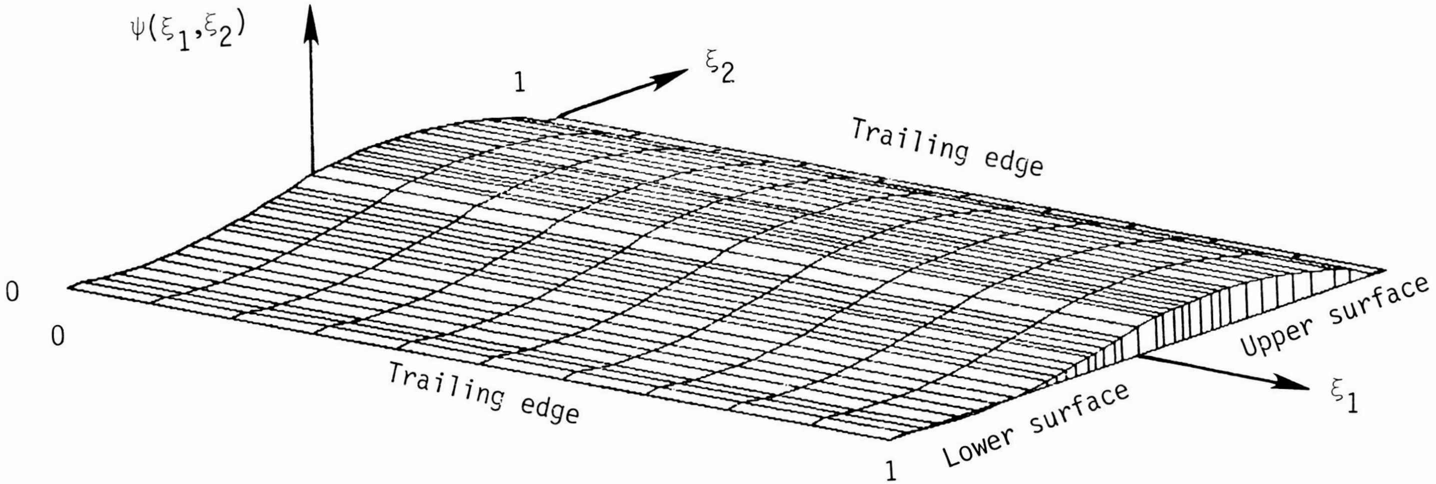

Figure 5.- Airfoil section in computational space.

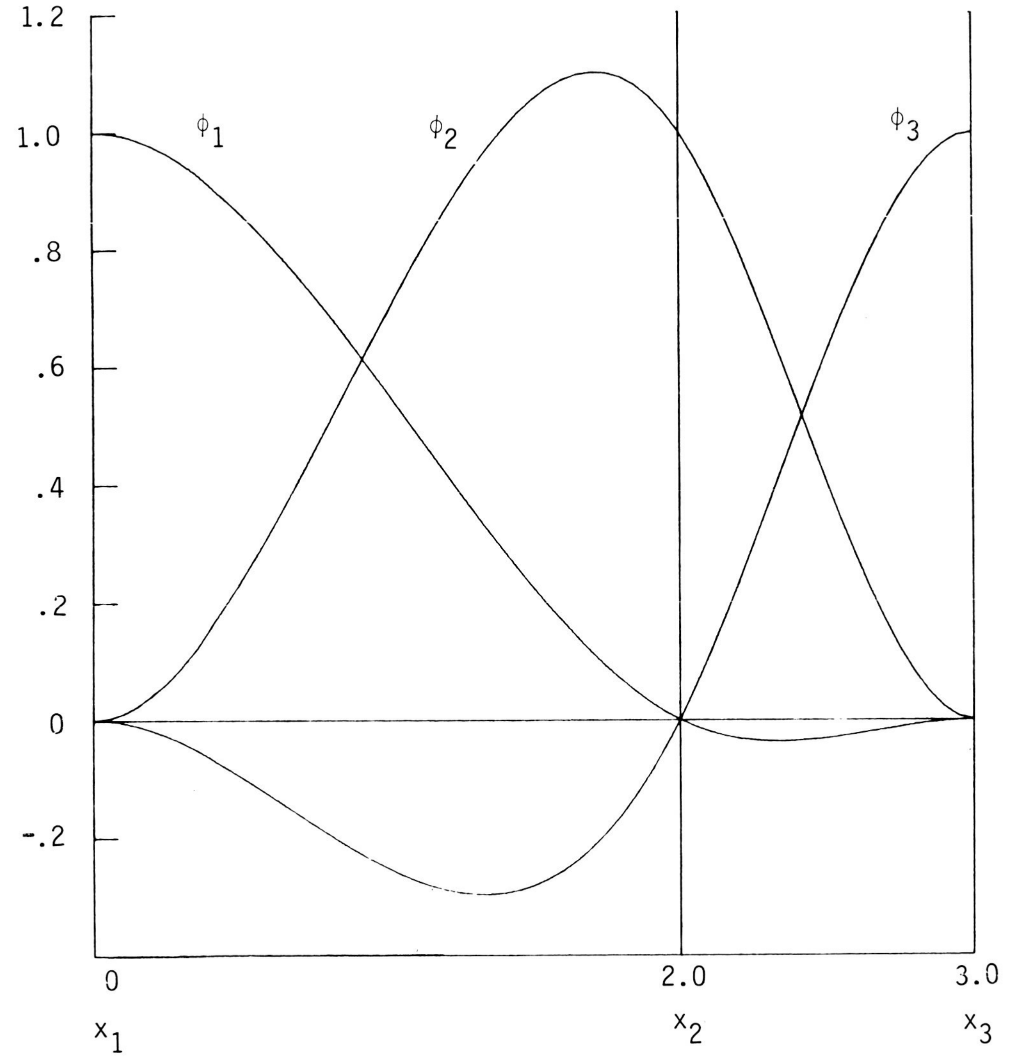

Figure 6.- Cubic spline basis function for three unevenly spaced nodes.

10.3 BLADE SECTION AERODYNAMICS MODULE

William E. Zorumski
Langley Research Center

INTRODUCTION

Detailed knowledge of the aerodynamic loading on a rotating blade is important for the prediction of rotational and broadband noise. The Blade Section Aerodynamics Module computes the pressure forces acting on the upper and lower surfaces of a two-dimensional airfoil for specified angle of attack and Mach number values. This aerodynamic output provides input information to the Propeller Loading Module, which computes the time dependent aerodynamic loading on the rotating blade.

The local flow field on a blade section can be subsonic, transonic, or supersonic, depending upon the free-stream velocity and location from the hub. Only the incompressible and low subsonic computation methodologies are included in this module.

This module produces a table of the pressure coefficient as a function of blade coordinates, angle of attack, and Mach number. Theodorsen's method (ref. 1) of successive conformal mapping, which yields good comparison with experiments for incompressible flow (i.e., $M \leq 0.4$), is used. The Blade Shape Module provides the airfoil shape in elliptic coordinates. An application of the inverse Joukowski transformation maps this airfoil into a nearly circular curve. An inversion of the Theodorsen mapping function transforms this near-circle into a perfect circle on another complex plane. Since the velocity potential for flow around a circle is well-known, two successive transforms produce the flow field around the airfoil. Circulation is determined by the Kutta condition at the trailing edge, and the leading-edge stagnation point is found by the mapping from the perfect circle. The section lift coefficient is found from the Kutta-Joukowski theorem. The surface velocity on the airfoil is found by the mapping functions and the coefficient of pressure is then found by Bernoulli's equation. The incompressible pressure coefficient is extended to subsonic flow (i.e., $M \leq 0.7$) by the simple Karman-Tsien compressibility correction.

SYMBOLS

A_n, B_n	conformal mapping coefficients from ζ- to ζ'-plane
a	radius of perfect circle, re R
b	Joukowski transformation parameter, re R
C	chord length

C_ℓ	section lift coefficient, $\frac{\ell}{\frac{1}{2}\rho_\infty V_\infty^2 C}$
$C_{m,c}$	section moment coefficient about aerodynamic center, positive when nose up, $\frac{m}{\frac{1}{2}\rho_\infty V_\infty^2 C^2}$
C_p	local pressure coefficient , $\frac{p - p_\infty}{\frac{1}{2}\rho_\infty V_\infty^2}$
$\tilde{F}(\zeta)$	complex velocity potential function in ζ-plane
ℓ	section lift
M	Mach number
m	section aerodynamic moment
p	local aerodynamic pressure
r	radial distance in polar coordinates
R	blade length, m (ft)
V_∞	free-stream velocity
W(z)	complex velocity in z-plane
$\tilde{W}(\zeta)$	complex velocity in ζ-plane
z	physical plane of airfoil in elliptical coordinates (ψ, ξ_2)
α	blade section angle of attack, measured from abscissa of airfoil elliptic coordinate, deg
Γ	circulation, positive clockwise when viewed from hub, m-m/s (ft-ft/s)
ε	$= \theta - 2\pi\xi_2$, rad
ε_T	ε evaluated at airfoil trailing edge, rad
ζ	complex quantity defining transformation plane containing perfect circle $\zeta = be^{\psi_0 + i\theta}$
ζ'	complex quantity defining transformation plane containing an almost circular curve, $be^{\psi + 2\pi i \xi_2}$

$\eta_{1,c}$	abscissa of aerodynamic center, re R
$\eta_{3,c}$	ordinate of aerodynamic center, re R
$\eta_{1,\ell}$	leading-edge abscissa, re R
$\eta_{3,\ell}$	leading-edge ordinate, re R
ξ_1	spanwise surface coordinate
ξ_2	chordwise surface coordinate
θ	polar angle in transformation plane ζ, rad
ψ	blade surface elliptic radial coordinate
ψ_0	$= \frac{1}{2\pi}\int_0^{2\pi} \psi \, d\theta$, rad
ρ	air density, kg/m^3 (slug/ft^3)

Subscripts:

s	stagnation point
T	trailing edge
∞	ambient

INPUT

The basic independent variables are the airfoil elliptical coordinates $\psi(\xi_1,\xi_2)$ and arrays of Mach numbers and angles of attack.

Blade Geometry

ξ_1	array of spanwise surface coordinates
ξ_2	array of chordwise surface coordinates
$\eta_{1,\ell}(\xi_1)$	leading-edge abscissa, re R
$\eta_{3,\ell}(\xi_1)$	leading-edge ordinate, re R
$b(\xi_1)$	Joukowski transformation parameter, re R
$C(\xi_1)$	chord length, re R
$\psi(\xi_1,\xi_2)$	blade surface elliptic radial coordinate

Output Controls

N_α	number of angles of attack
N_M	number of Mach numbers
α	array of angles of attack, deg
M	array of Mach numbers

OUTPUT

This module produces tables of C_p as functions of surface position, angle of attack, and Mach number. This module also computes the section aerodynamic lift coefficients C_ℓ, moment coefficients $C_{m,c}$, the aerodynamic-center locations, and the leading-edge stagnation point.

ξ_1	array of spanwise surface coordinates
ξ_2	array of chordwise surface coordinates
α	array of angles of attack, deg
M	array of Mach numbers
$C_p(\xi_1,\xi_2,\alpha,M)$	local pressure coefficient
$C_\ell(\xi_1,\alpha,M)$	section lift coefficient
$C_{m,c}(\xi_1,M)$	section moment coefficient about aerodynamic center
$\eta_{1,c}(\xi_1)$	abscissa of aerodynamic center, re R
$\eta_{3,c}(\xi_1)$	ordinate of aerodynamic center, re R
$\xi_{2,s}(\xi_1,\alpha,M)$	leading-edge stagnation point, rad

METHOD

This module computes airfoil section aerodynamics for subsonic flow. Theodorsen's method (ref. 1) is adopted for low subsonic flow with a pressure compressibility correction for high subsonic flow.

Conformal Mapping

The Theodorsen method starts with an airfoil located in an elliptical coordinate system in the z-plane. Under an inverse Joukowski transform, an ellipse in the z-plane of the airfoil will be mapped onto a circle. Thus, an airfoil will be mapped onto a ζ'-plane as a near-circle. The Joukowski transformation is given by

$$z = \zeta' + b^2/\zeta' \tag{1}$$

A second transform will map the near-circle onto another plane, ζ-plane, as a perfect circle.

Letting

$$\zeta' = be^{\psi(\xi_1,\xi_2)+2\pi i\xi_2} \tag{2}$$

be the near-circle and

$$\zeta = be^{\psi_0}\, e^{i\theta} \tag{3}$$

be the perfect circle with be^{ψ_0} as its radius, a general transform from the near-circle to the perfect circle can be written as

$$\zeta' = \zeta \exp\left(\sum_{n=1}^{\infty} (A_n + iB_n)/\zeta^n \right) \tag{4}$$

Combining equations (2) and (3) gives

$$\zeta' = \zeta e^{(\psi-\psi_0)} e^{\,i(2\pi\xi_2-\theta)} \tag{5}$$

Equations (4) and (5) yield

$$\psi - \psi_0 + i(2\pi\xi_2 - \theta) = \sum_{n=1}^{\infty} (A_n + iB_n)/\zeta^n \tag{6}$$

A general point on the ζ-plane can also be represented in polar coordinates as

$$\zeta = re^{i\theta} \tag{7}$$

Hence, equating real and imaginary parts in equation (6) gives

$$\psi - \psi_0 = \sum_{n=1}^{\infty} \left[\frac{A_n}{r^n} \cos n\theta + \frac{B_n}{r^n} \sin n\theta \right] \tag{8}$$

$$2\pi\xi_2 - \theta = \sum_{n=1}^{\infty} \left[\frac{B_n}{r^n} \cos n\theta - \frac{A_n}{r^n} \sin n\theta \right] \tag{9}$$

In equation (8), ψ_0 is the zeroth term of Fourier series expansion for ψ; thus

$$\psi_0 = \frac{1}{2\pi}\int_0^{2\pi} \psi \, d\theta \tag{10}$$

That is, the radius of the perfect circle is an average of the radii of the near-circle. We further have

$$\frac{A_n}{r^n} = \frac{1}{\pi}\int_0^{2\pi} \psi \cos n\theta \, d\theta \tag{11}$$

$$\frac{B_n}{r^n} = \frac{1}{\pi}\int_0^{2\pi} \psi \sin n\theta \, d\theta \tag{12}$$

Equations (8) through (12) constitute a system of equations which under iteration yields $2\pi\xi_2 - \theta$. Theodorsen adopted the symbol ε to denote the shift in arguments going from the ζ'- to ζ-plane, that is,

$$\varepsilon = \theta - 2\pi\xi_2 \tag{13}$$

Iterative Solution for $\varepsilon(\xi_2)$

From the tabulated values of ψ and ξ_2, repeated iteration will yield new values of ψ and θ, or equivalently, the difference of $\theta - 2\pi\xi_2$. The iteration procedure is

1. Assume an initial approximation, $\theta(\xi_2) = 2\pi\xi_2$
2. Evaluate $\psi_0 = \frac{1}{2\pi}\int_0^{2\pi} \psi(\xi_2(\theta)) \, d\theta$; note that numerical integration will involve uneven increments of $\Delta\theta$ because θ is a function of ξ_2 which has even increments $\Delta\xi_2$
3. Evaluate $\frac{A_n}{r^n} = \frac{1}{\pi}\int_0^{2\pi} \psi(\xi_2(\theta)) \cos n\theta \, d\theta$ and

   $\frac{B_n}{r^n} = \frac{1}{\pi}\int_0^{2\pi} \psi(\xi_2(\theta)) \sin n\theta \, d\theta$
4. Evaluate $2\pi\xi_2 - \theta = \sum_1^n \left[\frac{B_n}{r^n} \cos n\theta - \frac{A_n}{r^n} \sin n\theta\right]$
5. Loop from step b with $\theta(\xi_2) = 2\pi\xi_2 + \varepsilon(\xi_2)$
6. Iteration stops when $\varepsilon(\xi_2)$ converges

Coefficient of Lift

The flow field about the perfect circle is used to find the pressure distribution on the airfoil section. An arbitrary point on the surface of the perfect circle is

$$\zeta = ae^{i\theta} \tag{14}$$

where

$$a = be^{\psi_0} \tag{15}$$

The velocity potential in the ζ-plane is

$$\tilde{F}(\zeta) = V_\infty \left(\zeta e^{-i\alpha} + \frac{a^2}{\zeta} e^{i\alpha}\right) + i\frac{\Gamma}{2\pi} \ln \left(\frac{\zeta}{a} e^{-i\alpha}\right) \tag{16}$$

where α is the angle of attack as measured from the real axes (airfoil chord) in both the ζ-and z-planes. The complex velocity is determined from the velocity potential by

$$\tilde{W}(\zeta) = \frac{d\tilde{F}}{d\zeta} = V_\infty\left(e^{-i\alpha} - \frac{a^2}{\zeta^2} e^{i\alpha}\right) + i\frac{\Gamma}{2\pi\zeta} \tag{17}$$

The stagnation points are determined by the condition that the complex velocity is zero on the perfect circle:

$$\tilde{W}(\zeta)\Big|_{|\zeta|=a} = 0 \tag{18}$$

This is equivalent to

$$\sin(\theta - \alpha) + \frac{\Gamma}{4\pi a V_\infty} = 0 \tag{19}$$

The Kutta condition requires that the complex velocity at the trailing edge in the z-plane be finite. This is equivalent to requiring the trailing edge in the ζ-plane to be a stagnation point because the Joukowski transformation is singular at the trailing edge. At the trailing edge, $\theta = \epsilon_T$ so that the circulation Γ is

$$\Gamma = 4\pi a V_\infty \sin(\alpha - \epsilon_T) \tag{20}$$

The leading-edge stagnation point is a solution to equation (19) with the circulation given by equation (20). The relationship is

$$\sin(\theta_s - \alpha) + \sin(\alpha - \epsilon_T) = 0 \tag{21}$$

Of the two solutions to the arcsin function, one is the trailing-edge stagnation point

$$\theta_s = \varepsilon_T \tag{22}$$

The leading-edge stagnation point is found from

$$\sin(\theta_s - \alpha) + \sin(\pi - (\alpha - \varepsilon_T)) = 0$$

or

$$\theta_s = \pi + 2\alpha - \varepsilon_T \tag{23}$$

The section lift is given by the Kutta-Joukowski law

$$\ell = \rho V_\infty \Gamma \tag{24}$$

so that the coefficient of lift for the section becomes

$$C_\ell = 2\pi \frac{4a}{C} \sin(\alpha - \varepsilon_T) \tag{25}$$

Coefficient of Pressure

The coefficient of pressure is found from Bernoulli's equation and the complex velocity in the z-plane. Bernoulli's equation gives

$$C_p = 1 - \left| \frac{W(z)}{V_\infty} \right|^2 \tag{26}$$

To adjust for compressibility effects, the Karman-Tsien pressure correction formula

$$C_p = \left\{ \frac{C_p}{\sqrt{1 - M^2} + \frac{M^2}{1 + \sqrt{1 - M^2}} \frac{C_p}{2}} \right\}_{\text{incompressible}} \tag{27}$$

is applied, and the complex velocity $W(z)$ is found by the transform

$$\frac{W(z)}{V_\infty} = \left(\frac{d\zeta}{d\zeta'}\right) \left(\frac{dz}{d\zeta'}\right)^{-1} \frac{\tilde{W}(\zeta)}{V_\infty} \tag{28}$$

The independent variable in equation (28) is ζ', the complex position in the Joukowski plane. Both ζ and z are given functions of ζ' as discussed earlier. The derivative of z with respect to ζ' is

$$\frac{dz}{d\zeta'} = \frac{(\zeta' - b)(\zeta' + b)}{(\zeta')^2} \tag{29}$$

so that the expression for the complex velocity becomes

$$\frac{W(z)}{V_\infty} = (\zeta')^2 \frac{d\zeta}{d\zeta'} \frac{\tilde{W}(\zeta)/V_\infty}{(\zeta' - b)(\zeta' + b)} \quad (|\zeta' \pm b| \approx O(b)) \tag{30}$$

The complex velocity $\tilde{W}(\zeta)$ in equation (30) is

$$\frac{\tilde{W}(\zeta)}{V_\infty} = e^{-i\alpha}\left[1 + 2 \sin (\alpha - \varepsilon_T) \frac{iae^{i\alpha}}{\zeta} + \left(\frac{iae^{i\alpha}}{\zeta}\right)^2\right] \tag{31}$$

and for points on the airfoil surface

$$\frac{d\zeta}{d\zeta'} = \frac{1 + \varepsilon'}{1 - i\psi'} \frac{\zeta}{\zeta'} \tag{32}$$

Primes denote differentiation with respect to ξ_2. For points near $\zeta' = \pm b$, equation (30) must be evaluated in the limit as ζ' approaches $\pm b$.

Trailing edge.- First consider the trailing-edge point where $\zeta' = b$ and $\zeta = \zeta(b) = \zeta_T$. Near this point,

$$\tilde{W}(\zeta) = \tilde{W}(\zeta_T) + \frac{d\tilde{W}(\zeta_T)}{d\zeta}(\zeta - \zeta_T) \tag{33}$$

and

$$(\zeta - \zeta_T) = \frac{d\zeta(b)}{d\zeta'}(\zeta' - b) \tag{34}$$

Since $\tilde{W}(\zeta_T) = 0$ by definition,

$$\frac{W(z)}{V_\infty} = \frac{(\zeta')^2}{\zeta' + b} \frac{d\zeta(\zeta')}{d\zeta'} \frac{d\zeta(b)}{d\zeta'} \left[\frac{1}{V_\infty} \frac{d\tilde{W}(\zeta_T)}{d\zeta}\right] (|\zeta' - b| << b) \tag{35}$$

where

$$\frac{1}{V_\infty} \frac{d\tilde{W}(\zeta)}{d\zeta} = \frac{-2ia}{\zeta^2}\left[\sin (\alpha - \varepsilon_T) + \frac{iae^{i\alpha}}{\zeta}\right] \tag{36}$$

Leading edge.- For points on the leading edge near both $\zeta' = -b$ and the stagnation point ζ'_s, an expansion around $\zeta' = -b$ gives

$$\tilde{W}(\zeta) = \tilde{W}[\zeta(-b)] + \frac{d\tilde{W}[\zeta(-b)]}{d\zeta}[\zeta - \zeta(-b)] \tag{37}$$

with

$$[\zeta - \zeta(-b)] = \frac{d\zeta(-b)}{d\zeta'}(\zeta' + b) \tag{38}$$

The expansion for $\tilde{W}(\zeta)$ in terms of ζ' is then

$$\tilde{W}(\zeta) = \tilde{W}[\zeta(-b)] + \frac{d\tilde{W}[\xi(-b)]}{d\zeta} \frac{d\zeta(-b)}{d\zeta'}(\zeta' + b) \tag{39}$$

If the stagnation point ζ_s' is near $-b$; that is, if

$$|\zeta_s' + b| \ll b$$

then equation (39) may be used to solve for $\tilde{W}[\zeta(-b)]$ and the resulting expression for $\tilde{W}(\zeta)$ becomes

$$\tilde{W}(\zeta) = \frac{d\tilde{W}[\zeta(-b)]}{d\zeta} \frac{d\zeta(-b)}{d\zeta'}(\zeta' - \zeta_s') \tag{40}$$

The expression for $W(z)$ is then

$$\frac{W(z)}{V_\infty} = \frac{(\zeta')^2}{\zeta' - b} \frac{d\zeta(\zeta')}{d\zeta'} \frac{d\zeta(-b)}{d\zeta'} \frac{1}{V_\infty} \frac{d\tilde{W}[\zeta(-b)]}{d\zeta} \frac{\zeta' - \zeta_s'}{\zeta' + b} \left(\begin{matrix} |\zeta' + b| << b \\ |\zeta_s' + b| << b \end{matrix} \right) \tag{41}$$

The last term in equation (41) is of order unity as long as $|\zeta_s' + b| << b$ in accordance with the assumption for $W(\zeta)$. The field point ζ' must also be near $-b$ in order for expansion (39) to be used. The two conditions are shown in the following sketch:

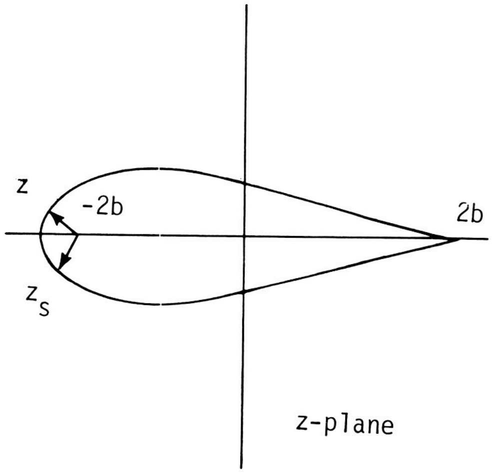

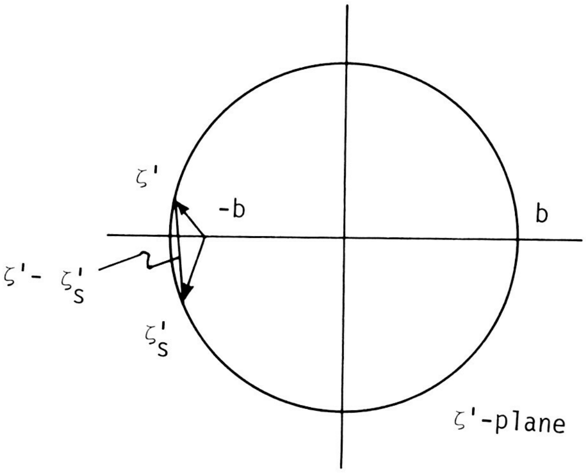

The largest side of the triangle $(-b, \zeta', \zeta_s')$ in the Joukowski plane must have a length that is small compared with b, the approximate radius of the near-circle in order for equation (41) to be used. Since two sides of the triangle determine the third side, we place the conditions on $|\zeta' + b|$ and $|\zeta_s' + b|$. The latter condition limits the angle of attack α.

$$\left|\frac{\zeta_s' + b}{b}\right| = \left|e^{\psi_s + i\xi_{2s}} + 1\right| << 1 \tag{42}$$

The angle $\varepsilon(\xi_2)$ is typically small everywhere and $\psi(\xi_2)$ is small, especially near the leading edge where stagnation is likely to occur. With the use of equation (23), condition (42) is therefore approximated by

$$\left|-e^{i2\alpha} + 1\right| << 1 \tag{43}$$

or

$$|\alpha| << 1$$

Consequently, equation (41) may be used near the leading edge when α is small.

Based on the foregoing discussion, the following sequence of computations are used to compute $C_p(\xi_1, \xi_2, \alpha)$. The steps are the same for each doublet of values (ξ_1, α) and are as follows:

1. Compute a by equation (15)

2. Find the stagnation point $\xi_{2,s}$ by equation (23)

```
3.  Find $\zeta'_s$ by equation (2)
4.  Begin a loop on increasing values of $\xi_2$
5.  Compute $\zeta'$ by equation (2)
6.  Compute $\theta$ by equation (13), interpolating on $\varepsilon(\xi_2)$ if necessary
7.  Compute $\zeta$ by equation (14)
8.  Compute $\frac{d\zeta}{d\zeta'}$ by equation (32)
9.  If $\left|\zeta' - b\right| << b$, then
        Compute $\frac{d\zeta(b)}{d\zeta'}$ by equation (32)
        Compute $\frac{1}{V_\infty} \frac{d\tilde{W}(\zeta)}{d\zeta}$ by equation (36)
        Compute $\frac{W(z)}{V_\infty}$ by equation (35)
10. If $\left|\zeta'+b\right| < < b$, then
        Compute $\frac{d\zeta(-b)}{d\zeta'}$ by equation (32)
        If $\left|\zeta'_s+b\right| < < b$, then
            Compute $\frac{1}{V_\infty} \frac{d\tilde{W}[\zeta(-b)]}{d\zeta}$ by equation (36)
            Compute $\frac{W(z)}{V_\infty}$ by equation (41)
        Else give warning that $\zeta'_s$ is out of range for this angle of attack and station
11. Else compute $\frac{W(\zeta)}{V_\infty}$ by equation (31)
```

12. Compute $\frac{W(z)}{V_\infty}$ by equation (30)

13. Compute C_p by equations (26) and (27)

14. Continue looping steps 4 through 13 until all ξ_2 values are completed

Calculation of $C_{m,c}$ and Aerodynamic Center

The aerodynamic center is defined as the chordwise location where $\frac{dC_{m,c}}{d\alpha} = 0$. For thin airfoils, its location is observed to be about quarter-chord from the leading edge according to the following translation:

$$\eta_{1,c} = \eta_{1,\ell} + b \cos \theta_T$$

$$\eta_{3,c} = \eta_{3,\ell} - b \sin \theta_T$$

The moment about the aerodynamic center can be computed from the pressure coefficient $C_p(\xi_2)$ and the complex coordinate ζ by the integral

$$C_{m,c} = \int_0^{2\pi} C_p(\xi_2) \, \mathrm{Re}(\zeta+b) \frac{d\zeta}{d\xi_2} \, d\xi_2$$

where the aerodynamic center is taken at $x = -b$ and Re denotes the real part of the complex number.

REFERENCE

1. Theodorsen, T.; and Garrick, I. E.: General Potential Theory of Arbitrary Wing Sections. NACA Rep. 452, 1933.

10.4 BLADE SECTION BOUNDARY-LAYER MODULE

Donald S. Weir
PRC Kentron, Inc.

INTRODUCTION

The Blade Section Boundary-Layer Module computes the two-dimensional boundary layer on airfoil sections using integral formulations for the boundary-layer thicknesses. The methods here are taken directly from Schlichting's Boundary-Layer Theory (ref. 1). The blade surface arc length is derived from data supplied by the Blade Shape Module and the external velocity distribution is supplied by the Blade Section Aerodynamics Module for each section angle of attack and Mach number. The method of Holstein and Bohlen is used to integrate the momentum equation in the laminar regime. Transition is assumed to occur at either x_m, where the velocity is maximum, or at a trip location x_{tr} supplied by the user, whichever is the lesser. Truckenbrodt's method is used to integrate the energy equation from the transition point to the trailing edge. Error messages are given if separation occurs in the laminar regime. The profile drag is computed by the method of Squire and Young. The module outputs the displacement and momentum thicknesses, the skin friction coefficient, and the profile drag coefficient for the section.

SYMBOLS

b	Joukowski transformation parameter, re R
C	chord length, re R
C_D	turbulent energy dissipation coefficient, $-\int_0^\delta \frac{u}{U} \frac{\partial}{\partial y}\left(\frac{\tau}{\rho U^2 c_\infty^2}\right) dy$
C_f	local skin friction coefficient, $\frac{\tau}{\frac{1}{2}\rho M^2 c_\infty^2}$
C_T	local skin friction coefficient, $\frac{\tau}{\rho U^2 c_\infty^2}$
c_∞	ambient speed of sound, m/s (ft/s)
g_{22}	metric coefficient for surface arc length, re R
H	modified shape factor

H_{ij}	$= \delta_i / \delta_j$
M	Mach number of blade section
R	blade length measured from axis to tip, m (ft)
R_2	Reynolds number based on momentum thickness, $\frac{U\delta_2}{\nu}$
R_3	Reynolds number based on energy thickness, $\frac{U\delta_3}{\nu}$
R_∞	Reynolds number, $\frac{c_\infty R}{\nu}$
U	potential flow velocity, re c_∞
u	velocity inside boundary layer, re c_∞
x	arc length measured from stagnation point, re C
α	angle of attack, rad
$\alpha(H)$	skin friction function
$\beta(H)$	energy dissipation function
δ	boundary-layer thickness, re C
δ_1	displacement thickness, $\int_0^\delta (1 - \frac{u}{U})\, dy$, re C
δ_2	momentum thickness, $\int_0^\delta (1 - \frac{u}{U}) \frac{u}{U}\, dy$, re C
δ_3	energy thickness, $\int_0^\delta [1 - (\frac{u}{U})^2] \frac{u}{U}\, dy$, re C
ν	kinematic viscosity
ξ_1	spanwise surface coordinate
ξ_2	chordwise surface coordinate
ρ	density, kg/m^3 (slugs/ft^3)
τ	skin friction stress, N/m^2 (lb/ft^2)
ψ	blade thickness function, rad

Subscripts:

ℓ	lower surface
m	maximum velocity point
s	stagnation point
t	trailing edge
tr	trip location
u	upper surface
∞	ambient

INPUT

User Parameter

R_∞	Reynolds number based on blade length, speed of sound, and ambient viscosity, Rc_∞/ν

Functions of Span

ξ_1	array of spanwise surface coordinates
$b(\xi_1)$	Joukowski transformation parameter, re R
$C(\xi_1)$	airfoil section chord, re R
$\xi_{2,tr,u}(\xi_1)$	upper surface trip location, rad
$\xi_{2,tr,\ell}(\xi_1)$	lower surface trip location, rad

Functions of Span and Chord

ξ_1	array of spanwise surface coordinates
ξ_2	array of chordwise surface coordinates
$\psi(\xi_1,\xi_2)$	blade surface elliptic system radial coordinates

Functions of Position, Angle of Attack, and Mach Number

α	array of angles of attack
M	array of Mach numbers

$\xi_{2,s}(\xi_1,\alpha,M)$	stagnation point location, rad
$C_p(\xi_1,\xi_2,\alpha,M)$	coefficient of pressure

OUTPUT

ξ_1	array of spanwise surface coordinates
ξ_2	array of chordwise surface coordinates
α	array of angles of attack, deg
M	array of Mach numbers
$C_d(\xi_1,\alpha,M)$	profile drag coefficient
$\delta_{1,u,t}(\xi_1,\alpha,M)$	upper surface trailing-edge displacement thickness, re $C(\xi_1)$
$\delta_{2,u,t}(\xi_1,\alpha,M)$	upper surface trailing-edge momentum thickness, re $C(\xi_1)$
$\delta_{1,\ell,t}(\xi_1,\alpha,M)$	lower surface trailing-edge displacement thickness, re $C(\xi_1)$
$\delta_{2,\ell,t}(\xi_1,\alpha,M)$	lower surface trailing-edge momentum thickness, re $C(\xi_1)$
$C_f(\xi_1,\xi_2,\alpha,M)$	skin friction coefficient

METHOD

Boundary-Layer Equations

The integral equations (ref. 1) for boundary layers are based on several thickness functions, shape factors, and coefficients defined here for later use in analysis and computation. The basic thickness functions are the displacement thickness

$$\delta_1 = \int_0^\delta (1 - u/U)\ dy \tag{1}$$

the momentum thickness

$$\delta_2 = \int_0^\delta (1 - u/U)(u/U)\ dy \tag{2}$$

and the energy thickness

$$\delta_3 = \int_0^\delta (1 - (u/U)^2)(u/U)\ dy \tag{3}$$

Reynolds numbers based on these thicknesses are defined by

$$R_i = \frac{U\delta_i}{\nu} \qquad (i = 1, 2, 3) \tag{4}$$

Shape factors which give the ratios of these thicknesses are

$$H_{ij} = \frac{\delta_i}{\delta_j} = \frac{R_i}{R_j} \qquad (i,j = 1, 2, 3;\ \ i \neq j) \tag{5}$$

The skin friction coefficient based on local velocity at the edge of the boundary layer is

$$C_T = \frac{\tau_0}{\rho U^2 c_\infty^2} \tag{6}$$

and the skin friction coefficient based on the blade section velocity is

$$C_f = \frac{\tau_0}{\frac{1}{2}\rho M^2 c_\infty^2} \tag{7}$$

so that

$$C_f = 2\left(\frac{U}{M}\right)^2 C_T \tag{8}$$

The energy dissipation coefficient is

$$C_D = -\int_0^\delta (u/U)\ \frac{\partial}{\partial y}\left(\frac{\tau}{\rho U^2 c_\infty^2}\right) dy \tag{9}$$

The basic governing equations for momentum and energy in the boundary layer are

$$\frac{d\delta_2}{dx} + (2 + H_{12})\frac{\delta_2}{U}\ \frac{dU}{dx} = C_T \tag{10}$$

and

$$\frac{d\delta_3}{dx} + 3\ \frac{\delta_3}{U}\ \frac{dU}{dx} = 2C_D \tag{11}$$

The displacement thickness is found from these thicknesses and an assumed form of the boundary-layer profile. This profile is different in the laminar and turbulent cases and is defined later.

Arc Length.- The boundary-layer analysis is carried out on both the upper surface and lower surface of the airfoil. In this analysis, these two surfaces are defined in terms of two continuous arcs measured from the stagnation point. The arc length on the airfoil surface is

$$dx = \pm\sqrt{g_{22}}\ d\xi_2 \tag{12}$$

where the metric coefficient for arc length is

$$g_{22} = 4\left(\frac{b}{C}\right)^2 \left[1 + \left(\frac{d\psi}{d\xi_2}\right)^2\right](\sinh^2 \psi + \sin^2 2\pi\xi_2)$$

$$(\xi_1 = \text{Constant}) \tag{13}$$

The arc length begins with $x = 0$ at the stagnation point ξ_{2S}. Equation (12) is integrated on the upper surface with the negative sign in equation (12) being used because the arc length increases as ξ_2 decreases to 0 at the trailing edge. On the lower surface, the positive sign of equation (12) is used with ξ_2 increasing to 1 at the trailing edge.

Local velocity.- The local velocity is found from the coefficient of pressure C_p by

$$U(x) = M\sqrt{1 - C_p(x)} \tag{14}$$

This velocity is actually a Mach number since the speed of sound c_∞ is used for a reference. The symbol M is saved for the local section Mach number which does not depend on chord position.

Maximum velocity.- Both $U(x)$ and $U'(x)$ are used in the computation. After finding $U'(x)$, the maximum point for U is found from

$$\frac{dU(x_m)}{dx} = 0 \quad (x_m > 0) \tag{15}$$

Local Reynolds number.- With $U(x)$ given relative to c_∞ and $\delta(x)$ given relative to chord length C, the kinematic viscosity must be relative to Cc_∞. Thus the local kinematic viscosity is given in terms of the input Reynolds number parameter $R_\infty = Rc_\infty/\nu$ by

$$\nu = \frac{1}{R_\infty C} \tag{16}$$

The local Reynolds number is

$$R = MCR_\infty = \frac{M}{\nu} \tag{17}$$

Laminar Boundary Layer

The laminar boundary-layer equations are integrated by the method of Holstein and Bohlen as described in chapter X of reference 1. The integration is carried out with a shape function $K(x)$ defined by

$$K(x) = \frac{\delta_2^2}{\nu} \frac{dU}{dx} \tag{18}$$

and a function of the momentum thickness

$$Z(x) = \frac{\delta_2^2(x)}{\nu} \tag{19}$$

Four auxiliary functions of K are used in the integration. These are given in table 10.2 of reference 1 and here as table I and figure 1. The auxiliary functions are Pohlhausen's shape factor Λ

$$-12 < \Lambda(K) < 12 \tag{20}$$

the shape factor H_{12}

$$H_{12} = f_1(K) \tag{21}$$

the wall stress factor $f_2(K)$ which gives C_T by

$$R_2 C_T = f_2(K) \tag{22}$$

and a function $F(K)$ in the following differential equation for Z

$$\frac{d(ZU)}{dx} = F(K) + K \tag{23}$$

As equation (23) is integrated, K is calculated from

$$K = Z \frac{dU}{dx} \tag{24}$$

The limit $\Lambda = -12$ indicates separation and the limit $\Lambda = 12$ constrains the boundary-layer profile such that $\max [u(y)/U] < 1$.

Stagnation point.- The value of Z at the stagnation point is

$$Z(0) = \frac{K(0)}{U'(0)} \tag{25}$$

where

$$K(0) = K_0 = 0.0770 \tag{26}$$

The boundary-layer momentum thickness at the stagnation point is

$$\delta_2(0) = \sqrt{\nu Z(0)} \tag{27}$$

and the displacement thickness is

$$\delta_1(0) = f_1(K_0)\ \delta_2(0) \tag{28}$$

The skin friction coefficient at the stagnation point is

$$C_f(0) = 0 \tag{29}$$

Laminar range.- Equation (23) is integrated over the laminar range until either (1) the trailing edge is reached or (2) Λ is out of range, $|\Lambda|>12.0$. The end of this region is denoted x_L and saved for future reference. In the laminar range $0 < x < x_L$, the boundary-layer parameters are

$$\delta_2(x) = \sqrt{(\nu Z(x))} \tag{30}$$

$$\delta_1(x) = f_1(K(x))\delta_2(x) \tag{31}$$

and

$$C_f(x) = \frac{2U(x)\nu\ f_2(K(x))}{M^2 \delta_2(x)} \tag{32}$$

The skin friction coefficient is taken to be negative on the upper surface where $0 \leq \xi_2 < \xi_{2,s}$ and positive on the lower surface where $\xi_{2,s} < \xi_2 \leq 1$. This convention allows the friction stress to be in the direction of ξ_2 everywhere.

Transition

The transition from laminar to turbulent flow is influenced by a number of factors, but the strongest influence (Ch. XVII of ref. 1) is the pressure gradient in the boundary layer. When this gradient is positive, the boundary layer is unstable and transition to turbulent flow soon follows. It is assumed here that the transition point is the point of minimum pressure or the point of maximum velocity. Thus, the point of transition x_{tr} is found by solving

$$\frac{dU(x_{tr})}{dx} = 0 \qquad (x > 0) \tag{33}$$

for the transition point x_{tr}. Since equation (33) is identical to equation (15), we use $x_{tr} = x_m$.

Turbulent Boundary Layer

Modified shape factor.- An additional shape factor introduced by Truckenbrodt (Ch. XXII of ref. 1) is used in the calculations for turbulent boundary layers. Truckenbrodt's modified shape factor is defined by

$$H = \exp\left[\int_{H_{32,\infty}}^{H_{32}} \frac{dH_{32}}{(H_{21} - 1)H_{32}}\right] \tag{34}$$

The velocity profile assumed for the turbulent boundary layer is such that

$$H_{12} \equiv \frac{H_{32}}{(3H_{32} - 4)} \tag{35}$$

so that equation (34) can be integrated. The value of H_{32} for a flat plate is denoted $H_{32,\infty}$ and is the lower limit of the integral in equation (34).

Truckenbrodt's modified shape factor is then

$$H = G_\infty H_{23} \sqrt{\frac{H_{23}}{H_{23} - G_1}} \tag{36}$$

where

$$G_1 = 0.5049 \qquad G_\infty = 0.5442 \tag{37}$$

are empirically determined constants. Equation (36) may be inverted by solving a cubic equation in H_{23}. The solution is given in two steps

$$\phi = \frac{1}{3} \text{Arctan} \sqrt{\frac{1}{3} \left(\frac{4H}{3G_\infty} \right)^2 - 1} \tag{38}$$

and

$$H_{23} = \sqrt{\frac{4}{3}} \; \frac{H}{G_\infty} \cos \phi \tag{39}$$

Energy method.- Truckenbrodt's energy method is based on integrating differential equations for the energy Reynolds number R_3 and the modified shape factor H. The differential equations are a transformation of equations (10) and (11).

$$\frac{dR_3}{dx} = -2\left(\frac{1}{U}\frac{dU}{dx}\right)R_3 + U\,\Phi_3(R_3,H) \tag{40}$$

$$\frac{dH}{dx} = \left(\frac{1}{U}\frac{dU}{dx}\right)H + \frac{U}{R_3}\,\Psi_3(R_3,H) \tag{41}$$

The functions $\Phi(R_3,H)$ and $\Psi(R_3,H)$ are empirical functions which are described later.

Initial conditions.- The initial conditions for these differential equations are found from $H_{12} = f_1(K) - \Delta H_{12}$ at the end of the laminar range where $x = x_m = x_{tr}$. The correction ΔH_{12} is an empirical function relating the laminar and turbulent shape factors and is given in table II and figure 2. From equation (35),

$$H_{32}(x_{tr}) = \frac{4H_{12}}{3H_{12} - 1} \tag{42}$$

and, from equation (36),

$$H(x_{tr}) = \frac{G_\infty}{H_{32}} \sqrt{\frac{1}{1 - G_1 H_{32}}} \tag{43}$$

The boundary-layer thickness is

$$\delta_3(x_{tr}) = H_{32}(x_{tr})\ \delta_2(x_{tr}) \tag{44}$$

and the Reynolds number is

$$R_3(x_{tr}) = \frac{\delta_3(x_{tr})\ U(x_{tr})}{\nu} \tag{45}$$

Equation (45) gives the initial condition for $R_3(x)$ and equation (43) gives the initial condition for $H(x)$.

Empirical functions.- The empirical functions give the effects of the skin friction and energy dissipation coefficients in equations (10) and (11). These functions are defined in reference 1 as

$$\Phi_3 = \frac{2C_D}{\nu} \tag{46}$$

and

$$\Psi_3 = \frac{H}{\nu}\ \frac{2C_D - H_{32}C_T}{H_{12} - 1} \tag{47}$$

The shape factor H_{32} is found from equation (39) and H_{12} is found from equation (35). The coefficients C_T and C_D are defined as

$$C_T = \frac{\alpha(H)}{R_2^a} \tag{48}$$

and

$$C_D = \frac{\beta(H)}{R_3} \tag{49}$$

with a, α, b, and β given as

$$a = 0.268 \tag{50}$$

$$\alpha = 0.245(1 - 2.007 \log H_{12})^{1.705} \tag{51}$$

$$b = 0.2317H_{32} - 0.2644 - (0.896 \times 10^5)\ (2 - H_{32})^{20} \tag{52}$$

$$\beta = [0.00481 + 0.0822(H_{32} - 1.5)^{4.81}]H_{32}{}^b \tag{53}$$

Turbulent separation.- The point of separation for the turbulent boundary layer is a function of the modified shape factor H. This factor is near unity at the transition point and generally decreases with distance along the airfoil. The condition for attachment of the boundary layer is thus

$$H > H_s = 0.723 \tag{54}$$

The boundary layer is prone to separation at slightly larger values of H_s, referred to as H_s' where

$$H_s' = 0.761 \tag{55}$$

The separation point should be set by the user with a parameter $0.723 < H_s < 0.761$.

Profile Drag

The profile drag or total drag of an airfoil is the sum of the skin friction drag and the pressure drag or form drag (ch. XXV of ref. 1). The method of Squire and Young presented in reference 1 is based on the wake momentum thickness at the trailing edge:

$$\delta_{21} = \delta_{2,u}(x_{u,t}) + \delta_{2,\ell}(x_{\ell,t}) \tag{56}$$

The profile drag coefficient is given by the wake momentum thickness far from the trailing edge as

$$C_d = \frac{2\delta_{2,\infty}}{C} \tag{57}$$

The method of Squire and Young relates the far wake momentum thickness to the trailing edge thickness by the empirical formula

$$\delta_{2,\infty} = \delta_2 \left(\frac{U_1}{U_\infty}\right)^{3.2} \tag{58}$$

where U_1 is the potential velocity at the trailing edge. Since there may be small numerical differences between $U(x_t)$ on the upper and lower surfaces, U_1 is defined here as the average:

$$U_1 = \frac{U_u(x_{u,t}) + U_\ell(x_{\ell,t})}{2} \tag{59}$$

Computation Method

1. For each section, angle of attack, and Mach number,

   Compute the local viscosity ν

   Compute $U(\xi_2)$ from equation (14)

   Compute $\frac{dU}{d\xi_2}$ at the stagnation point $\xi_{2,s}$

2. Compute the arc lengths on the upper and lower surfaces

3. Locate the point of maximum velocity x_m on the upper and lower surfaces. Repeat steps 4 to 7 for each section

4. Find the initial conditions at the stagnation point $x = 0$ for the laminar functions K and Z

5. Integrate the laminar equation to the transition point $x_{tr} = x_m$ or a point $x_{tr} < x_m$ specified by the user, stop the integration and issue an error if laminar separation occurs

6. Find the initial conditions for the turbulent equations at x_{tr}

7. Integrate the turbulent equations to the trailing edge or until separation occurs as indicated by the limiting shape factor H_s

8. Compute the profile drag coefficient.

REFERENCE

1. Schlichting, Hermann (J. Kestin, transl.): Boundary-Layer Theory, Seventh ed. McGraw-Hill Book Co., c.1979.

TABLE I.- AUXILIARY FUNCTIONS FOR LAMINAR BOUNDARY-LAYER COMPUTATION

K	$\Lambda(K)$	$F(K)$	$f_1(K)$	$f_2(K)$
-0.1567	-12	1.7241	3.500	0
-0.1474	-11	1.6257	3.383	0.019
-0.1369	-10	1.5229	3.276	0.039
-0.1254	-9	1.4167	3.176	0.059
-0.1130	-8	1.3080	3.085	0.079
-0.0999	-7	1.1981	2.999	0.100
-0.0862	-6	1.0877	2.921	0.120
-0.0720	-5	0.9780	2.847	0.140
-0.0575	-4	0.8698	2.779	0.160
-0.0429	-3	0.7640	2.716	0.179
-0.0284	-2	0.6609	2.647	0.199
-0.0140	-1	0.5633	2.604	0.217
0	0	0.4698	2.554	0.235
0.0135	1	0.3820	2.508	0.252
0.0264	2	0.3004	2.466	0.268
0.0385	3	0.2255	2.427	0.283
0.0497	4	0.1579	2.392	0.297
0.0599	5	0.0979	2.361	0.310
0.0689	6	0.0459	2.333	0.321
0.0706	6.2	0.0363	2.328	0.324
0.0721	6.4	0.0274	2.323	0.326
0.0737	6.6	0.0186	2.318	0.328
0.0752	6.8	0.0102	2.314	0.330
0.0767	7	0.0021	2.309	0.331
0.0770	7.052	0	2.308	0.332
0.0781	7.2	-0.0051	2.305	0.333
0.0794	7.4	-0.0132	2.301	0.335
0.0807	7.6	-0.0203	2.297	0.337
0.0819	7.8	-0.0271	2.293	0.338
0.0831	8	-0.0335	2.289	0.340
0.0882	9	-0.0608	2.273	0.347
0.0919	10	-0.0800	2.260	0.351
0.0941	11	-0.0912	2.253	0.355
0.0948	12	-0.0948	2.250	0.356

TABLE II.- VARIATION OF SHAPE FACTOR H_{12} AT TRANSITION

$R_{2,tr}$	ΔH_{12}
1×10^{3}	1.16
2×10^{3}	1.22
5×10^{3}	1.27
1×10^{4}	1.31
2×10^{4}	1.34
5×10^{4}	1.35
1×10^{5}	1.36

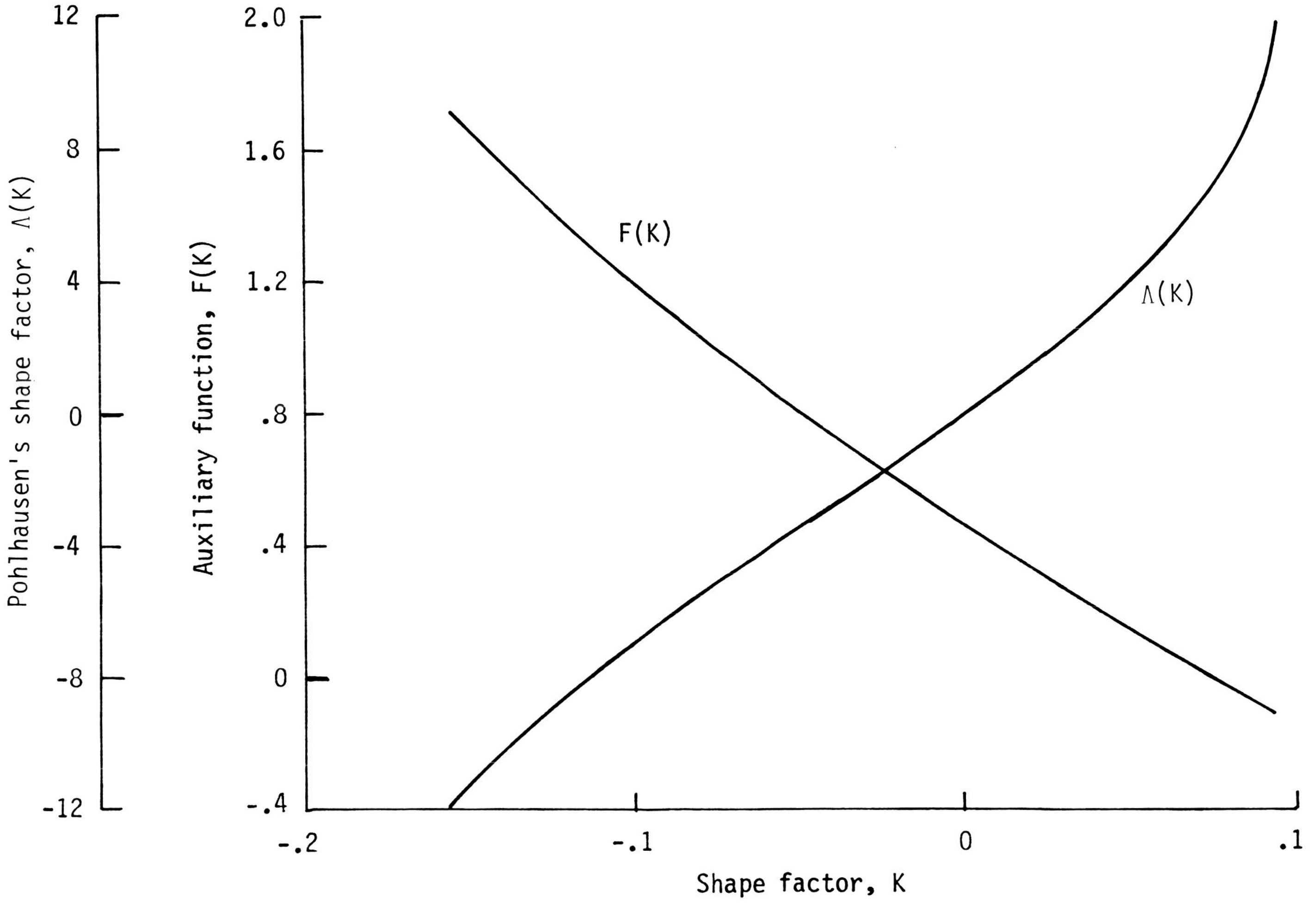

Figure 1.- Auxiliary functions for laminar boundary-layer computation.

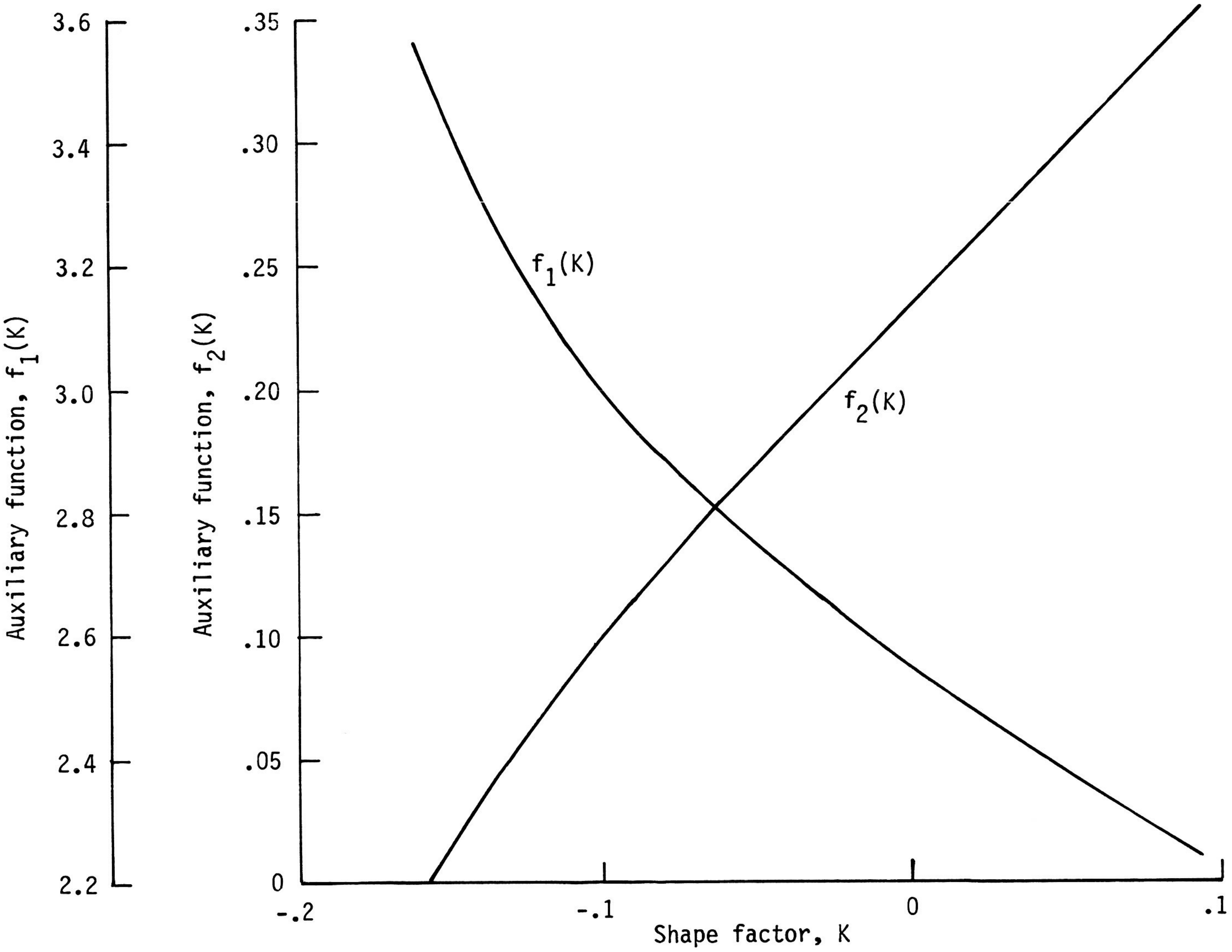

Figure 1.- Concluded.

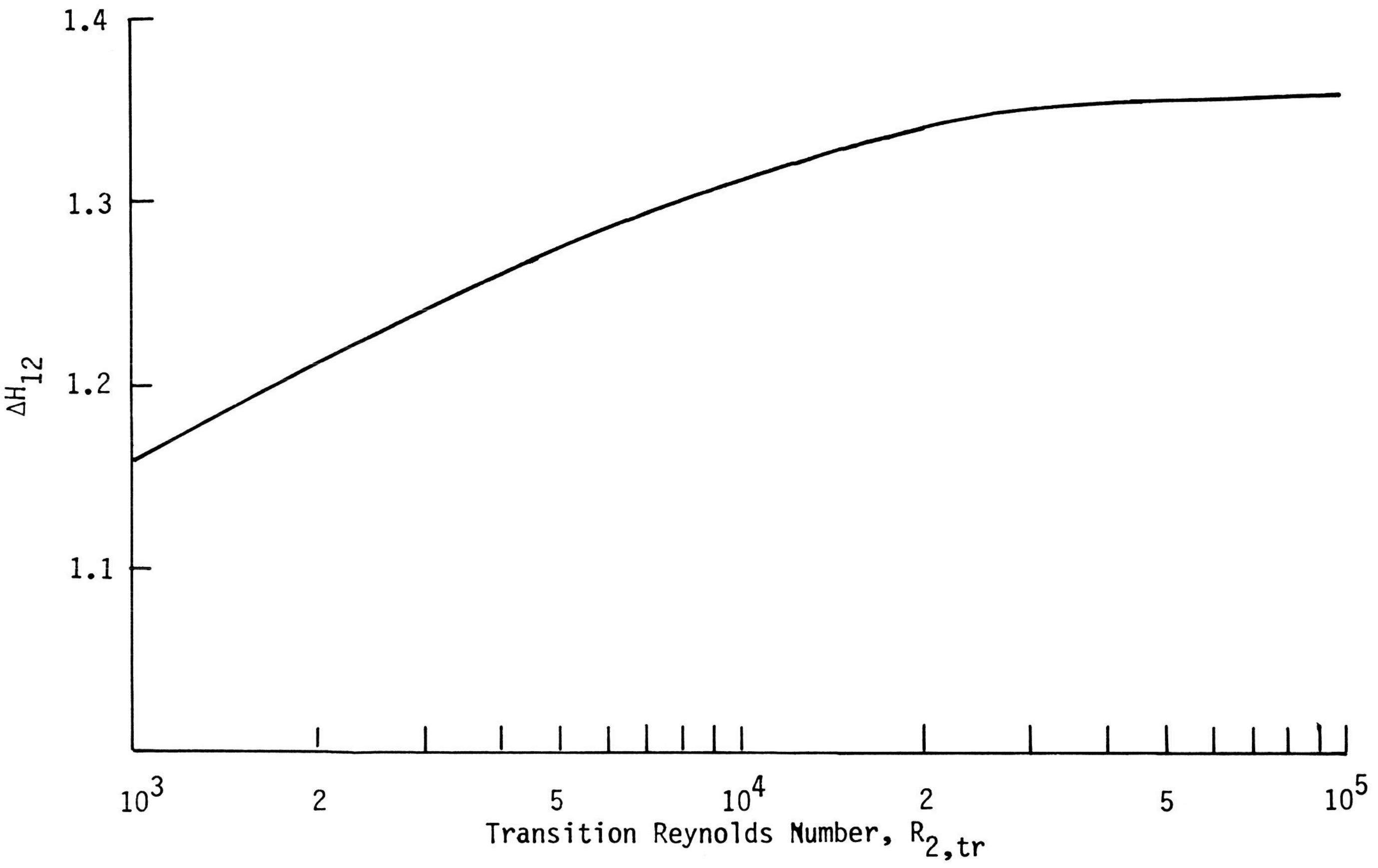

Figure 2.- Variation of shape factor H_{12} at transition.

10.5 PROPELLER PERFORMANCE MODULE

Ollie J. Rose
PRC Kentron, Inc.

INTRODUCTION

A knowledge of the effective velocity field in which a propeller operates is essential in order to predict the blade loading and noise. A prediction of thrust and efficiency is needed for flight path calculations and for comparison with experiments. The unknown quantity required for these purposes is the induced velocity field. Thus, the purpose of the Propeller Performance Module is to compute the induced velocity field and then the thrust coefficient, power coefficient, and efficiency for a given propeller under specified operating conditions. The induced flow calculation is performed with the propeller axis operating at zero angle of attack. Then, the kinematic effect of propeller angle of attack is included by a rotational transformation of the total velocity field.

SYMBOLS

a_1	induced axial velocity component, re $\lambda R\Omega$
a_2	induced tangential velocity component, re $rR\Omega$
C	blade section chord, re R
C_d	section drag coefficient
C_ℓ	section lift coefficient
C_P	power coefficient
C_Q	torque coefficient, $C_Q = C_P$
C_q	section torque coefficient
C_T	thrust coefficient
C_t	section thrust coefficient
c_∞	speed of sound, m/s (ft/s)
F	tip relief factor
M	Mach number

M_t	blade tip Mach number, $\frac{R\Omega}{c_\infty}$
M_Z	inflow Mach number normal to disk plane
N	number of propeller blades
P	power, re $\rho_\infty R^5\Omega^3$
Q	torque, re $\rho_\infty R^5\Omega^2$
R	radius of propeller disk, m (ft)
r	radial position on blade, re R
T	thrust, re $\rho_\infty R^4\Omega^2$
V	effective velocity relative to blade section, re $R\Omega$
V_z	resultant velocity of fluid in thrust direction
V_ψ	resultant velocity of fluid in disk plane in direction of rotation
x,y,z	right-hand reference coordinate system, z in thrust direction
α	blade section angle of attack, rad
α_p	propeller angle of attack, rad
ε	relative error
η	propeller efficiency
θ	blade twist angle, rad
θ_o	root pitch setting, rad
λ	local advance ratio
$\overline{\lambda}$	average advance ratio
ρ_∞	ambient density, kg/m^3 (slug/ft^3)
σ	blade element solidity, $\frac{NC(r)}{2\pi r}$
ϕ	inflow angle, rad
ψ	blade rotation angle, rad
Ω	angular velocity of blade, rad/s

Subscripts:

$_{,M}$	partial derivative with respect to M
$_{,\alpha}$	partial derivative with respect to α

INPUT

The quantities required by this module are grouped into four basic classes: blade geometry, flow field, operating parameters, and aerodynamic characteristics. A uniform or radially varying flow field can be specified.

Blade Geometry

N_r	number of spanwise stations
r	array of spanwise stations, re R
$C(r)$	blade chord array, re R
$\theta(r)$	section twist angle, rad

Flow Field

N_r	number of spanwise stations
r	array of spanwise stations, re R
$M_Z(r)$	inflow Mach number perpendicular to propeller rotation disk

Operating Parameters

N	number of blades
M_t	blade tip Mach number, $\frac{R\Omega}{c_\infty}$
θ_o	root pitch setting, rad
$(\frac{\sigma}{F})_{tip}$	ratio of solidity to tip loss factor at the blade tip

α_p	propeller angle of attack, rad
ε	error parameter

Aerodynamic Characteristics

N_r	number of spanwise stations
r	array of spanwise stations
N_α	number of angle-of-attack values in aerodynamic table
α	array of angle-of-attack values, deg
N_M	number of Mach number values in aerodynamic table
M	array of Mach numbers
$C_d(r,\alpha,M)$	section drag coefficient
$C_\ell(r,\alpha,M)$	section lift coefficient

OUTPUT

C_P	power coefficient
C_T	thrust coefficient
$\overline{\lambda}$	advance ratio
η	propeller efficiency
$\alpha(r,\psi)$	local angle-of-attack, rad
$M(r,\psi)$	local Mach number
$V_z(r,\psi)$	resultant velocity of fluid in the thrust direction, re $R\Omega$
$V_\psi(r,\psi)$	resultant velocity of fluid in disk plane in direction of rotation, re $R\Omega$
$a_1(r,\psi)\lambda(r)$	induced axial velocity, re $R\Omega$
$a_2(r,\psi)$	induced angular velocity, re Ω
$\phi(r,\psi)$	inflow angle, rad

METHOD

Induced Flow

Components of the incoming flow field are provided relative to the propeller disk. Radial velocity components and other three-dimensional effects are neglected; thus the use of blade element-momentum theory together with two-dimensional aerodynamic characteristics is allowed. In addition, the principle of momentum conservation is applied to annular control volumes and any interference effects between adjacent annuli are neglected. A further simplification is achieved by ignoring interference effects between successive blades; thus, the theory is restricted to axially symmetric inflows and induced velocities. The effects of propeller angle of attack are incorporated by a simple rotation of the resulting flow field.

An examination of figures 1 and 2 reveals that the relative section velocity at radial station r is given by

$$V(r) = \{[\lambda(1 + a_1)]^2 + [r(1 - a_2)]^2\}^{1/2} \tag{1}$$

where

$$\lambda(r) = M_Z(r)/M_t$$

The local inflow angle and angle of attack are given by

$$\tan\phi = \frac{\lambda(1 + a_1)}{r(1 - a_2)} \tag{2}$$

and

$$\alpha(r) = \theta_0 + \theta(r) - \phi(r) \tag{3}$$

The quantities θ_0, $\theta(r)$, and $\lambda(r)$, are presumed known, whereas a_1 and a_2 are to be calculated.

Equations for a_1 and a_2

Consider an annular control volume at station r and of width dr as indicated in figure 3. The element of thrust on this annulus is given by

$$dT = \frac{1}{2}V^2N\,C(r)[C_\ell \cos\phi - C_d \sin\phi]\,dr \tag{4}$$

Similarly, the element of torque on the same annular region is

$$dQ = \frac{1}{2}V^2N\,C(r)[C_\ell \sin\phi + C_d \cos\phi]r\,dr \tag{5}$$

On the other hand, linear and angular momentum increase through the annulus give the following expressions for the element thrust and torque:

$$dT = 4\pi r\lambda^2 a_1(1 + a_1)F\ dr \tag{6}$$

$$dQ = 4\pi r^3\lambda a_2(1 + a_1)F\ dr \tag{7}$$

Equating the two expressions for thrust and torque gives

$$4\pi r\lambda^2 a_1(1 + a_1)F = \frac{1}{2}\ V^2 N\ C(r)\ [C_\ell \cos\phi - C_d \sin\phi] \tag{8}$$

$$4\pi r^2\lambda a_2(1 + a_1)F = \frac{1}{2}\ V^2 N\ C(r)\ [C_\ell \sin\phi + C_d \cos\phi] \tag{9}$$

Division of equation (9) by equation (8) gives

$$\frac{ra_2}{\lambda a_1} = \frac{C_\ell \sin\phi + C_d \cos\phi}{C_\ell \cos\phi - C_d \sin\phi} \tag{10}$$

Using the notation

$$C_q = C_\ell \sin\phi + C_d \cos\phi \tag{11}$$

and

$$C_t = C_\ell \cos\phi - C_d \sin\phi \tag{12}$$

allows equation (10) to be written as

$$a_2 = \frac{C_q}{C_t}\frac{\lambda}{r}\ a_1 \tag{13}$$

Similarly, equation (8) becomes

$$4\lambda^2 a_1(1 + a_1)F = V^2\sigma C_t \tag{14}$$

The solidity $\sigma(r)$ is defined as

$$\sigma(r) = \frac{N\ C(r)}{2\pi r} \tag{15}$$

The tip relief factor F is taken to be unity for the blade element-momentum theory. A second option exists to account for three-dimensional effects. The Prandtl theory (refs. 1 and 2) gives an approximation for the radial flow effects based on the potential flow around the edge of a set of semi-infinite vortex sheets. The resulting value of the tip relief factor is

$$F = \frac{2}{\pi} \text{ Arccos} \left\{ \exp \left[\frac{-N(1 - r)(1 + \lambda^2)^{1/2}}{2\lambda} \right] \right\} \tag{16}$$

Note that F approaches zero with infinite slope as r approaches unity. For a nontrivial solution to equation (14), the ratio of σ/F must remain finite at the tip. If the chord $C(r)$ approaches zero with finite slope at the tip, then by L'Hôpital's rule, the ratio σ/F approaches zero at the tip. The user may specify a nonzero limit for the ratio $(\sigma/F)_{tip}$.

Solution Procedure

Solutions to equations (13) and (14) correspond to zeros of the following functions

$$H_1(a_1,a_2) \equiv C_q \lambda a_1 - rC_t a_2 \tag{17}$$

and

$$H_2(a_1,a_2) \equiv 4\lambda^2 a_1(1 + a_1)F - V^2\sigma\, C_t \tag{18}$$

This system of equations is solved iteratively using a general form of Newton's method. The procedure is written in vector form as

$$\begin{bmatrix} a_1^{(n+1)} \\ a_2^{(n+1)} \end{bmatrix} = \begin{bmatrix} a_1^{(n)} \\ a_2^{(n)} \end{bmatrix} - \begin{bmatrix} J_{11}^{(n)} & J_{12}^{(n)} \\ J_{21}^{(n)} & J_{22}^{(n)} \end{bmatrix}^{-1} \begin{bmatrix} H_1^{(n)} \\ H_2^{(n)} \end{bmatrix} \tag{19}$$

The elements J_{ij}, $i,j = 1, 2$, of the Jacobian matrix are determined from equations (17) and (18) as

$$\begin{aligned} J_{11}(a_1,a_2) = \frac{\partial H_1}{\partial a_1} &= C_q\lambda - \frac{\lambda^2 a_1}{V}[\cos\phi\,(\sin\phi\, C_{\ell,\alpha} + \cos\phi\, C_{d,\alpha} - C_t) \\ &\quad - M \sin\phi\,(\sin\phi\, C_{\ell,M} + \cos\phi\, C_{d,M})] \\ &\quad + \frac{r\lambda a_2}{V}\,[\cos\phi\,(\cos\phi\, C_{\ell,\alpha} - \sin\phi\, C_{d,\alpha} + C_q) \\ &\quad - M \sin\phi\,(\cos\phi\, C_{\ell,M} - \sin\phi\, C_{d,M})] \end{aligned} \tag{20}$$

$$J_{12}(a_1,a_2) = \frac{\partial H_1}{\partial a_2} = r\{-C_t - \frac{\lambda a_1}{V}[\sin\phi\,(\sin\phi\, C_{\ell,\alpha} + \cos\phi\, C_{d,\alpha} - C_t)$$

$$+ M\cos\phi\,(\sin\phi\, C_{\ell,M} + \cos\phi\, C_{d,M})]$$

$$+ \frac{ra_2}{V}\ [\sin\phi\,(\cos\phi\, C_{\ell,\alpha} - \sin\phi\, C_{d,\alpha} + C_q)$$

$$+ M\cos\phi\,(\cos\phi\, C_{\ell,M} - \sin\phi\, C_{d,M})]\} \qquad (21)$$

$$J_{21}(a_1,\ a_2) = \frac{\partial H_2}{\partial a_1} = 4\lambda^2 F(1 + 2a_1) - 2V\sigma\lambda\, C_t \sin\phi$$

$$+ V\sigma\lambda[\cos\phi\,(\cos\phi\, C_{\ell,\alpha} - \sin\phi\, C_{d,\alpha} + C_q)$$

$$- M\sin\phi\,(\cos\phi\, C_{\ell,M} - \sin\phi\, C_{d,M})] \qquad (22)$$

$$J_{22}(a_1,\ a_2) = \frac{\partial H_2}{\partial a_2} = V\sigma r[\sin\phi\,(\cos\phi\, C_{\ell,\alpha} - \sin\phi\, C_{d,\alpha} + C_q)$$

$$+ M\cos\phi\,(\cos\phi\, C_{\ell,M} - \sin\phi\, C_{d,M} + 2C_t \cos\phi)] \qquad (23)$$

With the initial values $a_1^{(0)} = a_2^{(0)} = 0$, the iteration defined by equation (18) is performed until the following error criterion is met:

$$\left|(a_1^{(n+1)},a_2^{(n+1)}) - (a_1^{(n)},a_2^{(n)})\right| < \varepsilon \left|(a_1^{(n)},a_2^{(n)})\right| \qquad (24)$$

Once the induced velocity a_1 and a_2 are obtained, the remaining output quantities are computed by direct analytical means as indicated in the the following formulas:

$$\overline{\lambda} = \pi \int_0^1 \lambda(r)\, dr \qquad (25)$$

$$V(r) = \{[\lambda(1 + a_1)]^2 + [r\,(1 - a_2)]^2\}^{1/2} \qquad (26)$$

$$M(r) = M_t\, V(r) \qquad (27)$$

$$\phi(r) = \text{Arctan}\ \frac{\lambda\,(1 + a_1)}{r\,(1 - a_2)} \qquad (28)$$

$$T = \frac{1}{2} N \left| \int_0^1 V^2\, C(r)\, (C_\ell \cos\phi - C_d \sin\phi)\, dr \right| \qquad (29)$$

$$P = \frac{1}{2} N \left[\int_0^1 rCV^2(C_\ell \sin \phi + C_d \cos \phi)\, dr \right] \quad (30)$$

$$C_T = \pi^2 T/4 \quad (31)$$

$$C_P = \pi^3 P/4 \quad (32)$$

$$\eta = \overline{\lambda} T/P \quad (33)$$

$$V_\psi(r) = -[r(1 - a_2)] \quad (34)$$

$$V_z(r) = -[\lambda(1 + a_1)] \quad (35)$$

Propeller Angle of Attack

To simulate the effects of a propeller angle of attack α_p, the resulting flow field is rotated. This introduces an angular dependence of the inplane angle ψ on the output quantities. Therefore, the thrust and inplane components of velocity become

$$V_\psi(r,\psi) = -[(r + \lambda \sin \alpha_p \cos \psi)(1 - a_2)] \quad (36)$$

$$V_z(r,\psi) = -[\lambda \cos \alpha_p (1 + a_1)] \quad (37)$$

Then, by using $V_\psi(r,\psi)$ and $V_z(r,\psi)$, the remaining angular dependent output is expressed as

$$\phi(r,\psi) = \text{Arctan} \frac{V_{z(r,\psi)}}{V_{\psi(r,\psi)}} \quad (38)$$

$$\alpha(r,\psi) = \theta_o + \theta_T - \phi(r,\psi) \quad (39)$$

and

$$M(r,\psi) = (V_z{}^2 + V_\psi{}^2)^{1/2} \quad (40)$$

REFERENCES

1. Glauert, H.: Airplane Propellers. Aerodynamic Theory, div. L, Volume IV, W. F. Durand, ed., Dover Publ., Inc., 1963, pp. 169-360.

2. Goldstein, Sydney: On the Vortex Theory of Screw Propellers. Proc. R. Soc. London, ser. A, vol. CXXIII, Apr. 1929, pp. 440-465.

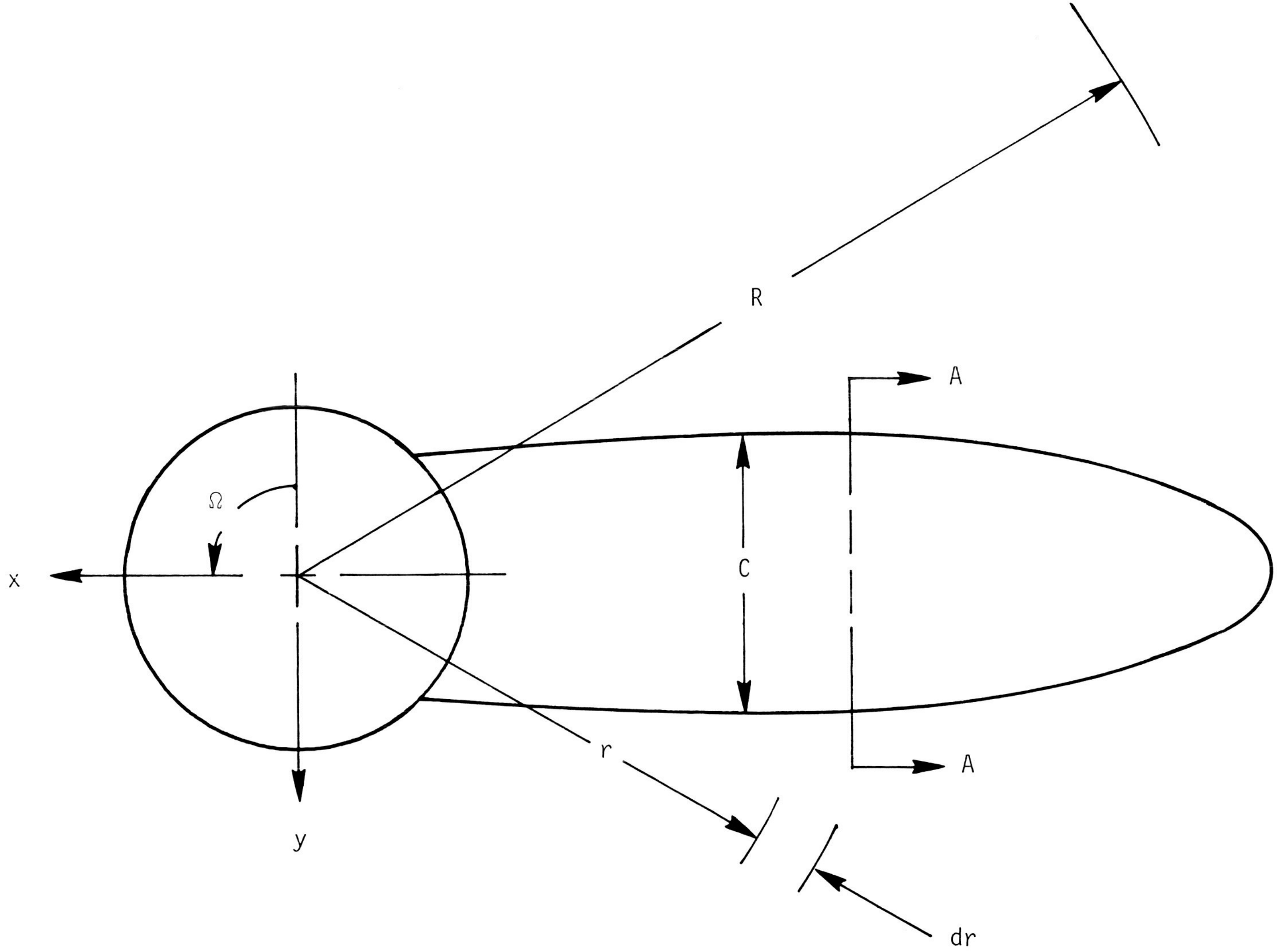

Figure 1.- Blade element nomenclature.

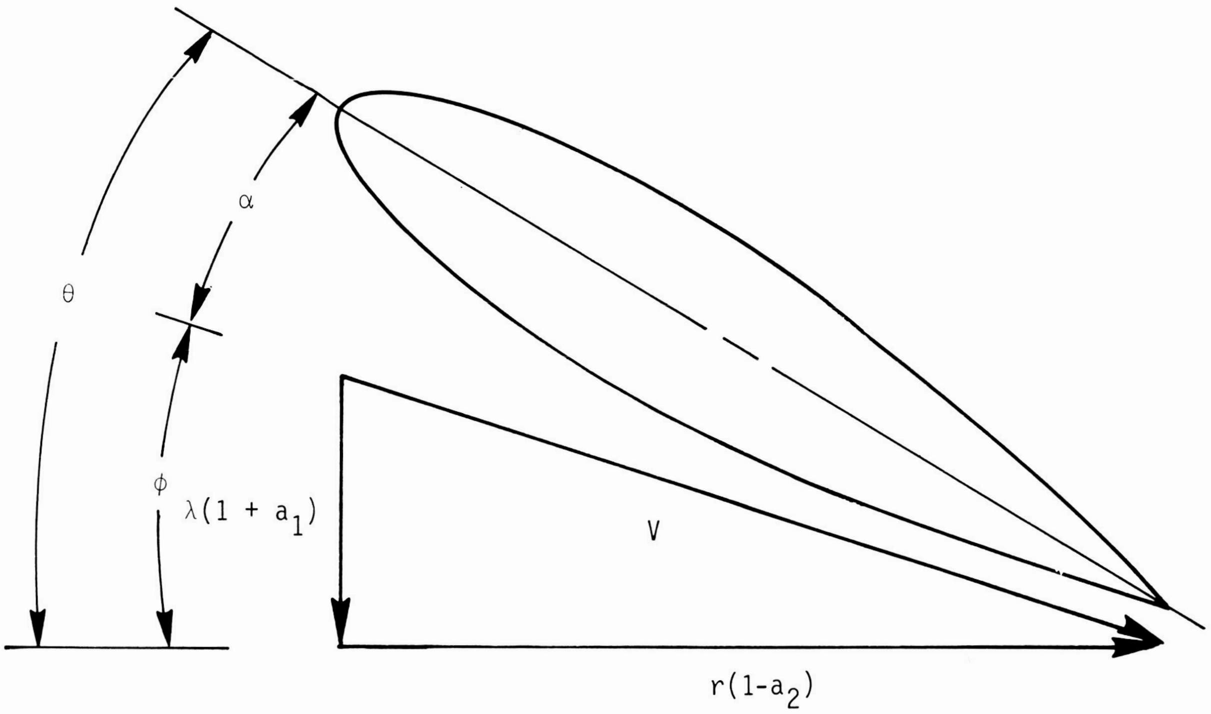

Section A-A from figure 1

Figure 2.- Blade section aerodynamics.

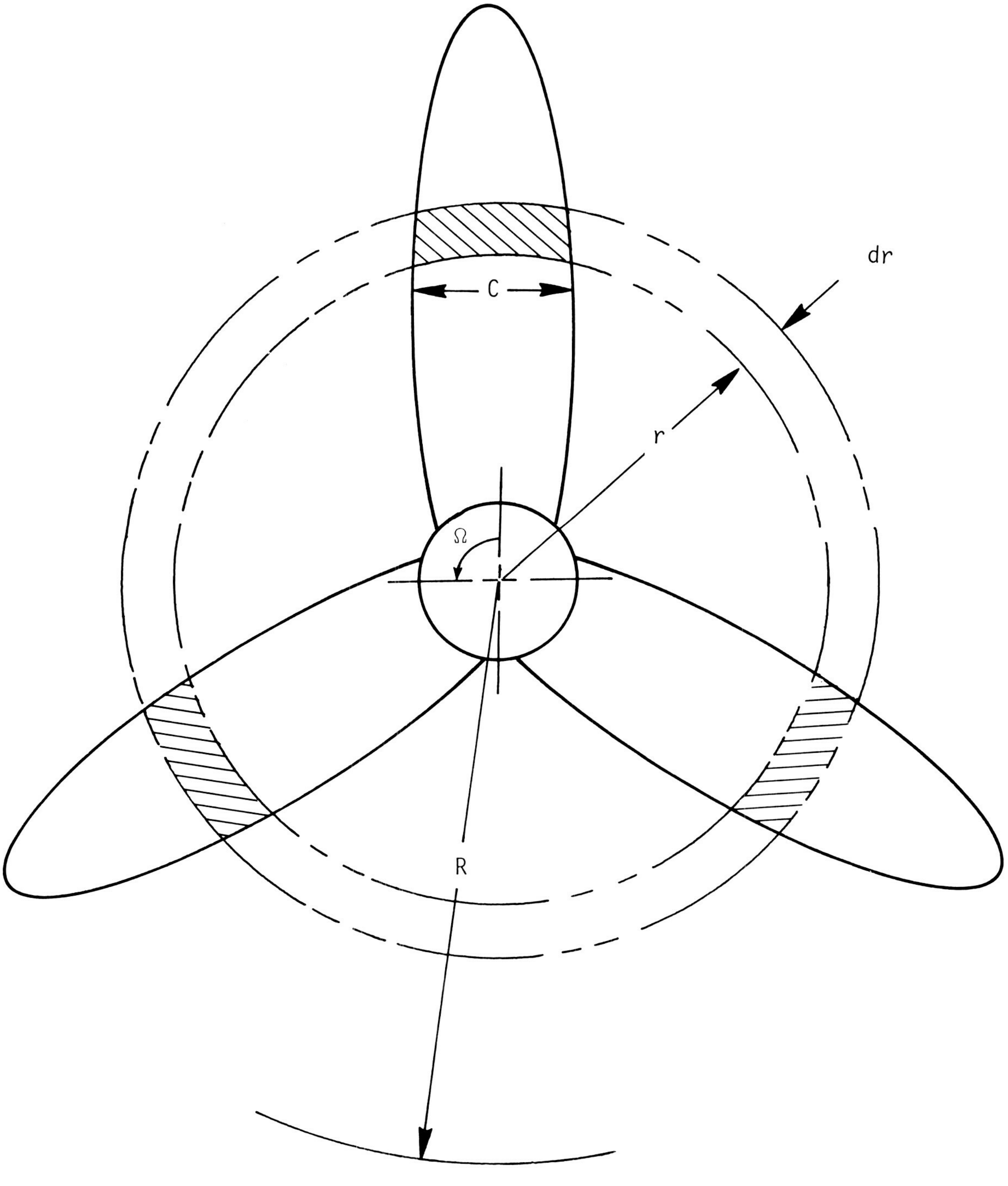

Figure 3.- Combined blade element and momentum theory.

10.6 PROPELLER LOADING MODULE

Ollie J. Rose
PRC Kentron, Inc.

INTRODUCTION

Noise prediction for rotating blades requires a knowledge of the forces exerted by the fluid on the blades. These quantities are needed at specified points on the blade and for time intervals identified by basic periodicity assumptions so that a value at any space/time point is available by interpolation. Thus the purpose of the Propeller Loading Module is to produce an array of loadings at specified blade surface points and for specified times.

SYMBOLS

a	innermost radial station, re R
b	outermost radial station, re R
C	blade chord, re R
C_d	section drag coefficient
C_f	local friction coefficient on blade surface
C_ℓ	section lift coefficient
C_p	local pressure coefficient
c_∞	speed of sound, m/s (ft/s)
F_d	section drag force, re $\rho R^3 \Omega^2$
F_ℓ	section lift force, re $\rho R^3 \Omega^2$
F_Q	net torque force acting on blade, re $\rho R^4 \Omega^2$, Q/r_Q
F_q	section torque force, re $\rho R^3 \Omega^2$
F_T	net thrust force acting on blade, re $\rho R^4 \Omega^2$, T

F_t	section thrust force, re $\rho R^3\Omega^2$
M	Mach number
p	pressure, re $\rho R^2\Omega^2$
Q	torque, re $\rho R^5\Omega^2$
R	propeller disk radius
r	distance of blade element from rotor axis, re R
T	thrust, re $\rho R^4\Omega^2$
V	velocity, re $R\Omega$
V_z	induced axial velocity component, re $R\Omega$
V_ψ	induced tangential velocity component, re $R\Omega$
x,y,z	nonrotating coordinate system moving with propeller hub
α	blade section angle of attack, rad
ξ_1,ξ_2	blade surface coordinates
ρ	fluid mass density, kg/m^3 (slug/ft^3)
τ	skin friction tangential stress, re $\rho R^2\Omega^2$
ϕ	inflow angle, rad
ψ	azimuth angle of blade, rad
Ω	angular speed of rotor, rad/s

Subscripts:

t	value at blade tip

INPUT

The quantities required by this module can be conveniently grouped into three basic classes: blade geometry, flow and operating parameters, and aerodynamic characteristics. Blade geometry is furnished in the form of tables by the Blade Shape Module, the flow field by the Propeller Performance Module, and aerodynamic characteristics by the Blade Section Aerodynamics and Blade Section Boundary-Layer Modules. Operating parameters are provided by the user.

Blade Geometry

N_{ξ_1}	number of spanwise stations
ξ_1	array of spanwise stations, re R
N_{ξ_2}	number of chordwise stations
ξ_2	array of chordwise stations, re 2π
$C(\xi_1)$	blade chord, re R

Flow and Operating Parameters

M_t	tip rotational Mach number, $\frac{R\Omega}{c_\infty}$
N_b	number of blades
N_ψ	number of rotation angles
ψ	array of rotation angles
$M(\xi_1,\psi)$	local effective Mach number of blade element
$\alpha(\xi_1,\psi)$	local angle of attack, rad
$\phi(\xi_1,\psi)$	local inflow angle, rad

Aerodynamic Characteristics

$C_d(\xi_1,\alpha,M)$	section drag coefficient
$C_f(\xi_1,\xi_2,\alpha,M)$	local skin friction coefficient
$C_\ell(\xi_1,\alpha,M)$	section lift coefficient
$C_p(\xi_1,\xi_2,\alpha,M)$	local pressure coefficient

OUTPUT

The output of this module is a table of pressure and friction loading together with lifting-line forces.

N_{ξ_1}	number of spanwise stations
ξ_1	array of spanwise stations, re R
N_{ξ_2}	number of chordwise stations
ξ_2	array of chordwise stations, re 2π
$p(\xi_1,\xi_2,\psi)$	pressure loading, re $\rho R^2\Omega^2$
$\tau(\xi_1,\xi_2,\psi)$	skin friction loading, re $\rho R^2\Omega^2$
N_ψ	number of rotation angles
ψ	array of rotation angles, rad
$F_t(\xi_1,\psi)$	section thrust force, re $\rho R^3\Omega^2$
$F_q(\xi_1,\psi)$	section torque force, re $\rho R^3\Omega^2$
$F_T(\psi)$	net thrust force, re $\rho R^4\Omega^2$
$F_Q(\psi)$	net torque force, re $\rho R^4\Omega^2$
$r_T(\psi)$	effective blade radius where net thrust force acts, re R
$r_Q(\psi)$	effective blade radius where net torque force acts, re R

METHOD

The Propeller Loading Module computes aerodynamic loads on a rigid propeller blade, which arise as the blade operates in a given flow environment. Local Mach number and angle of attack are provided in terms of an aircraft fixed cylindrical coordinate system as shown in figure 1. Radial Mach number and other three-dimensional effects are assumed to have a negligible effect on the loading, and this allows the algorithm to be based on blade element theory together with two-dimensional aerodynamic characteristics.

With figures 1 to 3 as guides, equations for the resultant blade loads are immediately written. Consider a typical blade section of width dr and chord C(r) located a distance r from the rotation axis. The local velocity seen by this element is given by

$$V(r,\psi) = M(r,\psi)/M_t \tag{1}$$

From figure 3, it is evident that the thrust and torque components of the section loading can be written as

$$F_t = F_\ell \cos\phi - F_d \sin\phi \tag{2}$$

$$F_q = F_\ell \sin\phi + F_d \cos\phi \tag{3}$$

The section lift and drag are written in terms of coefficients as

$$F_\ell = \frac{1}{2} V^2 C_\ell \, C(r) \tag{4}$$

$$F_d = \frac{1}{2} V^2 C_d \, C(r) \tag{5}$$

The section thrust and torque forces thus are written as

$$\begin{aligned} F_t(\xi_1,\psi) = \tfrac{1}{2}V^2 \, C(\xi_1) \, \{C_\ell[\xi_1,\alpha(\xi_1,\psi),M(\xi_1,\psi)] \cos\phi \\ - C_d[\xi_1,\alpha(\xi_1,\psi),M(\xi_1,\psi)] \sin\phi\} \end{aligned} \tag{6}$$

$$\begin{aligned} F_q(\xi_1,\psi) = \tfrac{1}{2}V^2 \, C(\xi_1) \, \{C_\ell[\xi_1,\alpha,(\xi_1,\psi),M(\xi_1,\psi)] \sin\phi \\ + C_d[\xi_1,\alpha(\xi_1,\psi),M(\xi_1,\psi)] \cos\phi\} \end{aligned} \tag{7}$$

In a similar way, equations for the surface pressure and tangential stress are derived as

$$p(\xi_1,\xi_2,\psi) = \frac{1}{2} V^2 \, C_p(\xi_1,\xi_2,\alpha,M) \tag{8}$$

$$\tau(\xi_1,\xi_2,\psi) = \frac{1}{2} V^2 \, C_f(\xi_1,\xi_2,\alpha,M) \tag{9}$$

Net thrust and torque forces are obtained by integrating with respect to the radial variable. The results are given as follows:

$$F_T = \int_a^b F_t(\xi_1,\psi)\, d\xi_1 \tag{10}$$

$$F_Q = \int_a^b F_q(\xi_1,\psi)\, d\xi_1 \tag{11}$$

Effective radii based on the net thrust and torque forces are calculated by the following equations:

$$r_T(\psi) = \frac{1}{F_T} \int_a^b \xi_1\, F_t(\xi_1,\psi)\, d\xi_1 \tag{12}$$

$$r_Q(\psi) = \frac{1}{F_Q} \int_a^b \xi_1\, F_q(\xi_1,\psi)\, d\xi_1 \tag{13}$$

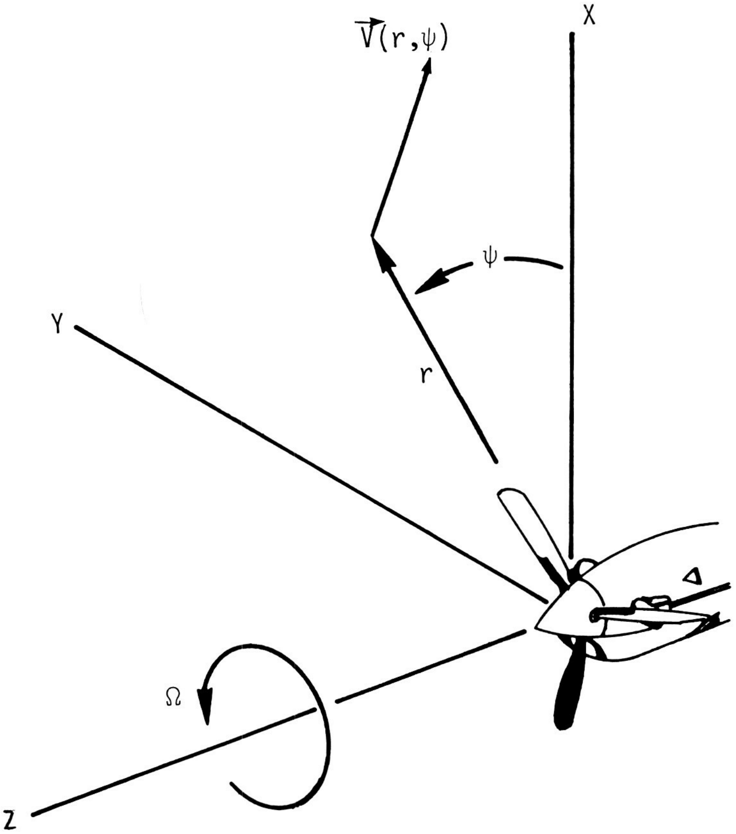

Figure 1.- Aircraft fixed coordinate system.

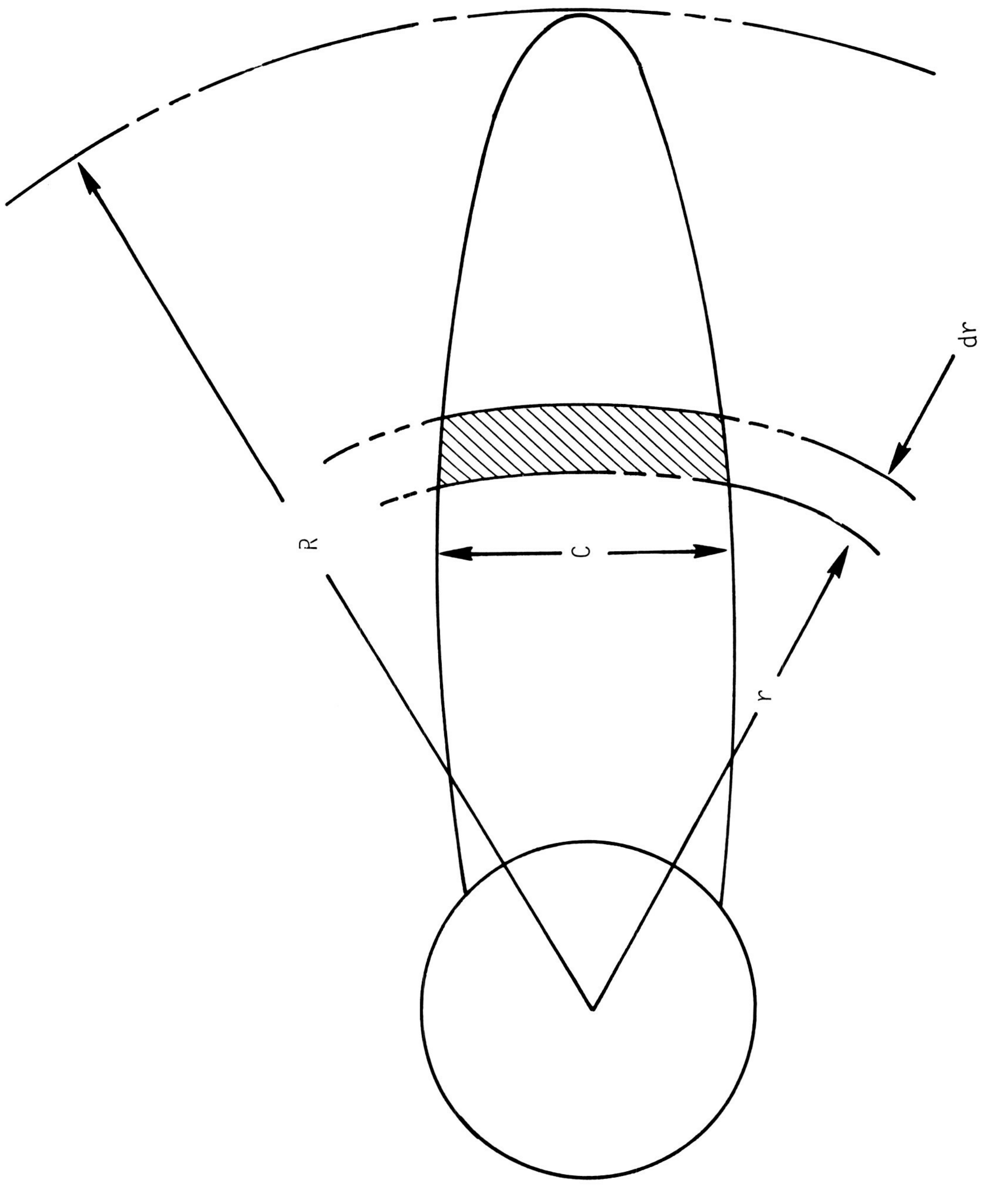

Figure 2.- Blade element geometry.

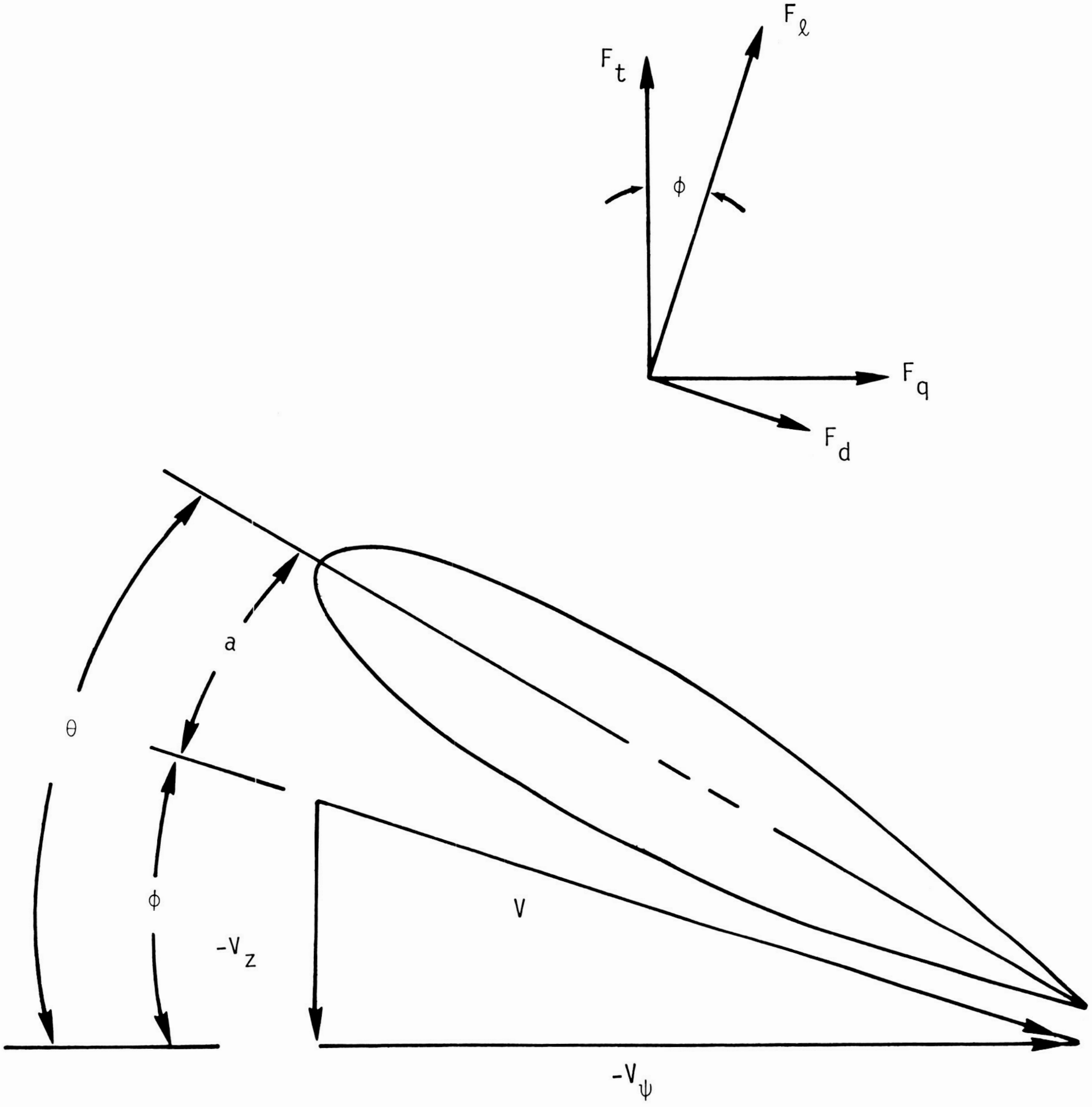

Figure 3.- Blade section vector diagram.

11. PROPELLER NOISE

11.1 SUBSONIC PROPELLER NOISE MODULE

Sharon L. Padula
Langley Research Center

INTRODUCTION

The Subsonic Propeller Noise Module computes the periodic acoustic pressure signature and spectrum of a propeller with subsonic tip speed. The computation is based on a solution of the Ffowcs Williams-Hawkings (FW-H) equation without the quadrupole source term. (See refs. 1 to 3.) The blade surface pressure and geometry are assumed known. The surface pressure can also be periodic in time. The observer is always assumed to be moving with the aircraft; only in such a frame is the acoustic pressure periodic. The main acoustic formulation uses the source distribution on the actual blade surface. Several approximations to the full solution are also included as options.

SYMBOLS

A	area of blade section, m^2 (ft^2)
c	ambient speed of sound, m/s (ft/s)
d_x	radial distance of observer from x_3-axis, m (ft)
d_y	radial distance of source from x_3-axis, m (ft)
F	symbol substituted for integrands in equation (41)
FFT	Fast Fourier Transform
f	function defining blade surface
f_k	frequency, Hz
G	symbol substituted for integrands in equation (45a)
g	equation $g = 0$ describes relationship between source and observer time
H	azimuthal force on single blade, N (lbf)

k	harmonic number
$\vec{L}$	net force of blade acting on fluid, N (lbf)
$\vec{L}'$	net force per unit radial distance, N/m (lbf/m)
$\vec{\ell}$	local force per unit area of blade acting on fluid, Pa (lbf/ft^2)
M	source Mach number
m	exponent; 2^m is number of time points used by FFT routine
N_b	number of blades
N_s	maximum harmonic number in calculations
N_t	number of times
n	blade surface normal vector
p	surface pressure $p_a - p_o$, Pa (lbf/ft^2)
Δp	difference between lower and upper surface pressure, Pa (lbf/ft^2)
p_a	absolute surface pressure, Pa (lbf/ft^2)
p'_L	acoustic pressure produced by loading, Pa (lbf/ft^2)
p_o	ambient pressure, Pa (lbf/ft^2)
p_{ref}	reference pressure for definition of dB, 20 μPa
p'	acoustic pressure, Pa (lbf/ft^2)
p'_p	total acoustic pressure produced by propeller, re p'_{rms}, Pa (lbf/ft^2)
p'_{rms}	root-mean-square acoustic pressure
p'_T	acoustic pressure produced by thickness, Pa (lbf/ft^2)
R_E	effective radial distance to be used in point source approximation, m (ft)
r	distance from source point at emission time to observer, $(r = \lvert \vec{x} - \vec{y}\,(\tau^*) \rvert)$, m (ft)

S	surface area
SPL_k	acoustic spectrum, dB
T	net thrust from single blade, N (lbf)
t	time at which noise signal is received by observer, s
$\hat{t}$	blade surface unit tangent vector
V_F	forward velocity of aircraft, m/s (ft/s)
v	source velocity, m/s (ft/s)
$\vec{X}$	observer position in aircraft-fixed frame, m (ft)
$\vec{x}$	observer position in ground-fixed frame, m (ft)
$\vec{y}$	source position in ground-fixed frame, m (ft)
δ	Dirac delta function
$\vec{\eta}$	source position in blade-fixed frame, m (ft)
Θ	angle between radiation vector and surface normal vector, rad
Θ'	angle between radiation vector and surface tangent vector, rad
θ_0	root pitch change angle, rad
ξ_1, ξ_2	elliptic surface coordinates
ρ_0	ambient density, kg/m^3 (slug/ft^3)
σ	local tangential stress, N/m^2 (lbf/ft^2)
τ	time at which noise signal is emitted at source position, s
τ^*	solution to retarded time equation, $g = 0$, for given observer time, s
Υ	parameter defined by equations 27
ϕ	solution to retarded time equation as solved by Newton's method, $\Omega(\tau - t)$, rad
Ψ	blade volume, m^3 (ft^3)
ψ	angle between x_1- and η_1-axes, rad
Ω	angular velocity of blade, rad/s

Subscripts:

i	component along ith coordinate axis ($\ell_i\hat{r}_i$ implies summation convention); also inner radius
L	loading
m	property of mean blade surface
n	component in direction of surface normal
o	ambient condition; also outer radius
r	component in direction of radiation vector
T	thickness

Notation:

_	mean
^	unit vector
·	time derivative
*	complex conjugate; specific solution to retarded time equation

INPUT

The computation of subsonic propeller noise requires data of the blade shape characteristics, aerodynamic characteristics, flow and operating parameters, and observer geometry. The noise signature is calculated by using the following methods: (1) full blade formulation, (2) mean surface approximation, (3) compact chord approximation, or (4) compact source approximation. Option numbers in parentheses identify the inputs which correspond to each method.

User Parameters (1, 2, 3, 4)

N_b	number of blades
N_s	highest harmonic number desired
R	blade length measured from axis to tip, m (ft)
V_F	aircraft forward velocity, m/s (ft/s)

θ_0	root pitch change angle, rad
ψ_0	initial azimuth angle of first blade, rad
Ω	angular velocity of blade, rad/s
Ψ	blade volume, re R^3

Blade Shape Table (1, 2)

ξ_1	spanwise location, re R
ξ_2	chordwise location, rad
$\eta_1(\xi_1,\xi_2)$	blade surface abscissa, re R
$\eta_3(\xi_1,\xi_2)$	blade surface ordinate, re R
Φ_1,Φ_2	slopes of basis functions at nodes

Spanwise Function Table (3)

$A(\xi_1)$	blade section area, re R^2
$\eta_{1,\ell}(\xi_1)$	abscissa of leading edge, re R
$\eta_{3,\ell}(\xi_1)$	ordinate of leading edge, re R

Aerodynamic Characteristics Table (1, 2)

ξ_1	spanwise location, re R
ξ_2	chordwise location, rad
ψ	azimuthal location, rad
$p(\xi_1,\xi_2,\psi)$	pressure loading, re $\rho_0(R\Omega)^2$
$\sigma(\xi_1,\xi_2,\psi)$	skin friction loading, re $\rho_0(R\Omega)^2$

Observer Table (1, 2, 3, 4)

$\vec{x}$	initial observer position, m (ft)

Atmospheric Properties Table (1, 2, 3, 4)

ρ_0	ambient fluid density, kg/m^3 (slugs/ft^3)
c	local sound speed, m/s (ft/s)

Performance Characteristics Table

$F_z(\xi_1,\psi)$	axial section force, re $\rho_0 R^3\Omega^2$ (3)
$F_\psi(\xi_1,\psi)$	azimuthal section force, re $\rho_0 R^3\Omega^2$ (3)
$T(\psi)$	net thrust for a single blade, re $\rho_0 R^4\Omega^2$ (4)
$H(\psi)$	net azimuthal force for a single blade, re $\rho_0 R^4\Omega^2$ (4)
$\xi_T(\psi)$	effective radius based on net thrust, re R (4)
$\xi_Q(\psi)$	effective radius based on azimuthal force, re R (4)

OUTPUT

This module provides the complex pressure spectrum and pressure time history at a fixed observer location measured from the center of the hub. Complex pressures are given with the $e^{-i\Omega t}$ time harmonic convention and all spectra are understood to be two sided with $p_p(x,-k) = p_p^*(x,k)$. With this convention, the mean-squared pressure is $2p_p p_p^*$ for each harmonic (where $2p'_p p'^*_p = p'_{rms}$).

Complex Pressure Spectrum

k	harmonic number
f_k	frequency, Hz
$C_k(\vec{x})$	complex acoustic pressure, re $\rho_0(R\Omega)^2$
$SPL_k(\vec{x})$	sound pressure level associated with $C_k(\vec{x})$

Pressure Time History

t	time, s
$p_p(\vec{x},t)$	acoustic pressure, re p_{rms}

METHOD

Acoustic Formulation

The governing acoustic equation is the following inhomogeneous wave equation:

$$\frac{1}{c^2}\frac{\partial^2 p'}{\partial t^2} - \nabla^2 p' = \frac{\partial}{\partial t}\left[\rho_o v_n \left|\nabla f\right| \delta(f)\right] - \frac{\partial}{\partial x_i}\left[\vec{\ell}_i \left|\nabla f\right| \delta(f)\right] \tag{1}$$

This is the FW-H equation without the quadrupole source term. The blade surface is described by $f(\vec{x},t) = 0$. The acoustic pressure is denoted by p', v_n is the local normal velocity of the blade, and $\vec{\ell}_i$ is the local force per unit area of the blade acting on the fluid. The density and the speed of sound in the undisturbed medium are denoted as ρ_o and c, respectively. The symbol $\delta(f)$ stands for the Dirac delta function. The two terms on the right of equation (1) are known as the thickness and loading noise sources, respectively. Note that equation (1) is written in a Cartesian frame fixed to the undisturbed medium which is called the ground-fixed frame. Two other frames of reference are more suitable for describing the solution and computation of the noise.

The FW-H equation is valid in the entire three-dimensional unbounded space. The Green's function of the wave equation for the unbounded space is $\delta(g)/4\pi r$ where $g = \tau - t + r/c$ and $r = |\vec{x} - \vec{y}|$. Here τ and t are the source and the observer times and $\vec{y}$ and $\vec{x}$ are the source and observer positions, respectively. With this Green's function, the formal solution of equation (1) is

$$4\pi p'(\vec{x},t) = \frac{\partial}{\partial t}\int \frac{1}{r}\rho_o v_n \left|\nabla f\right| \delta(f)\ \delta(g)\ d\vec{y}\ d\tau - \frac{\partial}{\partial x_i}\int \frac{1}{r}\ \ell_i \left|\nabla f\right| \delta(f)\ \delta(g)\ d\vec{y}\ d\tau \tag{2}$$

Note that the integrals in equation (2) are four-dimensional as written below:

$$\int \cdots\ d\vec{y}\ d\tau = \int_{-\infty}^{t}\int_{-\infty}^{\infty}\int_{-\infty}^{\infty}\int_{-\infty}^{\infty} \cdots\ d\vec{y}\ d\tau \tag{3}$$

Before integrating equation (2), the following identity, established by differentiation, is used

$$-\frac{\partial}{\partial x_i}\left[\frac{\delta(g)}{r}\right] = \frac{1}{c}\frac{\partial}{\partial t}\left[\frac{\hat{r}_i\,\delta(g)}{r}\right] + \frac{\hat{r}_i\,\delta(g)}{r^2} \tag{4}$$

where $\hat{r}_i = (x_i - y_i)/r$ is the unit vector in radiation direction. Since only the function $\delta(g)/r$ is dependent on $\vec{x}$, the second term in equation (2) may be rewritten as

$$- \frac{\partial}{\partial x_i} \int \frac{1}{r} \ell_i \left|\nabla f\right| \; \delta(f) \; \delta(g) \; d\vec{y} \; d\tau = \frac{1}{c} \frac{\partial}{\partial t} \int \frac{1}{r} \ell_r \left|\nabla f\right| \; \delta(f) \; \delta(g) \; d\vec{y} \; d\tau$$

$$+ \int \frac{1}{r^2} \ell_r \left|\nabla f\right| \delta(f) \; \delta(g) \; d\vec{y} \; d\tau \quad (5)$$

where $\ell_r = \ell_i \hat{r}_i$. Using equation (5) in equation (2) gives

$$4\pi p'(\vec{x},t) = \frac{1}{c} \; \frac{\partial}{\partial t} \int \frac{1}{r} \left(\rho_o c v_n + \ell_r\right) \left|\nabla f\right| \; \delta(f) \; \delta(g) \; d\vec{y} \; d\tau$$

$$+ \int \frac{1}{r^2} \ell_r \; \left|\nabla f\right| \; \delta(f) \; \delta(g) \; d\vec{y} \; d\tau \quad (6)$$

Now a Cartesian frame, denoted as the $\vec{\eta}$-frame, fixed to the blade is introduced. This frame is referred to as the blade-fixed frame. It is assumed that the blade is rigid so that its surface description in the $\vec{\eta}$-frame is time independent. To integrate equation (6), the following steps are employed:

(1) Use the transformation of variable $\vec{y} \rightarrow \vec{\eta}$

(2) Use the transformation $\tau \rightarrow g$ to integrate with respect to the variable g

(3) Integrate the remaining delta functions

Step 1: Since the Jacobian of the transformation is 1, it follows that the volume elements in the two spaces are equal. Also note that in the $\vec{\eta}$-frame the equation of the blade surface depends on $\vec{\eta}$ only. This is obtained as follows:

$$f[y(\vec{\eta},\vec{\tau}),\tau] \equiv \tilde{f}(\vec{\eta}) = 0 \quad (7)$$

That is, the equation of the blade surface in the $\vec{\eta}$-frame is obtained by substituting for $\vec{y}$ in terms of $\vec{\eta}$ and τ. Note that since the blade-fixed frame is in motion, the transformation $\vec{y} \rightarrow \vec{\eta}$ is time dependent and $\vec{y} = \vec{y}(\vec{\eta},\tau)$. To reduce confusion, the tilde on $\tilde{f}(\vec{\eta})$ is dropped in the following results. The function g is defined as follows:

$$g = \tau - t + \left|\vec{x} - \vec{y}(\vec{\eta},\tau)\right|/c \quad (8)$$

Step 2: Now fix $\vec{\eta}$ and use the transformation $\tau \rightarrow g$. The Jacobian of the transformation is

$$J = \frac{1}{\left|\partial g/\partial \tau\right|_{\vec{\eta}}} = \frac{1}{\left|1 - M_r\right|} \tag{9}$$

where $M_r = v_i \hat{r}_i / c$. Here $\vec{v}$ is the velocity of the point with position vector $\vec{\eta}$ in the blade-fixed frame relative to the ground-fixed frame. In step 3, this velocity will be defined more carefully. The result of steps 1 and 2 is

$$4\pi p'(\vec{x},t) = \frac{1}{c}\frac{\partial}{\partial t}\int \left[\frac{\rho_o c v_n + \ell_r}{r\left|1 - M_r\right|}\right]_{\tau^*} \left|\nabla f\right| \delta(f)\, d\vec{\eta}$$

$$+ \int \left[\frac{\ell_r}{r^2\left|1 - M_r\right|}\right]_{\tau^*} \left|\nabla f\right| \delta(f)\, d\vec{\eta} \tag{10}$$

Here the integrals are evaluated in the blade-fixed frame over the entire space. The source time τ^* is the emission time obtained by finding the root of the equation

$$g = \tau^* - t + \left|\vec{x} - \vec{y}(\vec{\eta},\tau^*)\right|/c = 0 \tag{11}$$

For subsonic propellers considered herein, this equation has only one root.

Step 3: In this step, the integrations over the delta functions in equation (10) are performed by using the relation

$$d\vec{\eta} = \frac{df\, dS}{\left|\nabla f\right|} \tag{12}$$

where at this stage dS is the element of surface area of the surface f = Constant. This relation is derived in reference 2. Substituting equation (12) into equation (10) and integrating with respect to f result in the following equation:

$$4\pi p'(\vec{x},t) = \frac{1}{c}\frac{\partial}{\partial t}\int_{f=0} \left[\frac{\rho_o c v_n + \ell_r}{r\left|1 - M_r\right|}\right]_{\tau^*} dS + \int_{f=0} \left[\frac{\ell_r}{r^2\left|1 - M_r\right|}\right]_{\tau^*} dS \tag{13}$$

Here, $M_r = v_i \hat{r}_i / c$, where $\vec{v}$ is the local velocity of points on the blade surface itself. Since $M_r < 1$ for all points on a subsonic blade, the absolute value signs about $1 - M_r$ are dropped in the following formulas.

Equation (13) has been used for high-speed propeller noise calculations by Farassat. (See ref. 4.) Since for subsonic propellers $M_r < 1$, the time derivative can be taken inside the integral. The following terms are functions of time in the first integral of equation (13):

$$\ell_i \qquad \frac{1}{r(1 - M_r)} \qquad \frac{\hat{r}_i}{r(1 - M_r)}$$

The chain rule of differentiation is then used to differentiate the integrand of the first integral in equation (13):

$$\frac{\partial}{\partial t} = \frac{\partial \tau^*}{\partial t} \frac{\partial}{\partial \tau^*} \tag{14}$$

From equation (11), by differentiating with respect to t, the following is obtained:

$$\frac{\partial \tau^*}{\partial t} = \frac{1}{1 - M_r}. \tag{15}$$

Therefore, from equation (14),

$$\frac{\partial}{\partial t} = \frac{1}{1 - M_r} \frac{\partial}{\partial \tau^*} \tag{16}$$

The following relations are thus established:

$$\frac{\partial r}{\partial \tau^*} = -v_r \tag{17}$$

$$\frac{\partial \hat{r}_i}{\partial \tau^*} = \frac{\hat{r}_i v_r - v_i}{r} \tag{18}$$

$$\frac{\partial M_r}{\partial \tau^*} = \frac{1}{cr} \left[r_i \frac{\partial v_i}{\partial \tau^*} + v_r^2 - v^2 \right] \tag{19}$$

By using equations (16) through (19), the time derivative in equation (13) is carried out explicitly to give:

$$4\pi p'_L(\vec{x},t) = \frac{1}{c} \int_{f=0} \left[\frac{\dot{\ell}_i \hat{r}_i}{r(1 - M_r)^2}\right]_{\tau^*} dS$$

$$+ \int_{f=0} \left[\frac{\ell_r - \ell_i M_i}{r^2(1 - M_r)^2}\right]_{\tau^*} dS$$

$$+ \frac{1}{c} \int_{f=0} \left[\frac{\ell_r(r\dot{M}_i \hat{r}_i + cM_r - c\,M^2)}{r^2\,(1 - M_r)^3}\right]_{\tau^*} dS \qquad (20a)$$

$$4\pi p'_T(\vec{x},t) = \int_{f=0} \left[\frac{\rho_o v_n (r\dot{M}_i \hat{r}_i + cM_r - cM^2)}{r^2(1 - M_r)^3}\right]_{\tau^*} dS \qquad (20b)$$

and

$$p'(\vec{x},t) = p'_L(\vec{x},t) + p'_T(\vec{x},t) \qquad (20c)$$

where p'_L and p'_T denote the loading and thickness noise, respectively. Equations (20) are used when the sources on the full-blade surface are specified. They are related to an equation derived by Woan and Gregorek. (See refs. 4 and 5.)

The symbols M_i and $\dot{M}_i$ are defined as follows:

$$M_i = \frac{v_i}{c} \qquad (21)$$

$$\dot{M}_i = \frac{\dot{v}_i}{c} \qquad (22)$$

Note that v_i and $\dot{v}_i$ are the local velocity and acceleration of the blade with respect to the ground-fixed frame. It is assumed here that the propeller blades are rigid. It is important to note that $\dot{\ell}_i$ is the rate of change of the vector ℓ_i as seen from the ground-fixed frame. This means that even if ℓ_i is steady in the blade-fixed frame, $\dot{\ell}_i$ is not zero.

The force intensity vector ℓ_i can be written as

$$\ell_i = p\hat{n}_i + \sigma\hat{t}_i \qquad (23)$$

where p is the surface pressure defined as $p_a - p_o$. Here p_a is the absolute surface pressure and p_o is the ambient pressure in the undisturbed medium. The local tangential stress is denoted by σ and the unit tangent vector pointing toward the section leading edge is denoted by $\hat{t}_i$. From equation (23), the rate of change of ℓ_i is found to be

$$\dot{\ell}_i = \dot{p}\hat{n}_i + p\dot{\hat{n}}_i + \dot{\sigma}\hat{t}_i + \sigma\dot{\hat{t}}_i \tag{24}$$

It can be shown that

$$\dot{\hat{n}}_i = (\vec{\Omega} \times \hat{n})_i \tag{25a}$$

$$\dot{\hat{t}}_i = (\vec{\Omega} \times \hat{t})_i \tag{25b}$$

From equations (25) and (24), the following results are obtained:

$$\dot{\ell}_i\hat{r}_i = \dot{p} \cos \Theta + \dot{\sigma} \cos \Theta' + pT_1 + \sigma T_2 \tag{26a}$$

$$\ell_i\hat{r}_i = p \cos \Theta + \sigma \cos \Theta' \tag{26b}$$

$$\ell_i M_i = pM_n + \sigma M_t \tag{26c}$$

Note that Θ is the angle between $\hat{n}$ and $\hat{r}$, Θ' is the angle between $\hat{t}_i$ and $\hat{r}_i$, and T_1 and T_2 are defined as follows:

$$T_1 = \vec{r} \cdot (\vec{\Omega} \times \hat{n}) \tag{27a}$$

$$T_2 = \vec{r} \cdot (\vec{\Omega} \times \hat{t}) \tag{27b}$$

Also M_t is defined as $v_i\hat{t}_i/c$. Equations (26) are substituted into equations (20) and the result is solved numerically.

A useful approximation to equations (20) is written next. If the propeller blades are assumed to be thin, the acoustic sources can be moved to the mean surface of the blades. The mean surface is defined to be that surface formed by generating the section mean curves along the leading-edge curve. Let the surface be denoted by the equation $f^{\rightarrow}_m (x,t) = 0$. The FW-H equation becomes

$$\frac{1}{c^2} \frac{\partial^2 p'}{\partial t^2} - \nabla^2 p' = 2 \frac{\partial}{\partial t} \left[\rho_o \overline{v}_n \left|\nabla f_m\right| \delta(f_m)\right] + \frac{\partial}{\partial x_i} \left[\Delta p \, n_{im} \left|\nabla f_m\right| \delta(f_m)\right] \tag{28}$$

where $\Delta p = p_{lower} - p_{upper}$ and n_{im} is the unit normal to $f_m = 0$ pointing toward the upper side of the blade. Here $\overline{v}_n$ is the local normal velocity of the blade on one side of the mean surface due to thickness distribution alone (i.e., the camber effect is ignored). Note that $\overline{v}_n$ is calculated by evaluating v_n at each upper surface point and v_n at the corresponding point on the lower surface and then averaging. Furthermore, skin friction is neglected.

Following a procedure similar to that leading to equations (20), an expression for $p'(\vec{x},t)$ is

$$4\pi p_L'(\vec{x},t) = -\frac{1}{c}\int_{f_m=0}\left[\frac{\Delta\dot{p}\cos\Theta + \Delta p T_1}{r(1-M_r)^2}\right]_{\tau^*} dS$$

$$-\int_{f_m=0}\left[\frac{\Delta p(\cos\Theta - M_n)}{r^2(1-M_r)^2}\right]_{\tau^*} dS$$

$$-\frac{1}{c}\int_{f_m=0}\left[\frac{\Delta p\cos\Theta\,(r\dot{M}_i\hat{r}_i + cM_r - cM^2)}{r^2(1-M_r)^3}\right]_{\tau^*} dS \qquad (29a)$$

$$4\pi p_T'(\vec{x},t) = \int_{f_m=0}\left[\frac{2\rho_o\,\overline{v}_n(r\dot{M}_i\hat{r}_i + cM_r - cM^2)}{r^2(1-M_r)^3}\right]_{\tau^*} dS \qquad (29b)$$

$$p'(\vec{x},t) = p_L'(\vec{x},t) + p_T'(\vec{x},t) \qquad (29c)$$

In equation (29a), Θ is the angle between the radiation vector $\vec{r}$ and $\hat{n}_{im}$.

Two compact-source approximations for the subsonic propeller noise calculation are also used. In the first approximation, each blade is replaced by a single point source involving both the thickness and loading effects. The loading noise formula of Lowson and the thickness noise formula of Succi are used. (See refs. 6 and 7.) Let L_i be the net force by each blade on the fluid and Ψ be the net volume of each blade. Then the loading and thickness noise are

$$4\pi p_L'(\vec{x},t) = \left\{ \frac{1}{cr(1-M_r)^2} \left[\hat{r}_i \dot{L}_i + \frac{\hat{r}_i L_i}{(1-M_r)} \left[\dot{M}_r + \frac{c}{r}(1-M^2) \right] - \frac{c}{r} M_i L_i \right] \right\} \Bigg|_{\tau=\tau^*}$$

$$= F_L(\vec{x},t,R_E) \tag{30}$$

and

$$4\pi p_T'(\vec{x},t) = \left\{ \frac{\rho_o \Psi}{r(1-M_r)^5} \left[(1-M_r)\left(\ddot{M}_r - 3\frac{c}{r}\vec{M}\cdot\dot{\vec{M}}\right) + 3\left(\frac{c}{r}M_r\right)^2 \right.\right.$$

$$\left.\left. + 3\left(\dot{M}_r - \frac{c}{r}M^2\right)^2 + \frac{c}{r}\left(\dot{M}_r - \frac{c}{r}M^2\right)(1 + 4M_r + M_r^2) \right] \right\} \Bigg|_{\tau=\tau^*}$$

$$= F_T(\vec{x},t,R_E) \tag{31}$$

Here the sources are assumed to be located at some effective radial distance R_E (usually about 0.8 radius of the propeller). The effect of each blade is computed separately and summed to get the total noise.

A second compact-source formulation is obtained by assuming that each blade can be approximated by a line source (chordwise compactness assumption). In equations (30) and (31), let $L_i'(\xi_1)$ and $A(\xi_1)$ be substituted for L_i and Ψ, respectively, and represent the force per unit distance and blade volume per unit distance. Here ξ_1 is the radial distance in the blade-fixed frame. The noise due to loading and thickness of the propeller is then given by

$$4\pi p'(\vec{x},t) = \int_{R_i}^{R_o} \left[F_L'(\vec{x},t,\xi_1) + F_T'(\vec{x},t,\xi_1) \right] d\xi_1 \tag{32a}$$

where the integrands F_L' and F_T' are defined by

$$F_L'(\vec{x},t,\xi_1) = \frac{1}{cr(1-M_r)^2} \left\{ \hat{r}_i \dot{L}_i' + \frac{\hat{r}_i L_i'}{(1-M_r)} \left[\dot{M}_r + \frac{c}{r}(1-M^2) \right] \right.$$

$$\left. - \frac{c}{r} M_i L_i' \right\} \tag{32b}$$

and

$$F_T' (\vec{x},t,\xi_1) = \frac{\rho_0 \, A(\xi_1)}{r(1 - M_r)^5} \left[(1 - M_r)(\ddot{M}_r - 3 \frac{c}{r} \dot{\vec{M}} \cdot \dot{\vec{M}}) + 3(\frac{c}{r} M_r)^2 \right.$$

$$\left. + 3 (\dot{M}_r - \frac{c}{r} M^2)^2 + \frac{c}{r} (\dot{M}_r - \frac{c}{r} M^2)(1 + 4M_r + M_r^2) \right] \qquad (32c)$$

The symbols R_i and R_0 in equation (32a) represent the inner and the outer radii of the blade. The effect of several blades is taken into account by a method requiring a single blade calculation as discussed later.

Frames of Reference

In this section, the coordinate systems used in the acoustic calculations will be discussed. Basically there are two reference frames: the ground-fixed $\vec{x}$-frame and the blade-fixed $\vec{\eta}$-frame. The $\vec{x}$-frame which remains fixed to the undisturbed medium is set up as follows:

The origin of this frame is at the propeller center at time $t = 0$

The propeller disk is in the x_1x_2-plane and the x_3-axis coincides with the propeller axis, with positive direction in the flight direction

The x_1-axis is assumed to be orthogonal to the x_3-axis, upward and parallel to the plane of symmetry of the aircraft

The x_2-axis is defined in such a way that the $\vec{x}$-frame is right-handed (see fig. 1)

The observer position is always specified in this frame as is explained shortly.

The blade-fixed frame is set up as follows:

The origin coincides with the origin of the $\vec{x}$-frame at $t = 0$

The η_3-axis coincides with the x_3-axis

The η_2-axis lies on the pitch change axis of the blade

The $\eta_1\eta_2$-plane is normal to the propeller shaft

The η_1-axis is defined to make the $\vec{\eta}$-frame right-handed (see fig. 2)

Note that the blade mean surface does not lie in the $\eta_1\eta_2$-plane but makes an angle equal to the geometric pitch angle at each radial position. Note also that the $\vec{\eta}$-frame rotates with angular velocity Ω.

In the acoustic formulas presented in the previous section, many operations involving dot products or cross products of two vectors are required. When the products involve blade normals or surface pressures, it is convenient to transform the components of these vectors to the $\vec{\eta}$-frame and then perform the operation. However, note that the source position $\vec{y}$ always refers to a source point in the $\vec{x}$-frame with a known position $\vec{\eta}$ in the blade-fixed frame. The quantities $\vec{r} = \vec{x} - \vec{y}$ and $\hat{r} = \vec{r}/r$ are calculated in the $\vec{x}$-frame, and then the vector components are calculated in the $\vec{\eta}$-frame. Note that for any variable which has a velocity term, such as $M_r = M_i\hat{r}_i$ and $v_n = \vec{v}\cdot\hat{n}$, the velocity is with respect to the $\vec{x}$-frame. In other words

$$v_i = \frac{\partial y_i}{\partial \tau} \tag{33}$$

The components of this vector must then be calculated in the $\vec{\eta}$-frame to get M_r and v_n.

Another frame of reference which is used conceptually is <u>the aircraft-fixed nonrotating $\vec{X}$-frame</u>. This frame coincides with the ground-fixed $\vec{x}$-frame at $t = 0$. The acoustic pressure $p'(\vec{X},t)$ for an observer in the aircraft-fixed frame with the position vector $\vec{X}$ is found as follows: Since both $\vec{X}$ and t are known, the relative position of the ground-fixed frame and the aircraft-fixed frame is known. From this, calculate the observer position $\vec{x}$ in the ground-fixed frame. By using this $\vec{x}$ and t, calculate $p'(\vec{x},t)$ which is the same as the acoustic pressure at position $\vec{X}$ in the aircraft-fixed frame and at time t. Thus, the $\vec{X}$-frame itself is never used in acoustic calculations, even though the pressure signal which results is $p'(\vec{X},t)$.

The transformation from one frame to the other at time t, in matrix notation is

$$\begin{bmatrix} X_1 \\ X_2 \\ X_3 \end{bmatrix} = \begin{bmatrix} \cos\psi & -\sin\psi & 0 \\ \sin\psi & \cos\psi & 0 \\ 0 & 0 & 1 \end{bmatrix} \begin{bmatrix} \eta_1 \\ \eta_2 \\ \eta_3 \end{bmatrix} \tag{34a}$$

$$\begin{bmatrix} x_1 \\ x_2 \\ x_3 \end{bmatrix} = \begin{bmatrix} X_1 \\ X_2 \\ X_3 \end{bmatrix} + \begin{bmatrix} 0 \\ 0 \\ V_F t \end{bmatrix} \tag{34b}$$

where (η_1,η_2,η_3) is a point in the rotating $\vec{\eta}$-frame, (X_1,X_2,X_3) is the corresponding point in the moving $\vec{X}$-frame, (x_1,x_2,x_3) is the corresponding point in the ground-fixed frame, and ψ $(= \Omega t)$ is the angle between the X_1- and η_1-axes.

A final coordinate transformation is necessary to account for changes in the root pitch setting. This rotation through a small angle θ_0 is applied to the blade surface coordinates, which are calculated by the Blade Shape Module:

$$\vec{\eta}(\xi_1,\xi_2) = \begin{bmatrix} \cos\theta_0 & 0 & \sin\theta_0 \\ 0 & 1 & 0 \\ -\sin\theta_0 & 0 & \cos\theta_0 \end{bmatrix} \begin{bmatrix} \eta_1'(\xi_1,\xi_2) \\ \xi_1 \\ \eta_3'(\xi_1,\xi_2) \end{bmatrix} \tag{35}$$

Whenever the $\vec{\eta}$-frame or pitch axis coordinate system is mentioned herein, it is assumed that the above corrective transformation has occurred. Often the Blade Shape Module and Subsonic Propeller Noise Module will be executed without change to the collective pitch setting. Thus, $\theta_0 = 0$ and the last transformation is unnecessary.

Computational Strategy

A pressure time history of a multibladed propeller is calculated by summing the acoustic pressures of each blade as a function of time. The signals are periodic because the observer position is a fixed distance from the hub at all times. Thus, the signal produced by 1 revolution of a single blade can be used to determine the time history and spectrum of the propeller. The general computational strategy is outlined below. Details concerning the different methods for calculating $p'(\vec{X},t)$ are contained in later sections.

The steps involved in calculating the acoustic time signature for a single blade are as follows. Assume that the initial pitch change axis of the blade is aligned with the X_2-axis. That is, assume

$t = \psi = 0$ and the $\vec{x}$-frame, $\vec{X}$-frame, and $\vec{\eta}$-frame coincide. Divide the time required for 1 full revolution of the blade into even time increments such that

$$t_i = \frac{(i - 1)\, 2\pi}{N_t \Omega} \qquad (i = 1, 2, \ldots, N_t)$$

Likewise, represent the blade by a set of source points $\vec{\eta}(j)$, where the number and location of the source points depend on which method for calculating noise is selected. Then, for each time t_i and each source point $\vec{\eta}(j)$, determine the source $\vec{y}$ and observer $\vec{x}$ locations in the ground-fixed frame. With these, solve the retarded time equation and calculate distances and velocities at emission time. Next, calculate vector components in the rotating $\vec{\eta}$-frame and calculate the influence of this source point on the total noise. Finally, accumulate the information for each time and source point into a complete time history.

The steps involved in producing a time history and spectrum for the propeller are as follows:

Tabulate the time history for one blade so that intermediate values can be obtained by interpolation.

Decide how many evenly spaced time points are required by the Fast Fourier Transform (FFT) procedure. If N_s is the highest harmonic number of interest and N_t the number of time points, find an integer m such that 2^m is at least as large as $N_t \geq 2N_s$.

Calculate the total acoustic pressure time history by adding the contribution from each blade.

Finally, perform an FFT to get the pressure spectrum.

The above process can be stated mathematically as follows. The time required for 1 revolution of the blade is divided equally into 2^m points such that

$$t_k = \frac{(k - 1)2\pi}{(2^m)\Omega} \qquad (k = 1, 2, \ldots, 2^m)$$

$$m = \text{INT}\,(\log_2 N_t) + 1 \tag{36}$$

where the INT function turns a real number into the largest integer not exceeding the real number.

The acoustic signal generated by a propeller is just the sum of the pressures produced by each blade. The pressure produced at time t by blade b, which had an initial angle $\psi_b = \psi_0 + 2\pi(b - 1)/N_b$ relative to the X_2 axis, can be found by interpolating into the single blade pressure table for $p'(\vec{X},t+\psi_b/\Omega)$. Thus, the total acoustic signal is

$$p_T(\vec{X},t_k) = \sum_{b=1}^{N_b} p'(\vec{X},t_k + \psi_b/\Omega) \quad (k = 1, 2, \ldots, 2^m) \tag{37}$$

where $\vec{X}$ is the observer position in the aircraft fixed frame, N_b is the number of blades, and ψ_b is the initial position of each blade. The spectrum associated with this time history is calculated by using a standard FFT routine. Appendix A contains further details.

Retarded Time Equation

This section describes a method for solving the retarded time equation, $g = \tau - t + r/c = 0$. As noted previously, the root $\tau = \tau^*$ of this equation must be found for each source point used to represent the blade and for each observer time t. Since the roots of the equation are calculated repeatedly it is imperative to solve the equation in an efficient way. Details of the solution technique are reserved for appendix B.

The problem can be stated in terms of arbitrary receiver location $\vec{x}$ and source location $\vec{y}$ defined in the ground-fixed coordinate system at time t. As described in reference 4, the equation is written

$$\begin{aligned} r^2 &= x_3^2 + d_x^2 + d_y^2 - 2d_x d_y \cos(\Omega\tau + \psi_y - \psi_x) \\ &\quad + V_F^2\tau^2 - 2x_3 V_F \tau \\ &= c^2(\tau - t)^2 \end{aligned} \tag{38}$$

where d_x and d_y are the radial distances between the x_3-axis and the observer and source points, and ψ_x and ψ_y are the observer and source angles of rotation at $t = 0$. For instance, if the source point is located on the pitch change axis then $d_y = \eta_2$ and $\psi_y = 0$. (See fig. 2.) After some manipulation,

$$\begin{aligned} r^2 &= (x_3 - V_F t)^2 + d_x^2 + d_y^2 - 2d_x d_y \cos[\Omega(\tau - t) + \psi_y - (\psi_x - \Omega t)] \\ &\quad + V_F^2(\tau - t)^2 - 2V_F(x_3 - V_F t)(\tau - t) \\ &= c^2(\tau - t)^2 \end{aligned} \tag{39}$$

Letting $\phi = \Omega(\tau - t)$, equation (39) is written as

$$A\phi^2 + B\phi + C + \cos(\phi + D) = 0 \tag{40}$$

where

$$A = (c^2 - V_F^2)/2\Omega^2 d_x d_y \qquad (A > 0)$$

$$B = V_F(x_3 - V_F t)/\Omega d_x d_y$$

$$C = -[(x_3 - V_F t)^2 + d_x^2 + d_y^2]/2d_x d_y$$

$$D = \psi_y - \psi_x + \Omega t$$

Based on the transformation given in equation (34b), the term $(x_3 - V_F t)$ can be replaced by the constant X_3 for all times. Consequently, the coefficients A, B, and C in equation (40) change only if source position changes. Thus, the solution to equation (40) for one source point and source time will be a good initial guess for the same source point at a slightly later time.

Equation (40) can be solved very efficiently by using Newton's method. Only one root such that $(\tau - t) < 0$ is physically possible in the subsonic case. With the initial guess outlined in appendix B, Newton's method will converge to the proper root.

Full Blade Formulation

This section discusses the calculation of the periodic acoustic pressure signal for a single rotating blade with subsonic tip speed. The method described requires a detailed knowledge of the blade geometry and blade surface pressures. The three sections which follow discuss simplifying approximations to the full blade formulation which are used in the absence of full blade information.

The acoustic pressure at time t for an observer at point $\vec{x}$ is given by equations (20) as

$$4\pi p_L'(\vec{x},t) = \frac{1}{c} \int_{f=0} \left[\frac{\dot{\ell}_i \hat{r}_i}{r(1 - M_r)^2}\right]_{\tau^*} dS$$

$$+ \int_{f=0} \left[\frac{\ell_r - \ell_i M_i}{r^2(1 - M_r)^2}\right]_{\tau^*} dS$$

$$+ \frac{1}{c} \int_{f=0} \left[\frac{\ell_r (r\dot{M}_i \hat{r}_i + cM_r - cM^2)}{r^2(1 - M_r)^3}\right]_{\tau^*} dS \qquad (41a)$$

$$4\pi p_T'(\vec{x},t) = \int_{f=0} \left[\frac{\rho_o v_n (r\dot{M}_i \hat{r}_i + cM_r - cM^2)}{r^2(1 - M_r)^3}\right]_{\tau^*} dS \qquad (41b)$$

with

$$p'(\vec{x},t) = p_L'(\vec{x},t) + p_T'(\vec{x},t) \qquad (41c)$$

Using symbols F_{L1}, F_{L2}, and F_{L3} to stand for the integrands which are evaluated at retarded time τ^*, allows equations (41) to be written in short form as

$$4\pi p_L' = \frac{1}{c} \int_{f=0} F_{L1}(\vec{\eta})\, dS + \int_{f=0} F_{L2}(\vec{\eta})\, dS + \frac{1}{c} \int_{f=0} F_{L3}(\vec{\eta})\, dS \qquad (42a)$$

$$4\pi p_T' = \int_{f=0} F_T(\vec{\eta})\, dS \qquad (42b)$$

Using the Blade Shape Module, the surface of a propeller blade is described by a set of points $\vec{\eta}(j)$. The three components of each point $\vec{\eta}(j)$ are tabulated with respect to spanwise and chordwise station parameters ξ_1 and ξ_2. (See fig. 3.) Thus each term in equations (42) may be replaced by an equivalent double integral over ξ_1 and ξ_2. For instance,

$$\int_{f=0} F_{L1}(\vec{\eta})\, dS \equiv \int_0^1 \int_0^{2\pi} F_{L1}(\vec{\eta}(\xi_1,\xi_2))J\, d\xi_2\, d\xi_1 \qquad (43)$$

where J is the Jacobian of the transformation,

$$J = \left| \frac{\partial\vec{\eta}}{\partial\xi_1} \times \frac{\partial\vec{\eta}}{\partial\xi_2} \right| \qquad (44)$$

Equation (43) is evaluated by using a compound rule. Thus,

$$\int_0^1 \int_0^{2\pi} F_{L1} J \, d\xi_2 \, d\xi_1 = \int_0^1 G_{L1}(\xi_1) \, d\xi_1 \tag{45}$$

where

$$G_{L1}(\xi_1) = \int_0^{2\pi} F_{L1}(\xi_1,\xi_2) \, J(\xi_1,\xi_2) \, d\xi_2 \tag{46}$$

Each of the integrals over a single parameter is evaluated by using a standard procedure based on cubic splines.

Conceptually, the process of evaluating equations (41) to get $p'(\vec{x},t)$ involves calculating the values of each integrand at a set of blade surface points $\vec{n}(j)$ and accumulating them in a way which gives a sufficiently good approximation to the integral.

Mean Surface Approximation

In this section, approximation formulas for noise calculations based on the assumption of a thin airfoil are presented. The mean blade surface is defined to be that surface generated by the mean section curves. The calculation procedure is derived from equations (29) which are

$$\begin{aligned} 4\pi p_L'(\vec{x},t) = & -\frac{1}{c} \int_{f_m=0} \left[\frac{\Delta\dot{p} \cos\Theta + \Delta p \, T_1}{r(1 - M_r)^2} \right]_{\tau^*} dS \\ & - \int_{f_m=0} \left[\frac{\Delta p(\cos\Theta - M_n)}{r^2(1 - M_r)^2} \right]_{\tau^*} dS \\ & - \frac{1}{c} \int_{f_m=0} \left[\frac{\Delta p \cos\theta \, (r\dot{M}_i \hat{r}_i + cM_r - cM^2)}{r^2 \, (1 - M_r)^3} \right]_{\tau^*} dS \end{aligned} \tag{47a}$$

$$4\pi p_T'(\vec{x},t) = \int_{f_m=0} \left[\frac{2\rho_0 \, \bar{v}_n (r\dot{M}_i \hat{r}_i + cM_r - cM^2)}{r^2(1 - M_r)^3} \right]_{\tau^*} dS \tag{47b}$$

$$p'(\vec{x},t) = p_L'(\vec{x},t) + p_T'(\vec{x},t) \tag{47c}$$

Equations for the various terms of the integrands as functions of known quantities are determined as follows:

Coordinates of mean surface:

For a given radial distance, ξ_1, ξ_2 varies in the range $0 \leq \xi_2 \leq \pi$ and defines a mean section line as

$$\bar{\eta}_i(\xi_1,\xi_2) = \frac{1}{2}\left[\eta_i(\xi_1,\xi_2) + \eta_i(\xi_1,2\pi-\xi_2)\right] \qquad (i = 1,\ 2,\ 3) \tag{48}$$

Differential element on mean surface:

In terms of the independent variables ξ_1 and ξ_2, the differential area element dS is given as

$$dS = \bar{J}(\xi_1,\xi_2)\, d\xi_1\, d\xi_2 = \sqrt{EG - F^2}\, d\xi_1\, d\xi_2 \tag{49}$$

The symbols E, F, and G are written in terms of the mean surface coordinates as

$$E = \left(\frac{\partial\bar{\eta}_1}{\partial\xi_1}\right)^2 + \left(\frac{\partial\bar{\eta}_2}{\partial\xi_1}\right)^2 + \left(\frac{\partial\bar{\eta}_3}{\partial\xi_1}\right)^2 \tag{50}$$

$$F = \frac{\partial\bar{\eta}_1}{\partial\xi_1}\frac{\partial\bar{\eta}_1}{\partial\xi_2} + \frac{\partial\bar{\eta}_2}{\partial\xi_1}\frac{\partial\bar{\eta}_2}{\partial\xi_2} + \frac{\partial\bar{\eta}_3}{\partial\xi_1}\frac{\partial\bar{\eta}_3}{\partial\xi_2} \tag{51}$$

$$G = \left(\frac{\partial\bar{\eta}_1}{\partial\xi_2}\right)^2 + \left(\frac{\partial\bar{\eta}_2}{\partial\xi_2}\right)^2 + \left(\frac{\partial\bar{\eta}_3}{\partial\xi_2}\right)^2 \tag{52}$$

Since $\eta_2 = \xi_1$ and $\bar{\eta}_2$ is independent of ξ_2, equations (50) and (51) simplify to

$$E = \left(\frac{\partial\bar{\eta}_1}{\partial\xi_1}\right)^2 + \left(\frac{\partial\bar{\eta}_3}{\partial\xi_1}\right)^2 + 1 \tag{53}$$

and

$$F = \frac{\partial\bar{\eta}_1}{\partial\xi_1}\frac{\partial\bar{\eta}_1}{\partial\xi_2} + \frac{\partial\bar{\eta}_3}{\partial\xi_1}\frac{\partial\bar{\eta}_3}{\partial\xi_2} \tag{54}$$

Velocities and Mach numbers:

The position of a point on the blade is obtained by using the transformation defined by equations (34)

$$\begin{bmatrix} y_1 \\ y_2 \\ y_3 \end{bmatrix} = \begin{bmatrix} \cos \Omega t & -\sin \Omega t & 0 \\ \sin \Omega t & \cos \Omega t & 0 \\ 0 & 0 & 1 \end{bmatrix} \begin{bmatrix} \eta_1 \\ \eta_2 \\ \eta_3 \end{bmatrix} + \begin{bmatrix} 0 \\ 0 \\ V_F t \end{bmatrix} \qquad (55)$$

The velocity of the point is

$$\vec{v} = \begin{bmatrix} v_1 \\ v_2 \\ v_3 \end{bmatrix} = \begin{bmatrix} \dot{y}_1 \\ \dot{y}_2 \\ \dot{y}_3 \end{bmatrix} = \Omega \begin{bmatrix} -\sin \Omega t & -\cos \Omega t & 0 \\ \cos \Omega t & -\sin \Omega t & 0 \\ 0 & 0 & 0 \end{bmatrix} \begin{bmatrix} \eta_1 \\ \eta_2 \\ \eta_3 \end{bmatrix} + \begin{bmatrix} 0 \\ 0 \\ V_F \end{bmatrix} \qquad (56)$$

The position of a source point on the mean surface is, by analogy with equation (55),

$$\begin{bmatrix} \bar{y}_1 \\ \bar{y}_2 \\ \bar{y}_3 \end{bmatrix} = \begin{bmatrix} \cos \Omega t & -\sin \Omega t & 0 \\ \sin \Omega t & \cos \Omega t & 0 \\ 0 & 0 & 1 \end{bmatrix} \begin{bmatrix} \bar{\eta}_1 \\ \bar{\eta}_2 \\ \bar{\eta}_3 \end{bmatrix} + \begin{bmatrix} 0 \\ 0 \\ V_F t \end{bmatrix} \qquad (57)$$

The unit normal to the mean surface is

$$\underline{\hat{n}} = \frac{\dfrac{\partial \vec{\bar{\eta}}}{\partial \xi_1} \times \dfrac{\partial \vec{\bar{\eta}}}{\partial \xi_2}}{\left| \dfrac{\partial \vec{\bar{\eta}}}{\partial \xi_1} \times \dfrac{\partial \vec{\bar{\eta}}}{\partial \xi_2} \right|} \qquad (58)$$

and the unit vector in the radiation direction from a point on the mean surface is written as

$$\hat{\vec{r}} = \frac{\vec{x} - \vec{\bar{y}}}{\left| \vec{x} - \vec{\bar{y}} \right|} \qquad (59)$$

By analogy with equation (56), the velocity of a point on the mean surface is

$$\vec{\bar{v}} = \Omega \begin{bmatrix} -\sin \Omega t & -\cos \Omega t & 0 \\ \cos \Omega t & -\sin \Omega t & 0 \\ 0 & 0 & 0 \end{bmatrix} \begin{bmatrix} \bar{\eta}_1 \\ \bar{\eta}_2 \\ \bar{\eta}_3 \end{bmatrix} + \begin{bmatrix} 0 \\ 0 \\ V_F \end{bmatrix} \qquad (60)$$

The acceleration therefore becomes

$$\frac{d\vec{\bar{v}}}{dt} = \Omega^2 \begin{bmatrix} -\cos \Omega t & \sin \Omega t & 0 \\ -\sin \Omega t & -\cos \Omega t & 0 \\ 0 & 0 & 0 \end{bmatrix} \begin{bmatrix} \bar{\eta}_1 \\ \bar{\eta}_2 \\ \bar{\eta}_3 \end{bmatrix} \qquad (61)$$

Hence the local Mach number and its time rate of change are

$$\begin{bmatrix} M_1 \\ M_2 \\ M_3 \end{bmatrix} = \frac{\Omega}{c} \begin{bmatrix} -\sin \Omega t & -\cos \Omega t & 0 \\ \cos \Omega t & -\sin \Omega t & 0 \\ 0 & 0 & 0 \end{bmatrix} \begin{bmatrix} \bar{\eta}_1 \\ \bar{\eta}_2 \\ \bar{\eta}_3 \end{bmatrix} + \frac{1}{c} \begin{bmatrix} 0 \\ 0 \\ V_F \end{bmatrix} \qquad (62)$$

and

$$\begin{bmatrix} \dot{M}_1 \\ \dot{M}_2 \\ \dot{M}_3 \end{bmatrix} = \frac{\Omega^2}{c} \begin{bmatrix} -\cos \Omega t & \sin \Omega t & 0 \\ -\sin \Omega t & -\cos \Omega t & 0 \\ 0 & 0 & 0 \end{bmatrix} \begin{bmatrix} \bar{\eta}_1 \\ \bar{\eta}_2 \\ \bar{\eta}_3 \end{bmatrix} \qquad (63)$$

The mean normal velocity and radiation Mach number are written as

$$\bar{v}_n = \frac{1}{2} \left[\vec{v}(\xi_1,\xi_2) \cdot \hat{n}(\xi_1,\xi_2) + \vec{v}(\xi_1,2\pi - \xi_2) \cdot \hat{n}(\xi_1,2\pi - \xi_2)\right] \qquad (64)$$

and

$$M_r = \vec{M} \cdot (\vec{x} - \vec{y}) \Big/ \left|\vec{x} - \vec{y}\right| \qquad (65)$$

Miscellaneous integrand terms:

The differential pressure Δp is defined as

$$\Delta p = p(\xi_1,\xi_2) - p(\xi_1,2\pi-\xi_2) \qquad (66)$$

The radiation angle is given by

$$\cos \Theta = \hat{n} \cdot \hat{r} \qquad (67)$$

and the symbol T_1 is defined to be

$$T_1 = (\vec{\Omega} \times \hat{n}) \cdot (\vec{x} - \vec{y})/|\vec{x} - \vec{y}| \qquad (68)$$

In summary, equations (47) are expressed as double integrals in the variables ξ_1 and ξ_2. The equations are

$$\begin{aligned}
4\pi p_L'(\vec{x},t) = & -\frac{1}{c} \int_0^{\pi} \int_0^{1} \left[\frac{\Delta \dot{p} \cos \Theta + \Delta p\ T_1}{r(1 - M_r)^2} \right]_{\tau^*} J(\xi_1,\xi_2)\, d\xi_1\, d\xi_2 \\
& - \int_0^{\pi} \int_0^{1} \left[\frac{\Delta p(\cos \Theta - M_n)}{r^2\ (1 - M_r)^2} \right]_{\tau^*} J(\xi_1,\xi_2)\, d\xi_1\, d\xi_2 \\
& - \frac{1}{c} \int_0^{\pi} \int_0^{1} \left[\frac{\Delta p \cos \Theta\ (r\dot{M}_i \hat{r}_i + cM_r - cM^2)}{r^2\ (1 - M_r)^3} \right]_{\tau^*} J(\xi_1,\xi_2)\, d\xi_1\, d\xi_2
\end{aligned} \qquad (69)$$

and

$$4\pi p_T'(x,t) \overset{\rightarrow}{=} \int_0^{\pi} \int_0^{1} \left[\frac{2\bar{\rho}_0 v_n (r\dot{M}_i \hat{r}_i + cM_r + cM^2)}{r^2\ (1 - M_r)^3} \right]_{\tau^*} J(\xi_1,\xi_2)\, d\xi_1\, d\xi_2 \qquad (70)$$

where $J = \sqrt{EG - F^2}$, with E, G, and F having the definitions given by equations (50) to (51).

Compact Chord Approximation

In this section, approximation formulas based on the assumption of a line source are presented. The basis for the calculation procedure is the set of equations found in equations (32):

$$4\pi p'(\vec{x},t) = \int_{R_i}^{R_o} [F_L'(\vec{x},t,\xi_1) + F_T'(\vec{x},t,\xi_1)]\, d\xi_1 \qquad (71)$$

where

$$F_L'(\vec{x},t,\xi_1) = \frac{1}{cr(1 - M_r)^2} \left\{ \hat{r}_i \dot{L}_i' + \frac{\hat{r}_i L_i'}{(1 - M_r)} [\dot{M}_r + \frac{c}{r}(1 - M^2)] - \frac{c}{r} M_i L_i' \right\} \qquad (72)$$

and

$$F_T'(\vec{x},t,\xi_1) = \frac{\rho_o A(\xi_1)}{r(1 - M_r)^5} \left\{ (1 - M_r)(\ddot{M}_r - 3\frac{c}{r}\vec{M} \cdot \dot{\vec{M}}) + 3(\frac{c}{r}M_r)^2 + 3(\dot{M}_r - \frac{c}{r}M^2)^2 + \frac{c}{r}(\dot{M}_r - \frac{c}{r}M^2)(1 + 4M_r + M_r^2) \right\} \qquad (73)$$

In equation (71), the quantities $\vec{M}$, $\dot{\vec{M}}$, M_r, and r are computed as in equations (55) to (64) of the mean-surface approximation section. The leading-edge curve of the propeller is taken as the line source, so that all positions $\vec{r}$ are on the leading-edge curve. The quantity $A(\xi_1)$ is the cross-sectional area of a given blade section.

The key quantities to be calculated in equation (72) are $\vec{L}'$ and $d\vec{L}'/dt$, which represent the loading per unit length and its time rate of change. The loading per unit length is given by

$$\begin{bmatrix} L_1' \\ L_2' \\ L_3' \end{bmatrix} = \begin{bmatrix} \cos \Omega t \, F_\psi(\xi_1,t) \\ \sin \Omega t \, F_\psi(\xi_1,t) \\ -F_z(\xi_1,t) \end{bmatrix} \qquad (74)$$

where F_ψ and F_z are provided by the Propeller Loading Module. The time rate of change of $\vec{L}'$ becomes

$$\frac{d}{dt}\begin{bmatrix} L_1' \\ L_2' \\ L_3' \end{bmatrix} = \begin{bmatrix} -\Omega \sin \Omega t\, F_\psi + \cos \Omega t \dfrac{\partial F_\psi}{\partial t} \\ +\Omega \cos \Omega t\, F_\psi + \sin \Omega t \dfrac{\partial F_\psi}{\partial t} \\ -\dfrac{\partial F_z}{\partial t} \end{bmatrix} \tag{75}$$

The quantities $\partial F_\psi/\partial t$ and $\partial F_z/\partial t$ must be calculated as needed.

Point Source Approximation

In this section, approximation formulas based on the assumption of a single noise source representing each blade are presented. The basis for the calculation procedure is equations (30) and (31) which are

$$4\pi p_L'(\vec{x},t) = \left\{\frac{1}{cr(1 - M_r)^2}\left[\hat{r}_i\dot{L}_i + \frac{\hat{r}_i L_i}{(1 - M_r)}\left[\dot{M}_r + \frac{c}{r}(1 - M^2)\right] - \frac{c}{r}\, M_i L_i\right]\right\}\Bigg|_{\tau=\tau^*} \tag{76}$$

and

$$4\pi p_T'(\vec{x},t) = \left\{\frac{\rho_0 \Psi}{r(1 - M_r)^5}\left[(1 - M_r)\left(\ddot{M}_r - 3\frac{c}{r}\vec{M}\cdot\dot{\vec{M}}\right) + 3\left(\frac{c}{r}M_r\right)^2 + 3\left(\dot{M}_r - \frac{c}{r}M^2\right)^2 + \frac{c}{r}\left(\dot{M}_r - \frac{c}{r}M^2\right)(1 + 4M_r + M_r^2)\right]\right\}\Bigg|_{\tau=\tau^*} \tag{77}$$

The local quantities such as r, M, and M_r are evaluated at some effective radial distance, $\xi_1 = R_E$, usually about 0.8 of the propeller radius (appendix C). The effective blade load is given by

$$\begin{bmatrix} L_1 \\ L_2 \\ L_3 \end{bmatrix} = \begin{bmatrix} H \cos \Omega t \\ H \sin \Omega t \\ -T \end{bmatrix} \tag{78}$$

where H and T are the azimuthal force and net thrust from a single blade and are provided by the Propeller Loading Module. The time rate of change of $\vec{L}$ becomes

$$\begin{bmatrix} \dot{L}_1 \\ \dot{L}_2 \\ \dot{L}_3 \end{bmatrix} = \begin{bmatrix} -\Omega H \sin \Omega t + \dot{H} \cos \Omega t \\ +\Omega H \cos \Omega t + \dot{H} \sin \Omega t \\ -\dot{T} \end{bmatrix} \tag{79}$$

The quantities $\dot{H}$ and $\dot{T}$ must be calculated as needed. If it is assumed that the effective source point is located on the η_2-axis at the effective radius R_E, then the local Mach number at this point is given by

$$\begin{bmatrix} M_1 \\ M_2 \\ M_3 \end{bmatrix} = \frac{\Omega}{c} \begin{bmatrix} -\sin \Omega t & -\cos \Omega t & 0 \\ \cos \Omega t & -\sin \Omega t & 0 \\ 0 & 0 & 0 \end{bmatrix} \begin{bmatrix} 0 \\ R_E \\ 0 \end{bmatrix} + \begin{bmatrix} 0 \\ 0 \\ V_F/c \end{bmatrix} \tag{80}$$

The first and second time derivatives are

$$\begin{bmatrix} \dot{M}_1 \\ \dot{M}_2 \\ \dot{M}_3 \end{bmatrix} = \frac{\Omega^2}{c} \begin{bmatrix} -\cos \Omega t & \sin \Omega t & 0 \\ -\sin \Omega t & -\cos \Omega t & 0 \\ 0 & 0 & 0 \end{bmatrix} \begin{bmatrix} 0 \\ R_E \\ 0 \end{bmatrix} \tag{81}$$

and

$$\begin{bmatrix} \ddot{M}_1 \\ \ddot{M}_2 \\ \ddot{M}_3 \end{bmatrix} = \frac{\Omega^3}{c} \begin{bmatrix} \sin \Omega t & \cos \Omega t & 0 \\ -\cos \Omega t & \sin \Omega t & 0 \\ 0 & 0 & 0 \end{bmatrix} \begin{bmatrix} 0 \\ R_E \\ 0 \end{bmatrix} \tag{82}$$

The position of the source is

$$\begin{bmatrix} y_1 \\ y_2 \\ y_3 \end{bmatrix} = \begin{bmatrix} \cos \Omega t & -\sin \Omega t & 0 \\ \sin \Omega t & \cos \Omega t & 0 \\ 0 & 0 & 1 \end{bmatrix} \begin{bmatrix} 0 \\ R_E \\ 0 \end{bmatrix} + \begin{bmatrix} 0 \\ 0 \\ V_F t \end{bmatrix} \qquad (83)$$

and the unit vector in the radiation direction is given by the expression

$$\cdot \quad \hat{\vec{r}}(R_E) = \frac{\vec{x} - \vec{y}(R_E)}{\left|\vec{x} - \vec{y}(R_E)\right|} \qquad (84)$$

APPENDIX A

ACOUSTIC SPECTRUM CALCULATION

The acoustic spectrum is calculated from the amplitude of the complex coefficients of the Fourier series for $p_p'(\vec{x},t)$. A standard Fast Fourier Transform routine based on the Cooley-Tukey algorithm is used for this purpose.

Let N_s be the number of harmonics desired. Find m such that $2^{m-1} < 2N_s \leq 2^m$ and form the complex array:

$$Z_j = (p_p'(\vec{x},t_j),0) \qquad (j = 1, 2, \ldots, N_t-1) \tag{A1}$$

where

$$N_t = 2^m \qquad t_j = (2\pi j/N_t) \tag{A2}$$

Now find the inverse Fourier transform

$$C_k = \frac{1}{N_t} \sum_{j=0}^{N_t-1} Z_j e^{-2\pi ikj/N_t} \qquad (k = 0, 1, \ldots, N_t) \tag{A3}$$

The acoustic spectrum is given by

$$SPL_k = 10 \log (2|C_k|^2/p_{ref}^2) \qquad (k = 1, 2, \ldots, N_s) \tag{A4}$$

APPENDIX B

ROOTS OF RETARDED TIME EQUATION

The retarded time equation is written as

$$A\phi^2 + B\phi + C + \cos(\phi + D) = 0 \qquad \text{(B1)}$$

where only the root $(\phi/\Omega) < 0$ is of interest. Since both equation (B1) and its first derivative have an oscillating term, a close initial guess is required to ensure the convergence of Newton's method. This guess is accomplished by replacing the cosine term by a parabola and solving the resulting quadratic equation. Details are given as follows.

Step 1 - Bracket the root:

Figure B1 illustrates that the roots of equation (B1) are the intersection of a parabola and a cosine curve. As a first approximation to the root, find ϕ_1 such that

$$A\phi_1{}^2 + B\phi_1 + C = 0 \qquad (\phi_1 < 0) \qquad \text{(B2)}$$

Next determine which half-cycle of the cosine curve to replace by a quadratic.

Let

$$\ell = \left\{ \begin{array}{ll} \text{INT}\ [(\phi_1 + D)/\pi] & (\phi_1 + D) \geq 0) \\ \text{INT}\ [(\phi_1 + D)/\pi] - 1 & (\phi_1 + D) < 0) \end{array} \right\} \qquad \text{(B3)}$$

where ℓ is the integer half-cycle number and INT stands for the truncation integer function.

Step 2 - Determine initial guess:

The cosine term is replaced either by a straight line or by a parabola depending on whether ℓ is an even integer or an odd integer:

$$\cos(\phi + D) = \left\{ \begin{array}{ll} -\phi - D + (\ell + 1/2)\pi & (\ell \text{ even}) \\ 1 - 4[\phi + D + (\ell + 1)\pi]^2/\pi^2 & (\ell \text{ odd}) \end{array} \right\} \qquad \text{(B4)}$$

With this substitution, equation (B1) is solved by using the quadratic formula to give an initial guess ϕ_2.

Step 3 - Newton's method:

The roots of equation (B1) are determined through an iterative process,

$$\phi_{n+1} = \phi_n - \frac{\left[A\phi_n^2 + B\phi_n + C + \cos(\phi_n + D)\right]}{\left[2A\phi_n + B - \sin(\phi_n + D)\right]} \tag{B5}$$

which terminates when $\left|\phi_{n+1} - \phi_n\right|$ is smaller than a user-specified convergence criterion or if the number of iterations exceeds a limit set by the user.

Step 4 - Return answer:

If $(\phi_{n+1}/\Omega) > 0$ or if ϕ_{n+1} substituted in equation (B1) does not return a value less in magnitude than a user-specified tolerance, then an error condition results; otherwise, $\phi_{n+1} = \Omega(\tau^* - t)$.

Note that the retarded time equation is solved for one source point at many receiver times. Thus, ϕ_{n+1} may be a close initial guess to the next required root. In this case, Steps 1 and 2 are omitted.

APPENDIX C

EFFECTIVE POINT SOURCE RADIUS

Let T be the net thrust for a single blade located at radius R_T and H the net inplane force located at R_H (fig. C1). A resultant force F_E and corresponding effective radius R_E are calculated based on the concepts of equivalent forces and moments.

An expression for the equivalent force $\vec{F}_E$ is

$$\vec{F}_E = \vec{T} + \vec{H} \tag{C1}$$

Since $\vec{T}$ and $\vec{H}$ are orthogonal, the magnitude of $\vec{F}_E$ is

$$F_E = \left|\vec{F}_E\right| = (T^2 + H^2)^{1/2} \tag{C2}$$

The magnitude of the total moment supplied by $\vec{T}$ and $\vec{H}$ is given by

$$M = \left|\vec{M}\right| = (T^2R_T^2 + H^2R_H{}^2)^{1/2} \tag{C3}$$

On the other hand, the magnitude of the moment due to F_E acting at distance R_E is

$$M = R_EF_E \tag{C4}$$

Equating the two moment expressions,

$$R_EF_E = (T^2R_T^2 + H^2\,R_H^2)^{1/2} \tag{C5}$$

or

$$R_E = (T^2R_T{}^2 + H^2\,R_H{}^2)^{1/2} / F_E \tag{C6}$$

Using equation (C2),

$$R_E = (T^2R_T^2 + H^2R_H^2)^{1/2} / (T^2 + H^2)^{1/2} \tag{C7}$$

or in terms of dimensionless quantities

$$\xi_E = \left(T^2\xi_T^2 + H^2\ \xi_Q^2\right)^{1/2} \Big/ \left(T^2 + H^2\right)^{1/2} \tag{C8}$$

Equation (C8) represents the effective radius value used by the Subsonic Propeller Noise Module.

REFERENCES

1. Ffowcs Williams, J. E.; and Hawkings, D. L.: Sound Generation by Turbulence and Surfaces in Arbitrary Motion. Philos. Trans. R. Soc. London, ser. A, vol. 264, no. 1151, May 8, 1969, pp. 321-342.

2. Farassat, F.: Theory of Noise Generation From Moving Bodies With an Application to Helicopter Rotors. NASA TR-451, 1975.

3. Farassat, F.: Linear Acoustic Formulas for Calculation of Rotating Blade Noise. AIAA J., vol. 19, no. 9, Sept. 1981, pp. 1122-1130.

4. Nystrom, Paul A.; and Farassat, F.: A Numerical Technique for Calculation of the Noise of High-Speed Propellers With Advanced Blade Geometry. NASA TP-1662, 1980.

5. Woan, C. J.; and Gregorek, G. M.: The Exact Numerical Calculation of Propeller Noise. AIAA Paper 78-1122, July 1978.

6. Lowson, M. V.: The Sound Field for Singularities in Motion. Proc. R. Soc. London, ser. A, vol. 286, no. 1407, Aug. 1965, pp. 559-572.

7. Succi, George P.: Design of Quiet Efficient Propellers. SAE Tech. Paper Ser. 790584, Apr. 1979.

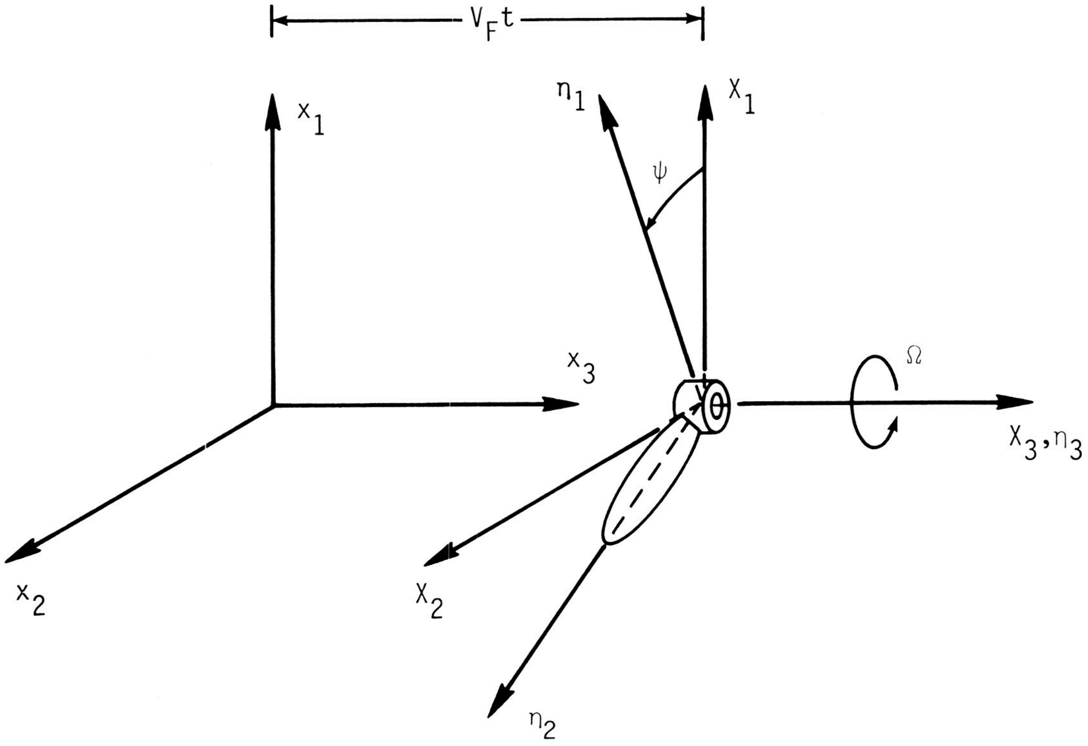

Figure 1.- Transformation of coordinates.

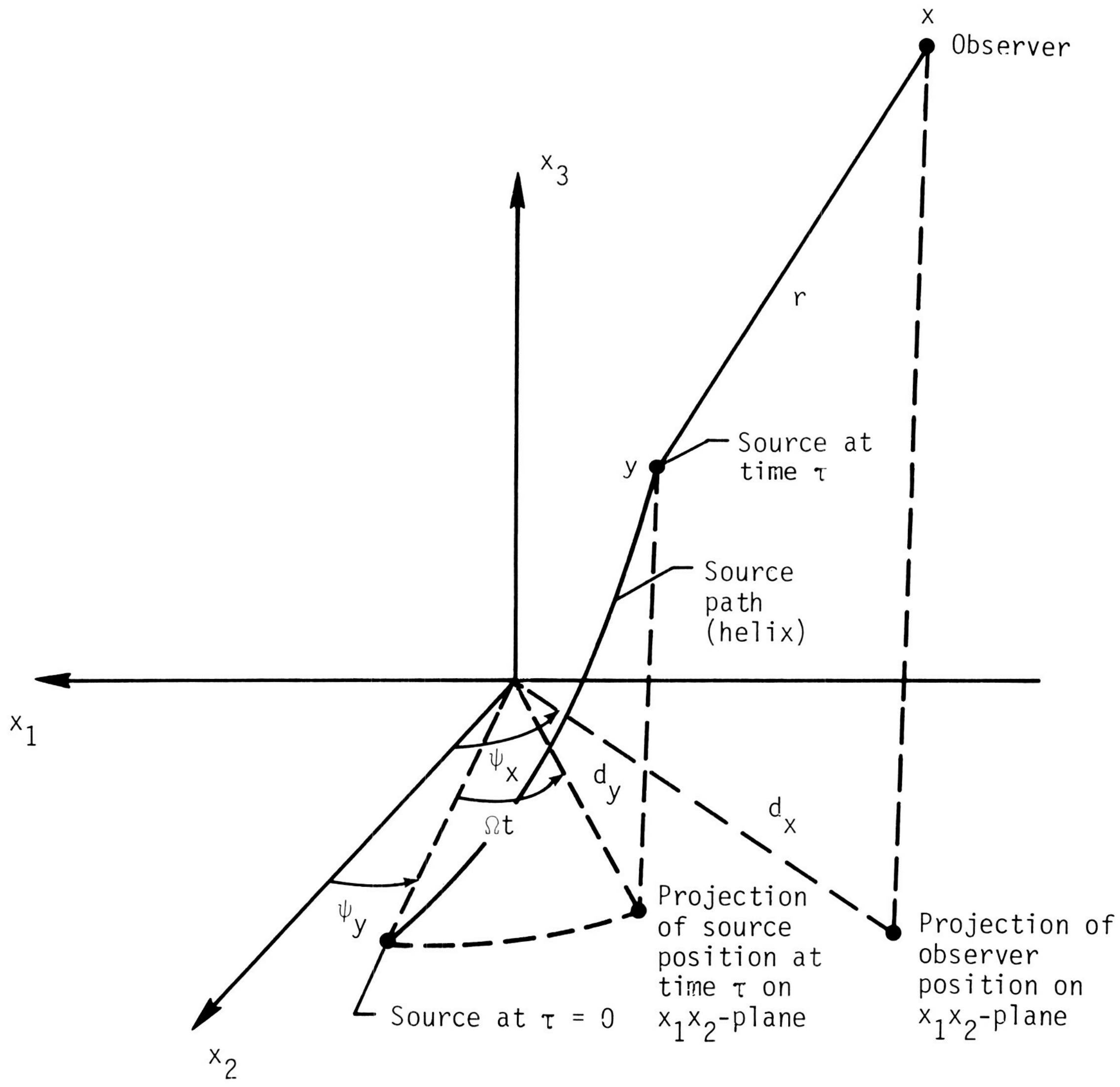

Figure 2.- Geometry of source and observer position used for calculation of emission time.

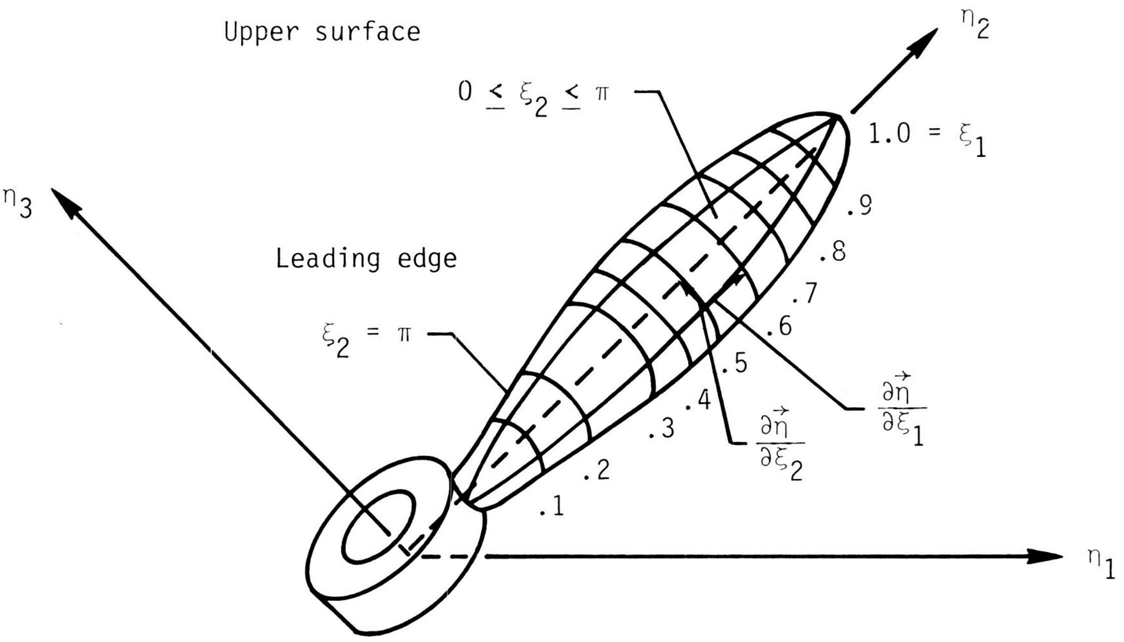

Figure 3.- Blade surface coordinate system.

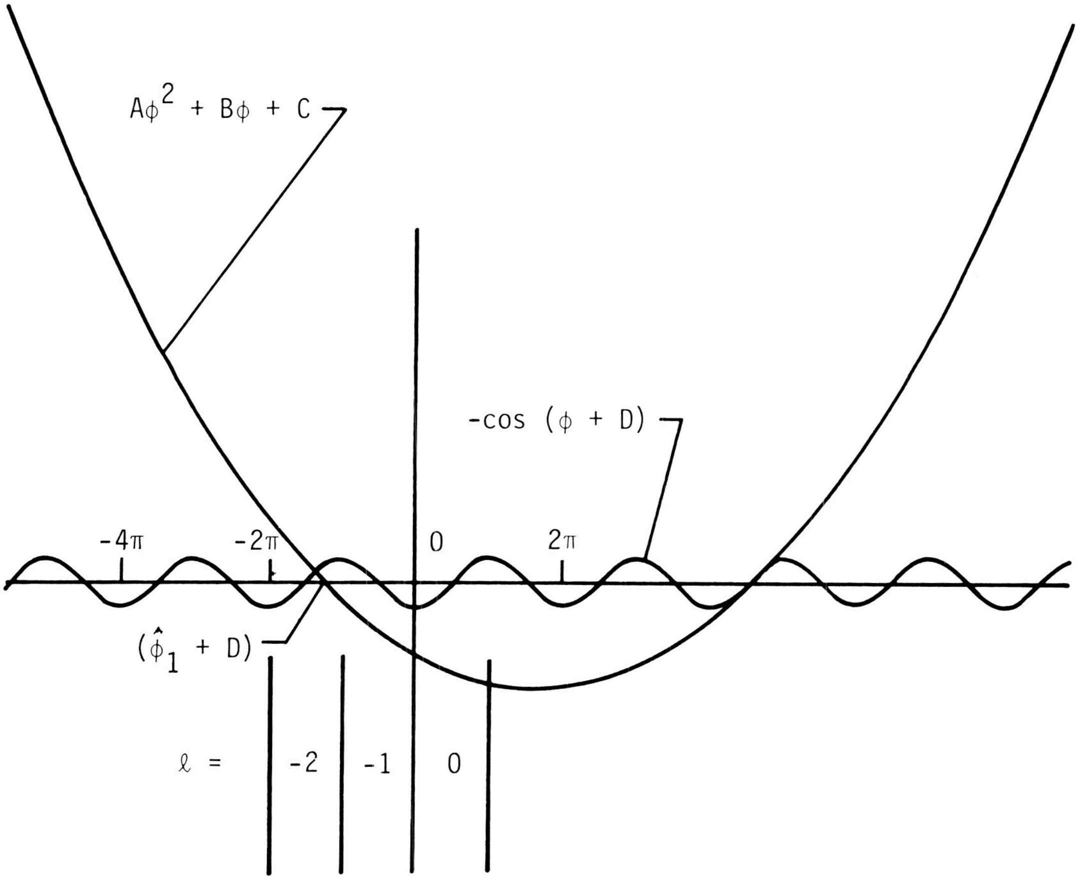

Figure A1.- Roots of the retarded time equation.

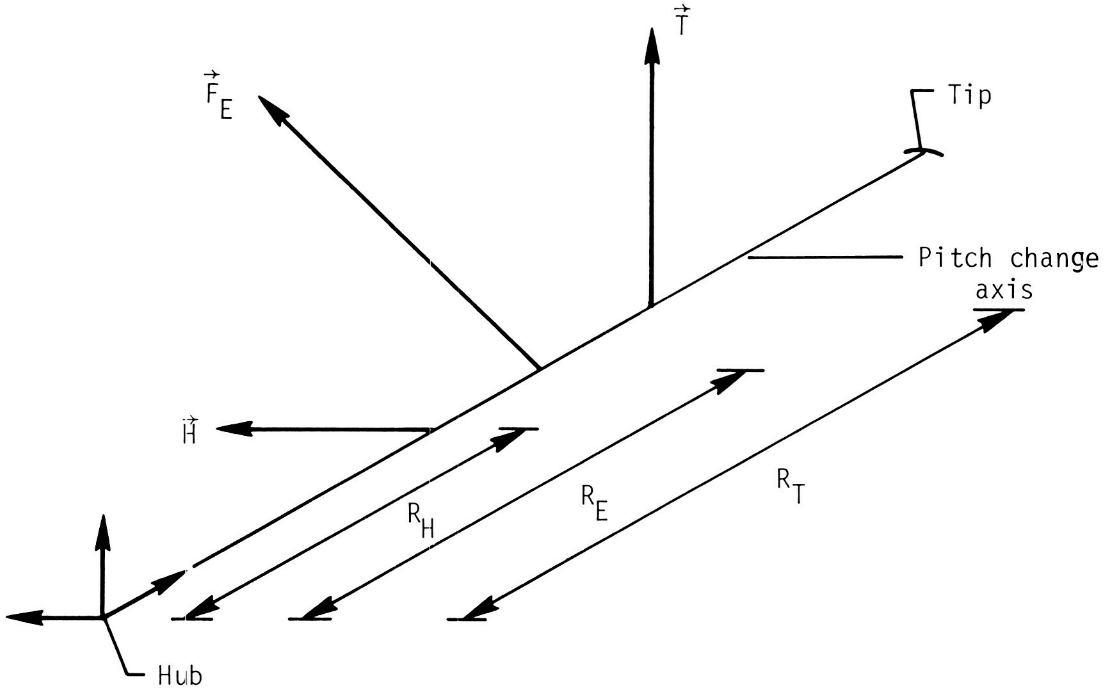

Figure C1.- Relationships of effective forces on a single blade.

11.2 TRANSONIC PROPELLER NOISE MODULE

Sharon L. Padula
Langley Research Center

INTRODUCTION

The Transonic Propeller Noise Module computes the periodic acoustic pressure signature and spectrum of a propeller with transonic tip speed. The computation is based on a solution of the Ffowcs Williams-Hawkings (FW-H) equation without the quadrupole source term. (See refs. 1 to 3.) The blade surface pressure is assumed to be steady and must be specified on a grid of points covering the blade surface. The observer is always assumed to be moving with the aircraft; only in such a frame is the acoustic pressure periodic. The solution to the FW-H equation is given by two different formulations that assume a source distribution on the full blade surface. The formulation that is suitable for blade sections moving at transonic speeds is used only when necessary.

SYMBOLS

c	ambient speed of sound, m/s (ft/s)
f	function defining blade surface S
g	= 0 (describes relationship between source and observer time)
k	harmonic number
$\vec{\ell}$	local force per unit area of blade acting on fluid, Pa (lbf/ft^2)
M	source Mach number
N_b	number of blades
N_s	maximum harmonic number of interest
N_t	number of time points in time history
n	blade-surface normal vector
p	surface pressure, $p_a - p_0$, Pa (lbf/ft^2)

p'	acoustic pressure, Pa ($\mathrm{lbf/ft^2}$)
p'_L	acoustic pressure produced by loading, Pa ($\mathrm{lbf/ft^2}$)
p'_P	total acoustic pressure produced by propeller, Pa ($\mathrm{lbf/ft^2}$)
p'_T	acoustic pressure produced by thickness, Pa ($\mathrm{lbf/ft^2}$)
p_a	absolute surface pressure, Pa ($\mathrm{lbf/ft^2}$)
p_0	ambient pressure, Pa ($\mathrm{lbf/ft^2}$)
p_{ref}	reference pressure for definition of decibels, 2×10^{-5} Pa
r	distances from source point at emission time to observer, $r = \lvert\vec{x} - \vec{y}\,(\tau^*)\rvert$, m (ft)
SPL	sound pressure level with respect to p_{ref}, dB
t	time at which noise signal is received by observer, s
V_F	forward velocity of aircraft, m/s (ft/s)
v	source velocity, m/s (ft/s)
X	observer position in aircraft-fixed frame, m (ft)
x	observer position in ground-fixed frame, m (ft)
y	source position in ground-fixed frame, m (ft)
Γ	locus of points associated with emission time τ
η	source position in blade-fixed frame, m (ft)
θ	angle between radiation vector and surface normal vector, rad
θ_0	pitch change angle at root, rad
ξ_1, ξ_2	elliptic surface coordinates
ρ_0	ambient density, $\mathrm{kg/m^3}$ ($\mathrm{slug/ft^3}$)

τ	time at which noise signal is emitted at source position, s
τ^*	solution to retarded time equation, $g = 0$, for a given observer time, s
ϕ	solution to retarded time equation as solved by Newton's method, $\Omega(\tau - t)$
ψ	angle between aircraft-fixed x_1-axis and blade-fixed η_1-axis, rad
Ω	angular velocity of blade, rad/s

Subscripts:

i	component along ith coordinate axis (note: $\ell_i \hat{r}_i$ implies summation convention)
n	component in direction of surface normal
0	ambient condition
r	component in direction of radiation vector

Notation:

$\rightarrow$	vector
$\hat{}$	unit vector
$\cdot$	time derivative
$*$	complex conjugate; specific solution to retarded time equation

INPUT

The computation of transonic propeller noise requires definition of the blade shape characteristics, aerodynamic characteristics, flow and operating parameters, and observer coordinates. The noise signature is calculated by using two different full-blade formulations, depending on the radiation Mach number of the blade section. The input is consistent with that for the Subsonic Propeller Noise Module, and the two modules will give identical results for subsonic cases.

User Parameters

N_b	number of blades
N_s	highest harmonic number desired
N_t	number of time points in time history
M_z	aircraft Mach number
R	blade length measured from axis to tip, m (ft)
θ_0	pitch change angle at root, rad
ψ_0	initial azimuth angle of first blade, rad
Ω	angular velocity of blade, rad/s

Blade Shape Table

ξ_1	spanwise location, re R
ξ_2	chordwise location, rad
$\eta_1(\xi_1,\xi_2)$	blade surface abscissa, re R
$\eta_3(\xi_1,\xi_2)$	blade surface ordinate, re R
Φ_1,Φ_2	slopes of basis functions at nodes

Aerodynamic Characteristics Table

ξ_1	spanwise location, re R
ξ_2	chordwise location, rad
ψ	azimuth location, rad
$p(\xi_1,\xi_2,\psi=0)$	pressure loading, re $\rho_0(R\Omega)^2$

Observer Table

$\vec{x}$	initial observer position, m (ft)

Atmospheric Properties Table

ρ_0	ambient fluid density, kg/m^3 ($slugs/ft^3$)
c	local sound speed, m/s (ft/s)

OUTPUT

This module provides the complex pressure spectrum and pressure time history at a fixed observer location measured from the center of the hub. Complex pressures are given with the $e^{-i\Omega t}$ time harmonic convention, and all spectra are understood to be two-sided with $p_p'(x,-k) = p_p'^*(x,k)$. With this convention, the mean-squared pressure is $2p_p'p_p'^*$ (where the square root of $2\, p_p'p_p'^*$ is p_{rms}') for each harmonic.

Complex Pressure Spectrum

k	harmonic number
f_k	frequency, Hz
$C_k(\vec{x})$	complex acoustic pressure, re $\rho_0(R\Omega)^2$
$SPL_k(\vec{x})$	sound pressure level associated with $C_k(\vec{x})$

Pressure Time History

t	time, s
$p_p'(\vec{x},t)$	acoustic pressure, re p_{rms}

METHOD

Acoustic Formulation

The equation used to calculate the acoustic pressure time signature of a high-speed propeller (see ref. 4), derived in the Subsonic Propeller Noise Module, is

$$4\pi p'(\vec{x},t) = \frac{1}{c}\frac{\partial}{\partial t}\int_{f=0}\left[\frac{\rho_0 c v_n + \ell_r}{r\left|1 - M_r\right|}\right]_{\tau^*} dS + \int_{f=0}\left[\frac{\ell_r}{r^2\left|1 - M_r\right|}\right]_{\tau^*} dS \quad (1)$$

Equation (1) contains a potentially singular term, $|1 - M_r|$, in the denominator. As long as each point on the blade moves subsonically in the direction of the observer, the solution behaves nicely. In this case, equation (1) can be written in the following computationally efficient form:

$$4\pi p'_L(\vec{x},t) = \frac{1}{c}\int_{f=0}\left[\frac{\dot{\ell}_i\,\hat{r}_i}{r(1 - M_r)^2}\right]_{\tau^*} dS + \int_{f=0}\left[\frac{\ell_r - \ell_i M_i}{r^2(1-M_r)^2}\right]_{\tau^*} dS$$

$$+\frac{1}{c}\int_{f=0}\left[\frac{\ell_r\,(r\dot{M}_i\hat{r}_i + cM_r - cM^2)}{r^2(1 - M_r)^3}\right]_{\tau^*} dS \qquad (2a)$$

$$4\pi p'_T(\vec{x},t) = \int_{f=0}\left[\frac{\rho_0 v_n(r\dot{M}_i\hat{r}_i + cM_r - cM^2)}{r^2(1 - M_r)^3}\right]_{\tau^*} dS \qquad (2b)$$

and

$$p'(\vec{x},t) = p'_L(\vec{x},t) + p'_T(\vec{x},t) \qquad (2c)$$

where p'_L and p'_T denote the loading and thickness noise, respectively. The symbols M_i, $\dot{M}_i$, ℓ_i, and $\dot{\ell}_i$ are defined as follows:

$$M_i = v_i/c \qquad (3)$$

$$\dot{M}_i = \dot{v}_i/c \qquad (4)$$

$$\ell_i = p\hat{n}_i \qquad (5)$$

$$\dot{\ell}_i = \dot{p}\hat{n}_i + p\hat{n}_i \qquad (6)$$

where

$$\hat{n}_i = (\vec{\Omega} \times \hat{n})_i \qquad (7)$$

When the radiation Mach number approaches or exceeds unity for a given point on the blade at a given time, then the following equation is used in place of equations (2):

$$4\pi\, p'_L(\vec{x},t) = \frac{\partial}{\partial t}\int_{\substack{f=0\\g=0}} \frac{\ell_r}{r\sin\Theta}\, d\Gamma\, d\tau + \int_{\substack{f=0\\g=0}} \frac{c\ell_r}{r^2\sin\Theta}\, d\Gamma\, d\tau \qquad (8a)$$

$$4\pi\, p'_T(x,t) = \frac{\partial}{\partial t}\int \frac{\rho_0 c v_n}{r\sin\Theta}\, d\Gamma\, d\tau \qquad (8b)$$

$$p'_P(\vec{x},t) = p'_L(\vec{x},t) + p'_T(\vec{x},t) \qquad (8c)$$

where Θ is the angle between the blade normal $\vec{n}$ and the radiation vector $\vec{r}$. The symbol Γ is used to denote the locus of points on the blade that are at a distance r from the observer at emission time τ. In other words, Γ is the curve of the intersection of the surfaces $f = 0$ and $g = \tau - t + (r/c) = 0$.

The Transonic Propeller Noise Module uses equations (2) and (8) to calculate $p'(\vec{x},t)$. Equations (2) are used whenever possible because the computer implementation is simple and efficient. A thorough discussion of these and other acoustic formulas for calculating propeller noise is contained in reference 3.

Frames of Reference

In this section the coordinate frames used in the acoustic calculations will be discussed. Basically, there are two reference frames: the ground-fixed $\vec{x}$-frame and the blade-fixed $\vec{\eta}$-frame. The $\vec{x}$-frame, which remains fixed to the undisturbed medium, is set up as follows:

The origin of this frame is at the propeller center at time $t = 0$.

The propeller disk is in the x_1x_2-plane and the x_2-axis coincides with the propeller axis, with the positive direction in the flight direction.

The x_1-axis is assumed to be orthogonal to x_3, upward and parallel to the plane of symmetry of the aircraft.

The x_2-axis is defined in such a way that the $\vec{x}$-frame is right-handed.

The observer position is always specified in this frame as will be explained shortly.

The blade-fixed frame is set up as follows:

The origin coincides with the origin of the $\vec{x}$-frame at $t = 0$.

The η_3-axis coincides with the x_3-axis.

The η_2-axis lies on the pitch change axis of the blade.

The $\eta_1\eta_2$-plane is normal to the propeller shaft.

The η_1-axis is defined to make the $\vec{\eta}$-frame right-handed.

Note that the blade mean surface does not lie in the $\eta_1\eta_2$-plane but makes an angle equal to the geometric pitch angle at each radial position. Note also that the $\vec{\eta}$-frame rotates with angular velocity Ω.

In the acoustic formulas presented in the previous section, many operations involving dot products or cross products of two vectors are required. When the products involve blade normals or surface pressures, it is convenient to transform the components of these vectors to the $\vec{\eta}$-frame and then perform the operation. However, note that the source position $\vec{y}$ always refers to a source point in the $\vec{x}$-frame with a known position $\vec{\eta}$ in the blade-fixed frame. The quantities $\vec{r} = \vec{x} - \vec{y}$ and $\hat{r} = \vec{r}/r$ are calculated in the $\vec{x}$-frame, and then the vector components are calculated in the $\vec{\eta}$-frame. Note that for any variable that has a velocity term, such as $M_r = M_i \hat{r}_i$ and $v_n = \vec{v} \cdot \hat{n}$, the velocity is with respect to the $\vec{x}$-frame. In other words,

$$v_i = \frac{\partial y_i}{\partial \tau} \tag{9}$$

The components of this vector must then be calculated in the $\vec{\eta}$-frame to get M_r and v_n.

Another frame of reference that is used conceptually is the aircraft-fixed, nonrotating $\vec{X}$-frame. This frame coincides with the ground-fixed $\vec{x}$-frame at $t = 0$. The acoustic pressure $p'(\vec{X},t)$ for an observer in the aircraft-fixed frame with the position vector $\vec{X}$ is found as follows: Since both $\vec{X}$ and t are known, the relative position of the ground-fixed frame and the aircraft-fixed frame is known. From this, calculate the observer position $\vec{x}$ in the ground-fixed frame. Using this $\vec{x}$ and t, calculate $p'(\vec{x},t)$, which is the same as the acoustic pressure at position $\vec{X}$ in the aircraft-fixed frame and at time t. Thus, the $\vec{X}$-frame itself is never used in acoustic calculations, even though the pressure signal that results is $p'(\vec{X},t)$.

The transformation from one frame to the other at time t can be written in matrix notation as

$$\begin{bmatrix} X_1 \\ X_2 \\ X_3 \end{bmatrix} = \begin{bmatrix} \cos\psi & -\sin\psi & 0 \\ \sin\psi & \cos\psi & 0 \\ 0 & 0 & 1 \end{bmatrix} \begin{bmatrix} \eta_1 \\ \eta_2 \\ \eta_3 \end{bmatrix} \tag{10a}$$

$$\begin{bmatrix} x_1 \\ x_2 \\ x_3 \end{bmatrix} = \begin{bmatrix} X_1 \\ X_2 \\ X_3 \end{bmatrix} + \begin{bmatrix} 0 \\ 0 \\ V_F t \end{bmatrix} \tag{10b}$$

where (η_1,η_2,η_3) is a point in the rotating $\vec{\eta}$-frame, (X_1,X_2,X_3) is the corresponding point in the moving $\vec{X}$-frame, (x_1,x_2,x_3), is the corresponding point in the ground-fixed frame, and ψ (where $\psi = \Omega t$) is the angle between the X_1- and η_1-axes.

A final coordinate transformation is necessary to account for changes in the root pitch setting. This rotation through a small angle θ_0, is applied to the blade surface coordinates that are calculated by the Blade Shape Module. Thus,

$$\vec{\eta}(\xi_1,\xi_2) = \begin{bmatrix} \cos\theta_0 & 0 & \sin\theta_0 \\ 0 & 1 & 0 \\ -\sin\theta_0 & 0 & \cos\theta_0 \end{bmatrix} \begin{bmatrix} \eta_1'(\xi_1,\xi_2) \\ \xi_1 \\ \eta_2'(\xi_1,\xi_2) \end{bmatrix} \tag{11}$$

Whenever the $\vec{\eta}$-frame or pitch-axis coordinate system is mentioned herein, it is assumed that the previously given corrective transformation has occurred. Often the Blade Shape Module and Transonic Propeller Noise Module will be executed without change to the collective pitch setting. Thus, $\theta_0 = 0$ and the last transformation is unnecessary.

Computational Strategy

Three elements that influence the computational strategy for noise prediction are numerical accuracy, computational efficiency, and conceptual simplicity. The trade-offs are never straightforward, but the simplest method that gives numerically stable answers in a reasonable amount of computer time is desired. A good balance is particularly crucial to the Transonic Propeller Noise Module. Moreover, it is important that the transonic and subsonic propeller noise methods give identical results for propellers with subsonic Mach numbers. These objectives guide the computational strategy.

The first step in computing an acoustic pressure time history is to discretize one full revolution of the blade into even time increments t_i and to represent the blade by a set of source points $\vec{n}(j)$. Even though the tip of the blade is moving supersonically, some portion of the blade is subsonic. It will be helpful to define a subset of source points $\vec{n}_s$ that move subsonically. That is,

$$\vec{n}_s = \left\{ (n_1, n_2, n_3) : \frac{(\Omega n_2)^2 + V_f^2}{c^2} < 1.0 \right\} \qquad (12)$$

For each time point, the noise produced by the part of the blade represented by $\vec{n}_s$ can be calculated by using equations (2). The numerical evaluation of equations (2) is discussed in detail in the Subsonic Propeller Noise Module. The noise produced by the supersonic tip of the blade is calculated by either equations (2) or equations (8), depending on the value of M_r for each source point. If M_r exceeds some transitional value (usually 0.98) for any source point, then equations (8) are used for the entire supersonic tip at that time. In practice, equations (8) are used for less than one-fourth of the time points even in the worst case.

Equations (8) are evaluated by dividing the blade tip into panels and by defining a set of possible emission times $\{\tau_j\}$. Each integral $\iint[\,]\, d\Gamma\, d\tau$ is approximated by applying a one-dimensional trapezoidal rule for a fixed τ_j and then applying another one-dimensional trapezoidal rule as τ_j varies. The partial derivative with respect to source time t is approximated by using a central difference formula after the integral over the supersonic tip has been calculated at times $(t_i + \Delta t)$ and $(t_i - \Delta t)$.

The execution time required to compute equations (8) is greatly influenced by the set of emission times τ_j that are chosen. If the span of all possible emission times is divided evenly, a very large number of times will be required. A better plan is to determine one, two, or three time intervals during which the Γ curve intersects the current panel. Each of these intervals can then be divided evenly. The time intervals themselves can be determined by solving the retarded time equation at the four corners of the panel. This gives at least 4, and at most 12, times τ_j^* at which the Γ curve is touching a single point on the panel. The time interval $[\tau_j^*, \tau_j^*+1]$ will contribute to the integral over the current panel if the Γ curve is inside the panel during that time. It is sufficient to test the location of the curve at the median time $(\tau_j^* + \tau_j^*+1)/2$. If the distance from the observer to the Γ curve is in the same range as the distance from the observer to each of the four corners of the panel, then the time interval will contribute.

There are several sources of error in this prediction method that the user must understand. The most important involves the geometric model of the blade. The blade position vectors $\vec{\eta}$ and normal vectors $\vec{n}$ describe the blade shape very smoothly and accurately. Each panel of the supersonic tip is actually a curved surface. However, since the trapezoidal rule is used to approximate the integrals and since linear interpolation is used to calculate the integrands at points along the edges of the panel, computationally the curved panel is replaced by a flat plate. **It is very important that the user supply a grid that has a large number of nodes in those regions where the blade is highly curved.** One good way to accomplish this is to use the same chordwise grid that was used for the Blade Shape Module but add extra points near the leading edge. It may be necessary to add extra spanwise grid points as well. It is wise to have at least five spanwise grid points in the subsonic region and five in the supersonic tip. Finally, the user must take care to specify enough time points N_t to represent the pressure time history accurately. Unfortunately, the computation time will increase dramatically as the number of time points and grid points increases.

The Retarded Time Equation

As discussed in the Subsonic Propeller Noise Module, The retarded time equation can be written in the form

$$f(\phi) = A\phi^2 + B\phi + C + \cos(\phi + D) = 0 \tag{13}$$

where only the roots $(\phi/\Omega) < 0$ are of interest. Figure 1 is a typical graph of the retarded time equation that often results when the source points are moving at close to sonic speeds. It is not clear from the figure whether this graph has one or more negative roots. In order to solve numerically for the roots using Newton's method, the number and approximate location of the roots must be determined.

Notice that equation (13) could be easily solved if the cosine term were absent. The first step in finding approximate roots is to set $\cos(\phi + D) = -1$ and solve for the negative root ϕ_0. The location of the actual roots must be in the interval $[\phi_0,0]$ because the cosine term cannot have a value smaller than -1. Next, approximate the cosine curve by a parabola that has the same minimum point and the same intercepts, and then solve again. The resulting approximate retarded time equation may have one, two, or no real roots in the interval $[\phi_0,0]$. If there is only one root to the approximate equation, then it is a good initial guess to the one negative root of equation (13). If there are no real roots to the approximate equation, then ϕ_0 will be a good initial guess to the one root of equation (13). If, however, there are two roots to the approximate equation, then the situation must be further clarified.

Figure 2 is an exploded view of the graph in figure 1. Note that there are three roots in this particular case. The best way to find them is to find first the local minimum and maximum points on the curve. That is, solve

$$\frac{df}{d\phi} = 2A\phi + B - \sin(\phi + D) = 0 \qquad (14)$$

Approximate solutions, ϕ_1 and ϕ_2, to equation (14) are adequate. If $f(\phi_1)$ and $f(\phi_2)$ have opposite signs, then there is a root of f between them. Similarly, if $f(\phi_0)$ and $f(\phi_1)$ have opposite signs, then a root exists between them. If it is determined that three roots exist, then $(\phi_0 + \phi_1)/2$, $(\phi_1 + \phi_2)/2$, and $\phi_2/2$ will be very good initial guesses for use by Newton's method.

REFERENCES

1. Ffowcs Williams, J. E.; and Hawkings, D. L.: Sound Generation by Turbulence and Surfaces in Arbitrary Motion. Philos. Trans. R. Soc. London, ser. A, vol. 264, no. 1151, May 8, 1969, pp. 321-342.

2. Farassat, F.: Theory of Noise Generation From Moving Bodies With an Application to Helicopter Rotors. NASA TR R-451, 1975.

3. Farassat, F.: Linear Acoustic Formulas for Calculation of Rotating Blade Noise. AIAA J., vol. 19, no. 9, Sept. 1981, pp. 1122-1130.

4. Nystrom, Paul A.; and Farassat, F.: A Numerical Technique for Calculation of the Noise of High-Speed Propellers With Advanced Blade Geometry. NASA TP-1662, 1980.

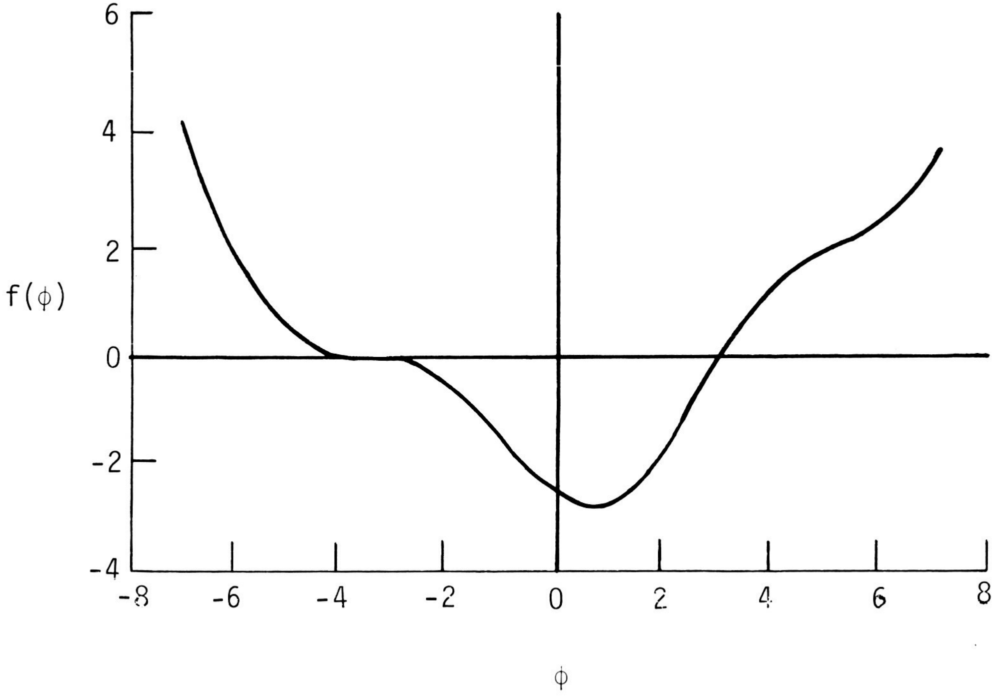

Figure 1.- Typical transonic retarded time equation.

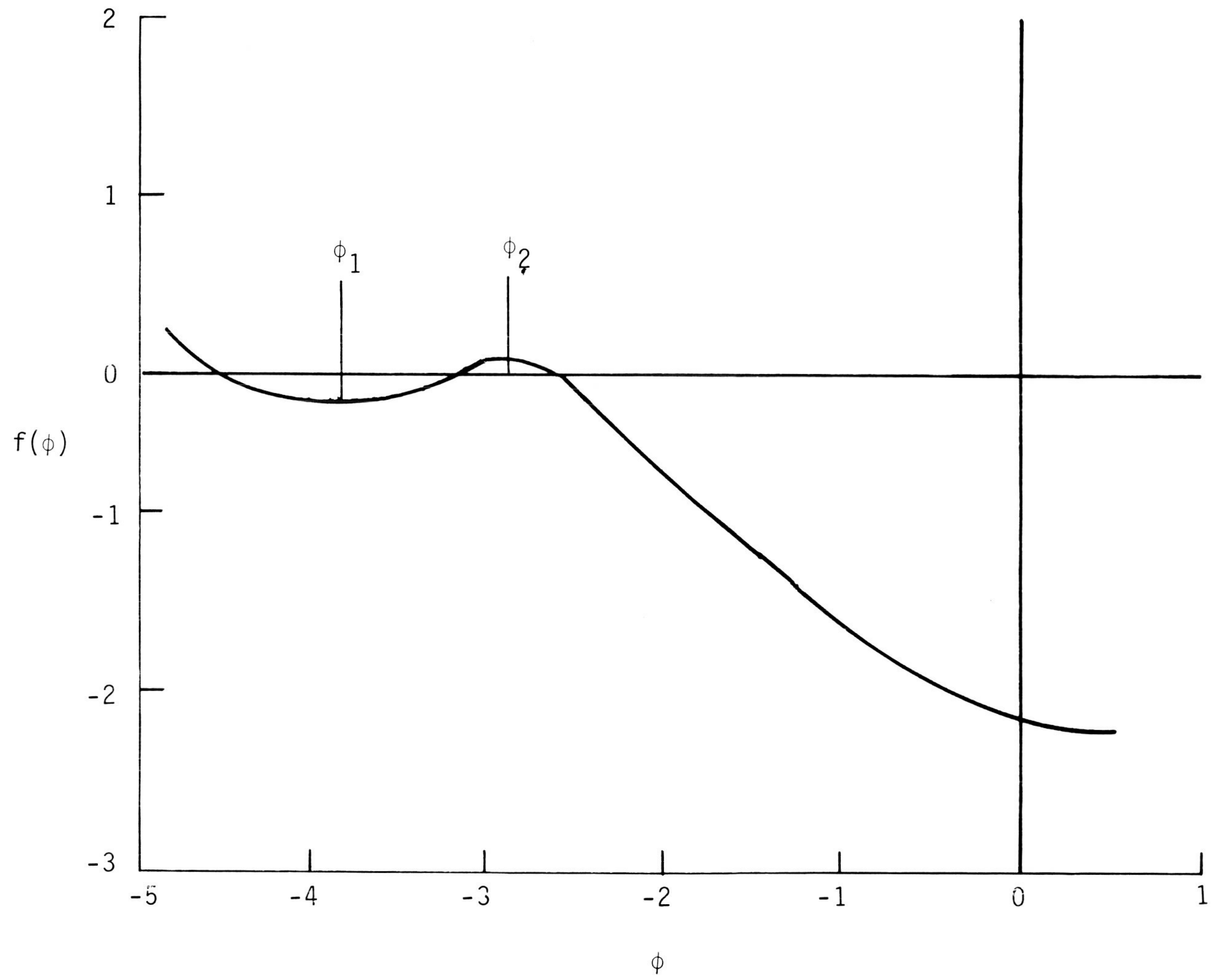

Figure 2.- Exploded view of transonic retarded time equation.

11.3 PROPELLER TRAILING-EDGE NOISE MODULE

Donald S. Weir
PRC Kentron, Inc.

INTRODUCTION

This module computes the trailing-edge noise produced by a propeller based on the method developed by Schlinker and Amiet (ref. 1). The propeller geometry and flow characteristics are provided by the Blade Shape Module, the Blade Section Boundary-Layer Module, and the Propeller Performance Module. The observer is assumed to be moving with the aircraft, and the propeller is modeled as a noncompact source. The module produces a 1/3-octave-band spectrum due to the broadband noise source at each observer position.

SYMBOLS

b	blade section semichord, m (ft)
C	blade chord length, re R
c_∞	ambient speed of sound, m/s (ft/s)
D	directivity function
E^*	combination of Fresnel integrals
F	spectrum function
f	frequency, Hz
g_r	acceleration due to gravity, m/s^2 (ft/s^2)
k_x	wave number, ω/U, m^{-1} (ft^{-1})
L	chordwise integral of surface loading
ℓ_y	turbulence correlation length, m (ft)
M	Mach number
$\vec{M}_f$	Mach number of airfoil section relative to fluid
M_o	reference Mach number

$\vec{M}_f$	Mach number of airfoil section relative to fluid
M_o	reference Mach number
$\vec{M}_r$	Mach number of airfoil section relative to observer
m	molecular weight of air
N	number of points
N_b	number of blades
$N_{\xi 1}$	number of spanwise stations
$\langle p^2 \rangle$	mean-square acoustic pressure, Pa^2 (lb^2/ft^4)
R	blade length, m (ft)
R_a	gas constant for air, $m^2/K\text{-}s^2$ ($ft^2/°R\text{-}s^2$)
r	magnitude of $\vec{r}$
$\vec{r}$	position vector, m (ft)
S	surface pressure spectrum, Pa^2-s ($lb^2\text{-}s/ft^4$)
S_t	Strouhal number, $f_{1/3}\delta/U$
s	span of airfoil segment, m (ft)
T_r	standard sea level temperature, K (°R)
t	time, s
U	velocity, m/s (ft/s)
X,Y,Z	coordinates of $\vec{X}$
$\vec{X}$	nonrotating coordinate system fixed to propeller hub, m (ft)
x,y,z	coordinates of $\vec{x}$
$\vec{x}$	coordinate system fixed to blade trailing edge, m (ft)

β	compressibility factor, $(1 - M^2)^{1/2}$
δ	boundary-layer thickness, m (ft)
δ^*	boundary-layer displacement thickness, m (ft)
ζ_0	$= \mu(x^2 + \beta^2 z^2)^{1/2}/\sigma$
η_1, η_2, η_3	coordinates of $\vec{\eta}$
$\vec{\eta}$	rotating coordinate system centered on propeller hub, m (ft)
Θ	$= \bar{\lambda} + \bar{\mu}\,(M - x/\sigma)$
θ	polar directivity angle, deg
θ_0	root pitch angle, rad
θ_T	blade twist angle, rad
λ	wave number, ω/U_c
μ	$= Mk_x/\beta^2$
ξ_1	spanwise position, re R
ρ_∞	ambient density, kg/m^3 (slug/ft^3)
σ	$= [x^2 + \beta^2(y^2 + z^2)]^{1/2}$
ϕ	azimuthal directivity angle, deg
ψ	blade rotation angle, rad
Ω	blade angular rotation frequency, rad/s
ω	angular frequency, rad/s
$\tilde{\omega}$	Strouhal number, $\omega\delta^*/U$

Subscripts:

b	blade
c	convection
e	emission time
f	due to M. R. Fink

h	high-frequency approximation
ℓ	low-frequency approximation
o	observer
t	trailing edge
1/3	1/3-octave-band value

Notation:

—	normalized
^	unit vector
'	modified

INPUT

The computation of propeller trailing-edge noise requires knowledge of the blade shape characteristics, flow and operating characteristics, boundary-layer thickness, and observer geometry. The blade shape characteristics can be computed by the Blade Shape Module, the boundary-layer thickness can be computed by the Blade Section Boundary-Layer Module, and the flow characteristics can be computed by the Propeller Performance Module.

User Parameters

M_c	turbulence convection Mach number, re M
M_o	reference Mach number, $\Omega R/c_\infty$
N_b	number of blades
N_s	highest harmonic number desired
R	blade length, m (ft)
z	aircraft altitude, m (ft)
θ_o	root pitch change angle, rad
ψ_b	array of blade initial azimuth angles, rad

Blade Shape Data

ξ_1	spanwise station, re R
$C(\xi_1)$	blade chord length, re R
$\theta_T(\xi_1)$	blade twist angle, rad
$\eta_{1t}(\xi_1)$	blade trailing-edge abscissa, re R
$\eta_{3t}(\xi_1)$	blade trailing-edge ordinate, re R

Observer Geometry

$\begin{bmatrix} X_o \\ Y_o \\ Z_o \end{bmatrix}$	array of observer coordinates, m (ft)

Propeller Performance Data

ξ_1	spanwise station, re R
$M(\xi_1)$	local Mach number
$\alpha(\xi_1)$	angle of attack, rad

Boundary-Layer Data

ξ_1	spanwise station, re R
α	angle of attack, rad
M	Mach number
$\delta^*(\xi_1,\alpha,M)$	boundary-layer displacement thickness, m (ft)

Atmospheric Data

z	altitude, re $R_a T_r/mg_r$
$c_\infty(z)$	ambient speed of sound, re c_r
$\rho_\infty(z)$	ambient density, re ρ_r

Independent Variable Arrays

ξ_1	array of spanwise stations, re R
$f_{1/3}$	array of 1/3-octave-band center frequency, Hz

OUTPUT

This module produces broadband noise data due to the source.

Broadband Noise Data

$f_{1/3}$	1/3-octave-band center frequencies, Hz
$\vec{x}$	observer location, m (ft)
$\langle p^2(\vec{x},f_{1/3})\rangle_{1/3}$	mean-square pressure spectrum, re $\rho_\infty^2 c_\infty^4$

METHOD

The methodology of this module is based on the work of Schlinker and Amiet (ref. 1), who present a technique for predicting helicopter rotor trailing-edge noise. Several refinements have been made for improved accuracy and compatibility with the propeller prediction problem to include

1. A change of coordinate systems to maintain consistency with other propeller analysis modules
2. A modification of the problem definition to extend its validity to the geometric near field

The presentation of the methodology is divided into several parts. First, a description of the theoretical noise prediction for a two-dimensional airfoil is presented. Second, an empirical two-dimensional airfoil noise prediction method is presented for comparison. Then, a description of the various options for directivity and spectrum functions is presented. Finally, the two-dimensional trailing-edge noise model is applied to predict propeller noise.

Theoretical Noise Prediction for Two-Dimensional Airfoil

For the coordinate system shown in figure 1, the mean-square acoustic pressure per unit frequency due to trailing-edge noise is given by

$$\langle p^2(\vec{x},\omega)\rangle = \left(\frac{k_x M z b}{2\pi\sigma^2}\right)^2 \frac{S}{2} \left|L\right|^2 \ell_y(\omega)\ S(\omega) \qquad (1)$$

This result was developed in previous theoretical investigations by Amiet (refs. 2, 3, and 4). It is based on modeling the turbulent flow past the trailing edge of an airfoil as a frozen surface pressure pattern which convects downstream at a Mach number M_c past the trailing edge. The pressure jump must be forced to zero at the trailing edge to satisfy the Kutta condition; thus, an induced pressure field that propagates away from the airfoil is produced. The details of the derivation of equation (1) are presented in reference 1.

Several terms in equation (1) require further explanation. The wave number k_x is defined as

$$k_x = \frac{\omega}{U} \qquad (2)$$

and the length scale σ is

$$\sigma = \left[x^2 + \beta^2(y^2 + z^2)\right]^{1/2} \qquad (3)$$

The chordwise integral of the surface loading $\left|L\right|$ is expressed as

$$\left|L\right| = \frac{1}{\Theta}\left| e^{i2\Theta}\left\{1 - (1 + i)E^*\left[2(\bar{\lambda} + \bar{\mu}M + \bar{\zeta}_0)\right]\right\} \times \left(\frac{\lambda + \mu M + \zeta_0}{\mu x/\sigma + \zeta_0}\right)^{1/2} (1 + i)E^*\left[2(\bar{\mu}x/\sigma + \bar{\zeta}_0)\right]\right| \qquad (4)$$

where

$$\Theta = \bar{\lambda} + \bar{\mu}\,(M - x/\sigma) \qquad (5)$$

$$\lambda = \omega/U_c \qquad (6)$$

$$\mu = M\,k_x/\beta^2 \qquad (7)$$

$$\zeta_0 = \mu\,(x^2 + \beta^2 z^2)^{1/2}/\sigma \qquad (8)$$

and the overbar denotes normalized by the airfoil semichord b. The function $E^*[x]$ is the complex conjugate of the integral

$$E[x] = \int_0^x e^{it}\,\frac{dt}{(2\pi t)^{1/2}} \qquad (9)$$

Alternately, $E^*[x]$ can be written as a combination of Fresnel integrals as

$$E^*[x] = Ci(x) - i\,Si(x) \tag{10}$$

where $Ci(x)$ and $Si(x)$ are the Fresnel cosine and sine integrals, respectively.

The surface pressure spectrum function $S(\omega)$ is approximated by the empirical relation

$$S(\omega) = 2 \times 10^{-5} \left(\frac{1}{2}\rho_\infty U^2\right)^2 \frac{\delta^*}{U} F(\tilde{\omega}) \tag{11}$$

where the function $F(\tilde{\omega})$ is defined as

$$F(\tilde{\omega}) = (1 + \tilde{\omega} + 0.217\tilde{\omega}^2 + 0.00562\tilde{\omega}^4)^{-1} \tag{12}$$

and the Strouhal number $\tilde{\omega}$ is

$$\tilde{\omega} = \frac{\omega\delta^*}{U} \tag{13}$$

This surface pressure spectrum function was obtained from the empirical data of Willmarth and Roos (ref. 5). The spanwise turbulent correlation length $\ell_y(\omega)$ is estimated from data obtained by Corcos (ref. 6) as

$$\ell_y(\omega) = 2.1U_c/\omega \tag{14}$$

By collecting all terms in equation (1) that are a function of position, a directivity function can be defined as

$$D(\theta,\phi,\omega) = \left(\frac{zr_e}{\sigma^2}\right)^2 |L|^2 \tag{15}$$

where the retarded source radius r_e is introduced for dimensional consistency and θ and ϕ are the polar and azimuthal directivity angles, respectively (fig. 1). Substituting equation (15) into equation (1) yields

$$\langle p^2(\vec{x},\omega)\rangle = \left(\frac{k_x Mb}{2\pi}\right)^2 \frac{s\,\ell_y(\omega)}{2r_e^2} D(\theta,\phi,\omega)\,S(\omega) \tag{16}$$

Note that the directivity function D is a function of frequency in addition to the two directivity angles. It will be shown later that when properly normalized, the frequency dependence can be removed.

Equation (16) is the primary result of the theoretical analysis of reference (1). Its directivity and spectrum characteristics are discussed in later sections. In addition, comparisons are made between the theoretical prediction and the empirical trailing-edge noise prediction method.

Empirical Noise Prediction for Two-Dimensional Airfoil

Schlinker and Amiet (ref. 1) also present a scaling law for the trailing-edge noise of a two-dimensional airfoil. From analysis of the theoretical approach and available experimental data, they conclude that the dependence of the mean-square pressure on flow parameters is

$$<p^2> \propto M^5 \frac{\delta s}{r_e^{\,2}} \overline{D} \qquad (17)$$

where $\overline{D}$ is the normalized directivity function given by $D(\theta,\phi,\omega)/D(\pi/2,\pi/2,\omega)$.

The normalized spectrum function developed by Fink (ref. 7) for 1/3-octave-band data

$$\overline{F}_f(S_t) = 0.613(10S_t)^4[(10S_t)^{3/2} + 0.5]^{-4} \qquad (18)$$

where the Strouhal number S_t defined as

$$S_t = \frac{f_{1/3}\delta}{U} \qquad (19)$$

accurately predicted the available spectrum data for clean airframe noise where trailing-edge noise was assumed to dominate. The resulting prediction equation is

$$\frac{<p^2>_{1/3}}{\rho_\infty^{\,2} c_\infty^{\,4}} = 5.279 \times 10^{-7} M^5 \frac{\delta s}{r_e^{\,2}} \overline{D}\,\overline{F}_f \qquad (20)$$

where the proportionality constant was obtained from experimental data.

Directivity Functions for Two-Dimensional Airfoil

Both prediction equations (16) and (20) require usage of a directivity function. The three options available for a directivity function are

1. High-frequency limit to equation (15)
2. Low-frequency limit to equation (15)
3. Modified directivity function proposed by Fink (ref. 7)

First, some analysis of the geometry of the problem is required. Equation (1) was derived in terms of the present airfoil position $\vec{x}$, that is, the position of the airfoil when the sound is received. As can be seen from figure 1, for an airfoil moving in the -x-direction, the observer coordinate at the time of sound emission is

$$r_e \cos\theta = x - Ut_e \tag{21}$$

where $t_e = r_e/c_\infty$ is the propagation time from source to observer. Thus, the present source position is

$$x = r_e(M + \cos\theta) \tag{22}$$

and the y and z observer coordinates remain unchanged by the airfoil motion. Expressing these in the spherical coordinates of figure 1 yields

$$y = r_e \sin\theta \cos\phi \tag{23}$$

and

$$z = r_e \sin\theta \sin\phi \tag{24}$$

Substituting equations (22) to (24) into equation (3) for σ yields

$$\sigma = r_e(1 + M\cos\theta) \tag{25}$$

and equations (22) to (25) allow equation (15) to be written as

$$D(\theta,\phi,\omega) = \frac{\sin^2\theta \sin^2\phi}{(1 + M\cos\theta)^4} \left|L\right|^2 \tag{26}$$

Equation (26) serves as a more useful form to evaluate the four directivity options.

Full theoretical directivity. Substituting equation (4) for the chordwise integral of the surface loading into equation (26) yields

$$D(\theta,\phi,\omega) = \frac{\sin^2\theta\sin^2\phi}{(1 + M\cos\theta)^4}\,\frac{1}{\Theta^2}\Bigg| e^{i2\Theta}\{1 - (1 + i)E^*\,[2(\bar{\lambda} + \bar{\mu}M + \bar{\zeta}_0)]\} + \left(\frac{\lambda + \mu M + \zeta_0}{\mu x/\sigma + \zeta_0}\right)^{1/2}(1 + i)E^*\,[2(\bar{\mu}x/\sigma + \bar{\zeta}_0)]\Bigg|^2 \qquad (27)$$

The normalization of equation (27) requires the evaluation of $D(\pi/2,\pi/2,\omega)$. Substituting $\theta = \pi/2$ and $\phi = \pi/2$ into equations (22) to (25) gives $x = Mr_e$, $\underline{y} = 0$, $z = r_e$, and $\sigma = r_e$. Then from equations (5) and (8), $\Theta = \bar{\lambda}$ and $\zeta_0 = \mu$; therefore,

$$D(\pi/2,\pi/2,\omega) = \frac{1}{\bar{\lambda}^2}\Bigg|e^{i2\bar{\lambda}}\{1 - (1 + i)E^*[2\bar{\lambda} + 2\bar{\mu}(M + 1)]\} + \left(\frac{\lambda + \mu(M + 1)}{\mu(M + 1)}\right)^{1/2}(1 + i)E^*[2\bar{\mu}(M + 1)]\Bigg|^2 \qquad (28)$$

Dividing equation (27) by equation (28) yields, for the normalized directivity

$$\bar{D}(\theta,\phi,\omega) = \frac{\sin^2\theta\sin^2\phi}{(1 + M\cos\theta)^4}\,\frac{\bar{\lambda}^2}{\Theta^2}\times$$

$$\frac{\left|e^{i2\Theta}\{1 - (1 + i)E^*[2(\bar{\lambda} + \bar{\mu}M + \bar{\zeta}_0)]\} + \left(\frac{\lambda + \mu M + \zeta_0}{\mu x/\sigma + \zeta_0}\right)^{1/2}(1 + i)E^*\,[2(\bar{\mu}x/\sigma + \bar{\zeta}_0)]\right|^2}{\left|e^{i2\bar{\lambda}}\{1 - (1 + i)E^*[2\bar{\lambda} + 2\bar{\mu}(M + 1)]\} + \left[\frac{\lambda + \mu(M + 1)}{\mu(M + 1)}\right]^{1/2}(1 + i)E^*[2\bar{\mu}(M + 1)]\right|^2} \qquad (29)$$

Since λ, μ, ζ_0, and Θ are all proportional to ω, the only frequency dependency in equation (29) is in the arguments of the exponential and E^* functions.

Equation (29) is obviously awkward and time consuming to use for multiple calculations. Fortunately, simplifying assumptions can be made without significant loss in accuracy.

High-frequency approximation.- For a case where $\omega b \gg 1$, corresponding to a large chord length or high frequency, the arguments of E^* in equation (29) become large. Since

$$\lim_{x\to\infty} E^*[x] = \frac{1 - i}{2} \qquad (30)$$

equation (29) in the high-frequency limit becomes

$$\bar{D}_h(\theta,\phi) = \frac{\sin^2\theta\,\sin^2\phi}{(1 + M\cos\theta)^4}\,\frac{\bar{\lambda}^2}{\theta^2}\left[\frac{\lambda + \mu M + \zeta_o}{\lambda + \mu(M+1)}\right]\left[\frac{\mu(M+1)}{(\mu x/\sigma) + \zeta_o}\right] \quad (31)$$

Note that in the high-frequency limit, the directivity function is independent of frequency.

Additional insight into the high-frequency approximation can be gained by examining $D_h(\theta,\pi/2)$. Setting $\phi = \pi/2$, substituting equations (5) to (8) and (22) to (25) into equation (31), and rearranging yield

$$\bar{D}_h(\theta,\pi/2) = \frac{2\sin^2(\theta/2)}{(1 + M\cos\theta)\,[1 + (M - M_c)\cos\theta]^2} \quad (32)$$

The normalization factor $D_h(\pi/2,\pi/2)$, which is required for substituting equation (31) into equation (20), is

$$D_h(\pi/2,\pi/2,\omega) = \frac{1}{\bar{\lambda}^2}\left[\frac{1 - (M - M_c)}{M_c}\right] \quad (33)$$

where $D_h(\theta,\phi) = D_h(\pi/2,\pi/2,\omega)\,\bar{D}_h(\theta,\phi)$.

Low-frequency approximation. - For a case where $\omega b << 1$, corresponding to a small chord length or small frequency, the value of $E^*[x]$ approaches zero. Therefore, in the low-frequency limit, equation (29) becomes

$$\bar{D}_\ell(\theta,\phi) = \frac{\sin^2\theta\,\sin^2\phi}{(1 + M\cos\theta)^4}\,\frac{\bar{\lambda}^2}{\theta^2} \quad (34)$$

Again, the directivity function is independent of frequency. Following the same logic as for the high-frequency case,

$$\bar{D}_\ell(\theta,\pi/2) = \frac{\sin^2\theta}{(1 + M\cos\theta)^2\,[1 + (M - M_c)\cos\theta]^2} \quad (35)$$

$$D_\ell(\pi/2,\pi/2,\omega) = \frac{1}{\bar{\lambda}^2} \quad (36)$$

The low-frequency approximation of the normalized directivity function is also shown in figure 2 for comparison. Direct comparison between equations (32) and (35) shows that

$$\frac{\overline{D}_h(\theta,\pi/2)}{\overline{D}_\ell(\theta,\pi/2)} = \frac{1 + M\cos\theta}{1 + \cos\theta} \tag{37}$$

and that in the limit as the Mach number approaches zero, the two normalized directivity functions become identical at $\phi = \pi/2$. In addition to the difference in directivity shape, the two directivity functions have different normalizations. The ratio of equations (33) and (36) is

$$\frac{D_h(\pi/2,\pi/2,\omega)}{D_\ell(\pi/2,\pi/2,\omega)} = \frac{1 - (M - M_c)}{M_c} \tag{38}$$

Thus, if the turbulence convection Mach number is set equal to the free-stream Mach number, the peak overall sound pressure level in the high-frequency approximation is $1/M$ larger than the low-frequency approximation overall sound pressure level.

Modified directivity by Fink. - In the prediction method for airframe noise developed by Fink (ref. 7), the normalized directivity function for wing trailing-edge noise is

$$D_f(\theta,\phi) = \sin^2(\theta/2)\sin^2\phi \tag{39}$$

This function was modified for the Doppler amplification of a point source with velocity M in the ANOPP Airframe Noise Module (ref. 8, sec. 8.8) to yield

$$D_f(\theta,\phi) = \frac{\sin^2(\theta/2)\sin^2\phi}{(1 + M\cos\theta)^4} \tag{40}$$

which, since $D_f(\pi/2,\pi/2) = 1/2$, results in the normalized directivity

$$\overline{D}_f(\theta,\phi) = \frac{2\sin^2(\theta/2)\sin^2\phi}{(1 + M\cos\theta)^4} \tag{41}$$

This function is similar in shape to the other approximate directivity functions shown in figure 2. It differs in shape from the high-frequency approximation by the ratio

$$\frac{\overline{D}_h(\theta,\pi/2)}{\overline{D}_f(\theta,\pi/2)} = \frac{(1 + M\cos\theta)^3}{[1 + (M - M_c)\cos\theta]^2} \tag{42}$$

Note that the Fink directivity function D_f has no frequency dependence, whereas D, D_h, and D_ℓ are all proportional to $1/\omega^2$ before normalization. Since the Fink directivity function was obtained independent of the Amiet theoretical analysis, it is not surprising that it is not compatible with equation (16). Therefore, equation (41) will only be applied to the empirical prediction given by equation (20).

Spectrum Functions for Two-Dimensional Airfoil

The theoretical noise prediction equation (16) has several terms which are a function of frequency. If it is assumed that the high-frequency approximation is valid, substituting equations (2), (11), (14), (32), and (33) into equation (16) and collecting all frequency terms yield

$$\frac{\langle p^2(x,\omega)\rangle}{\rho_\infty{}^2 c_\infty{}^4} = (1.330 \times 10^{-7}) \; \frac{s\delta^*}{r_e{}^2} \; M^5 \left(\frac{M_c}{M}\right)^2 \left[1 - (M - M_c)\right]\bar{D}_h(\theta,\phi)\,\frac{F(\tilde{\omega})}{\omega} \tag{43}$$

Equation (43) describes a narrow-band spectrum. It is often convenient to examine the 1/3-octave-band spectrum for comparison to experimental data. The definition of the 1/3-octave-band spectrum function is

$$F_{1/3}(\tilde{\omega}) = \int_{\omega_\ell}^{\omega_u} \frac{F(\tilde{\omega})}{\omega}\, d\omega = \int_{f_\ell}^{f_u} \frac{F(\tilde{\omega})}{f}\, df \tag{44}$$

where ℓ and u refer to the lower and upper limits of the band. Evaluating the integral, assuming that the mean value of the spectrum equals the center value, yields for the 1/3-octave-band spectrum function

$$F_{1/3}(\tilde{\omega}) = 0.23077F(\tilde{\omega}) \tag{45}$$

where $\tilde{\omega}$ is understood to be a 1/3-octave-band center frequency value. Therefore, from the definition of $F(\tilde{\omega})$,

$$F_{1/3}(\tilde{\omega}) = \frac{0.23077}{1 + \tilde{\omega} + 0.217\,\tilde{\omega}^2 + 0.00562\tilde{\omega}^4} \tag{46}$$

or, expressed in terms of the Strouhal number $S_t = f_{1/3}\delta/U$, and converting the left-hand side from an $\tilde{\omega}$ spectrum to a frequency spectrum

$$F_{1/3}(S_t) = \frac{0.23077}{1 + 0.785S_t + 0.134S_t^2 + 0.00213S_t^4} \tag{47}$$

To convert from $\tilde{\omega}$ to S_t, it is assumed that $\delta^* = \delta/8$, which is typical for a flat-plate boundary layer. From equation (47), a normalized spectrum $\overline{F}_{1/3}(S_t)$ can be defined such that

$$\sum \overline{F}_{1/3}(S_t) = 1 \tag{48}$$

where the summation is over all 1/3 octave bands. In addition, the original spectrum function was a two-sided spectrum for $-\infty < \tilde{\omega} < \infty$. Converting to a one-sided spectrum, multiplying by two for both sides of the airfoil, and applying the normalization condition yield

$$\overline{F}_{1/3}(S_t) = \frac{0.0754}{1 + 0.785S_t + 0.134S_t^2 + 0.00213S_t^4} \tag{49}$$

Therefore, for a 1/3-octave-band analysis, the $F(\omega)/\omega$ term should be replaced with $F_{1/3}(S_t)$, where

$$F_{1/3}(S_t) = 12.243\ \overline{F}_{1/3}(S_t) \tag{50}$$

and $\overline{F}_{1/3}(S_t)$ is given by equation (49).

Schlinker and Amiet (ref. 1) made comparisons of the spectrum function $F(\tilde{\omega})$ with available experimental data for the surface pressure spectrum of an airfoil. They determined that equation (11), which is based on flat-plate surface pressure data, tended to underestimate the airfoil data by as much as 7.0 dB. They determined the difference between the flat plate and airfoil data. This difference function $\Delta F(\tilde{\omega})$ is defined in table I. They recommended a modified surface pressure spectrum function $F'(\tilde{\omega})$ as

$$F'(\tilde{\omega}) = F(\tilde{\omega})\ \Delta F(\tilde{\omega}) \tag{51}$$

This can be converted to a normalized 1/3-octave-band spectrum, following the procedure of equations (44) to (47), with the result

$$\overline{F}'_{1/3}(S_t) = \frac{0.0215\ \Delta F(S_t)}{1 + 0.785S_t + 0.134S_t^2 + 0.00221S_t^4} \tag{52}$$

Therefore, for the Schlinker and Amiet modified spectrum function, the term $F(\omega)/\omega$ should be replaced by $F'_{1/3}(S_t)$, where

$$F'_{1/3}(S_t) = 42.923\ \overline{F}'_{1/3}(S_t) \qquad (53)$$

In summary, the three normalized 1/3-octave-band spectrum functions available for trailing-edge noise prediction are

1. $\overline{F}_{1/3}(S_t)$ given by equation (47) based on flat-plate surface pressure spectrum data
2. $\overline{F}'_{1/3}(S_t)$ given by equation (52) based on airfoil surface pressure data
3. $\overline{F}_f(S_t)$ given by equation (18) obtained by Fink (ref. 7)

All three spectrum functions may be used for the empirical trailing-edge noise prediction method. Only the first two can be used for the theoretical method since the constant for normalization of the Fink spectrum function is unknown. A comparison of the three normalized spectrum functions is given in figure 3.

The 1/3-octave-band mean-square pressure for the full theoretical directivity and the low-frequency approximation can be determined in the same manner. In general, the 1/3-octave-band form of the theoretical prediction equation (16) is

$$\langle p^2(\vec{x},\omega)\rangle_{1/3} = 0.923\omega \left(\frac{k_x Mb}{2\pi}\right)^2 \frac{s\ell_y(\omega)}{2r_e^{\,2}}\ D(\theta,\phi,\omega)\ S(\omega) \qquad (54)$$

where conversion to a one-sided spectrum and both sides of the airfoil are taken into account. The frequency ω is assumed to be a 1/3-octave-band center frequency value.

Comparison of Two-Dimensional Prediction Methods

The theoretical prediction in the high-frequency approximation given by equation (43) can now be directly compared with the empirical prediction method. Assuming that the convection Mach number M_c equals the free-stream Mach number M, the boundary-layer displacement thickness δ^* equals $\delta/8$, and the modified spectrum function of Schlinker and Amiet given by equations (52) and (53) is valid, equation (43) is written in 1/3-octave-band form as

$$\frac{\langle p^2\rangle_{1/3}}{\rho_\infty^{\,2} c_\infty^{\,4}} = (7.136 \times 10^{-7}) \quad \frac{s\delta}{r_e^{\,2}} M^5\ \overline{D}_h(\theta,\phi)\ \overline{F}'_{1/3}(S_t) \qquad (55)$$

Using the high-frequency approximation for the normalized directivity function $\bar{D}$, the empirical prediction equation (20) is written as

$$\frac{\langle p^2 \rangle_{1/3}}{\rho_\infty{}^2 c_\infty{}^4} = (5.279 \times 10^{-7}) \; \frac{s\,\delta}{r_e{}^2} M^5 \, \bar{D}_h(\theta,\phi) \; \bar{F}_f(S_t) \tag{56}$$

Comparison of equations (55) and (56) shows that the theoretical method predicts an overall mean-square pressure about 1.3 dB higher than the empirical method and the spectrum shapes differ as shown in figure 3. It should be noted, however, that equation (54), not equation (55), represents the full theoretical model.

Geometry for Propeller Application

Application of the two-dimensional airfoil trailing-edge noise prediction to a propeller is accomplished by modeling the propeller as the sum of individual airfoil segments. The noise contributed by each segment is summed at the observer to produce the noise signature at a fixed time. As time changes, the observed noise spectrum changes because the relative motion of the blade about the hub. The resulting time-dependent noise spectra must be further analyzed to produce the complete noise signature.

The geometry of the propeller application is shown in figure 4. The nonrotating coordinate system fixed to the propeller hub is denoted by $\vec{X} = (X,Y,Z)$. The observer is fixed relative to the hub and its location denoted by $\vec{r}_0 = (X_0,Y_0,Z_0)$ in the $\vec{X}$ coordinate system. The position of the trailing edge of a specific airfoil segment is denoted by $\vec{r}_b$. The components of the trailing-edge location are provided by the Blade Shape Module in the rotating coordinate system $\vec{\eta}$, where $\vec{r}_b = (\eta_{1t}(\xi_1),\xi_1,\eta_{3t}(\xi_1))$ and ξ_1 is the spanwise blade coordinate. The blade position $\vec{r}_b$ must be transformed twice to express it in the $\vec{X}$ coordinate system. The first transformation to the $\vec{\eta}'$ coordinate system accounts for the blade root pitch θ_0 as

$$\vec{r}_b \Big|_{\vec{\eta}'} = \begin{bmatrix} \cos\theta_0 & 0 & \sin\theta_0 \\ 0 & 1 & 0 \\ -\sin\theta_0 & 0 & \cos\theta_0 \end{bmatrix} \vec{r}_b \Big|_{\vec{\eta}} \tag{57}$$

The second transformation removes the rotation of the $\vec{\eta}'$ coordinate system, which results in

$$\vec{r}_b\Big|_{\vec{X}} = \begin{bmatrix} \cos\psi & -\sin\psi & 0 \\ \sin\psi & \cos\psi & 0 \\ 0 & 0 & 1 \end{bmatrix} \vec{r}_b\Big|_{\vec{\eta}'} \tag{58}$$

where ψ is the blade rotation angle defined in figure 4.

The observer position relative to the airfoil segment is now defined in the $\vec{X}$-coordinate system at the time of sound emission as

$$\vec{r}_e\Big|_{\vec{X}} = \vec{r}_o - \vec{r}_b\Big|_{\vec{X}} \tag{59}$$

The airfoil trailing-edge noise predictions are expressed in terms of the $\vec{x} = (x\ y,z)$ coordinate system. Thus, r_e must be transformed to this coordinate system. The inverse of the transformations (57) and (58) can be used to transform to the $\vec{\eta}$-coordinate system. Data in the $\vec{x}$-coordinate system is transformed to the $\vec{\eta}$-coordinate system in the Blade Shape Module by

$$r\Big|_{\vec{\eta}} = \begin{bmatrix} \cos\theta_T & 0 & \sin\theta_T \\ 0 & 1 & 0 \\ -\sin\theta_T & 0 & \cos\theta_T \end{bmatrix} r\Big|_{\vec{x}} \tag{60}$$

where θ_T is the blade twist angle. Thus, $\vec{r}_e$ is expressed in the $\vec{x}$ coordinate system as

$$\vec{r}_e = \begin{bmatrix} \cos\theta_T & 0 & \sin\theta_T \\ 0 & 1 & 0 \\ -\sin\theta_T & 0 & \cos\theta_T \end{bmatrix}^{-1} \begin{bmatrix} \cos\theta_o & 0 & \sin\theta_o \\ 0 & 1 & 0 \\ -\sin\theta_o & 0 & \cos\theta_o \end{bmatrix}^{-1} \begin{bmatrix} \cos\psi & -\sin\psi & 0 \\ \sin\psi & \cos\psi & 0 \\ 0 & 0 & 1 \end{bmatrix}^{-1} \vec{r}_e\Big|_{\vec{X}} \tag{61}$$

Substituting equations (57) to (59) into equation (61) and evaluating the inverse of the matrices yield

$$\vec{r}_e(\xi_1,\psi) = \begin{bmatrix} \cos(\theta_T + \theta_o) & 0 & -\sin(\theta_T + \theta_o) \\ 0 & 1 & 0 \\ \sin(\theta_T + \theta_o) & 0 & \cos(\theta_T + \theta_o) \end{bmatrix} \begin{bmatrix} \cos\psi & \sin\psi & 0 \\ -\sin\psi & \cos\psi & 0 \\ 0 & 0 & 0 \end{bmatrix} \begin{bmatrix} X_o \\ Y_o \\ Z_o \end{bmatrix}$$

$$- \begin{bmatrix} \cos\theta_T & 0 & -\sin\theta_T \\ 0 & 1 & 0 \\ \sin\theta_T & 0 & \cos\theta_T \end{bmatrix} \begin{bmatrix} \eta_{1t}(\xi_1) \\ \xi_1 \\ \eta_{3t}(\xi_1) \end{bmatrix} \qquad (62)$$

Note that equation (62) is conveniently written in terms of input quantities.

The position of the airfoil at the observer time is

$$\vec{r}(\xi_1,\psi) = \vec{r}_e(\xi_1,\psi_e) + c_\infty(M,0,0)\ \Delta t \qquad (63)$$

where the airfoil is assumed to have rectilinear motion after sound emission. Since $\Delta t = (\psi - \psi_e)/\Omega$ and $t = \psi/\Omega$, equation (63) can be written as

$$\vec{r}(\xi_1,\psi) = \vec{r}_e(\xi_1,\psi_e) + c_\infty(M,0,0)\ (\psi - \psi_e) \qquad (64)$$

The time of sound emission $t_e = \psi_e/\Omega$ is found from the retarded time equation

$$t_e + \frac{r_e}{c_\infty} = t \qquad (65)$$

or

$$\psi_e = \psi - \frac{\Omega r_e}{c_\infty} \qquad (66)$$

where r_e is the magnitude of $\vec{r}_e$. Thus, for each observer time, equation (66) is solved for the emission time $t_e = \psi_e/\Omega$. Then, the present airfoil position is determined from equation (64). The resulting value of $\vec{r}$ is used for the airfoil segment noise predictions.

In the propeller application, the directivity angles θ and ϕ are not related to x, y, and z in the same manner as equations (22) to (24). They are defined in terms of the coordinates $\vec{r}_e = (x_e, y_e, z_e)$ as

$$\cos\theta = \frac{x_e}{r_e} \tag{67}$$

and

$$\cos\phi = \frac{y_e}{r_e \sin\theta} \tag{68}$$

The present source coordinates are

$$x = r_e(M + \cos\theta) \tag{69}$$

$$y = r_e \sin\theta \cos\phi \tag{70}$$

$$z = r_e \sin\theta \sin\phi \tag{71}$$

Note that the motion of the airfoil relative to the observer does not equal the motion of the airfoil relative to the fluid.

Computation of Acoustic Pressure

The 1/3-octave-band mean-square acoustic pressure for each airfoil segment can be computed by either equation (20) or equation (54), depending on whether the user desires an empirical or theoretical prediction. The desired directivity and spectrum functions must also be selected. Then, the total mean-square pressure at a given time for a single blade is

$$<p^2\,(X_o, \vec{S}_t; t)>_{1/3} = \sum_{i=1}^{N_{\xi_1}} <p^2\,(\vec{X}_o, S_t'; \xi_{1,i}, t)>_{1/3} \tag{72}$$

where the normalization by $\rho_\infty^2 c_\infty^4$ is assumed. The corrected Strouhal number S_t' has been introduced because it is necessary to account for the Doppler frequency shift due to the relative motion of each blade segment to the observer. This frequency shift is, in general a function of ξ_1 and ψ.

The general equation for the frequency shift of a source in a flow of Mach number $\vec{M}_f$ and relative source to observer motion $\vec{M}_r$ is

$$\frac{\omega}{\omega'} = 1 + \frac{\vec{M}_r \cdot \hat{r}_e}{1 - \vec{M}_f \cdot \hat{r}_e} \tag{73}$$

For the case of the motion of the airfoil segment,

$$\vec{M}_r = \frac{\Omega}{c_\infty} \frac{\partial \vec{r}_e}{\partial \psi} \tag{74}$$

and

$$\vec{M}_f = (-M,0,0) \tag{75}$$

where $\hat{r}_e$ is the unit vector in the $\vec{r}_e$ direction. Substituting equations (74) and (75) into (73) and noting that $\vec{r}_e = (x_e, y_e, z_e)$ yield

$$\frac{\omega}{\omega'} = 1 + \frac{\frac{\Omega}{c_\infty}\left(\frac{x_e}{r_e}\frac{\partial x_e}{\partial \psi} + \frac{y_e}{r_e}\frac{\partial y_e}{\partial \psi} + \frac{z_e}{r_e}\frac{\partial z_e}{\partial \psi}\right)}{1 - Mx_e/r_e} \tag{76}$$

Therefore, the corrected Strouhal number is

$$S_t = S_t' \left[1 + \frac{\frac{\Omega}{c_\infty}\left(\frac{\partial x_e}{\partial \psi}\cos\theta + \frac{\partial y_e}{\partial \psi}\sin\theta\cos\phi + \frac{\partial z_e}{\partial \psi}\sin\theta\sin\phi\right)}{1 - M\cos\theta}\right] \tag{77}$$

For multiple blades, each with an angle ψ_b relative to the initial blade, the contribution of each blade is summed by the relation

$$\langle p^2 (\vec{X}_0, S_t; t)\rangle_{1/3} = \sum_{b=1}^{N_b} \langle p^2 (\vec{X}_0, S_t'; t + \frac{\psi_b}{\Omega})\rangle_{1/3} \tag{78}$$

where the initial blade position ψ_1 is zero. Since equation (72) is evaluated at values of ψ given by

$$\psi = \frac{2\pi}{N}(i - 1) \qquad (i = 1, 2, \ldots, N) \tag{79}$$

Equation (78) can be evaluated for an even number of blades by simply time shifting the single blade solution. For an odd number of blades, interpolation is required. The resulting time-dependent spectrum $\langle p^2 (\vec{X}_0, S_t; t)\rangle_{1/3}$ represents the noise signature of the propeller to trailing-edge noise which is averaged by the relation

$$\langle p^2 (\vec{X}_0, S_t)\rangle_{1/3} = \frac{\Omega}{2\pi} \int_0^{\frac{2\pi}{\Omega}} \langle p^2 (\vec{X}_0, S_t; t)\rangle_{1/3} \, dt \qquad (80)$$

to yield the mean-square acoustic pressure at the observer.

REFERENCES

1. Schlinker, Robert H.; and Amiet, Roy K.: Helicopter Rotor Trailing Edge Noise. NASA CR-3470, 1981.

2. Amiet, R. K.: Noise Due to Turbulent Flow Past a Trailing Edge. J. Sound & Vib., vol. 47, no. 3, 1976, pp. 387-393.

3. Amiet, Roy K.: High Frequency Thin-Airfoil Theory for Subsonic Flow. AIAA J., vol. 14, no. 8, Aug. 1976, pp. 1076-1082.

4. Amiet, R. K.: Acoustic Radiation From an Airfoil in a Turbulent Stream. J. Sound & Vib., vol. 41, no. 4, Aug. 1975, pp. 407-420.

5. Willmarth, W. W.; and Roos, F. W.: Resolution and Structure of the Wall Pressure Field Beneath a Turbulent Boundary Layer. J. Fluid Mech., vol. 22, pt. 1, May 1965, pp. 81-94.

6. Corcos, G. M.: The Structure of the Turbulent Pressure Field in Boundary-Layer Flows. J. Fluid Mech., vol. 18, pt. 3, Mar. 1964, pp. 353-378.

7. Fink, Martin R.: Noise Component Method for Airframe Noise. AIAA Paper 77-1271, Oct. 1977.

8. Zorumski, William E.: Aircraft Noise Prediction Program Theoretical Manual. NASA TM-83199, Pt. 2, 1982.

TABLE I.- MODIFIED SPECTRUM FUNCTION $\Delta F(\tilde{\omega})$

$\tilde{\omega}$	ΔF
0.034	1.000
0.040	1.585
0.050	2.292
0.060	2.883
0.070	3.467
0.080	3.803
0.090	3.980
0.100	4.170
0.200	4.787
0.300	4.364
0.400	3.803
0.500	3.629
0.600	3.467
0.700	3.312
0.800	3.161
0.900	3.161
1.000	3.021
2.000	2.631
3.000	2.292
4.000	2.088
5.000	1.997
6.000	1.904
7.000	1.820
8.000	1.737
9.000	1.659
10.000	1.585

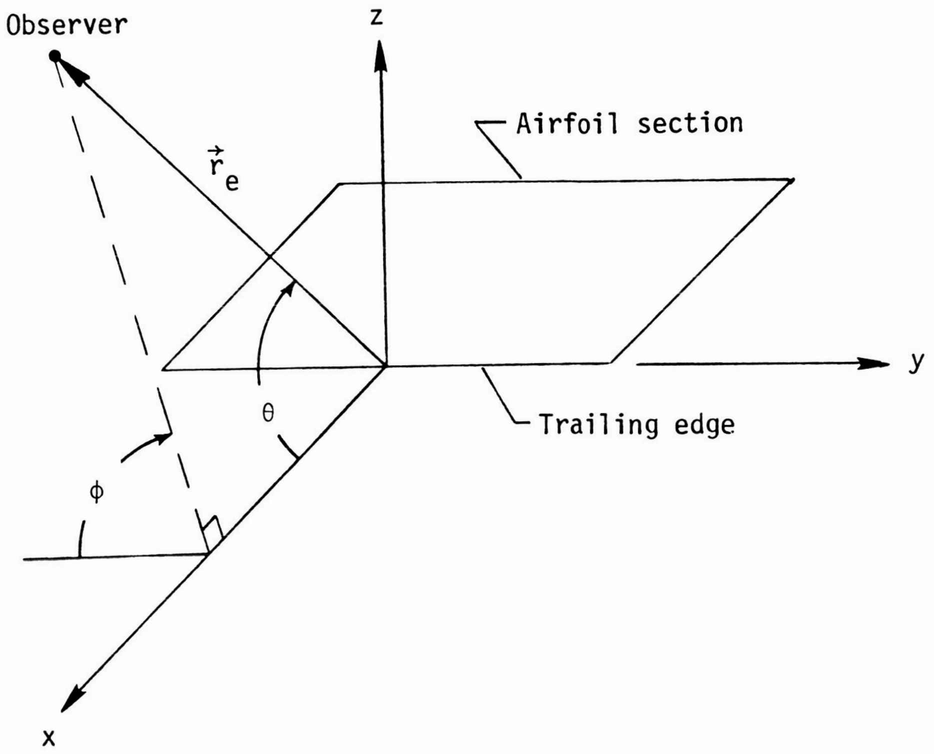

Figure 1.- Coordinate system for two-dimensional airfoil trailing-edge noise prediction.

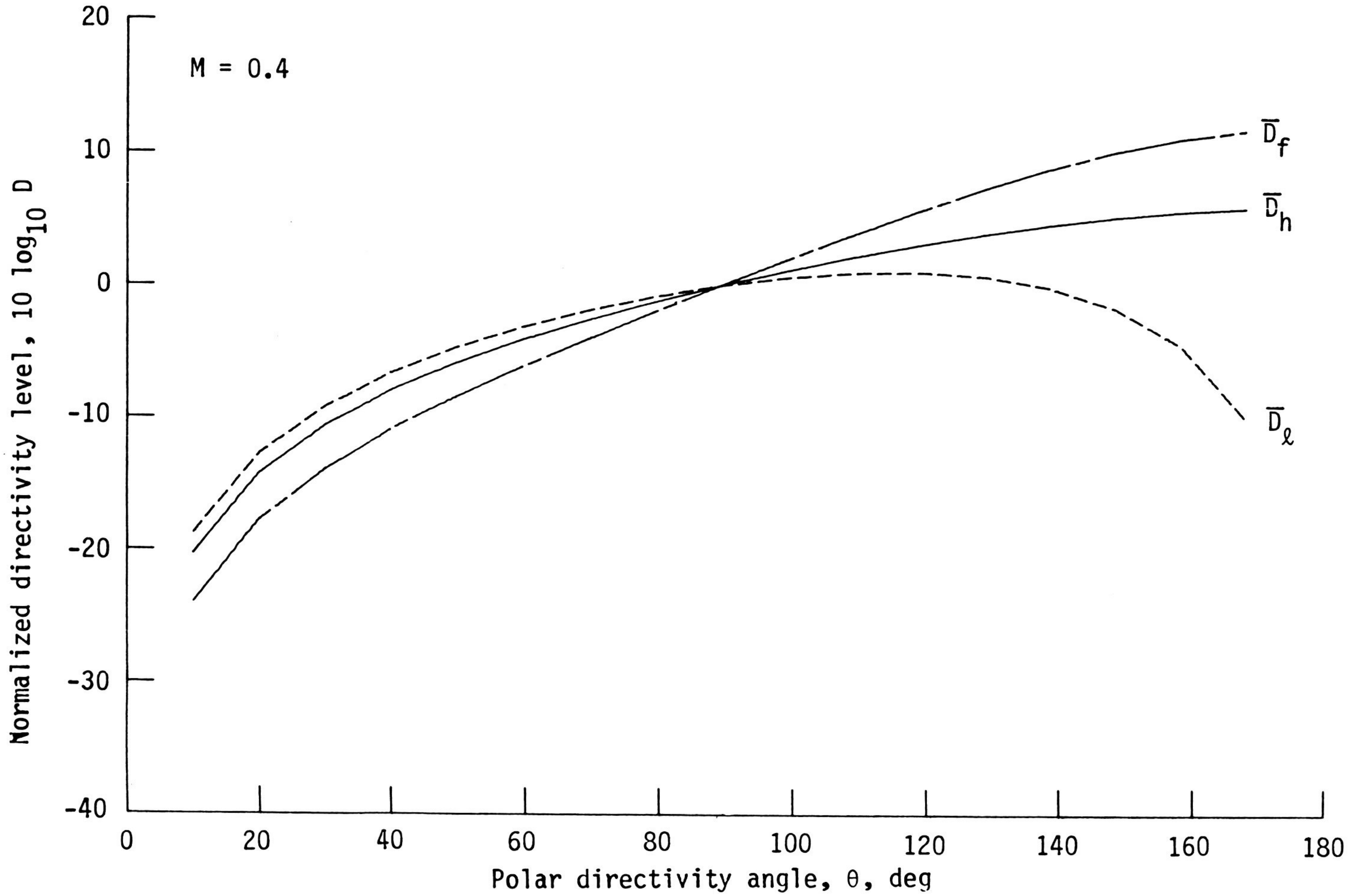

Figure 2.- Comparison of options for the normalized directivity function.

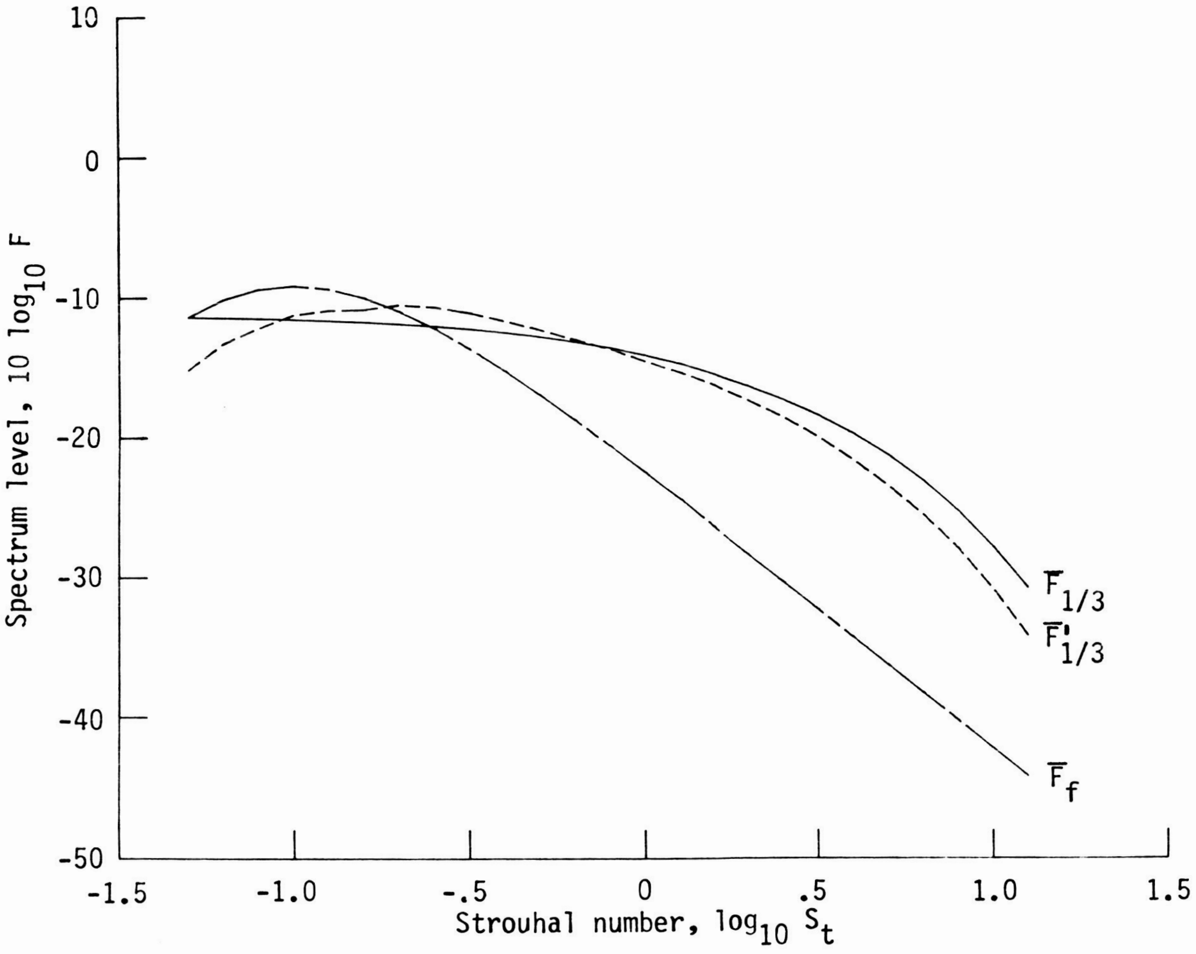

Figure 3.- Comparison of options for normalized spectrum function.

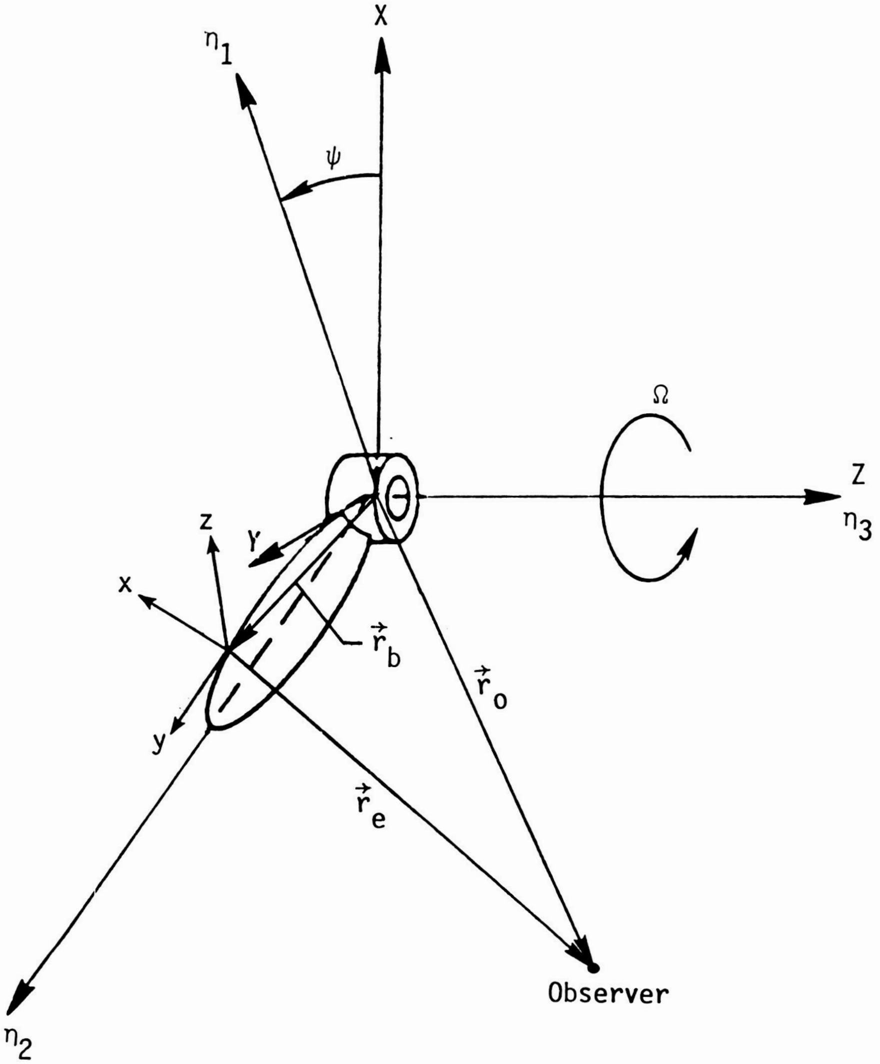

Figure 4.- Coordinate system for propeller trailing-edge noise prediction.

12. TONE PROPAGATION EFFECTS

12.1 BOUNDARY-LAYER PROPAGATION MODULE

Gerry L. McAninch
Langley Research Center

INTRODUCTION

The presence of a boundary layer, hydrodynamic or thermal, over a surface causes refraction and reflection of any acoustic wave incident upon the boundary layer. Consequently, the sound field at the surface differs from that which would be expected if the boundary layer was not present. The Boundary-Layer Propagation Module calculates the complex acoustic pressure at a plane surface of uniform admittance due to a specified acoustic field incident upon the boundary layer.

SYMBOLS

c_∞	sound speed in undisturbed free stream, m/s (ft/s)
c^*	local sound speed, re c_∞
$F(g)$	Fourier transform operator
f_1	fundamental frequency, Hz
i	$=\sqrt{-1}$
K	integer, number of points for which initial data are given
k_x^*	x-component of wave propagation vector, re $1/\delta$
k_y^*	y-component of wave propagation vector, re $1/\delta$
L	distance over which initial data are given, re δ
m	integer exponent of 2
N	integer, number of harmonics of interest
n	harmonic number
P	local pressure, N/m^2 (lb/ft^2)
p_r	reference pressure, N/m^2 (lb/ft^2)
p^*	total acoustic pressure, re $\rho_\infty c_\infty^2$

p_i^*	incident acoustic pressure, re $\rho_\infty c_\infty^2$
p_1^*	incident acoustic pressure evaluated at $y^* = 1$, re $\rho_\infty c_\infty^2$
T_∞	undisturbed free stream temperature, K (°R)
T^*	local temperature, re T_∞
U^*	local flow velocity, re c_∞
u^*	x-component of complex acoustic velocity, re c_∞
v^*	y-component of complex acoustic velocity, re c_∞
w^*	z-component of complex acoustic velocity, re c_∞
x,y,z	Cartesian coordinates, m (ft)
Δx	distance between data points, m (ft)
x^*,y^*,z^*	nondimensional Cartesian coordinates, re δ
x_o,y_o,z_o	observer coordinates, m (ft)
x_1	lowest value of x for which data are provided, m (ft)
x_2	highest value of x for which data are provided, m(ft)
y_s	location of singular point
α	distance from singular point at which numerical integration is reinstated
β	surface admittance, re $1/\rho_\infty c_\infty$
γ	ratio of specific heats
δ	boundary-layer thickness, m (ft)
δ^*	complex acoustic perturbation density, re ρ_∞
ε	radius of neighborhood around singular point where Frobenius solution is used
μ	Fourier transform, with respect to x, of u^*
ν	Fourier transform, with respect to x, of v^*
ν_i	Fourier transform, with respect to x, of incident normal acoustic velocity at top of boundary layer
ν_r	Fourier transform, with respect to x, of the reflected normal acoustic velocity at top of boundary layer

ν_T	Fourier transform, with respect to x, of total normal acoustic velocity at top of boundary layer
Π	Fourier transform, with respect to x, of p^*
Π_i	Fourier transform, with respect to x, of incident acoustic pressure at top of boundary layer
Π_r	Fourier transform, with respect to x, of reflected acoustic pressure at top of boundary layer
Π_T	Fourier transform, with respect to x, of total acoustic pressure at top of boundary layer
Π_1	Fourier transform, with respect to x, of p_1^*
ρ	local density, kg/m^3 (slug/ft^3)
ρ_∞	undisturbed free-stream density, kg/m^3 (slug/ft^3)
ρ^*	nondimensional local density, re ρ_∞
ω_n^*	circular frequency, re δ/c_∞

INPUT

Input to the module must specify the incident complex acoustic pressure at the top of the boundary layer, the acoustic admittance of the surface at the bottom of the boundary layer, the boundary-layer thickness, the local temperature within the boundary layer, and the properties of the undisturbed free stream.

For each observer, the observer coordinates must be specified. Further, the complex acoustic pressure, associated with the incident wave, must be provided at $K = 2^m$ equally spaced points along the line $(x,y,z) = (x,\delta,z_0)$, where z_0 is the observer's z-coordinate, and δ is the boundary-layer thickness. The lowest value of x, x_1, at which the pressure is provided, and Δx, the distance between points, must also be specified, as must be K, the number of data points for which initial data are given. The observers should be located at $x_0 = x_1 + (n - 1)\ \Delta x$.

A table of the local temperature as a function of y for $0 \leq y \leq \delta$ and a table of the surface admittance β as a function of f is required.

Parameters required are δ, U_∞, T_∞, and ρ_∞, the boundary-layer thickness, undisturbed free-stream velocity, temperature, and density, respectively. The frequency content of the incident wave is specified by supplying f_1, the fundamental source frequency, and N, the number of harmonics of interest.

Initial-Data Table

f	frequency, Hz
x_0, y_0, z_0	observer coordinates, m (ft)
$p_i(x,f)$	incident complex acoustic pressure, N/m^2 (lb/ft^2)

Surface Admittance Table

f	frequency, Hz
β	surface admittance, re $1/\rho_\infty c_\infty$

Boundary-Layer Mean-State Profile

y	distance above surface, m (ft)
$T(y)$	local temperature, K (°R)

Parameters

δ	boundary-layer thickness, m (ft)
U_∞	undisturbed free-stream velocity, m/s (ft/s)
T_∞	undisturbed free-stream temperature, K (°R)
ρ_∞	undisturbed free-stream density, kg/m^3 (slug/ft^3)
f_1	fundamental frequency, Hz
N	number of harmonics
x_1	lowest value of x-coordinate, m (ft)
Δx	distance between data points, m (ft)
K	number of data points required

OUTPUT

Output of the module consists of the complex acoustic pressure and the mean-square acoustic pressure at the surface as a function of x and frequency f.

Acoustic-Pressure Table

f	frequency, Hz
x	position on surface, m (ft)
$p^*(f,x)$	complex acoustic pressure, re $\rho_\infty c_\infty^2$
$\langle p^*(f,x)\rangle^2$	mean-square acoustic pressure, re $\rho_\infty^2 c_\infty^4$

METHOD

The complex acoustic pressure at the surface is to be determined from a knowledge of the incident pressure at the top of the boundary layer, p_i^*, and the complex surface admittance, $\beta(f)$. The problem is illustrated in figure 1. The equations governing the propagation of harmonic acoustic disturbances in a stratified moving medium are (refs. 1 and 2)

$$-i\omega_n^* u^* + U^* \frac{\partial u^*}{\partial x^*} + \frac{dU^*}{dy^*} v^* + c^{*2} \frac{\partial p^*}{\partial x^*} = 0 \tag{1}$$

$$-i\omega_n^* v^* + U^* \frac{\partial v^*}{\partial x^*} + c^{*2} \frac{\partial p^*}{\partial y^*} = 0 \tag{2}$$

$$-i\omega_n^* \delta^* + U^* \frac{\partial \delta^*}{\partial x^*} + \frac{d\rho^*}{dy^*} v^* + \rho^*\left(\frac{\partial u^*}{\partial x^*} + \frac{\partial v^*}{\partial y^*}\right) = 0 \tag{3}$$

$$-i\omega_n^* p^* + U^* \frac{\partial p^*}{\partial x^*} - c^{*2}\left(-i\omega_n^* \delta^* + U^* \frac{\partial \delta^*}{\partial x^*} + \frac{d\rho^*}{dy^*} v^*\right) = 0 \tag{4}$$

Equations (1) and (2) are the x- and y-components of the linearized momentum equation. The z-component is not required, as it is assumed that the problem is strictly two-dimensional; hence, w^* and the derivatives of all quantities with respect to z^* are identically zero. Further, the body-force terms and the viscous terms have been neglected. Equation (3) is the linearized mass conservation equation, while equation (4) is obtained by assuming that the propagation process is isentropic. As a result of neglecting the gravitational force, $c^{*2} = 1/\rho^*$, since $c^2 = \gamma P/\rho$, and since both γ and P are constant.

In equations (1) through (4), U^*, c^*, and ρ^* are the mean flow velocity, local sound speed, and density, respectively, and all are functions of y^* alone. The acoustic perturbation quantities are u^* and v^*, the x and y perturbation velocity components, δ^*, the density perturbation, and p^*, the acoustic pressure.

Further, all quantities have been nondimensionalized, the velocities with c_∞, the speed of sound in the undisturbed free stream, x^* and y^* with δ, the boundary-layer thickness, and the densities ρ^* and δ^* with ρ_∞, while

$$\omega_n^* = n 2\pi f_1 (\delta / c_\infty) \tag{5}$$

where f_1 is the fundamental frequency, and n, the harmonic number, is such that

$$1 \leq n \leq N \tag{6}$$

and N is the number of harmonics of interest.

The problem statement is completed by specifying the incident pressure at $y^* = 1$

$$p_i^*(x^*, 1; \omega_n^*) = p_1^*(x^*, \omega_n^*) \tag{7}$$

where $p_1^*(x^*, \omega_n^*)$ is the complex incident acoustic pressure at the top of the boundary layer, $p_i(x,f)$, in nondimensional form and the admittance of the surface at $y^* = 0$

$$\frac{v^*(x^*, 0; \omega_n^*)}{p^*(x^*, 0; \omega_n^*)} = -\beta(\omega_n^*) \tag{8}$$

where a change of variables from f to ω_n^* has been accomplished for the independent variable of the boundary admittance.

The acoustic density perturbation may be eliminated between equations (3) and (4) to yield

$$-i\omega_n^* p^* + U^* \frac{\partial p^*}{\partial x^*} + \left(\frac{\partial u^*}{\partial x^*} + \frac{\partial v^*}{\partial y^*}\right) = 0 \tag{9}$$

Equations (1), (2), and (9) form a complete set for the unknown functions p^*, u^*, and v^*, which is to be solved subject to the auxiliary conditions given in equations (7) and (8).

The first step in the solution procedure is to perform a Fourier transform, in the variable x*, on equations (1), (2), and (9), and on the auxiliary conditions of equations (7) and (8). The transform of g is defined as

$$F(g) = \frac{1}{x_2 - x_1}\int_{x_1}^{x_2} e^{-ik_x^* x^*} (g)\, dx^* \tag{10}$$

with $x_2 > x_1$.

The resulting system of equations is

$$(\omega_n^* - U^* k_x^*)\mu + i\nu \frac{dU^*}{dy^*} - k_x^* c^{*2}\Pi = 0 \tag{11}$$

$$(\omega_n^* - U^* k_x^*)\nu + ic^{*2}\Pi' = 0 \tag{12}$$

$$(\omega_n^* - U^* k_x^*)\Pi - k_x^*\mu + i\nu' = 0 \tag{13}$$

where

$$\mu(y^*;k_x^*,\omega_n^*) = F(u^*) \tag{14}$$

$$\nu(y^*;k_x^*,\omega_n^*) = F(v^*) \tag{15}$$

$$\Pi(y^*;k_x^*,\omega_n^*) = F(p^*) \tag{16}$$

and the prime notation indicates ordinary differentiation of the dependent variables with respect to y^*.

Equations (11) through (13) are to be solved subject to the auxiliary conditions

$$\Pi(1;k_x^*,\omega_n^*) = \Pi_1(k_x^*;\omega_n^*) \tag{17}$$

where

$$\Pi_1(k_x^*;\omega_n^*) = F[p_1(x^*;\omega_n^*)] \tag{18}$$

and

$$\nu(0;k_x^*,\omega_n^*) = -\beta(\omega_n^*)\ \Pi(0;k_x^*,\omega_n^*) \tag{19}$$

The unknown function μ can be eliminated between equations (11) and (13) to provide the system of equations

$$ic^{*2}\Pi' + (\omega_n^* - U^* k_x^*)\nu = 0 \tag{20}$$

$$i(\omega_n^* - U^*k_x^*)\nu' + ik_x^* \frac{dU^*}{dy^*} \nu + [(\omega_n^* - U^*k_x^*)^2 - c^{*2}k_x^{*2}]\Pi = 0 \qquad (21)$$

The initial data, $p_1^*(x^*;\omega_n^*)$, must be given at $K = 2^n$ evenly spaced points over the interval $x_1 \leq x^* \leq x_2$, with the first point at $x^* = x_1$. Use of the transform, as defined in equation (10), implies that the problem is solved for the periodic extension of $p_1^*(x^*;\omega^*)$ from $-\infty < x < \infty$. This function has the period $L = x_2 - x_1$. Note that L is dimensionless and gives the number of boundary-layer thicknesses over which data are provided. After the transform, $\Pi_1(k_x^*;\omega_n^*)$ will be known for K values of k_x^* in the range

$$\frac{-\pi K}{L} \leq k_x^* \leq \frac{\pi(K - 1)}{L} \qquad (22)$$

These values of k_x^* are equally spaced at increments $2\pi/L$. The integration of equations (20) and (21) from $y^* = 0$ to $y^* = 1$ with the auxiliary conditions

$$\Pi(0;k_x^*,\omega_n^*) = 1 \qquad (23)$$

$$\nu(0;k_x^*,\omega_n^*) = -\beta(\omega_n^*) \qquad (24)$$

ensure that the initial condition given by equation (19) is satisfied. The initial-value problem given by equations (20), (21), (23) and (24) can be solved by numerical integration, as long as the equation

$$U^* = \omega_n^*/k_x^* \qquad (25)$$

is not satisfied for any value of y^* in the range $0 \leq y^* \leq 1$. For the purposes of the current discussion, this will be assumed to be the case. If, at $y^* = y_S$, equation (25) is satisfied, y_S is a singular point of the system of equations (20) and (21). The discussion of this case is provided in appendix A.

The solution of equations (20) and (21), subject to the initial conditions given by equations (23) and (24), provides values of $\Pi(1;k_x^*,\omega_n^*) \equiv \Pi_T$ and $\nu(1;k_x^*,\omega_n^*) \equiv \nu_T$, the transform of total acoustic pressure p and total acoustic velocity v at the top of the boundary layer. It is necessary to decompose Π_T and ν_T into components propagating in the positive and negative y-directions. These may be denoted the reflected and the incident fields, respectively. Thus,

$$\Pi_T = \Pi_i + \Pi_r \qquad (26)$$

and

$$\nu_T = \nu_i + \nu_r \qquad (27)$$

The quantities Π_i and ν_i are related to each other through the equation

$$\nu_i = - \left. \frac{c^{*2} k_y^* \Pi_i}{(\omega_n^* - U^* k_x^*)} \right|_{y^*=1} \qquad (28)$$

while Π_r and ν_r are related through

$$\nu_r = \left. \frac{c^{*2} k_y^* \Pi_r}{(\omega_n^* - U^* k_x^*)} \right|_{y^*=1} \qquad (29)$$

In these equations, k_y^* is given by

$$k_y^* = \{[(\omega_n^* - U^*(y^*)k_x^*)^2/c^{*2}] - k_x^{*2}\}^{1/2} \qquad (30)$$

Since equations (28) through (30) are required only at $y^* = 1$ where $c^* = 1$, they may be written as

$$\nu_i = \left. \frac{-k_y^* \; \Pi_i}{(\omega_n^* - U^* k_x^*)} \right|_{y^*=1} \qquad (31)$$

$$\nu_r = \left. \frac{k_y^* \; \Pi_r}{(\omega_n^* - U^* k_x^*)} \right|_{y^*=1} \qquad (32)$$

and:

$$k_y^* = \{[\omega_n^* - U^*(1)k_x^*]^2 - k_x^{*2}\}^{1/2} \qquad (33)$$

Equations (26), (27), (31), and (32) can be solved for Π_i to yield

$$\Pi_i = \left. \frac{\Pi_T k_y^* - (\omega_n^* - U^* k_x^*) \; \nu_T}{2k_y^*} \right|_{y^*=1} \qquad (34)$$

Equation 34 gives the magnitude of the (ω_n^*, k_x^*) component of the pressure field which is required to produce a component at the surface of unit magnitude. The actual magnitude of this component at the top of the boundary layer is known from the Fourier transform of the input pressure and is given in equation (17). The value of $\Pi(0;k_x^*,\omega_n^*)$ is therefore given by

$$\Pi(0;k_x^*,\omega_n^*) = \left. \frac{2k_y^* \, \Pi_1(k_x^*,\omega_n^*)}{k_y^* \, \Pi_T - (\omega_n^* - U^* k_x^*) \, \nu_T} \right|_{y^*=1} \tag{35}$$

Once $\Pi(0;\, k_x^*,\omega_n^*)$ is found for all values of k_x^*, the inverse transform determines the time-harmonic components of the pressure field at the surface.

The sound speed at any point within the boundary layer, in nondimensional form, is found from

$$c^*(y^*) = \sqrt{T^*(y^*)} \tag{36}$$

where T^* is the local temperature $T(y)$ nondimensionalized by T_∞.

In this module, the velocity within the boundary layer is given by the Pohlhausen (ref. 3) profile

$$U^*(y^*) = (2y^* - 2y^{*3} + y^{*4}) \frac{U_\infty}{c_\infty} \tag{37}$$

The mean-square pressure is given by

$$\langle p^* \rangle^2 = 2p^*\overline{p^*} \tag{38}$$

where the bar indicates the complex conjugate. Finally, the sound pressure level (SPL) is given by

$$\mathrm{SPL} = 10 \log(\langle p^* \rangle^2) + 20 \log(\rho_\infty c_\infty{}^2) - 20 \log(p_r) \tag{39}$$

where

$$p_r = 2 \times 10^{-5} \ \mathrm{N/m^2} \tag{40a}$$

or

$$p_r = 4.1777 \times 10^{-7} \ \mathrm{lb/ft^2} \tag{40b}$$

APPENDIX A

SINGULAR POINT CALCULATION

The discussion in the section entitled "Method" is presented with the assumption that the quantity $(\omega_n^* - U^*k_x^*)$ is never zero in the region $0 \leq y^* \leq 1$. When this is not the case, equations (20) and (21) cannot be integrated numerically across the point $y^* = y_s$ where $(\omega_n^* - U^*k_x^*)\Big|_{y_s} = 0$.

In order to transfer the solution across the singular point $y^* = y_s$, it is necessary to expand the functions Π and ν in series about the point $y^* = y_s$. The determination of these series is, perhaps, easier if the unknown functions ν and ν' are eliminated from equations (20) and (21) to obtain the second-order ordinary differential equation

$$c^{*2}(\omega_n^* - U^*k_x^*)\ \Pi'' + 2\left[c^{*2}\frac{dU^*}{dy^*}k_x^* + c^*\frac{dc^*}{dy^*}(\omega_n^* - U^*k_x^*)\right]\Pi'$$
$$+ (\omega_n^* - U^*k_x^*)\ [(\omega_n^* - U^*k_x^*)^2 - c^{*2}\ k_x^{*2}]\Pi = 0 \qquad (A1)$$

for the function Π. The function ν is then determined from the equation

$$\nu = \frac{-ic^{*2}\Pi'}{(\omega_n^* - U^*k_x^*)} \qquad (A2)$$

As a first step in the solution procedure for equation (A1), the coefficients of this equation are expanded in a Taylor series about the point $y^* = y_s$. Thus,

$$c^{*2}(\omega_n^* - U^*k_x^*) = \sum_{j=1}^{\infty} a_{0j}\ \tau^j \qquad (A3)$$

$$2\left[c^{*2}\frac{dU^*}{dy^*}\ k_x^* + c^*\frac{dc^*}{dy^*}\ (\omega_n^* - U^*k_x^*)\right] = \sum_{j=0}^{\infty} a_{1j}\,\tau^j \qquad (A4)$$

$$(\omega_n^* - U^*k_x^*)\ [(\omega_n^* - U^*k_x^*)^2 - c^{*2}k_x^{*2}] = \sum_{j=1}^{\infty} a_{2j}\,\tau^j \qquad (A5)$$

where

$$\tau = y^* - y_s \qquad (A6)$$

Equations (20) and (21) of the section entitled "Method" are integrated numerically from $y^* = 0$ to $y^* = y - \varepsilon$, $0 < \varepsilon << 1$. The solutions $\Pi(y_s - \varepsilon)$ and $\nu(y_s - \varepsilon)$ are used to provide initial values for equation (A1). Here,

$$\Pi'(y_s - \varepsilon) = \frac{i(\omega_n^* - U^*k_x^*)}{c^{*2}} \nu \Bigg|_{y^*=y_s-\varepsilon} \tag{A7}$$

The series solution of equation (A1) about $y^* = y_s$ is then used to determine $\Pi(y_s + \alpha)$, while $\nu(y_s + \alpha)$ is found from

$$\nu(y_s + \alpha) = \frac{-ic^{*2}\Pi'}{(\omega_n^* - U^*k_x^*)} \Bigg|_{y^*=y_s+\alpha} \tag{A8}$$

Equations (20) and (21) are then integrated numerically from $y^* = y_s + \alpha$ to $y^* = 1$, subject to the initial conditions given by equation (A8) and to the known value of Π at $y^* = y_s + \alpha$. (See fig. 2.)

The parameter α is such that

$$0 \leq \alpha \leq \varepsilon \tag{A9}$$

and

$$y_s + \alpha \leq 1 \tag{A10}$$

If the inequality

$$y_s + \varepsilon \leq 1 \tag{A11}$$

is satisfied, α is set equal to ε. Otherwise α is given by

$$\alpha = 1 - y_s \tag{A12}$$

Since $\varepsilon << 1$, it is assumed that sufficient accuracy is maintained in the solution for Π, even if the series of equations (A3) and (A4) are truncated after the term multiplying τ^4. Thus, for $0 < \tau \leq \varepsilon$, it is assumed that Π is given by solutions of the equation

$$\begin{aligned}(a_{01}\tau + a_{02}\tau^2 + a_{03}\tau^3 + a_{04}\tau^4)\Pi'' + \\ (a_{10} + a_{11}\tau + a_{12}\tau^2 + a_{13}\tau^3 + a_{14}\tau^4)\Pi' + \\ (a_{21}\tau + a_{22}\tau^2 + a_{23}\tau^3 + a_{24}\tau^4)\Pi = 0\end{aligned} \tag{A13}$$

The coefficients a_{ij} of this equation are related to the functions $U^*(y^*)$ and $c^*(y^*)$ in appendix B. These coefficients are also presented in appendix C for the special case where $U^*(y^*)$ is given by the Pohlhausen solution (ref. 3) for flow over a flat plate

$$U^* = \frac{U_\infty}{c_\infty} (2y^{*2} - 2y^{*3} + y^{*4}) \tag{A14}$$

and $c^*(y^*) = 1$.

The solution of equation (A13) in the neighborhood of $\tau = 0$ can be determined by the method of Frobenius (refs. 4 and 5) and is of the form

$$\Pi(\tau) = A\ \Pi_1(\tau) + B\ \Pi_2(\tau) \tag{A15}$$

where $\Pi_1(\tau)$ and $\Pi_2(\tau)$ are independent solutions given by (refs. 5 and 6)

$$\Pi_1(\tau) = \tau^3 \sum_{n=0}^{\infty} b_n \tau^n \tag{A16}$$

$$\Pi_2(\tau) = d\Pi_1(\tau)\ \mathrm{Ln}(\tau) + 1 + \sum_{n=1}^{\infty} c_n \tau^n \tag{A17}$$

Here, the constant d is given by

$$d = \frac{-[a_{21}(a_{11} + a_{02}) + a_{22}\ a_{01}]}{3a_{01}^2} \tag{A18}$$

and the constants b_n and c_n can be determined through use of the equations presented in appendixes D and E. It should be noted that this solution is invalid whenever

$$a_{01} = -k_x^*\left(c^{*2} \frac{dU^*}{dy}\right)\bigg|_{y^*=y_s} = 0 \tag{A19}$$

Equation (A19) can be satisfied only when

$$\frac{dU^*}{dy^*}\bigg|_{y_s} = 0 \tag{A20}$$

For the Pohlhausen velocity profile, this implies that $y_s = 1$. If equation (A19) is satisfied, the solution procedure is terminated.

The values of $\Pi(y_s+\alpha)$ and $\nu(y_s+\alpha)$ can be determined from equation (A15) once the constants A and B are found. These constants are related to $\Pi(y_s-\varepsilon)$ and $\nu(y_s-\varepsilon)$ by

$$A = \left. \frac{c^{*2}\Pi\Pi_2' - i(\omega_n^* - U^*k_x^*)\ \nu\Pi_2}{c^{*2}(\Pi_1\Pi_2' - \Pi_1'\Pi_2)} \right|_{\tau=-\varepsilon} \tag{A21}$$

$$B = \left. \frac{c^{*2}\Pi\Pi_1' - i(\omega_n^* - U^*k_x^*)\ \nu\Pi_1}{c^{*2}(\Pi_2\Pi_1' - \Pi_1\Pi_2')} \right|_{\tau=-\varepsilon} \tag{A22}$$

The quantities $\Pi(y_s+\alpha)$ and $\nu(y_s+\alpha)$ can be determined from equations (A15) and (A2).

The solution is now complete except for locating the singular points. These points are given by the solution of the equation

$$(\omega_n^* - U^*k_x^*)_{y_s} = 0 \tag{A23}$$

For the Pohlhausen solution, this implies that

$$U^*\Big|_{y_s} = \frac{\omega_n^*}{k_x^*} = (2y_s - 2y_s^3 + y_s^4)\ \frac{U_\infty}{c_\infty} \tag{A24}$$

Thus,

$$y_s^4 - 2y_s^3 + 2y_s - \frac{c_\infty\omega_n^*}{U_\infty k_x^*} = 0 \tag{A25}$$

Letting

$$\phi = \frac{c_\infty\omega_n^*}{U_\infty k_x^*} \tag{A26}$$

it is clear that

$$0 \le \phi \le 1 \tag{A27}$$

since

$$0 \le y_s \le 1 \tag{A28}$$

For y_s and ϕ within this range, the solution of equation (A25) for y_s may be written as (ref. 7)

$$y_s = \frac{1 - (1 + z)^{1/2}}{2} + \frac{\left[2 - z + 2/(1 + z)^{1/2}\right]^{1/2}}{2} \qquad \text{(A29)}$$

where

$$z = A_s + B_s \qquad \text{(A30)}$$

$$A_s = \left\{2(1 - \phi) + \left[4(1 - \phi)^2 - \frac{64(1 - \phi)^3}{27}\right]^{1/2}\right\}^{1/3} \qquad \text{(A31)}$$

$$B_s = \left\{2(1 - \phi) - \left[4(1 - \phi)^2 - \frac{64(1 - \phi)^3}{27}\right]^{1/2}\right\}^{1/3} \qquad \text{(A32)}$$

The solution given is valid as long as ϕ and y_s are restricted to the regions given in equations (A27) and (A28).

APPENDIX B

CONSTANTS a_{ij} FOR GENERAL CASE[1] [2]

$$a_{01} = -k_x^*(c^{*2}U_1^*)$$

$$a_{02} = \frac{-k_x^*}{2}(c^{*2}U_2^* + 4c^*c_1^*U_1^*)$$

$$a_{03} = -k_x^*\left[\frac{c^{*2}U_3^*}{6} + (c_1^{*2} + c^*c_2^*)\,U_1^* + c^*c_1^*U_2^*\right]$$

$$a_{04} = \frac{-k_x^*}{24}\left[c^{*2}U_4^* + 8c^*c_1^*U_3^* + 12U_2^*(c_1^{*2} + c^*c_2^*) + 8U_1^*(3c_1^*c_2^* + c^*c_3^*)\right]$$

$$a_{10} = -2a_{01}$$

$$a_{11} = 2(c^{*2}U_2^* + c^*c_1^*U_1^*)k_x^*$$

$$a_{12} = (3U_2^*c^*c_1^* + U_3^*c^{*2})k_x^*$$

$$a_{13} = \frac{k_x^*}{3}\left[-(3c_1^*c_2^* + c^*c_3^*)U_1^* + 3(c_1^{*2} + c^*c_2^*)U_2^* + 5c^*c_1^*U_3^* + c^{*2}U_4^*\right]$$

$$a_{14} = \frac{k_x^*}{6}\left[-(3c_2^{*2} + 4c_1^*c_3^* + c^*c_4^*)U_1^* + (3c_1^*c_2^* + c^*c_3^*)U_2^*\right] + \frac{k_x^*}{12}\left[8(c_1^{*2} + c^*c_2^*)U_3^* + 7c^*c_1^*U_4^* + c^{*2}U_5^*\right]$$

$$a_{21} = -k_x^{*2}a_{01}$$

$$a_{22} = -k_x^{*2}a_{02}$$

$$a_{23} = -k_x^{*2}\left[a_{03} + k_x^*U_1^{*3}\right]$$

$$a_{24} = -k_x^{*2}\left[a_{04} + \frac{3}{2}\,(U_1^{*2}U_2^*)k_x^*\right]$$

---

[1] The functions U_i^* and c_i^* are defined by the equations

$$U_i^* = \frac{d^iU^*}{dy^{*i}} \quad \text{and} \quad c_i^* = \frac{d^ic^*}{dy^{*i}} \quad \text{for } i = 1, 2, 3, 4, 5.$$

[2] All functions are to be evaluated at $y^* = y_s$.

APPENDIX C

CONSTANTS a_{ij} FOR POHLHAUSEN FLOW AND CONSTANT[1] SOUND SPEED

$$a_{01} = -k_x^*(2 - 6y_s^2 + 4y_s^3)\,\frac{U_\infty}{c_\infty}$$

$$a_{02} = -k_x^*(6y_s^2 - 6y_s)\,\frac{U_\infty}{c_\infty}$$

$$a_{03} = -k_x^*\,\frac{U_\infty}{c_\infty}\,(4y_s)$$

$$a_{04} = -k_x^*\,\frac{U_\infty}{c_\infty}$$

$$a_{10} = -2a_{01}$$

$$a_{11} = -4a_{02}$$

$$a_{12} = -6a_{03}$$

$$a_{13} = -8a_{04}$$

$$a_{14} = 0$$

$$a_{21} = -k_x^{*2}a_{01}$$

$$a_{22} = -k_x^{*2}a_{02}$$

$$a_{23} = -k_x^{*2}a_{03} + a_{01}{}^3$$

$$a_{24} = 3a_{01}^2a_{02} - k_x^{*2}a_{04}$$

---

[1] For these equations, y_s is defined by equation (A29).

APPENDIX D

FORMULAS FOR CALCULATION OF THE CONSTANTS b_n

$$b_0 = 1$$

$$b_1 = \frac{-3(2a_{02} + a_{11})}{4a_{01}}$$

$$b_2 = \frac{-\{4(3a_{02} + a_{11})b_1 + [3(2a_{03} + a_{12}) + a_{21}]\}}{10a_{01}}$$

$$b_3 = \frac{-\{5(4a_{02} + a_{11})b_2 + [4(3a_{03} + a_{12}) + a_{21}]b_1 + [3(2a_{04} + a_{13}) + a_{22}]\}}{18a_{01}}$$

$$b_4 = \frac{-\{(3a_{14} + a_{23}) + [4(3a_{04} + a_{13}) + a_{22}]b_1 + [5(4a_{03} + a_{12}) + a_{21}]b_2 + 6[5a_{02} + a_{11}]b_3\}}{28a_{01}}$$

For $n \geq 5$, b_n is calculated as follows:

$$b_n = \frac{-\{(n + 2)\ [(n + 1)a_{02} + a_{11}]b_{n-1} + [(n + 1)(n\ a_{03} + a_{12}) + a_{21}]b_{n-2}\}}{(n + 3)na_{01}}$$

$$- \frac{\{n[(n - 1)a_{04} + a_{13}] + a_{22}\}b_{n-3}}{(n + 3)na_{01}} - \frac{\{[(n - 1)a_{14} + a_{23}]b_{n-4} + a_{24}b_{n-5}\}}{(n + 3)na_{01}}$$

APPENDIX E

FORMULAS FOR CALCULATION OF THE CONSTATNS c_n[1,2]

$$c_1 = 0$$

$$c_2 = \frac{a_{21}}{2\,a_{01}}$$

$$c_3 \approx \text{Arbitrary}$$

$$c_4 = \frac{-\{3(a_{11} + 2\,a_{02})c_3 + c_2[2(a_{12} + a_{03}) + a_{21}] + a_{23} + d[5(a_{01}b_1 + a_{02}) + a_{11}]\}}{4a_{01}}$$

$$c_5 = \frac{-\{4c_4(a_{11} + 3a_{02}) + c_3[3(a_{12} + 2a_{03}) + a_{21}] + c_2[2(a_{13} + a_{04}) + a_{22}]\}}{10\,a_{01}} - \frac{\{d[7a_{01}b_2 + b_1(7a_{02} + a_{11}) + 5a_{03} + a_{12}] + a_{24}\}}{10a_{01}}$$

$$c_6 = \frac{-\{5c_5(a_{11} + 4a_{02}) + c_4[4(a_{12} + 3a_{03}) + a_{21}] + c_3[3(a_{13} + 2a_{04}) + a_{22}] + c_2(2a_{14} + a_{23})\}}{18a_{01}} - \frac{d[9a_{01}b_3 + (9a_{02} + a_{11})b_2 + (7a_{03} + a_{12})b_1 + 5a_{04} + a_{13}]}{18a_{01}}$$

For $n \geq 7$, c_n is given by

$$c_n = \frac{-(n-1)[a_{11} + (n-2)\,a_{02}]\,c_{n-1}}{n(n-3)a_{01}} - \frac{\{(n-2)[a_{12} + (n-3)a_{03}] + a_{21}\}c_{n-2}}{n(n-3)a_{01}}$$

(Equation continued on next page.)

---

[1] The arbitrary constant c_3 may be set equal to zero.

[2] The constant d is given in equation (A18).

$$- \frac{\{(n - 3)[a_{13} + (n - 4)a_{04})] + a_{22}\}c_{n-3}}{n(n - 3)a_{01}}$$

$$- \frac{\{[(n - 4)\ a_{14} + a_{23}]\ c_{n-4} + a_{24}\ c_{n-5}\}}{n(n - 3)\ a_{01}}$$

$$- \frac{a\{b_{n-3}(2n - 3)a_{01} + b_{n-4}[(2n - 3)a_{02} + a_{11}] + b_{n-5}[(2n - 5)a_{03} + a_{12}]\}}{n(n - 3)a_{01}}$$

$$- \frac{d\{b_{n-6}[(2n - 7)a_{04} + a_{13}] + b_{n-7}a_{14}\}}{n(n - 3)a_{01}}$$

REFERENCES

1. Blokhintsev, D. I.: Acoustics of a Nonhomogeneous Moving Medium. NACA TM 1399, 1956.

2. Goldstein, Marvin E.: Aeroacoustics. NASA SP-346 1974.

3. Schlichting, Hermann (J. Kestin, transl.): Boundary-Layer Theory, Seventh ed. McGraw-Hill Book Co., c.1979.

4. Ince, E. L.: Ordinary Differential Equations. Dover Publ., Inc., 1956.

5. Boyce, William E.; and Di Prima, Richard C.: Elementary Differential Equations and Boundary Value Problems, Second ed. John Wiley & Sons, Inc., 1969.

6. Sánchez, David A.: Ordinary Differential Equations and Stability Theory: An Introduction. Dover Publ., Inc., c.1968.

7. Beyer, William H., ed.: Standard Mathematical Tables, Twenty-fourth ed. CRC Press, Inc., 1976, p. 85.

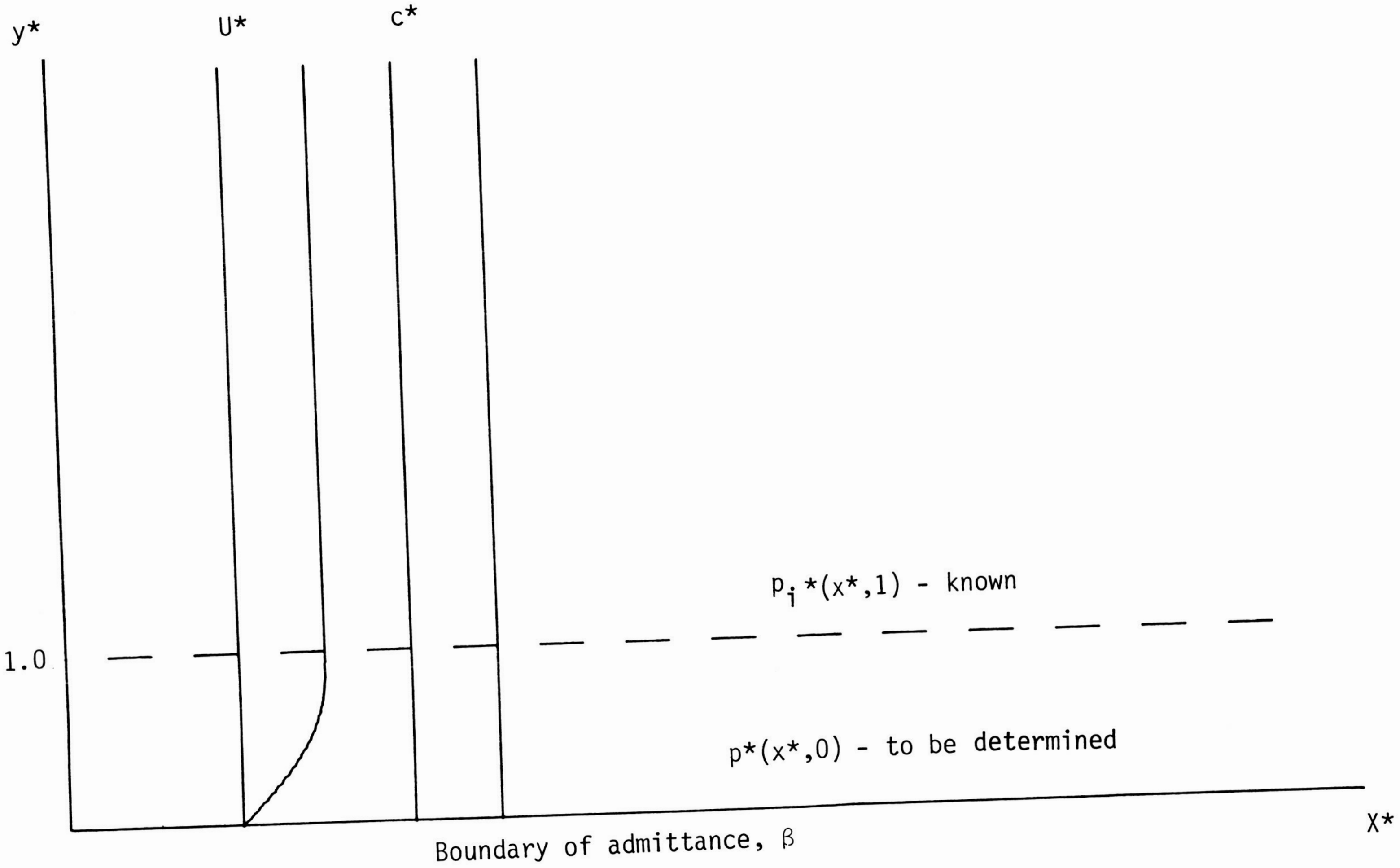

Figure 1.- Sketch of problem.

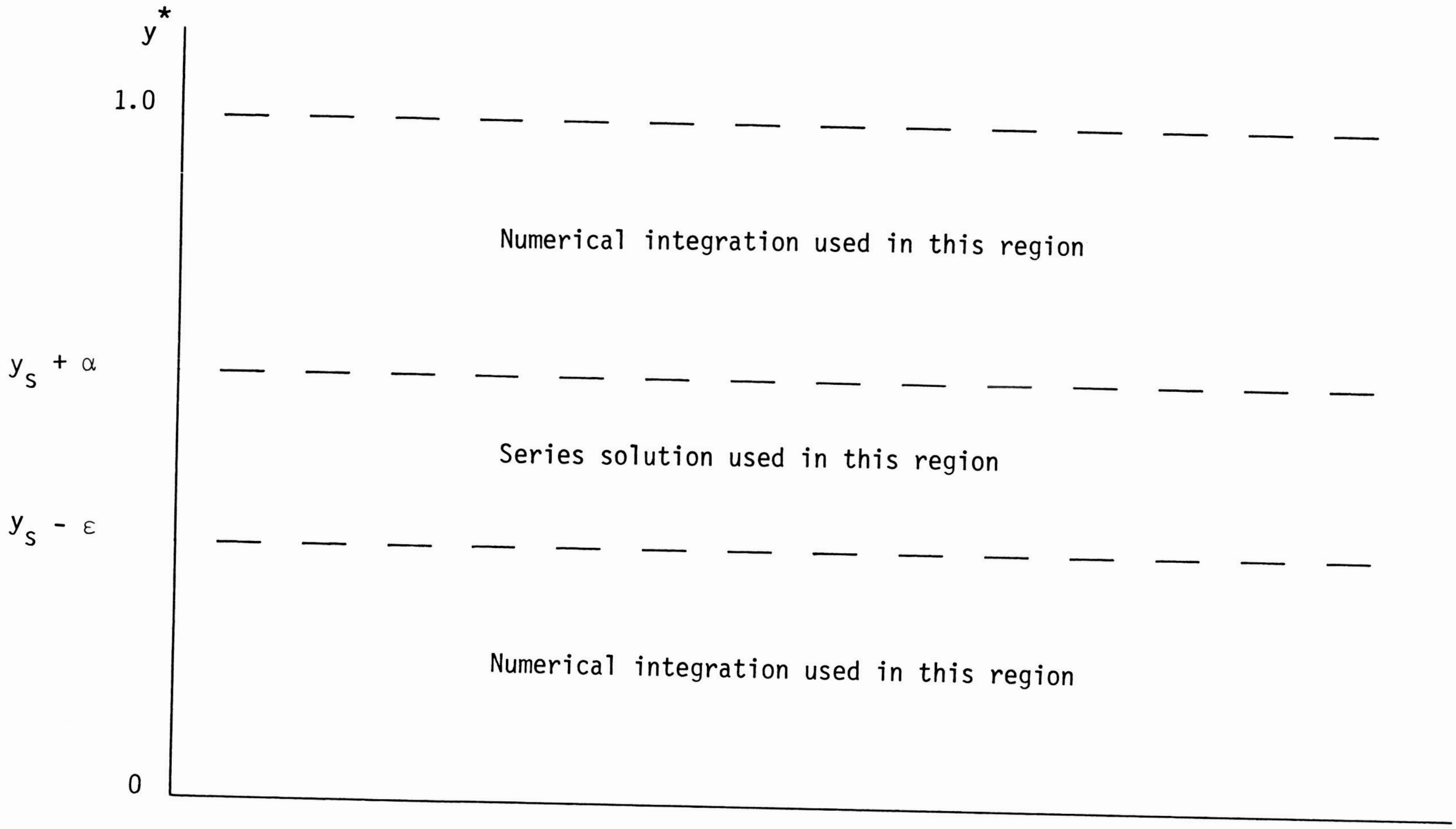

Figure 2.- Solution procedure used in each region.

12.2 TONE PROPAGATION MODULE

Gerry L. McAninch
Langley Research Center

INTRODUCTION

The transformation of pure tone data from the source frame of reference to the observer frame of reference and the determination of the sound field at each observer location is accomplished in a different manner than the same transformation of broadband data. The Tone Propagation Module performs this transformation for pure tone data, whereas the Propagation Module (PRO) must be used for the transformation of broadband data.

The five steps required to transform pure tone data from the source reference frame to the observer reference frame, in the order in which they are performed, are

1. Interpolation of the input source noise data, given as a function of emission time and observer directivity angle, to provide the mean-square acoustic pressure at the observer location as a function of observer time and source frequency
2. Doppler shift of the source frequencies to give the mean-square acoustic pressure at the observer location as a function of observer time and observed frequency
3. Determination of spherical spreading losses and characteristic impedance change effects
4. Determination of atmospheric absorption losses
5. Determination of ground reflection and attenuation losses

The resulting output table provides the mean-square acoustic pressure as a function of frequency, reception time, and observer.

SYMBOLS

a	incoherence constant
C	coherence coefficient
c	speed of sound, m/s (ft/s)
f	frequency, Hz

G	ground effects factor
g_r	acceleration due to gravity, m/s^2 (ft/s^2)
H	altitude, m (ft)
h	observer height, m (ft)
k	wave number, $2\pi f/c$, 1/m (1/ft)
M	source Mach number at emission time
M_a	molecular weight of air
n	frequency harmonic number
o	observer index
$\langle p^2 \rangle$	mean-square acoustic pressure, N^2/m^4 (lb^2/ft^4)
$\langle p^2 \rangle^* \rvert_{abs}$	mean-square acoustic pressure accounting for atmospheric absorption
$\langle p^2 \rangle^* \rvert_{gr}$	mean-square acoustic pressure accounting for ground effects
R	magnitude of spherical wave reflection coefficient
$\overline{R}$	universal gas constant, $m^2/(K\text{-}s^2)$ ($ft^2/(°R\text{-}s^2)$)
r	distance, m (ft)
Δr	path length difference, m (ft)
r_2	source-to-image distance, m (ft)
SPL	sound pressure level, dB
T	temperature, K (°R)
t	time, s
$U(s)$	unit step function
$W(z)$	complex error function
y	coordinate
α	argument of spherical wave reflection coefficient
γ	elevation angle

η	dimensionless frequency; $2\pi\rho f_o/\sigma$
Θ	incidence angle, deg
θ	polar directivity angle, deg
μ	absorption coefficient, nepers
$\bar{\mu}$	average absorption coefficient, nepers
ν	normalized ground admittance
θ_w	angle between source velocity vector and vector joining source and observer at emission time
ρ	density, kg/m^3 (slug/ft^3)
σ	specific flow resistance of ground, kg/(m^3-s) (slug/(ft^3-s))
ϕ	azimuthal directivity angle, deg
Ω	solid angle, sr

Subscripts:

a	ambient
e	emission
o	observed
r	standard sea level
s	source

Superscript:

*	dimensionless quantity

INPUT

The input to this module consists of one or more source noise data tables computed for the same source coordinate system on the aircraft. These data tables consist of pure tone data. When two or more data tables are input they are merged prior to the transformation to the observer frame of reference.

r_s	source radius, m (ft)
σ	specific flow resistance of ground, kg/(m^3-s) (slug/(ft^3-s))

Δf	frequency bandwidth, Hz

Source Noise Data Table

f_s	source frequency, Hz
θ_e	polar directivity angle, deg
ϕ_e	azimuthal directivity angle, deg
t_e	emission time, s
$\langle p^2(f_s,\theta_e,\phi_e,t_e)\rangle^*$	mean-square acoustic pressure, re $\rho_a^2 c_a^4$

Source Geometry Table

t	reception time, s
o	observer index
$r_e(t,o)$	distance, m (ft)
$t_e(t,o)$	emission time, s
$\theta_e(t,o)$	polar directivity angle, deg
$\gamma_e(t,o)$	elevation angle, deg
$h(o)$	observer height, m (ft)

Wind Axes Geometry Table

$\theta_w(t_e,o)$	angle between source velocity vector and vector joining source and observer

Atmospheric Properties Table

y	altitude, $M_a g_r(H - H_1)/\overline{R}T_r$
$c^*(y)$	speed of sound, re c_r
$\rho^*c^*(y)$	characteristic impedance, re $\rho_r c_r$
$\rho^*(y)$	density, re ρ_r

Absorption Coefficient Table

f	frequency, Hz
y	altitude, $M_a g_r (H - H_1)/\overline{R}T_r$
$\overline{\mu}$	average absorption coefficient, nepers/wavelength

Engine Variable Table

t	source time, s
$M(t)$	aircraft Mach number

OUTPUT

This module produces a table of the mean-square acoustic pressure as a function of observed frequency, time, and observer.

Received Noise Data Table

n	frequency harmonic number
t	observation time, s
o	observer index
$c_a^*(o)$	speed of sound at observer, re c_r
$\rho_a^*(o)$	density at observer, re ρ_r
$f_o(n,t,o)$	observed frequency, Hz
$<p^2(n,t,o)>^*$	mean-square acoustic pressure, re $\rho_a^2 c_a^4$

METHOD

Noise Data Interpolation

Data tables from two or more sources in the same reference frame may be input simultaneously. If two or more data tables are input they are first merged, with components at equal frequencies summed, to provide a single table of mean-square acoustic pressure as a function of source frequency f_s, emission time t_e, polar directivity angle θ, and azimuthal directivity angle ϕ. That is, this input table provides $<p^2(f_s,\theta_e,\phi_e,t_e)>^*$.

The transformation to the observer location is accomplished by using $\theta_e(t,o)$, $\phi_e(t,o)$, and $t_e(t,o)$, as provided by the Geometry Module, to convert $<p^2(f_s,\theta_e,\phi_e,t_e)>^*$ to $<p^2(f_s,t,o)>^*$.

Doppler Shift

Because of the relative velocity between the source and the observer, the observed frequencies are not the same as the source frequencies. The observer frequency is related to the source frequency through the equation

$$f_o(n,t,o) = \frac{f_s(n)}{1 - M \cos \theta_W} \tag{1}$$

where M is the source Mach number, and θ_W is the angle the source velocity vector makes with the vector joining the source and observer, both quantities defined at the emission time, as shown in figure 1. This step yields a table of mean-square acoustic pressure, uncorrected for the various attenuation mechanisms, as a function of harmonic number and observation time for each observer $\langle p^2(n,t,o)\rangle^*$.

Spherical Spreading and Characteristic Impedance Change Effects

The next step is to account for the attenuation due to spherical spreading and the change in mean-square pressure attributable to the difference in the characteristic impedance between the source and observer locations. These are determined by requiring conservation of acoustic energy.

Figure 2 provides a schematic diagram of a conical ray tube of solid angle $d\Omega$. The acoustic energy passing through any cross section of the ray tube, per unit time, is the product of the acoustic intensity and the cross-sectional area of the tube. Conservation of energy considerations implies that this product must be independent of the cross section of the tube considered. This is expressed by the equation

$$\frac{\langle p^2(r_s)\rangle}{(\rho c)\big|_{r_s}} r_s^2 \, d\Omega = \frac{\langle p^2(r_o)\rangle}{(\rho c)\big|_{r_o}} r_o^2 \, d\Omega \tag{2}$$

where r_s and r_o indicate source and observer locations, respectively.

Equation (2) may be solved for the mean-square acoustic pressure at the observer location in terms of the mean-square acoustic pressure at the source location, the characteristic impedance ratio $(\rho c)_{r_s}/(\rho c)_{r_o}$, and the spherical spreading or area ratio term $(r_s/r_o)^2$.

In dimensionless form, this relationship is

$$\langle p^2(r_o)\rangle^* = \frac{\rho^* c^*(y_o)}{\rho^* c^*(y_s)} \left(\frac{r_s}{r_o}\right)^2 \langle p^2(r_s)\rangle^* \tag{3}$$

where $\rho^*c^*(y_o)$ and $\rho^*c^*(y_s)$ are determined from the Atmospheric Properties Table for the observer height and source height, respectively. The dimensionless heights at the source and observer are given by

$$y_o = M_a g_r h/T_r\overline{R} \tag{4}$$

and

$$y_s = M_a g_r\,(r \sin\gamma + h)/T_r\overline{R} \tag{5}$$

The observer distance r, observer height h, and elevation angle γ, are found in the Geometry Table.

Atmospheric Absorption Losses

The atmospheric absorption losses are now determined. The atmospheric absorption coefficient μ is a function of frequency $f_o(n,t,o)$ and altitude y. The average absorption coefficient $\overline{\mu}$ is defined as

$$\overline{\mu}(f,y_s,y_o) = \frac{1}{y_s - y_o} \int_{y_s}^{y_o} \overline{\mu}(y,f)\ d\overline{y} = \frac{y_s\ \overline{\mu}(f,y_s) - y_o\ \overline{\mu}(f,y_o)}{y_s - y_o} \tag{6}$$

where y_o and y_s are given by equations (4) and (5), respectively, and $\overline{\mu}$ is obtained from the Atmospheric Absorption Table. The equation

$$\langle p^2\rangle^*\big|_{abs} = \langle p^2\rangle^*\ e^{-2(\overline{\mu}f/c_r)(r_o-r_s)} \tag{7}$$

provides the mean-square pressure at the observer. Equations (6) and (7) must be evaluated by using the observed frequency $f_o(n,t,o)$.

Ground Effects

The ground effect model used in ANOPP is based on the Chien-Soroka theory (ref. 1), coupled with the impedance function of Delany and Bazley (ref. 2).

The geometry required for the calculation of the ground effects is shown in figure 3. The source is located at an altitude H above a ground plane. The observer, located at a height h from the ground plane, receives sound which propagates along a direct path r and along a reflected path r_2. The path length difference $\Delta r = r_2 - r$ is the most significant parameter used in the ground effects calculation. Use of the law of cosines shows that Δr is given by

$$\Delta r = (r^2 + 4h^2 + 4rh \sin \gamma)^{1/2} - r \tag{8}$$

The derivation of the Chien-Soroka theory is presented in reference 1. The resulting expression for the mean-square pressure with ground effects is

$$\langle p^2 \rangle^* \Big|_{gr} = \langle p^2 \rangle^* \Big|_{abs} \left[1 + R^2 + 2RC \cos (\alpha + k \, \Delta r) \right] \tag{9}$$

where $\langle p^2 \rangle^* \big|_{abs}$ is the free-field mean-square acoustic pressure, in this case corrected for spherical spreading, characteristic impedance change effects, and atmospheric absorption. Further, C is the coherence coefficient, and k is the wave number based on observed frequency.

$$k = 2\pi \, f_0(n,t,o)/c(o) \tag{10}$$

where c(o) is the sound speed at the observer. The quantities R and α are the magnitude and argument, respectively, of the complex spherical wave reflection coefficient. The bracketed term in equation (9)

$$G = 1 + R^2 + 2RC \cos (\alpha + k \, \Delta r) \tag{11}$$

is the ground effects factor.

The coherence coefficient is the fraction of the initial acoustic energy which remains in phase throughout the propagation process. A reasonable approximation for the coherence coefficient is made by assuming a Gaussian distribution of the form

$$C = \exp \left[-(ak \, \Delta r)^2 \right] \tag{12}$$

where a is the incoherence constant. Generally, a is given the value 0.01 which yields a value of 0.37 for C at $k \, \Delta r = 32\pi$. Substituting equation (12) into equation (11) yields

$$G = 1 + R^2 + 2R \exp \left[-(ak\Delta r)^2 \right] \cos (\alpha + k \, \Delta r) \tag{13}$$

To account for a finite bandwidth, equation (13) must be averaged over the frequency width Δf to provide the relation

$$G = 1 + R^2 + 2R \exp\left[-(ak\ \Delta r)^2\right] \frac{\cos(\alpha + k\ \Delta r)\sin(\Delta k\ \Delta r/2)}{(\Delta k\ \Delta r/2)} \qquad (14)$$

where $\Delta k = 2\pi\ \Delta f/c(o)$.

The complex spherical wave reflection coefficient, as determined in reference 1, is

$$Re^{i\alpha} = \Gamma + (1 - \Gamma)\ F(\tau) \qquad (15)$$

where Γ is the plane wave reflection coefficient

$$\Gamma = \frac{\cos\Theta - \nu}{\cos\Theta + \nu} \qquad (16)$$

and $F(\tau)$ is given by

$$F(\tau) = 1 - \sqrt{\pi}\ \tau\ \ W(i\tau) \qquad (17)$$

with

$$\tau = (kr_2/2i)^{1/2}\ (\cos\Theta + r) \qquad (18)$$

and W is the complex error function

$$W(z) = \frac{i}{\pi} \int_{-\infty}^{\infty} \frac{e^{-t^2}}{z - t}\ dt\ \ (\mathrm{Im}(z) > 0) \qquad (19)$$

Further, $\cos\Theta$ is given by

$$\cos\Theta = \frac{r \sin\gamma + 2h}{r_2} \qquad (20)$$

For $|\tau| > 10$, an asymptotic approximation for the complex error function allows $F(\tau)$ to be expressed as

$$F(\tau) = -2\sqrt{\pi}\ U(-R_e\tau)\ \tau e^{\tau^2} + \frac{1}{2\tau^2} - \frac{3}{(2\tau^2)^2} \qquad (21)$$

where U is the unit step function

$$U(s) = \begin{Bmatrix} 1 & (s > 0) \\ 1/2 & (s = 0) \\ 0 & (s < 0) \end{Bmatrix} \qquad (22)$$

The remaining parameter to be determined is the normalized ground admittance ν. The empirical expression

$$\nu = \left[1 + (6.86\eta)^{-0.75} + i(4.36\eta)^{-0.73}\right]^{-1} \tag{23}$$

developed by Delany and Bazley (ref. 2) is used to determine ν. In equation (23), η is the dimensionless frequency defined as

$$\eta = 2\pi\rho f_0/\sigma \tag{24}$$

Here ρ is the air density at the observer location and σ is the specific flow resistance of the ground. A graph of the ground admittance is given in figure 4.

With the relations for Γ and $F(\tau)$, the magnitude and phase of the complex spherical wave reflection coefficient are computed through use of the equations

$$R = \left|\Gamma + (1 - \Gamma)\ F(\tau)\right| \tag{25}$$

and

$$\alpha = \arg\left[\Gamma + (1 - \Gamma)\ F(\tau)\right] \tag{26}$$

For an acoustically hard surface ($\eta = 0$), the theory is greatly simplified since $\eta = 0$, $\Gamma = 1$, $R = 1$, and $\alpha = 0$. The expression for the ground effects factor (eq. (14)) reduces to

$$G = 2 + 2\exp\left[-(ak\ \Delta r)^2\right] \frac{\cos\ (k\ \Delta r)\ \sin\ (\Delta k\ \Delta r/2)}{(\Delta k\ \Delta r/2)} \tag{27}$$

The mean-square pressure, with ground effects, is now calculated through use of the relation

$$\langle p^2\rangle^*\Big|_{gr} = \langle p^2\rangle^*\Big|_{abs} G \tag{28}$$

This final calculation provides a table of mean-square pressure at the observer locations as a function of harmonic number, observation time, and observer index, that is $\langle p^2(n,t,o)\rangle^*$.

User Options

The Tone Propagation Module always performs the spherical spreading and characteristic impedance change calculations. The user has four options concerning the application of atmospheric attenuation and ground effects:

1. No atmospheric attenuation or ground effects

2. Atmospheric attenuation only

3. Ground effects only

4. Both atmospheric attenuation and ground effects

The standard output form for the noise data at the observer is the dimensionless mean-square acoustic pressure $\langle p^2 \rangle^*$ as a function of observed frequency.

Further, the user may request printed output of the sound pressure level (SPL), in decibels, defined as

$$\mathrm{SPL} = 10 \log_{10} \langle p^2 \rangle^* + 20 \log_{10} \left[\rho_a^* (c_a^*)^2 \right] + 197 \qquad (29)$$

Here ρ_a^* and c_a^* are determined from the Atmospheric Properties Table at the observer altitude y_o.

Applicability of Module

In general the solution for the pressure field of a moving source contains two terms: one of which corresponds to the radiation field while the other is negligible at distances from the source which are large in comparison with both the source dimensions and the wavelength. The assumptions used to develop the theory used in this module imply that the observer is in the radiation field of the source. Further, it is assumed that the observer is much closer to the ground than to the source, that is $h/r \ll 1$.

REFERENCES

1. Chien, C. F.; and Soroka, W. W.: Sound Propagation Along an Impedance Plane. J. Sound & Vib., vol. 43, no. 1, Nov. 8, 1975, pp. 9-20.

2. Delany, M. E.; and Bazley, E. N.: Acoustical Properties of Fibrous Absorbent Materials. Appl. Acoust., vol. 3, no. 2, Apr. 1970, pp. 105-116.

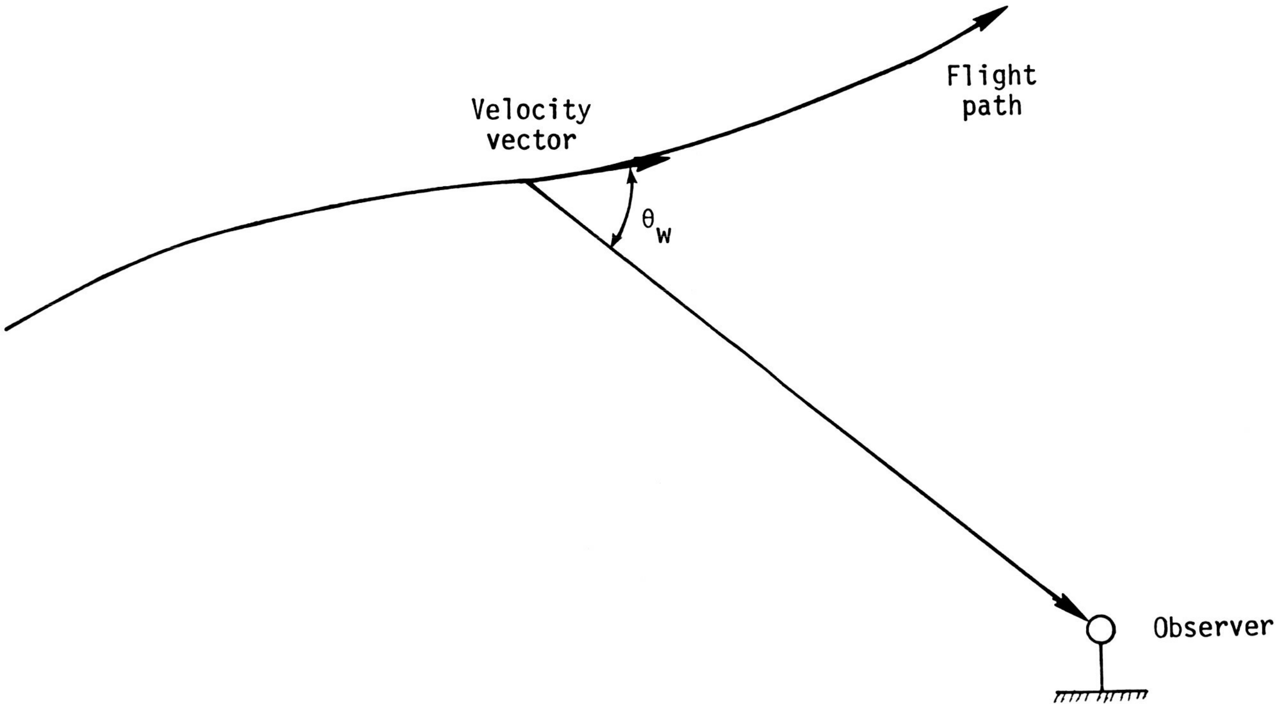

Figure 1.- Definition of source velocity vector, vector from source to observer, and angle θ_w.

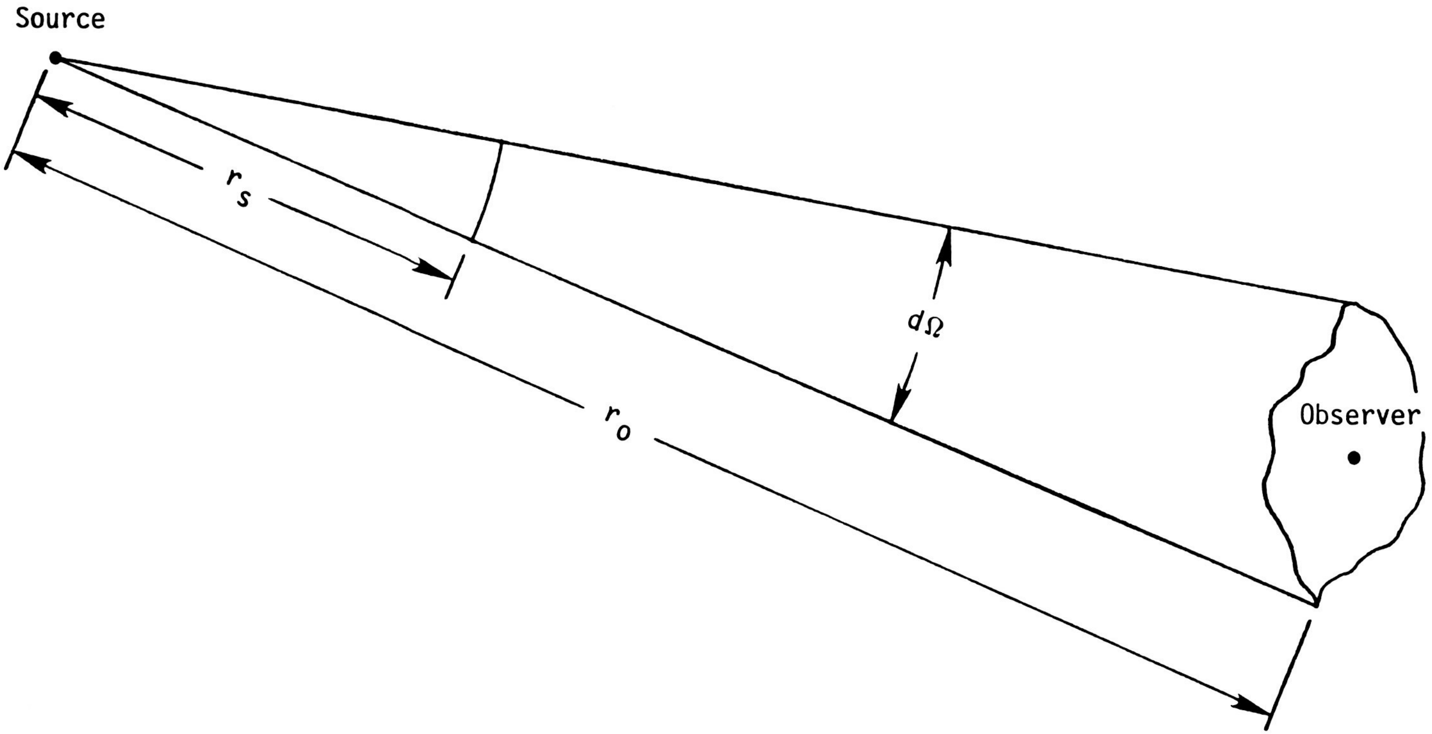

Figure 2.- Schematic diagram of a ray tube from a source to an observer.

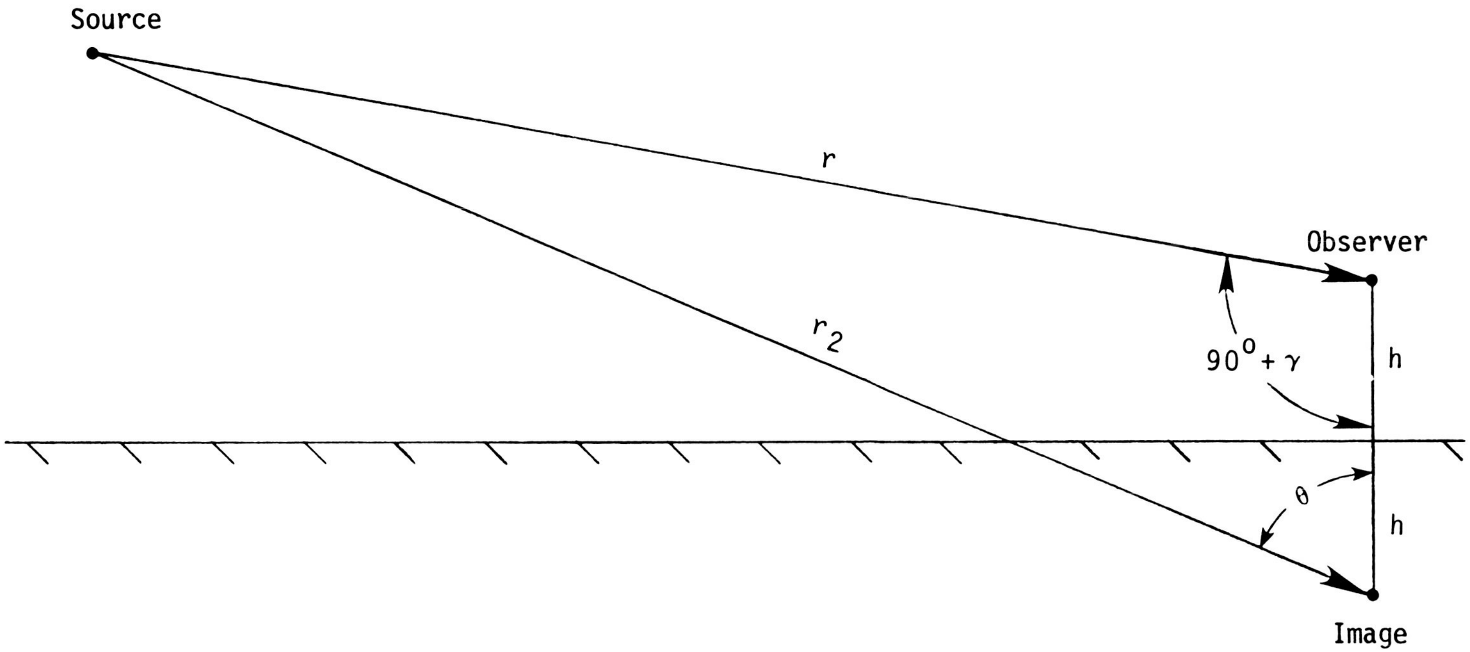

Figure 3.- Ground effects geometry.

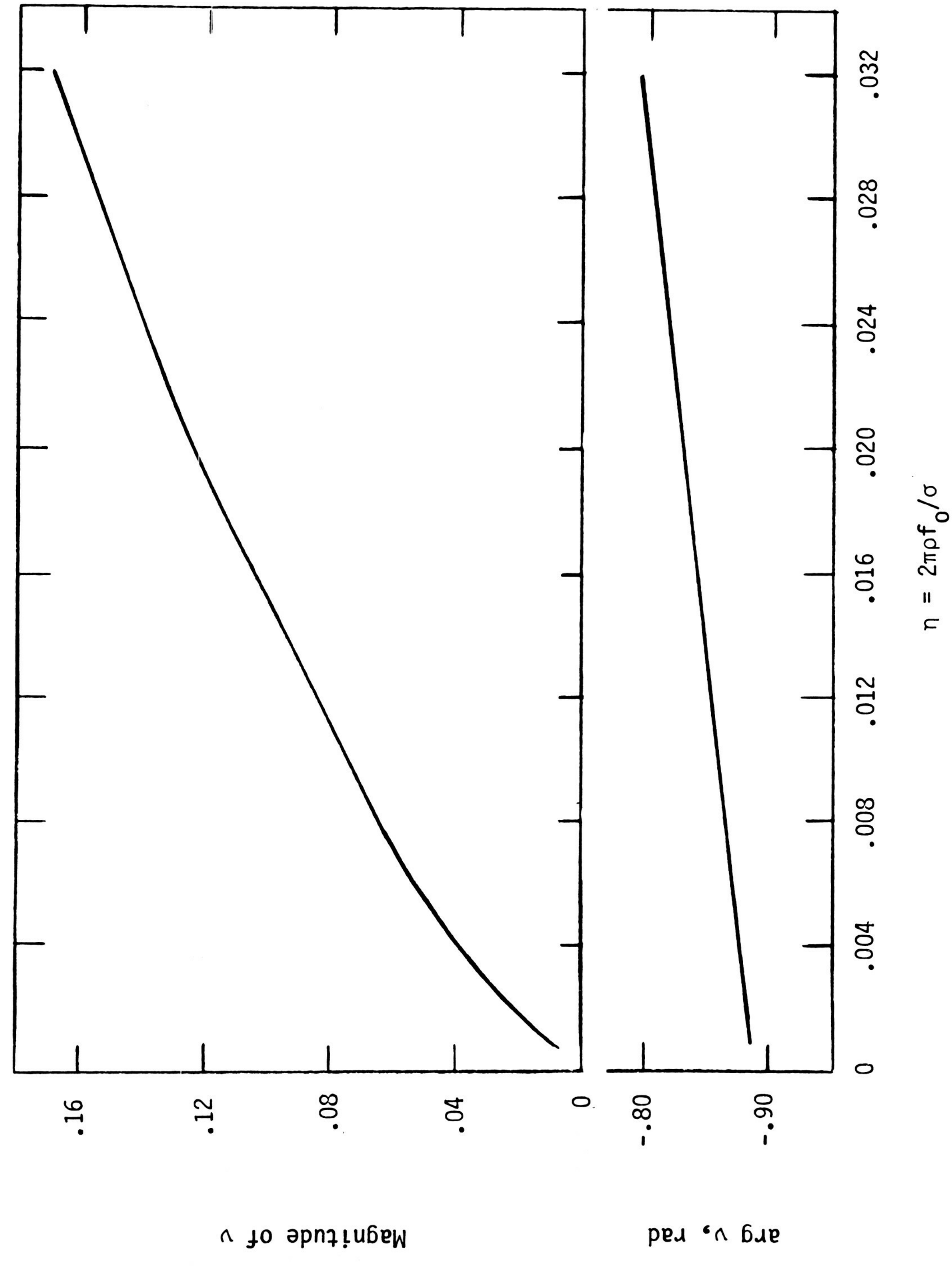

Figure 4.- Empirical function for normalized ground admittance.

1. Report No.
NASA TM-83199, Part 3

2. Government Accession No.

3. Recipient's Catalog No.

4. Title and Subtitle
Aircraft Noise Prediction Program Theoretical Manual -
Propeller Aerodynamics and Noise

5. Report Date
June 1986

6. Performing Organization Code
505-31-33-11

7. Author(s)
William E. Zorumski and Donald S. Weir, Editors

8. Performing Organization Report No.
L-15937

9. Performing Organization Name and Address
NASA Langley Research Center
Hampton, VA 23665-5225

10. Work Unit No.

11. Contract or Grant No.

12. Sponsoring Agency Name and Address
National Aeronautics and Space Administration
Washington, DC 20546-0001

13. Type of Report and Period Covered
Technical Memorandum

14. Sponsoring Agency Code

15. Supplementary Notes
William E. Zorumski: Langley Research Center, Hampton, Virginia.
Donald S. Weir: PRC Kentron, Inc., Hampton, Virginia.

Part 1 (N82-19946) and Part 2 (N82-19947) of this document were published February 1982.

16. Abstract

Analytic propeller noise prediction involves a sequence of computations culminating in the application of acoustic equations. This paper describes the prediction sequence currently used by NASA in its Aircraft Noise Prediction program (ANOPP). The elements of the sequence are called program modules. The first group of modules analyzes the propeller geometry, the aerodynamics, including both potential and boundary-layer flow, the propeller performance, and the surface loading distribution. This group of modules is based entirely on aerodynamic strip theory. The next group of modules deals with the noise prediction, based on data from the first group. Deterministic predictions of periodic thickness and loading noise are made with time-domain methods. Broadband noise is predicted by a semi-empirical method. Near-field predictions of fuselage surface pressures include the effects of boundary-layer refraction and scattering. Far-field predictions include atmospheric and ground effects.

17. Key Words (Suggested by Author(s))
Aircraft noise
Noise prediction
Propeller performance
Propeller noise

18. Distribution Statement
Unclassified - Unlimited

Subject Category 71

19. Security Classif. (of this report)
Unclassified

20. Security Classif. (of this page)
Unclassified

21. No. of Pages
266

22. Price
A12

For sale by the National Technical Information Service, Springfield, Virginia 22161

NASA-Langley, 1986